TECHNICKÁ UNIVERZITA V LIBERCI

Fakulta strojní

Katedra materiálu

Habilitační práce

K problematice fázové struktury a vysokoteplotních mechanických vlastností aluminidů na bázi FeAl a Fe_3Al v přítomnosti aditiv

2016 **Věra Vodičková**

Poděkování

Ráda bych na tomto místě poděkovala všem kolegům a spolupracovníkům, bez jejichž přispění by tato práce nevznikla. Především děkuji Prof. RNDr. Petru Kratochvílovi, DrSc. z Katedry fyziky materiálů MFF UK v Praze, který mě a mé kolegy k zajímavé problematice intermetalických slitin přivedl, za dlouholeté vedení a podněty, stejně jako za konzultace a praktické rady při přípravě této habilitační práce. Dále bych ráda poděkovala všem spoluautorům komentovaných prací za možnost podílet se na řešení jejich projektů, zejména Ing. Ferdinandu Dobešovi, DrSc., z Ústavu fyziky materiálů AV ČR. Za podporu a pomoc děkuji rovněž svým blízkým spolupracovníkům z Katedry materiálů v Liberci, a v neposlední řadě celé své rodině za podporu a trpělivost.

Abstrakt

Předkládaná habilitační práce představuje průřez výzkumem vlivu fázového složení na vysokoteplotní vlastnosti aluminidů železa s aditivy. Dlouhodobým cílem je uvést do praxe materiál na bázi aluminidu železa s dobrou vysokoteplotní odolností a vyrobený klasickou technologií.

Výzkum slitin s FeAl matricí s aditivy uhlíkem a křemíkem je historicky inspirován slitinami typu Pyroferal, vyvinutými v československu v padesátých letech minulého století. Ve slitinách s vyššími obsahy uhlíku byla potvrzena přítomnost karbidu Al_4C_3 ve struktuře slitin dopovaných křemíkem i ve slitinách bez křemíku a bylo prokázáno, že tato fáze účinně brání pohybu dislokací v matrici při vysokoteplotní deformaci.

Studium aluminidů železa na bázi Fe_3Al s přídavkem karbidotvorných prvků je zaměřeno na aditiva či kombinace aditiv zvyšujících vysokoteplotní odolnost slitin. Byl ukázán význam poměru legujících prvků Zr a C a stanoven jeho vliv na vysokoteplotní mechanické vlastnosti a vysokoteplotní oxidační odolnost.

Fázové složení slitin bylo studováno moderními metodami strukturní a fázové analýzy jako je elektronová mikroskopie, energiově disperzní analýza, rentgenová difrakce, případně difrakce zpětně odražených elektronů. Vliv fázového složení na vysokoteplotní mechanické vlastnosti byl sledován prostřednictvím vysokoteplotních testů v tahu či tlaku a testů creepové odolnosti.

Abstract

The submitted habilitation thesis represents a profile in research of phase composition effect on high temperature properties of iron aluminides with additives. The long term goal is to put into practice a material based on iron aluminide with good high temperature resistance (and produced by traditional technology).

The research of FeAl matrix alloys with additives carbon and silicon alloys is historically inspired by the Pyroferal alloys, developed here in the fifties of the last century. The presence of carbide Al_4C_3 was confirmed in the structure of alloys with higher carbon content doped by silicon and silicon-free. It has been shown that this phase effectively prevents the motion of dislocations in the matrix during the high temperature deformation.

The investigation of Fe_3Al-based iron aluminides with added carbid-forming elements is focused on additives or combinations of additives increasing the high temperature resistance

of alloys. It was shown the importance of the ratio of the alloying elements Zr and C. The effect of this ratio on high temperature mechanical properties and high temperature oxidation resistance was described.

The phase composition of alloys has been studied by modern methods of structural and phase analysis such as electron microscopy, energy dispersive analysis, X-ray diffraction, or electron backscatter diffraction. The influence of phase composition on high temperature mechanical properties was investigated by means of high-temperature tensile or pressure tests, and creep resistance tests.

Obsah

Úvod

Na konci 20. století se v českých zemích objevily snahy využít pozitivní fyzikální vlastnosti aluminidů železa. Kromě cenové dostupnosti (ve srovnání s niklem a chromem je hliník o mnoho lacinější) disponuje slitina také nízkou specifickou hmotností, dobrou odolností proti oxidaci a sulfidaci při vysokých teplotách, a rovněž odolnost vůči roztavené sklovině odvozená od vzniku oxidu hliníku je velmi zajímavá. Přesto mechanické vlastnosti při vysokých teplotách nejsou srovnatelné s chromniklovou ocelí a technologie (výroba potřebných zařízení) přináší řadu, jen zčásti dosud vyřešených, problémů.

První velmi úspěšné snahy o vývoj a zavedení slitiny na bázi FeAl se uskutečnily v padesátých letech minulého století v Praze pod vedením týmu Pluhař, Vyklický a Tůma. Vznikla tak v československém průmyslu velmi úspěšná slitina s obchodním označením Pyroferal, která byla bezprostředně poté uvedena do praxe. Její vývoj byl podnícen celoevropskou snahou o nalezení ekvivalentu pro náhradu žáruvzdorných a žárupevných ocelí, a tedy o snížení spotřeby velmi drahých strategických prvků používaných k legování těchto důležitých konstrukčních materiálů. Kromě českého Pyroferalu jsou známy slitiny Thermagal ve Francii nebo Čugal v bývalém Sovětském svazu.

Složení Pyroferalu podle ČSN 42 2484 je 29-31 hm.% (44.4-46.5 at.%) Al, 1.0-1.2 hm.% (3.4-4.0 at.%) C a s maximálním obsahem Si, S a P stanoveným normou. Matrice je tvořena tuhým roztokem C v intermetalické fázi FeAl s B2 strukturou, v níž jsou rozloženy v závislosti na obsahu C jehličkovité útvary karbidu Al_4C_3. Materiál má velmi dobrou žáruvzdornost, vynikající odolnost vůči chemickým vlivům prostředí. Úspěšně byla testována jeho odolnost vůči korozi, vůči roztavené sklovině a rovněž proti různým pecním atmosférám. Pevnost v ohybu pokojové teplotě - minimálně 350 MPa - a při teplotách jiných (zejména vyšších) a pevnost v tahu - při pokojové teplotě 250 MPa - lze zvýšit vhodnými aditivy.
Slitina byla od padesátých let 20. století využívána s úspěchem zejména v chemickém průmyslu (např. na lopatky kyzových pražicích pecí), pro výrobu cementačních hrnců a komůrek, roštnic parních kotlů pro elektrárny, krytí tepelně a erozně namáhaných trubek a pro výrobu součástí sklářských pecí a automatů.

Na konci 20. století se aluminidy železa typu FeAl staly znovu předmětem intenzívního výzkumu, který byl rozšířen také na slitiny na bázi Fe_3Al, a byl zaměřen zejména na uplatnění legur spojených se vznikem strukturních fází různého typu. Obě skupiny aluminidů železa se staly předmětem zájmu špičkových týmů v USA (ORNL) a v Německu (MPIE). Podobné snahy lze vysledovat ve Španělsku, ve Francii a v Polsku.

Také u nás vznikly v Praze, Brně, Liberci a Ostravě týmy, které subvencovány GAČR, MŠMT a MPO pracují dosud s cílem použít legurami modifikované aluminidy v různých prostředích pro různá technologická zařízení, a při tom popsat a vylepšit jejich fyzikální vlastnosti. V návaznosti na jejich potřeby a výsledky laboratorních zkoušek byly znalosti technologických postupů přípravy a zpracování aluminidů železa rozvinuty např. v PBS Velká Bíteš, Železárnách Hrádek u Rokycan, ČZ Strakonice apod. (odlévání větších šarží, válcování za horka, protlačování tyčí a trubek, lití součástek z pánve do písku).

Pro ilustraci situace uvádím problematiku, která byla v posledních letech předmětem výzkumu na TUL FS (Katedře materiálu):

- Vliv různých legur na mechanické vlastnosti aluminidů FeAl a Fe_3Al (testování v tahu i tlaku) při vysokých teplotách
- Studium struktury a popis vlivu fázového složení na mechanické vlastnosti studovaných slitin
- Studium vlivu tepelného zpracování na fázové složení a mechanické vlastnosti
- Studium obrábění aluminidů železa
- Studium svařování aluminidů železa
- Koroze aluminidů železa na vzduchu a ve sklovině
- Studium balistických vlastností aluminidů s perspektivou jejich využití pro lehké pancéřování

1 Aluminidy železa na bázi FeAl legované uhlíkem a křemíkem

Je známo, že vlastnosti intermetalických fází mohou být vylepšeny přídavkem nekovových prvků, které mohou ovlivnit zejména stabilitu uspořádané struktury při vyšších teplotách. Z tohoto pohledu se jeví velmi slibně právě systém Fe-Al-C. Uhlík lze v první řadě využít jako leguru cíleně - morfologie a způsob distribuce vznikajících karbidů může významně ovlivnit vlastnosti slitiny. Také historická inspirace slitinou Pyroferal vychází z faktu, že výborné (a v jistých směrech se dá říci i jedinečné) vlastnosti Pyroferalu nebyly nikdy dostatečně vysvětleny ve vztahu k fázovému složení slitiny.

Dalším důvodem pro studium ternárního systému Fe-Al-C je skutečnost, že uhlík je v aluminidech železa přítomen vždy, protože se dostane do železa jako nečistota již při tavbě. Železo používané v průmyslových aplikacích vždy bude určité množství uhlíku obsahovat, což souvisí s hlavní motivací vývoje aluminidů železa, a tou je nízká cena výchozích surovin. V ternárním systému Fe-Al-C existuje při nízkém obsahu uhlíku α fáze (bcc mřížka) v neuspořádaném stavu A2 stejně jako ve stavu s uspořádáním na dlouhou vzdálenost typu B2 nebo $D0_3$. Při vyšším obsahu uhlíku je stabilní tuhý roztok γ a ternární intermetalická fáze Fe_3AlC_x označovaná jako κ-karbid (nebo také K-fáze s perovskitickou strukturou či perovskit).

Upřesnění oblastí existence a koexistence fází v ternárním diagramu Fe-Al-C se stalo jedním z motivů předložené habilitační práce (vymezení oblasti perovskitického karbidu v ternárním diagramu a otázka existence karbidu Al_4C_3 v tomto systému).

1.1 Studium fázové struktury aluminidů železa legovaných uhlíkem a křemíkem

Z důvodů zmíněných v úvodu (inspirace Pyroferalem) jsme se v pracích P1-P4 zaměřili na ternární a kvaternární slitiny s FeAl matricí. Výběr tohoto typu slitin souvisí se skutečností, že fázové složení je dobře popsáno u slitin s obsahem hliníku okolo 28 at.%, zatímco oblast ternárního diagramu, která zahrnuje slitiny blízké Pyroferalu, zatím detailně popsána nebyla. Při složení Fe-40Al at.% se v ternárním systému Fe-Al-C mohou vyskytovat v závislosti na obsahu C a teplotě následující fáze: tuhý roztok uhlíku v mřížce B2, karbid perovskitického typu Fe_3AlC_x (tzv. κ-karbid), grafit a karbid Al_4C_3 (jehož přítomnost je jednou z otevřených otázek).

P1	Vodičková V.; Kratochvíl P.; Dobeš F.:*The effect of carbon on the structure of Fe-40Al-xC (at.%) ternary alloys,* **KOVOVÉ MATERIÁLY-METALLIC MATERIALS** 45 Issue 3 (2007) 153-158
P2	Kratochvíl P.; Dobeš F.; Vodičková V.: *The effect of silicon on the structure of Fe-40 at.% Al type alloys with high contents of carbon (1.9-3.8 at.%),* **INTERMETALLICS** 17 Issue 1-2 (2009) 39-45

Struktura souboru slitin na bázi Fe40Al (obsah Al 40.05-41.3 at.%) s postupně rostoucím obsahem uhlíku až do 1.9 at.% C byla studována v práci [P1]. Pro předběžnou identifikaci fází byla použita metoda měření mikrotvrdosti podle Vickerse, identifikace byla verifikována pomocí elektronové difrakce na transmisním elektronovém mikroskopu nebo pomocí difrakce rtg záření na difraktometru. Stabilita fází byla sledována na vzorcích slitin podrobených tepelnému zpracování při 600°C, 800°C a 1100°C. V [P2] byla analýza fázového složení rozšířena k vyšším obsahům uhlíku na slitiny blízké Pyroferalu (tj. okolo 40 at.% Al a 2-4 at.% C), a to buď s obsahem Si okolo 1 at.%, nebo bez Si.

Strukturní studie [P2] zahrnovala stav po válcování při 1200°C a následném chladnutí na vzduchu a stavy po nízkoteplotním (600°C) a vysokoteplotním (1100°C) žíhání, výsledky analýzy struktury byly prezentovány přehlednou tabulkou s uvedením metod identifikace stejně jako v předchozí studii [P1].

Hlavní dosažené výsledky:

- *Vymezení oblasti existence fází FeAlC slitin (κ-karbidu Fe_3AlC_x a grafitu) v kvazibinárním diagramu v oblasti s obsahem uhlíku do 2 at.%*

Původní strukturní data [1] byla doplněna o fázové složení stavu po válcování a stavů po tepelném zpracování. Na základě přesné identifikace strukturních fází byly fázové hranice kvazibinárního diagramu upraveny podle zjištěných skutečností [P1], Obr. 1.

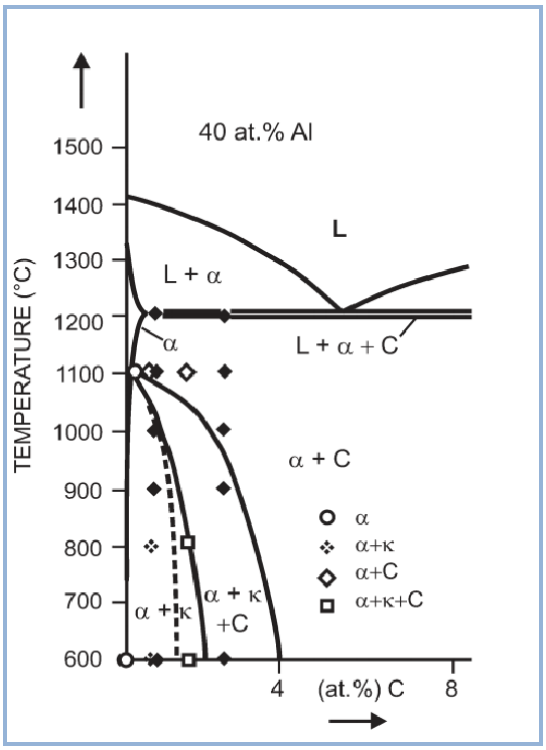

Obr. 1. Kvazibinární fázový diagram slitin Fe-40 at.%Al-C podle [1] doplněný o data získaná v [P1] s vyznačením posunu fázového rozhraní (Fig. 11, [P1])

- *Návrh posunutí fázového rozhraní α+κ / α+C+κ v ternárním diagramu Fe-Al-C*

Otázka vymezení oblasti existence karbidu κ je hlavním tématem komentované práce [P1]. Tato fáze zde byla identifikována současně s grafitem a tuhým roztokem α v oblasti, která byla v [2] popsána jako dvoufázová (α+grafit). Možný posun hranice mezi dvoufázovou a třífázovou oblastí [P1] je naznačen v obrázku Obr. 2.

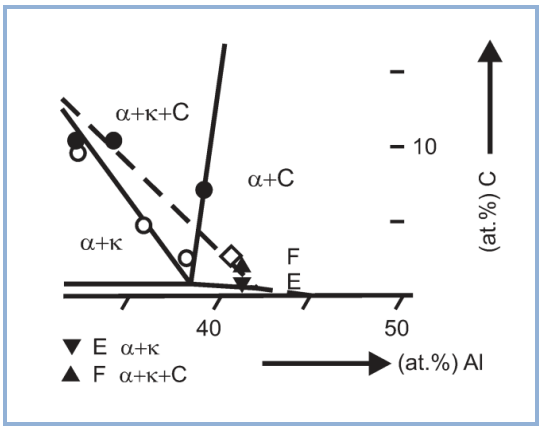

Obr. 2. Část ternárního Fe-Al-C diagramu při 800°C podle [3] doplněna o data slitin E a F, s naznačeným posunem fázového rozhraní (Fig. 12, [P1])

Hlavní příčinou obtíží při přesném vymezení hranic oblasti existence karbidu κ v ternárním fázovém diagramu byl od počátků výzkumu systému Fe-Al-C problém určení jeho přesné stechiometrie. Upřesnění hranic oblasti existence homogenního κ-karbidu provedli Palm a Inden [2]. Exaktní určení složení této fáze je obtížné především z důvodu problematického stanovení obsahu uhlíku v jemných precipitátech κ-karbidu, pro které v současné době neexistuje odpovídající metodika.

Výskyt κ-karbidu ve struktuře slitin s přísadou uhlíku může být výhodný z hlediska očekávaných vlastností. Je-li totiž tato fáze ve struktuře distribuována v dostatečně jemné formě, může její přítomnost významně zlepšit tažnost i creepovou odolnost aluminidů železa. Fázová rozhraní karbid - matrice pak fungují jako vodíkové pasti [4]. Blokování intersticiálních pozic v mřížce atomy uhlíku se rovněž podílí na snížení difuzivity vodíku.
U slitin bez Si s obsahem uhlíku nižším než 3 at.% [P2] byl dominantní sekundární fází grafit, a to ve formě protáhlých částic (lupínků) až 50μm dlouhých. Toto zjištění dobře koresponduje s oblastí α + C v ternárním diagramu podle [2]. Karbid perovskitického typu Fe_3AlC_x byl u těchto slitin identifikován pouze prostřednictvím transmisní elektronové mikroskopie jako reziduum ve formě drobných oválných částic (o průměru cca 200 nm).

Přítomnost částic grafitu ve struktuře slitin tohoto typu sice snižuje pevnost, ale může pozitivně ovlivnit jak tažnost, tak obrobitelnost slitiny. Ani příznivý vliv na tribologické vlastnosti intermetalických slitin není zanedbatelný [5].

- *Ověření přítomnosti karbidu Al_4C_3 ve struktuře slitin s vyšším obsahem uhlíku*

Zajímavým aspektem strukturního experimentu [P1] byl výskyt karbidu Al_4C_3 ve struktuře slitiny s obsahem uhlíku 1.9 at.% a obsahem 1.2 at.% Si. Skutečnost, že tato fáze byla identifikována ve struktuře slitiny s nižším obsahem hliníku, než odpovídá Pyroferalu, byla dále sledována v [P2]. Lze předpokládat, že právě tato fáze - její specifická morfologie a způsob distribuce - je příčinou vynikajících vlastností Pyroferalu.

Samotná existence karbidu Al_4C_3 v ternárním systému Fe-Al-C je doposud otevřenou záležitostí - tato fáze je zmíněna v ternárním diagramu Fe-Al-C podle [6], zatímco v jiném [2] její výskyt zaznamenán nebyl. Oproti tomu v teoretickém ternárním diagramu vypočteném metodou CALPHAD [7] je její existence predikována.
Pro diskusi experimentálních výsledků [P2] byly využity izotermální řezy pro 800°C a 1000°C ternárního diagramu Fe-Al-C podle [7], které oblast existence karbidu Al_4C_3 zahrnují, viz Obr. 3.

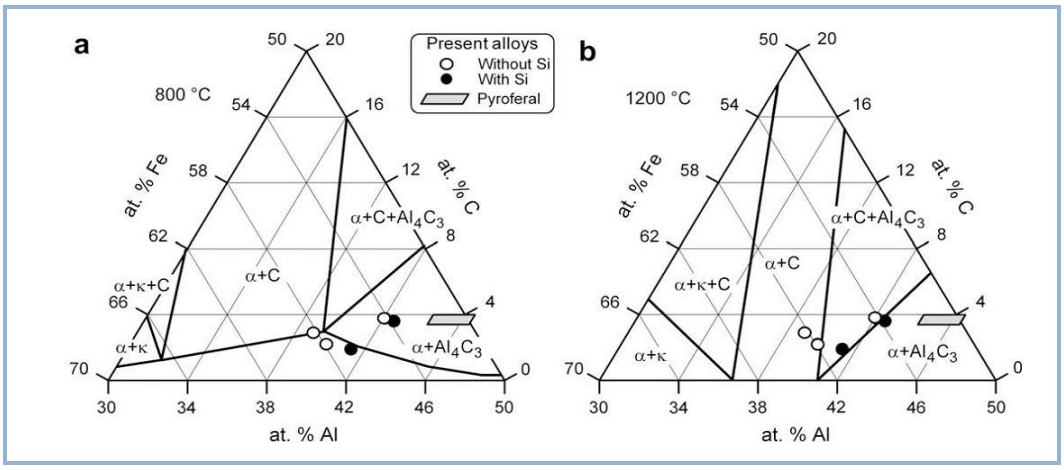

Obr. 3. Část ternárního Fe-Al-C fázového diagramu podle [7] pro a) 800°C b) 1200°C, vyznačeno složení slitin [P2] (Fig. 11, [P2])

Bylo prokázáno, že přítomnost karbidu Al_4C_3 ve struktuře slitin s obsahem C > 3 at.% dobře koresponduje s predikovanou oblastí jeho výskytu podle [7]. Na základě našich výsledků [P2] bylo fázové rozhraní mezi oblastmi (α + C) a (α + C+ Al_4C_3) posunuto k nižším koncentracím Al pro obě teploty oproti výsledkům [1] jak je patrno z Obr. 4.

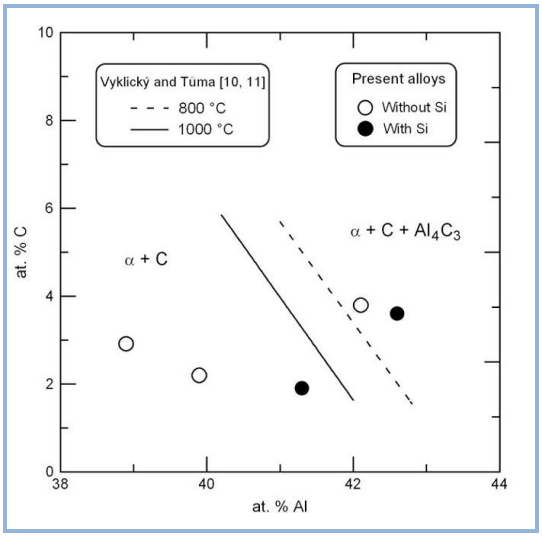

Obr. 4. Hranice prvního výskytu karbidu Al_4C_3 při 800°C a 1000°C v porovnání s [1], [8] (Fig. 12, [P2])

- *Role křemíku při vzniku karbidu Al_4C_3*

Markantní rozdíl ve fázovém složení oproti slitinám s obsahem C < 3 at.% (bez Si) byl zaznamenán u slitiny s obsahem uhlíku 3.8 at% (bez Si), která vykazovala hypoeutektickou

strukturu s dendrity FeAl a jehlicemi karbidu Al_4C_3 v mezidendritickém prostoru ([P2], Fig. 6a). Ojediněle byly ve struktuře identifikovány částice grafitu. Analogická struktura - dendritické oblasti tuhého roztoku α s mezidendritickými oblastmi vyplněnými jehlicemi karbidu Al_4C_3 - byla zjištěna rovněž u slitin s podobným obsahem C a přídavkem Si. Vysokoteplotní stabilita karbidu Al_4C_3 u slitin s obsahem Si byla výrazně lepší než u slitiny bez Si. Při vysokoteplotním žíhání materiálu s Si se jehlice karbidu Al_4C_3 rozpouštěly jen částečně a charakter struktury byl podobný jako ve stavu po válcování při 1200°C a následném chladnutí na vzduchu ([P2], Fig. 9ab), zatímco u slitiny bez Si došlo po vysokoteplotním žíhání k úplnému rozpuštění karbidu Al_4C_3 a majoritní sekundární fází žíhaného stavu byl grafit ve formě vloček ([P2], Fig. 6b).

Zjištění, že stabilita karbidické fáze během žíhání je u slitin s obsahem Si výrazně lepší, je pro další výzkum významné. Pochopení role Si při formování fáze Al_4C_3 může být podstatné například pro zlepšení korozní odolnosti slitin na bázi Fe-Al ve vodních prostředích, která je spojována právě s přítomností této fáze. Podpora vzniku fáze Al_4C_3 může spočívat v nahrazení atomů Al v mřížce atomy Si díky větší rozpustnosti Si v matrici typu FeAl (na rozdíl od jeho nízké rozpustnosti v jiných Fe-Al slitinách). Podobný mechanismus podpory vzniku karbidu hliníku malými obsahy Si byl popsán u Al/SiC kompozitních materiálů [9].

1.2 Vliv fázového složení na vysokoteplotní vlastnosti aluminidů železa legovaných uhlíkem a křemíkem

Vysokoteplotní mechanické vlastnosti materiálu mohou být popsány charakteristikami získanými z vysokoteplotní zkoušky v tlaku - vysokoteplotní mezí kluzu (YS) a maximálním napětím (UTS) - a charakteristikami získanými z creepových testů.

Pro hodnocení creepové odolnosti má podstatnou vypovídací hodnotu minimální creepová rychlost (MCR). Další creepové charakteristiky, které jsou spojeny s mechanismy creepu a mohou být použity k interpretaci vztahu struktura versus creepový mechanismus, jsou napěťový exponent n a aktivační energie creepu Q. Pro závislost rychlosti creepové deformace (creep rate) na aplikovaném napětí platí vztah

$$\dot{\varepsilon} = A\sigma^n \qquad (1)$$

kde $\dot{\varepsilon}$ je rychlost deformace, σ aplikované napětí, A teplotně závislá konstanta a n napěťový exponent.

Pro aktivační energii creepu platí

$$Q = -R\left(\frac{\partial \ln \dot{\varepsilon}}{\partial \frac{1}{T}}\right)_{\sigma} \qquad (2)$$

kde R je univerzální plynová konstanta a T absolutní teplota.

Obě tyto charakteristiky mohou být interpretovány buď v souvislosti s pohybem dislokací nebo z hlediska přítomnosti částic sekundární fáze.

P3	Dobeš F. , Kratochvíl P., Vodičková V., Milička K., Pešička J.:*The effect of carbon on high temperature deformation of Fe-40Al-xC (at.%) ternary alloys,* **KOVOVÉ MATERIÁLY-METALLIC MATERIALS** 46 Issue 4 (2008) 97-103
P4	Dobeš F.; Kratochvíl P.; Vodičková V.: *The effect of carbon and silicon additions on the creep properties of Fe-40 at.% Al type alloys at elevated temperatures,* **INTERMETALLICS** 19 Issue 10 (2011) 1526-1532

Vysokoteplotní mechanické vlastnosti souboru slitin na bázi Fe40Al s přídavkem uhlíku v intervalu 0.07-1.9 at.% byly studovány v práci [P3]. K vyšším obsahům uhlíku (až do 4.9 at.%) byl soubor slitin rozšířen v článku [P4] a zahrnoval jak slitiny s obsahem křemíku (0.7-1.2 at.%) tak slitiny bez křemíku. Byly vyhodnoceny creepové testy v tlaku a vysokoteplotní zkoušky v tlaku při teplotách 600°C-750°C [P3], resp. 600°C-800°C [P4], a sledována závislost vysokoteplotních mechanických vlastností na obsahu aditiv a na použitém tepelném zpracování.

Hlavní dosažené výsledky:

- *Stanovení vlivu obsahu uhlíku na creepovou odolnost slitin*

Výsledky vysokoteplotních testů pro slitiny s obsahem C do 2 at.% [P3] jsou shrnuty na Obr. 5 a Obr. 6. Jak je patrno, ani jedna z měřených závislostí není monotonní - nižší creepová odolnost stejně jako nižší hodnoty vysokoteplotních mechanických vlastností byly zjištěny u slitin E a F s obsahem uhlíku 0.8 resp. 1.7 at.%.

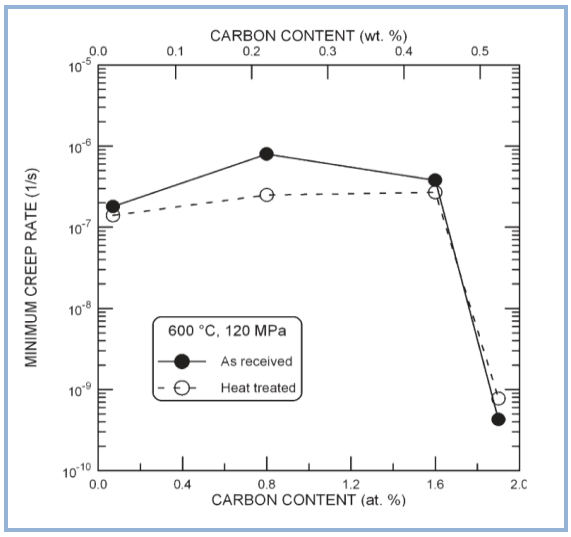

Obr. 5. Závislost minimální creepové rychlosti na obsahu uhlíku (Fig. 5, [P3])

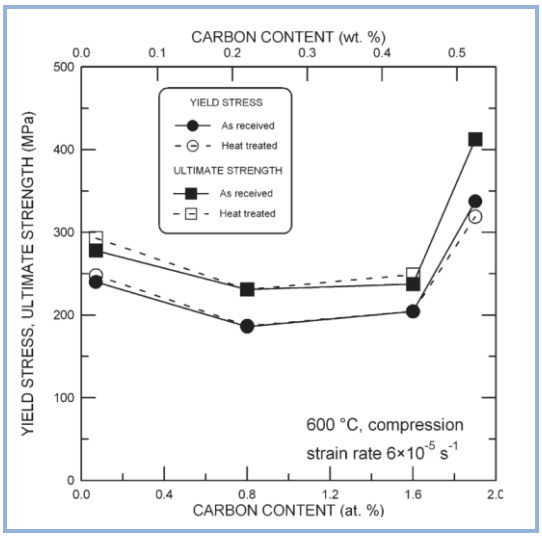

Obr. 6. Závislost meze kluzu a meze pevnosti v tlaku při 600°C na obsahu uhlíku (Fig. 7, [P3])

Jako účinná překážka pro pohyb dislokací se ve slitině s nejnižším obsahem uhlíku (označení D) ukázaly jemné precipitáty (pravděpodobně karbidy železa), na kterých zůstávaly dislokace ukotveny [P3], jak je patrno na Obr. 7.

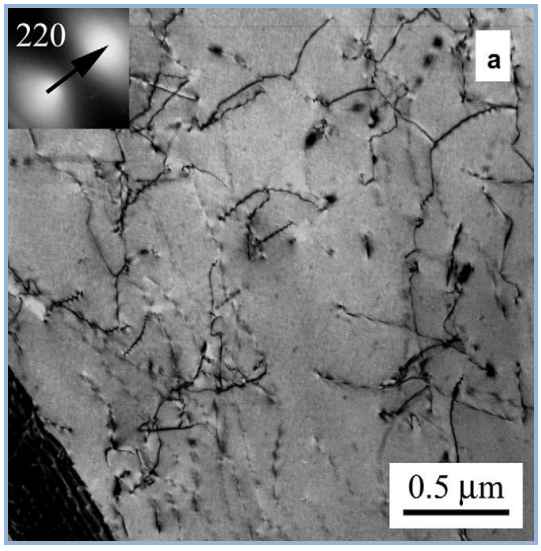

Obr. 7a. Dislokační struktura výchozího stavu (po válcování) slitiny D po creepu při 600°C (Fig. 8a, [P3])

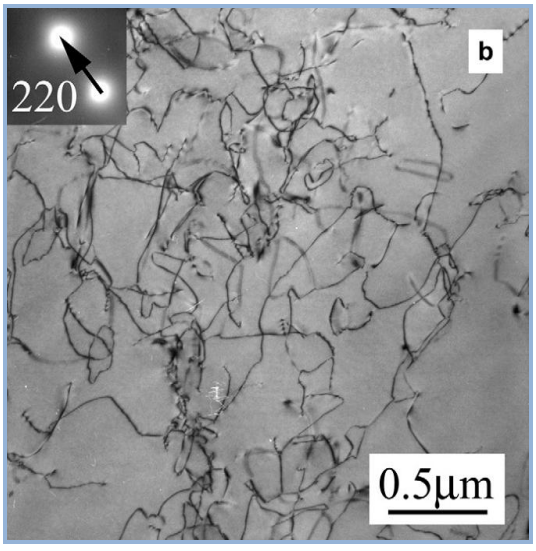

Obr. 7b. Dislokační struktura výchozího a následně žíhaného stavu slitiny D po creepu při 600°C (Fig. 8b, [P3])

Toto zjištění dobře koresponduje se studií [10] zaměřenou na vliv fázového složení na vysokoteplotní vlastnosti aluminidů železa na bázi FeAl s nižším přídavkem uhlíku. Zvýšení creepové odolnosti u aluminidů s obsahem 0.2-0.75 at.% C je spojováno především s přítomností jemných karbidických precipitátů a dislokačních smyček vznikajících ve struktuře během kondenzace vakancí.

Naproti tomu rozměrnější částice κ-karbidu identifikované ve slitinách E a F s obsahem uhlíku 0.8, resp. 1.7 at.% už neplní funkci překážek pohybu dislokací a charakteristiky vysokoteplotních mechanických vlastností jsou tudíž výrazně nižší. K podobným závěrům došli např. [11] pro slitiny s obsahem 24-28 at.% Al. Podle této práce κ-karbid nepřispívá ke zlepšení vysokoteplotní pevnosti kvůli rychlému hrubnutí precipitátu. Slitina H s nejvyšším obsahem C a přídavkem Si se odlišuje vysokým podílem karbidu Al_4C_3 ve struktuře a je charakterizována vynikající creepovou odolností. Ani během creepové deformace při 600°C nedojde k úplnému rozpouštění karbidických oblastí, dendritický charakter struktury zůstává zachován.

Zvýšení creepové odolnosti je u slitin s vyšším obsahem uhlíku zhruba spojeno s očekávaným nárůstem objemu sekundární fáze [P4], tj. κ-karbidu a grafitu v sekci (Fe-41Al-C) a karbidu Al_4C_3 v sekci (Fe-41Al-Al_4C_3), viz Obr. 8.

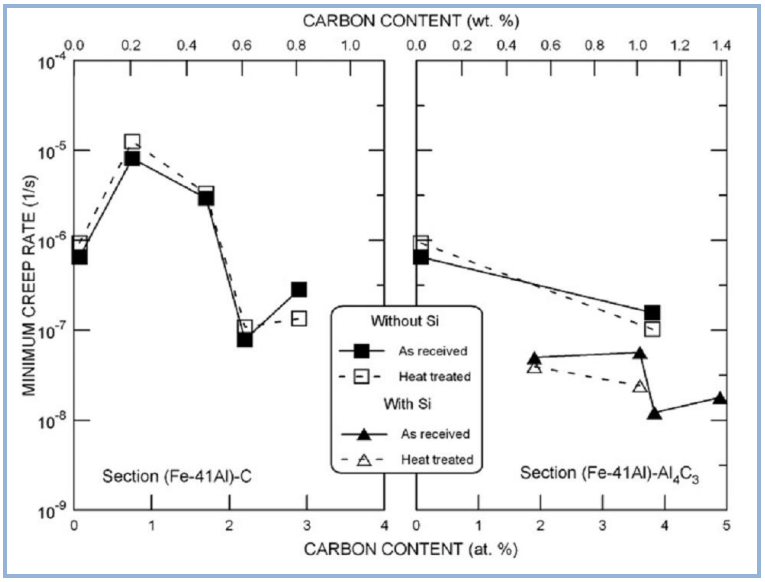

Obr. 8. Závislost minimální creepové rychlosti při 600°C a aplikovaném napětí 160 MPa na obsahu uhlíku (Fig. 7, [P4])

MCR slitiny L (2.9 at.% C) je sice vyšší oproti slitině K (2.2 at.% C), to ale může být zapříčiněno nepatrně nižším obsahem hliníku ve slitině L, protože rozpustnost uhlíku v B2

mřížce roste s klesající koncentrací Al, a tudíž je k dispozici méně uhlíku pro precipitaci grafitu.

- *Identifikace creepových mechanismů pomocí hodnot napěťových exponentů a aktivačních energií*

Výsledky testů vysokoteplotních mechanických vlastností ukázaly jednoznačnou souvislost s velikostí a způsobem distribuce částic sekundární fáze ve struktuře slitin. Hodnoty získané z creepových testů v tlaku v rozmezí 600-800°C byly interpretovány také prostřednictvím napěťového exponentu n a aktivační energie creepu Q, což umožnilo přiřadit slitinám (resp. fázovému složení) odpovídající creepový mechanismus.

Nižší hodnoty napěťového exponentu n (v intervalu 4-5) jsou obvykle charakteristické pro creep kontrolovaný šplháním dislokací v jednofázové matrici. Tyto hodnoty byly zjištěny za vyšších teplot creepové deformace pro slitiny s nižším obsahem uhlíku (E a F). Vyšší hodnoty napěťového exponentu n u slitin s vyšším obsahem uhlíku a s přídavkem Si ukazují na obtížnější pohyb dislokací bráněný částicemi sekundární fáze. Podobný mechanismus se uplatňuje u slitiny s nejnižším obsahem C, kde pohybu dislokací brání překážky, jejichž charakter nebylo možné stanovit. Může jít o velmi jemné karbidy či zakotvené konfigurace dislokací, podobně jako na Obr. 7a.

Ve slitinách s vyšším obsahem uhlíku a přídavkem křemíku je dominantní sekundární fáze - karbid hliníku Al_4C_3 - distribuována ve formě tenkých jehlic či destiček, které vyplňují prostor mezi dendrity tuhého roztoku α. Bylo prokázáno, že tato forma sekundární fáze brání pohybu dislokací v matrici velmi účinně a slitiny vykazují dobrou creepovou odolnost (o několik řádů lepší v porovnání s kvalitními austenitickými či martenzitickými ocelemi).
Z Obr. 8 je zřejmé, že ke zpevnění slitin přispívají jak jehlice karbidu Al_4C_3, tak i grafitická sekundární fáze (u slitin bez Si). Je-li objemový podíl sekundární fáze odpovídající, je možné nahlížet na slitinu jako na určitou formu kompozitního materiálu. Další příspěvek ke zpevnění je spojen s blokováním hranic zrn a obtížnějším pohybem dislokací přes zrna.

Analogické výsledky poskytuje i porovnání aktivačních energií creepu. Hodnotu $Q \approx 310$ kJ/mol, která je připisována creepovému mechanismu kontrolovanému šplháním dislokací v jednofázové matrici, lze přiřadit slitinám s nižším obsahem uhlíku, zatímco vyšší aktivační energie creepu ($Q \approx 450$-500 kJ/mol), která může být připisována mechanismu kontrolovanému pohybem dislokací omezeným přítomností sekundární fáze, charakterizuje především slitiny s vyšším obsahem C a přídavkem křemíku.

- *Příspěvek karbidu Al_4C_3 ke zvýšení creepové odolnosti, role Si*

Karbid hliníku Al_4C_3 se během dlouhodobého creepového zatěžování ukázal jako poměrně stabilní fáze, dendritický charakter struktury zůstal zachován i ve struktuře po absolvovaných dlouhodobých testech. Ke zvýšení creepové odolnosti slitin patrně přispívá jak přídavek uhlíku, tak i křemíku, ale vliv křemíku je zásadní. Podporuje tvorbu dendritické struktury s jehlicemi karbidu Al_4C_3 a přispívá ke stabilitě této fáze během působení vysokých teplot. Creepová odolnost slitin s obsahem Si je na dobré úrovni i v porovnání s nízkouhlíkovými slitinami prezentovaným v [12], jak je patrno na Obr. 9.

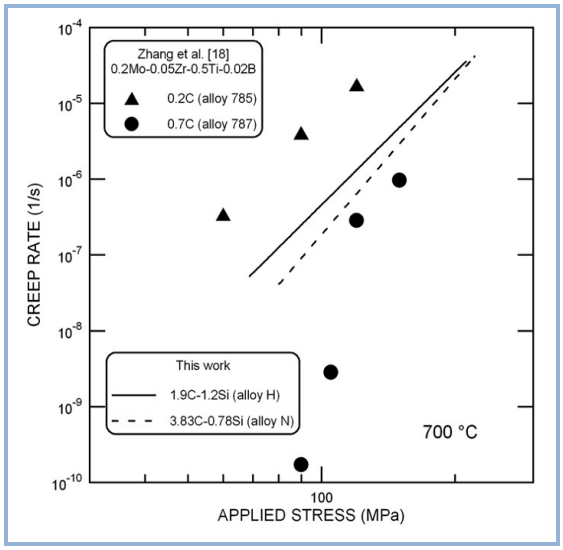

Obr. 9. Porovnání creepových rychlostí v závislosti na působícím napětí při 700°C pro slitiny s obsahem 1.9 a 3.8 at.% C a s obsahem Si [P4] a slitiny na bázi FeAl obsahující uhlík [12] (Fig. 10, [P4])

Slitiny obohacené Si [P4] sice vykazují nižší odolnost vůči creepu než slitina 787 [12], ale je nutno brát v úvahu, že k vynikající creepové odolnosti slitiny 787 pravděpodobně významně přispívá přídavek karbidotvorných prvků Mo, Zr a Ti.

2 Význam sekundární fáze (zejména při legování karbidotvornými prvky) pro zlepšování vysokoteplotních vlastností aluminidů železa

Hlavní výhodou aluminidů železa je kromě nižší ceny v poměru k běžně používaným konstrukčním materiálům dobrá odolnost vůči vlivům prostředí. Ta je u slitin s FeAl matricí a B2 strukturou na vynikající úrovni, nicméně z pohledu mechanických vlastností lépe splňují nároky kladené na materiály pro aplikace za vyšších teplot slitiny s Fe_3Al matricí. Binární Fe_3Al slitiny vykazují díky vysokému stupni uspořádanosti $D0_3$ struktury obecně vyšší pevnost při pokojové teplotě i za vysokých teplot jak v porovnání s Fe(Al) neuspořádanými slitinami, tak uspořádanými slitinami typu FeAl s B2 strukturou [13], [14]. Výzkum aluminidů železa ve spolupráci Praha - Liberec probíhal od počátku ve dvou směrech sledujících obě hlavní skupiny aluminidů železa typu FeAl (viz kap. 1) a Fe_3Al, v současné době je již výzkum vlivu fázového složení na vysokoteplotní vlastnosti orientován na slitiny s Fe_3Al matricí.

Vysokoteplotní vlastnosti aluminidů na bázi Fe_3Al mohou být ovlivňovány několika různými způsoby [15]:

- zpevněním prvky rozpustnými v tuhém roztoku, což je umožněno např. malými přídavky Cr, V, Mo, Ti
- zpevněním nekoherentními precipitáty, které mohou vznikat díky legování ternárními aditivy jako Zr, Ta, Nb, Ti, nebo užitím C resp. B (vznik karbidických či boridových precipitátů)
- zpevněním koherentními precipitáty (např. v systému Fe-Al-Ni, Fe-Al-Ti)
- zpevněním v důsledku krystalografického uspořádání, na principu stabilizace struktury vůči $B2/L2_1$ přechodu (vlivem vhodné legury - např. Ti - se teplota přechodu $L2_1 \rightarrow B2$ posune k vyšším teplotám, čímž se oblast existence $L2_1$ struktury rozšíří)

Druhá část předkládané habilitační práce je věnována zejména vlivu karbidotvorného Zr, které vzhledem k velmi nízké rozpustnosti v Fe_3Al matrici vytvoří převážně Lavesovu fázi $(Fe,Al)_2Zr$. Částice této fáze mohou podle [16-19] zabraňovat pohybu dislokací při deformaci. Její objemová koncentrace souvisí s přítomností karbidu zirkonia, jehož tvorba (většinou již v tavenině) je dána vysokou afinitou Zr k uhlíku. Studium vlivu karbidotvorných prvků na fázové složení je tedy s ohledem na perspektivu využití $D0_3$ - uspořádaných Fe_3Al slitin při vysokoteplotních aplikacích velmi důležité právě z již uvedeného důvodu časté přítomnosti uhlíku jako nečistoty v surovém železe.

2.1 Hledání vhodného aditiva pro zvyšování vysokoteplotních mechanických vlastností aluminidů na bázi Fe_3Al legovaných Cr

Efektivní způsob zvyšování HT vlastností může tedy spočívat buď v použití aditiv rozpustných v matrici anebo naopak na použití aditiv s nízkou rozpustností v Fe_3Al matrici. Ve fázi hledání optimálního aditiva (či kombinace aditiv) pro zpevnění aluminidů železa byly testovány slitiny legované chromem, který se rozpouští v matrici a tím ji zpevňuje. Důvody pro legování chromem mají historický základ, neboť vliv vliv 2-6 at.% Cr na zvýšení tvařitelnosti Fe_3Al slitin při pokojové teplotě prokázali již McKamey at al. [20]. Volba dalších aditiv (případně jejich kombinace) byla založena na motivech pro zpevnění aluminidů uvedených výše.

V prvním stadiu byly ke standartní slitině Fe_3Al s přídavkem Cr legovány Zr, TiB_2, ev. Ce, později také uhlík v kombinaci se Zr (experimenty popsané zde [P5], [P6], [P7] a další práce mých kolegů [21], [22], [23], [24]).

P5	Kratochvíl P.; Vodičková V.; Hakl J., Vlasák T., Hanus P., Pešička J.: *High temperature mechanical properties of Fe28Al4Cr alloy with additives TiB_2 and Zr,* **INTERMETALLICS 18** (2010) 1365-1368
P6	Vodičková V.; Hanus P., Kratochvíl P.; Málek Č.: *Effect of carbon addition on phase composition and high temperature strength of Fe_3Al-type iron aluminide with Zr,* **METAL 2010** - 19th International Conference on Metallurgy and Materials, Conference Proceedings, 765-769
P7	Kratochvíl P.; Dobeš F.; Pešička J., Málek P., Buršík J., Vodičková V., Hanus P.: *Microstructure and high temperature mechanical properties of Zr-alloyed Fe_3Al-type iron aluminides: The effect of carbon,* **Materials Science and Engeneering** A 548 (2012) 175-182

Vliv kombinace legur Zr+TiB_2 na fázové složení slitiny Fe28Al4Cr a na její vysokoteplotní mechanické vlastnosti byl studován v [P5]. Deformační testy – vysokoteplotní zkouška v tahu a creep - byly provedeny v rozsahu teplot od 600°C do 900°C. Na základě výsledků dosažených v [P5] jsme se v dalším výzkumu zpevnění aluminidů železa zaměřili na legování zirkoniem a uhlíkem při současném obsahu Cr [P6, P7]. Zde bylo studováno fázové složení u souboru slitin s nižšími obsahy Zr (0.2 - 0.3 at.%) a C (0.2 - 0.6 at.%) a jeho vliv na vysokoteplotní vlastnosti – vysokoteplotní mez kluzu v tahu a creepovou odolnost. Struktura

slitin ve stavu po válcování a následném žíhání při 1150°C pro stabilizaci struktury byla analyzována pomocí optické mikroskopie, rastrovací elektronové mikroskopie, energiově-disperzní rentgenové analýzy a rentgenové difrakční analýzy, a rovněž pomocí transmisní elektronová mikroskopie s využitím selektivní difrakce při studiu mikrostruktury vzorků po deformačních testech (vysokoteplotní zkouška v tahu [P6, P7] a creep v tlaku [P7]) provedených v teplotním intervalu 600°C až 800°C.

Hlavní dosažené výsledky:

- *Zpevňující role sekundárních fází při vysokoteplotní deformaci*

Ve struktuře slitiny s přídavkem kombinace Zr+TiB_2 ve stavu po válcování a následném žíhání byly pozorovány poměrně hrubé částice (~ 5 μm) kombinovaných boridů (Zr,Ti)B_2 podél hranic zrn [P5], Fig. 1. S ohledem na jejich velikost lze předpokládat, že příspěvek těchto částic ke zpevnění slitiny není významný. Studium struktury vzorků po creepových testech pomocí transmisní elektronové mikroskopie ukázalo, že při teplotách 600 a 650°C je creepový proces v materiálu omezován především velmi jemnými precipitáty ZrC (~ 10 nm) s kubickou strukturou [P5], jak je patrno na Obr. 10. Při vyšších teplotách creepové deformace, tj. při 800°C a 900°C, dochází k výraznému hrubnutí těchto precipitátů [P5], Fig. 5b, 5c. Toto zjištění velmi dobře koresponduje s výsledky creepových testů [P5] na Obr. 11, kde je creepová odolnost hodnocena prostřednictvím TTR (doby do lomu).

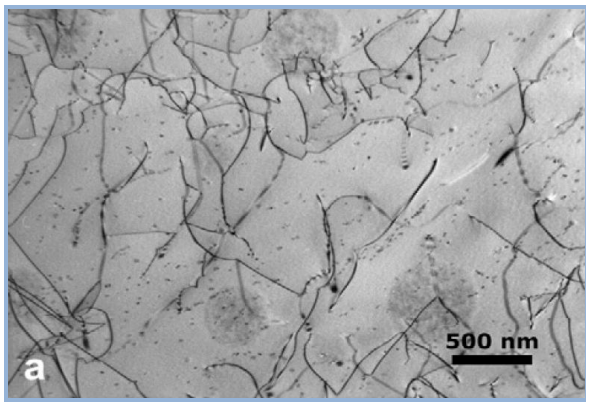

Obr. 10. Mikrostruktura vzorku slitiny Fe28Al4Cr s přídavkem Zr+TiB_2 po creepu při 600°C, 100 MPa, 5000 h (Fig. 5a, [P5])

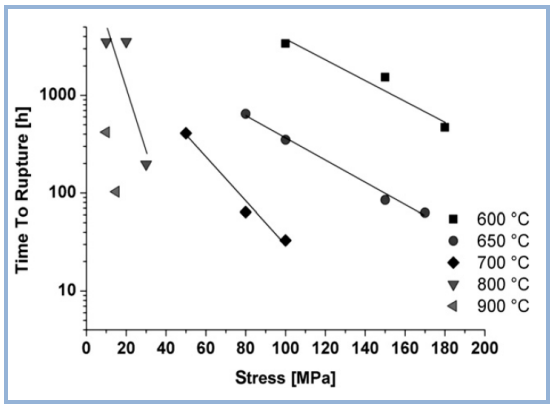

Obr. 11. Hodnoty TTR (doby do lomu) slitiny Fe28Al4Cr s přídavkem Zr+TiB_2 v rozsahu teplot 600°C-900°C (Fig. 4, [P5])

Vysoké hodnoty TTR pro teploty 600°C, resp. 650°C při napětích nad 100 MPa nepochybně souvisí s výskytem jemné disperze těchto částic ve struktuře slitiny, pokles hodnot TTR při 700°C a napětí 100 MPa zřejmě odpovídají počínajícímu hrubnutím precipitátů. Výskyt

jemných částic a jejich hrubnutí v závislosti na teplotě je popsán rovněž v [23], kde byly tyto částice rovněž identifikovány jako karbidy zirkonia ZrC.

Analýza fázového složení slitin legovaných Zr a C [P6, P7] ukázala, že hodnoty $\sigma_{0.2}$ a napěťového exponentu n při odpovídajících teplotách dobře korespondují s výskytem částic působících jako překážky pohybu dislokací. Zpevňující úloha fází majoritních u testovaných slitin [P6, P7], tedy Lavesovy fáze λ_1 $(Fe,Al)_2Zr$ a karbidů ZrC, je (s ohledem na jejich výskyt převážně na hranicích zrn [P7], Fig. 1 a Fig. 3) omezena na blokování těchto hranic. Vliv na pohyb dislokací uvnitř zrn je malý vzhledem k velkým vzdálenostem mezi jednotlivými částicemi. Transmisní elektronová mikroskopie na vzorcích slitin po creepových testech prokázala, že během deformačního procesu vznikají další jemné částice, které mohou interagovat s dislokacemi a zabraňovat jejich pohybu. Po deformaci při 600°C i 800°C byly ve slitinách identifikovány částice fáze Fe_2Zr, na niž lze nahlížet jako na limitní Lavesovu fázi λ_1 $(Fe,Al)_2Zr$, a další částice, které lze považovat za metastabilní fázi. Podobné částice popsali Morris et al. [25, 26] ve feritických slitinách. Jejich přítomnost je s největší pravděpodobností důsledkem koncentračních fluktuací, které se mohou ve slitinách objevit po vzniku rovnovážných fází. Změna hustoty a velikosti těchto překážek v závislosti na teplotě koresponduje se zaznamenanými změnami v hodnotách mechanických vlastností.

- *Srovnání použitých aditiv pro zlepšení vysokoteplotních vlastností aluminidů železa*

Výsledky deformačních testů [P5], které jsou shrnuty na Obr. 12 a Obr. 13, lze doplnit výsledky předchozích testů podobných slitin s různými aditivy [21], [22]. Porovnání hodnot vysokoteplotní meze kluzu $\sigma_{0.2}$ v tahu slitiny testované v [P5] s hodnotami získanými v [21] [22] ukazuje, že hodnoty $\sigma_{0.2}$ slitiny s kombinací aditiv TiB_2+Zr jsou pro všechny testované teploty nižší než u slitiny legované pouze Zr. Šedá oblast v diagramu na Obr. 12 poskytuje srovnání těchto hodnot s hodnotami $\sigma_{0.2}$ získanými pro disperzně zpevněné aluminidy železa (podle [15]). Z tohoto pohledu jsou velmi zajímavé výsledky slitiny legované Zr, jejíž vysokoteplotní charakteristiky jsou při teplotách 750°C-800° na horní úrovni oblasti hodnot $\sigma_{0.2}$ pro disperzně zpevněné aluminidy železa.

Creepová odolnost reprezentovaná minimální creepovou rychlostí při 600°C zkoumané slitiny s kombinací aditiv Zr+TiB_2 byla porovnána na Obr. 13 s obdobnými slitinami: dopovanými pouze Zr (FA6 a FA11 [21] v Obr. 13, použita data pro 650°C) nebo pouze TiB_2 (FA3 [22] v Obr. 13), ev. dopovanými Ce (FA1 [22] v Obr. 13).

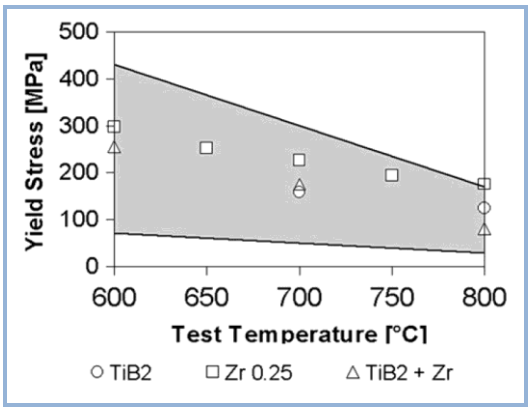

Obr. 12. Vysokoteplotní mez kluzu $\sigma_{0.2}$ testované slitiny v porovnání s výsledky [21] [22] (Fig2, [P5])

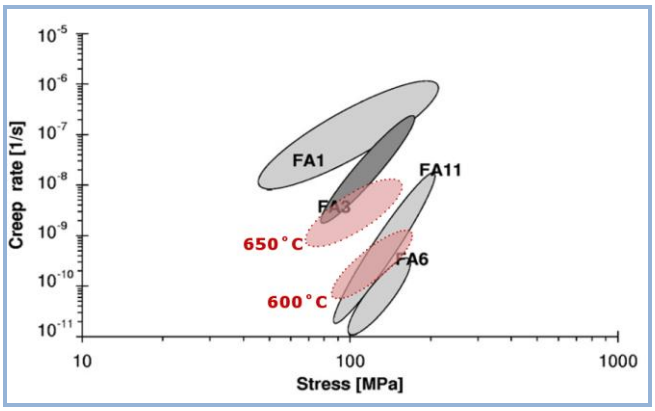

Obr. 13. Porovnání minimální rychlosti creepu pro slitinu Fe28Al4Cr s přídavkem Zr+TiB_2 (světle červené oblasti) s materiály [21] [22]

Z porovnání je patrné, že kombinace aditiv Zr a TiB_2 nevede ke zlepšení creepové odolnosti (ani s ohledem na rozdíl v testovacích teplotách). Částice fáze ZrB_2 vznikající (za účasti Zr nevyčerpaného na vznik ZrC) podél hranic zrn nepřispívají významně ke zpevnění slitiny. Velmi dobrou odolnost vůči creepu při teplotách do 650°C vykazují slitiny FA6 a FA11[21], u kterých přispívá ke zpevnění přídavek Zr a jako překážky pro pohyb dislokací se uplatňují jemné precipitáty ZrC.

Ve slitinách dopovaných pouze Zr vznikají v důsledku nízké rozpustnosti Zr v Fe_3Al matrici převážně částice Lavesovy fáze λ_1 $(Fe,Al)_2Zr$. Výsledky [P6, P7] naznačily, že při současném legování uhlíkem může hrát vzájemný poměr koncentrací uhlíku a zirkonia podstatnou roli. V takových slitinách mohou se zřetelem na poměr c(Zr)/c(C) nastat dva případy tvorby fází:

1. Při převaze uhlíku afinita Zr vůči uhlíku preferuje vznik karbidů zirkonia a zbývající Zr vytváří Lavesovu fázi. To je případ slitin s poměrem c(Zr)/c(C)<1 (v [P7] označeny 2A a 4A), kde je ZrC fází dominantní a objevuje se i ve formě jader v částicích Lavesovy fáze λ_1 $(Fe,Al)_2Zr$ [P7], Fig 1b.
2. Při převaze Zr se opět přednostně tvoří ZrC (díky vysoké afinitě Zr vůči C), ale po spotřebování uhlíku zbude dostatek Zr pro tvorbu Lavesovy fáze λ_1 $(Fe,Al)_2Zr$. Tento případ dokumentuje struktura slitiny s poměrem koncentrací zirkonia a uhlíku c(Zr)/c(C)>1 (v [P7] označena 1A), kde je majoritní fází Lavesova fáze λ_1 $(Fe,Al)_2Zr$ a ZrC je fází minoritní. Zpřesnění mechanismu působení vzájemného poměru těchto legur při tvorbě sekundárních

fází a jejich vliv na vysokoteplotní vlastnosti aluminidů železa bez obsahu chromu je hlavním tématem navazujícího výzkumu popsaného v kap. 2.2.

- *Vliv vzájemného poměru koncentrací aditiv Zr a C na creepovou odolnost slitin na bázi Fe_3Al*

K posouzení vlivu kombinace C a Zr na vysokoteplotní mechanické vlastnosti může být využit poměr jejich koncentrací [P7], jak je ukázáno na Obr. 14, kde je napětí působící creepovou rychlost 10^{-7} s^{-1} prezentováno jako funkce poměru koncentrací aditiv c(Zr)/c(C).

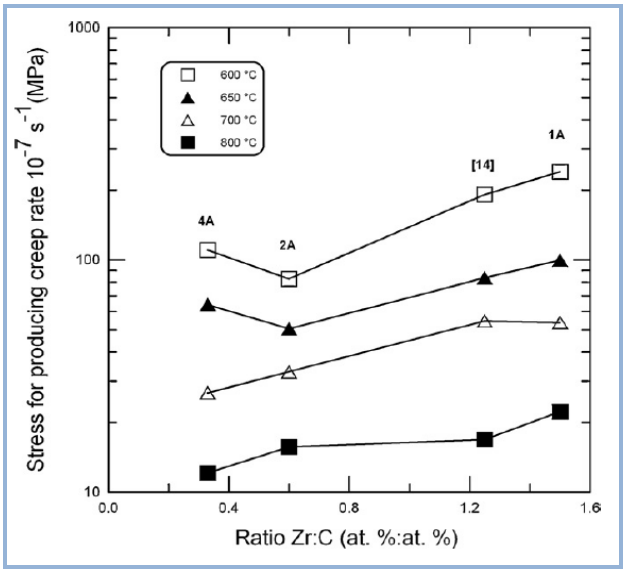

Obr. 14. Napětí nutné k vyvolání creepové rychlosti 10^{-7} s^{-1} jako funkce poměru koncentrací aditiv (Fig. 13, [P7]), k doplnění slitina označená [14] [1]

Mírný nárůst hodnoty napětí pro slitinu s poměrem c(Zr)/c(C) >1 (1A v Obr. 14) odpovídá přítomnosti Lavesovy fáze a jejímu příspěvku ke creepové odolnosti (výše zmíněné blokování hranic zrn). Vliv částic majoritních fází situovaných převážně podél hranic zrn na celkové zpevnění materiálu musí být brán v úvahu, i když vysokoteplotní chování slitin studovaných v [P6, P7] je podobně jako v [P5] determinováno přítomností malých částic pozorovaných TEM. Množství Zr, které je k dispozici pro vznik těchto fází, představujících překážky pro pohyb dislokací, je rovněž ovlivněno vzájemným poměrem koncentrací aditiv Zr a C. Celkový pokles creepové odolnosti a pevnosti v tahu při teplotě 800°C ve srovnání s hodnotami při 600°C odpovídá výraznému nárůstu velikosti a vzájemné vzdálenosti překážek pohybu dislokací.

[1] 0.25 at.% Zr a 0.19 at.% C [21]

Výsledky získané v [P6, P7] lze doplnit a porovnat s dříve publikovanými hodnotami creepové rychlosti aluminidů železa s přídavkem Zr [21], [26], [27], [28], [P7], Fig. 14. I přes rozdíly v podmínkách porovnávaných experimentů (např. ve výchozím stavu slitin, v množství Al, legování borem namísto uhlíkem) je zřejmé, že creepová odolnost slitin s poměrem c(Zr)/c(C) případně c(Zr)/c(B) >1 je lepší než u slitin s poměrem koncentrací menším než 1.

Vysokoteplotní oxidační chování slitin na bázi Fe_3Al s přídavkem Zr a C

Velmi příznivou vlastností všech slitin na bázi Fe-Al je dobrá vysokoteplotní korozní odolnost, která je zapříčiněna vznikem ochranné vrstvy α-Al_2O_3 v oxidačních prostředích [29], [30]. V závislosti na obsahu Al ve slitině, teplotě a délce expozice mohou vznikat rovněž oxidy železa a metastabilní γ-, δ- a θ- Al_2O_3 oxidy. Všechny tyto oxidy rostou rychleji než α-Al_2O_3 vrstva, jsou objemnější a více porézní, a z toho důvodu neplní tak dobře ochrannou funkci [31]. Oxidační odolnost lze ovlivnit vhodnými aditivy. Bylo prokázáno, že přídavek Zr může u aluminidů na bázi Fe_3Al zvýšit přilnavost ochranné vrstvy α- Al_2O_3 a potlačit tvorbu pórů na rozhraní vrstvy a matrice [32], [33].

P8	Hotař A., Palm M., Kratochvíl P., Vodičková V., Daniš S.: *High-temperature oxidation behaviour of Zr-alloyed Fe_3Al-type iron aluminide*, ***Corrosion Science*** 63 (2012) 71-81

Oxidační chování aluminidů železa legovaných Cr, Zr a C bylo v práci [P8] vztaženo k rozdílnému fázovému složení testovaných slitin. Majoritní sekundární fází první ze slitin s nižším obsahem C a s poměrem koncentrací zirkonia a uhlíku c(Zr)/c(C)>1 (v [P8] označena A) je Lavesova fáze λ_1 $(Fe,Al)_2Zr$. Karbid zirkonia je přítomen převážně ve formě jader částic Lavesovy fáze, zatímco u slitiny s vyšším obsahem C a s poměrem c(Zr)/c(C)<1 (v [P8] označena B) jsou dominantní fází karbidy zirkonia. Vliv poměru c(Zr)/c(C) se projevil i v oxidačním chování testovaných slitin.

Pro oxidační testy v teplotním intervalu 900-1200°C na zařízení Setaram SETSYS 16/18 (termováhy s kontinuálním záznamem hmotnostního přírůstku) byly použity vzorky jiskrově obráběných slitin ve válcovaném stavu. Vzorky byly oxidovány v umělé atmosféře při teplotách od 900 do 1200°C.

Hlavní dosažené výsledky:

- *Vliv fázového složení na oxidační odolnost*

Výsledky oxidačních testů [P8] jsou sumarizovány na Fig. 3 a Fig. 4, ze kterých je patrné, že s rostoucí teplotou hmotnostní přírůstek u obou slitin roste. Zatímco při 900°C obě slitiny vykazují velmi nepatrný nárůst hmotnostního přírůstku s časem, při vyšších teplotách byl zaznamenán nárůst výraznější. Po počáteční přechodné době jsou zaznamenané průběhy hmotnostních přírůstků parabolické s výjimkou slitiny s vyšším obsahem C při 1000°C, kde byl zaznamenán lineární nebo dokonce hyperbolický růst [P8], Fig3. U této slitiny je také při teplotách 1100°C a 1200°C nárůst přírůstků s časem výrazně vyšší než u slitiny s nižší koncentrací uhlíku [P8], Fig. 4.

Hodnocení povrchových oxidických vrstev pomocí SEM a EDX analýzy ukázalo, že při 900°C vznikaly na obou slitinách tenké a kompaktní vrstvy. Vyhodnocení řezů povrchem oxidovaných vzorků potvrdilo, že při 900°C dochází u obou slitin k oxidaci pouze na povrchu a díky tomu je oxidační odolnost obou slitin s přídavkem Zr a C v intervalu 900°C – 1000°C vynikající. Při vyšších teplotách byl u obou slitin potvrzen rozsáhlý průnik oxidů dovnitř vzorku díky přednostní korozi zpevňujících precipitátů bohatých na Zr. U slitiny s převažující Lavesovou fází je ovšem oxidace omezena na tuto fázi, kdežto u slitiny s majoritními ZrC karbidy nezůstává omezena na částice karbidů, ale šíří se do matrice (při 1200°C je oxidován značný objem matrice). Průnik oxidace z povrchu do materiálu pak vede u této slitiny k mnohem vyššímu hmotnostnímu přírůstku a lineárnímu oxidačnímu chování.

Předchozí výzkumy oxidační odolnosti Fe-Al-Zr slitin [34] uváděly škodlivý vliv přítomnosti částic Lavesovy fáze a τ-fáze. Výsledky [P8] ukazují, že také ZrC částice negativně ovlivňují oxidační chování zejména nad teplotou 900°C.

- *Mechanismus růstu vrstvy Al_2O_3*

Vrstva Al_2O_3 přednostně roste na částicích fáze ZrO_2 a má tendenci tyto částice obalovat [P8], Fig. 16. Také z dalších výsledků lze soudit, že ZrO_2 funguje jako katalyzátor pro nukleaci Al_2O_3. Je zde také patrný výskyt kolumnárních zrn Al_2O_3 namísto zrn rovnoosých v okolí fáze ZrO_2 [P8], Fig. 16, což potvrzuje vliv přítomnosti Zr na tvar Al_2O_3 zrn popsaný např. v [30], [35].

2.2 Hledání optimálního poměru koncentrací přísadových prvků Zr a C u aluminidů železa na bázi Fe_3Al bez Cr

Jak bylo ukázáno v kapitole 2.1, poměr Zr a C ovlivňuje fázové složení aluminidů železa legovaných Cr a tím i jejich mechanické vlastnosti za vysokých teplot, vysokoteplotní pevnost a creepovou odolnost. Cílem navazujícího výzkumu [P9, P10] bylo ověření vlivu vzájemného poměru Zr a C na strukturu a vysokoteplotní vlastnosti slitin, které chrom neobsahují.

Podobně byl posuzován vliv sekundárních fází - Lavesovy fáze a karbidů zirkonia - na zpevnění aluminidů železa také u slitin „bez uhlíku“, který je ale v malém množství (do 0.06 at.%) přítomen i v čistém železe s obchodním označením Arema, které bylo použito při výrobě slitin v [P11, P12].

Creepová odolnost v závislosti na přítomnosti Zr a C byla sledována v [P13].

P9	Vodičková V., Kratochvíl P., Daniš S., Švec M.: *The effect of zirconium content on the phase structure of Fe_3Al-xC type intermetallic alloys,* **METAL 2013** - 22nd International Conference on Metallurgy and Materials, Conf. Proceedings, 1597-1602.
P10	Kratochvíl P., Vodičková V., Král, R., Švec M.: *The effect of Laves phase $(Fe, Al)_2Zr$ on the high-temperature strength of carbon-alloyed Fe_3Al aluminide,* **Metallurgical and Materials Transactions** 47A (2016) 1128-1131
P11	Kratochvíl P., Kejzlar P., Král R., Vodičková V.: *The ffect of Zr addition on the structure and high temperature strength of Fe-30 at.% Al type alloys,* **INTERMETALLICS 20** (2012) 39-46
P12	Kejzlar P., Kratochvíl P., Král R., Vodičková V.: *Phase Structure and High – Temperature Mechanical properties of Two-Phase Fe-25Al-xZr Alloys Compared to Three-Phase Fe-30Al-xZr Alloys,* **Metallurgical and Materials Transactions** 45A (2014) 335-342
P13	Dobeš F., Vodičková V., Veselý J., Kratochvíl P.: *The effect of carbon additions on the creep resistance of Fe-25Al-5Zr Alloy,* (2016) přijato do **Metallurgical and Materials Transactions**

Pro charakterizaci sekundárních fází byla ve všech komentovaných pracích využita rastrovací elektronová mikroskopie a kombinace energiově-disperzní rentgenové analýzy s rentgenovou difrakční analýzou nebo s difrakcí zpětně odražených elektronů (EBSD).

Hlavní dosažené výsledky:

- *Vliv vzájemného poměru koncentrací přísadových prvků Zr a C na fázové složení a na vysokoteplotní pevnost aluminidů železa*

Studium struktury slitin s nižším obsahem Zr (1-2 at.%) bez obsahu chromu [P9] potvrdilo, že fázové složení podléhá stejným vztahům popisujícím vliv poměru koncentrací přísadových prvků Zr a C jako fázové složení aluminidů železa legovaných Cr [P7]. Byla ověřena vysokoteplotní stabilita sekundárních fází - žíhání při teplotách 1000°C a 1150°C [P9] neovlivnilo fázové složení slitin.

K posouzení vztahů mezi fázemi je v práci [P10] využit rozdíl koncentrací $c_{Zr} - c_{C,}$ lépe postihující množství Zr, které je k dispozici pro tvorbu Lavesovy fáze, namísto poměru koncentrací c(Zr)/c(C) ([P9], resp. [P7]). Fázové složení slitin ve vztahu k rozdílu koncentrací $c_{Zr} - c_C$ je uvedeno v Tab. 1.

Tab. 1 Složení slitin, hodnoty rozdílu koncentrací a objemových podílů sekundárních fází (Table I, [P10])

Alloy	Zr [at.%]	C [at.%]	$c_{Zr} - c_C$ [at.%]	f_v [%] ZrC	f_v [%] eutectic
1143	1.05	1.72	-0.67	1.9 + perovskit	-
1144	2.11	1.58	0.53	2.3	4.2
1181	4.9	1.4	3.5	1.2	41.7
1182	4.8	2.1	2.6	3.9	34.9

Ve slitině 1143 jsou částice ZrC deskovitého tvaru zčásti viditelné pouze jako hrany desek. Zbytek uhlíku je rozpuštěn v mřížce nebo se podílí na tvorbě perovskitického karbidu $Fe_3AlC_{0.5}$, který je patrný ve formě izolovaných tmavších oblastí v matrici [P10], Fig. 1. Ve struktuře slitiny 1144 jsou patrné částice ZrC a eutektika Lavesovy fáze $(Fe,Al)_2Zr$ a matrice [P10], Fig. 2. Struktura slitin 1181 a 1182 je charakteristická dendritickým uspořádáním eutektika a matrice [P10]: eutektikum složené z matrice a Lavesovy fáze $(Fe,Al)_2Zr$ kontinuálně vyplňuje mezidendritický prostor v matrici (Fig. 3 a Fig. 4). Částice karbidu ZrC jsou rozloženy nerovnoměrně a jejich objemový podíl je nízký v poměru k objemovému

podílu eutektika. Závěrem těchto úvah je, že hlavní podíl na zpevnění testovaných slitin má právě eutektická směs.

Pro charakterizaci vysokoteplotních mechanických vlastností testovaných slitin byly užity hodnoty vysokoteplotní meze kluzu v tlaku $\sigma_{0.2}$ [P10]. Z Obr. 15 je zřejmý růst hodnot $\sigma_{0.2}$ s rostoucím obsahem eutektika (matrice a Lavesova fáze $(Fe,Al)_2Zr$) pro všechny testovací teploty. Vzhledem k tomu, že se C podílí na tvorbě karbidů ZrC, je s rostoucím rozdílem koncentrací c_{Zr} - c_C k dispozici větší množství Zr pro vznik Lavesovy fáze $(Fe,Al)_2Zr$. Obr. 15 ukazuje porovnání křivek (1144, 1181 a 1182) s rozdílem c_{Zr} - $c_C > 0$ s křivkou slitiny 1143 s hodnotou c_{Zr} - $c_C < 0$.

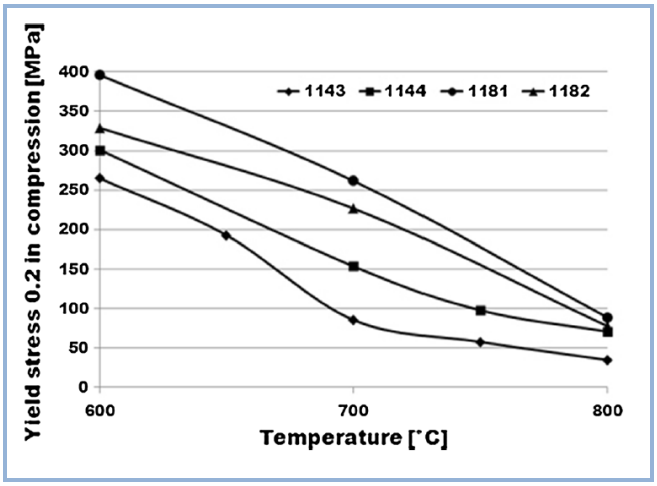

Obr. 15. Závislost hodnot $\sigma_{0.2}$ na teplotě pro slitiny 1143, 1144, 1181 a 1182 (Fig. 5, [P10])

Tento vztah (vliv koncentrace Zr a C) mezi čtyřmi testovanými slitinami přetrvává i v dalším průběhu deformace, tedy až do maximálního napětí ([P10], Tab II), které je dosaženo mezi 5-10 % tlakové deformace. Při teplotě 800°C je tato tendence méně výrazná, pravděpodobně díky změkčení matrice působením teploty. Hlavní vliv, tj. odpevnění vyčerpáním Zr v aluminidu tvorbou karbidů, přetrvává.

Bylo potvrzeno, že množství Lavesovy fáze λ_1 $(Fe,Al)_2Zr$ v aluminidech na bázi Fe_3Al legovaných Zr je ovlivňováno přítomností uhlíku (resp. výraznou afinitou Zr k C) [P10]. Vznik karbidů zirkonia má u tohoto typu slitin negativní vliv na vysokoteplotní pevnost v tlaku, protože snižuje množství Zr využitelného pro vznik Lavesovy fáze, která aluminidy zpevňuje. Vyšší podíl eutektika Lavesovy fáze a matrice zvyšuje vysokoteplotní mez kluzu v tlaku.

S přihlédnutím k podobnosti v železem bohaté oblasti fázových diagramů ternárních systémů Fe-Al-Zr a Fe-Al-Nb s Lavesovou fází [36], [37] lze k porovnání uvést fázové struktury a vysokoteplotní pevnosti slitin s přídavky 2 a 4 at.% Nb a 1 at.% C [38], [39]. Struktury obou slitin obsahovaly karbidy niobu NbC. Skutečnost, že přítomnost Lavesovy fáze $(Fe,Al)_2Nb$ byla popsána pouze ve slitině se 4 at.% Nb a 1 at.% C (nominální koncentrační rozdíl $c_{Nb} - c_C = 3$ at.%), pro kterou byly zjištěny vyšší hodnoty meze kluzu při vysokých teplotách, odpovídá výše uvedené argumentaci.

Pro ověření vlivu frakčního objemu Lavesovy fáze a matrice na vysokoteplotní mez kluzu byly testovány rovněž aluminidy železa legované pouze Zr. Vliv přídavku Zr v množství 0-1-2-5 at.% byl sledován na ternárních slitinách na bázích Fe-30 at.% Al [P11] a Fe-25 at.% Al [P12]. To umožnilo posoudit kromě vlivu obsahu Zr na strukturu a vysokoteplotní vlastnosti slitin rovněž vliv obsahu Al. Složení testovaných slitin je vyznačeno červenými body v ternárním diagramu (viz Fig. 1, [P12]). Pro označení slitin bylo v tabulkách objemových podílů (Tab. 2 a Tab. 3) použito značení vycházející z nominálních koncentrací (30_0, 30_1, atd.), reálné koncentrace blízké nominálním jsou uvedeny v Tab. 2.

Hlavní dosažené výsledky:

- *Vliv Zr na fázové složení a vysokoteplotní pevnost aluminidů železa*

Deformační testy byly provedeny v teplotním intervalu 600°C-880°C a vysokoteplotní mechanické vlastnosti jsou reprezentovány vysokoteplotní pevností σ_{max} a vysokoteplotní mezí kluzu v tlaku $\sigma_{0.2}$. Zpevňující vliv přídavku Zr u slitin typu Fe-30 at.% Al je zřejmý ([P11], Fig. 9b) - hodnoty $\sigma_{0.2}$ rostou s rostoucím obsahem Zr a tento nárůst je výrazný zejména při teplotách 600°C a 700°C. Struktura obou koncentračních řad slitin se ukázala být totožná co do typu sekundární fáze (lamelární eutektikum složené z matrice $B2/D0_3$ a Lavesovy fáze λ_1 $(Fe,Al)_2Zr$ ([P11], Fig. 3a-d, a [P12], Fig. 3a-d). Množství přidaného Zr přímo souvisí s podílem eutektika tvořeného směsí matrice a Lavesovy fáze λ_1. Objemový podíl eutektika u obou řad slitin v litém stavu narůstá lineárně s rostoucím obsahem Zr [P12], jak ukazuje Tab. 2.

Tab. 2 Chemické složení a objemové podíly eutektika f_v(e) v procentech u slitin v litém stavu

Alloy	Al [at.%]	Zr [at.%]	Volume fraction of eutectic [%]
25_0	25.7	0.3	3.9
25_1	25.7	1.0	7.9
25_2	25.5	2.0	18.1
25_3	25.4	5.0	47.6
30_0	29.3	0.4	3.4
30_1	29.2	0.9	8.7
30_2	28.6	1.9	20.9
30_5	30.1	5.2	55.2

Je patrné, že hodnota vysokoteplotní meze kluzu v tlaku s rostoucím frakčním objemem eutektika f_v roste, a to pro obě koncentrační řady slitin [P12], Fig. 12 a Fig. 13. Jako velmi efektivní prostředek pro zvýšení vysokoteplotní pevnosti se ukázal zejména přídavek Zr v množství 5 at.%, který zapříčinil distribuci Lavesovy fáze ve struktuře v poměrně kompaktní eutektické „síti“. Potvrzení zpevňující úlohy Lavesovy fáze vyplývá také z porovnání hodnot vysokoteplotní meze kluzu $\sigma_{0.2}$ slitiny Fe-30Al-5Zr (at.%) s výsledky [34], i když na nárůstu hodnot $\sigma_{0.2}$ pro slitinu Fe-30Al-5Zr (at.%) se jistě podílí také zvýšení uspořádanosti samotné matrice [P11], Fig. 13.

Ve struktuře všech slitin obou koncentračních řad byly identifikovány částice ZrC o velikosti ~ 2μm, jejichž objemový podíl nepřekročil 0.02 %. Tato fáze byla identifikována EDX analýzou buď jako individuální částice ZrC [P11] (patrné jako bílé částice např. na Fig. 3d) nebo jako jádra částic Lavesovy fáze [P12], jak ukazuje detail na obrázku Fig. 4a. Vzhledem k velikosti a velmi řídkému zastoupení ve struktuře lze předpokládat, že jejich příspěvek k celkovému zpevnění bude zanedbatelný.

Zatímco vysokoteplotní mechanické vlastnosti slitin na bázi Fe-25 at.% Al nebyly použitým tepelným zpracováním významně ovlivněny, u slitin na bázi Fe-30 at.% Al došlo po žíhání při 1000°C k výraznému zpevnění [P11], které se nejvíce projevilo při 600°C, jak je patrné na Obr. 16.

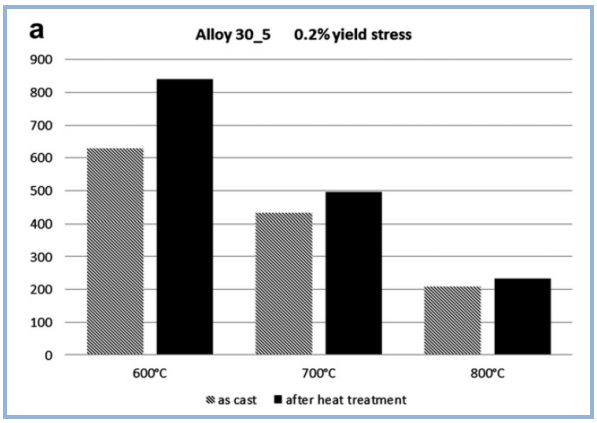

Obr. 16. Závislost $\sigma_{0.2}$ na teplotě pro slitinu Fe-30Al-5Zr (at.%) po tepelném zpracování (černá) a v litém stavu (šedá), (Fig. 12a, [P11])

Fázové složení sledovaných slitin po tepelném zpracování (žíhání při 1000°C) bylo rozdílné: zatímco slitiny na bázi Fe - 25 at.% Al si zachovaly dvoufázovou strukturu [P12], i když s odlišnou morfologií a distribucí λ_1 fáze (Fig. 4d), ve struktuře slitin na bázi Fe - 30 at.% Al došlo po rozpadu eutetika k precipitaci dvou fází – Lavesovy fáze λ_1 a další fáze τ_1 $(Fe,Al)_{12}Zr$ s tetragonální mřížkou [P11]. Fáze λ_1 je přítomna ve formě drobnějších i rozměrnějších globulárních částic, fáze τ_1 tvoří souvislé oblasti ([P11], Fig. 7cd). Rozdíly ve fázovém složení byly potvrzeny rentgenovou difrakční analýzou ([P11], Fig. 8). Objemový podíl obou fází narůstá s rostoucím obsahem Zr [P11], jak ukazuje Tab. 3.

Tab. 3 Fázové složení slitin typu Fe30Al po žíhání při 1000°C (Table 4, [P11])

Alloy	Microstructure after heat treatment	Volume fraction of λ_1 [%]	Volume fraction of τ_1 [%]
30_0	$B_2/D0_3 + \lambda_1 + \tau_1$	0.2	3.4
30_1	$B_2/D0_3 + \lambda_1 + \tau_1$	5.0	5.5
30_2	$B_2/D0_3 + \lambda_1 + \tau_1$	7.2	16.1
30_5	$B_2/D0_3 + \lambda_1 + \tau_1$	18.6	35.4

Je zřejmé, že precipitace další fáze (τ_1) a vznik třífázové struktury (matrice+λ_1 +τ_1) vede u slitin tohoto typu k významnému nárůstu hodnot $\sigma_{0.2}$. Oproti $\sigma_{0.2}$ cca 600 MPa při 600°C u slitiny Fe-25Al- 5Zr (at.%) v žíhaném stavu (s dvoufázovou strukturou) je na Obr. 16 patrný nárůst $\sigma_{0.2}$ při 600°C až nad 800 MPa pro slitinu Fe-30Al-5Zr (at.%) v žíhaném stavu (s třífázovou strukturou).

Zvýšení vysokoteplotních mechanických vlastností může být u slitin obou řad vysvětleno růstem celkového podílu tvrdých intermetalických fází λ_1 a τ_1 obsahujících Zr na

úkor měkké matrice Fe_3Al. Pevnost takového dvou nebo třífázového materiálu by mohla být interpretována jako pevnost kompozitního materiálu, pro jehož hodnoty $\sigma_{0.2}$ platí [P11]

$$\sigma_{0.2composite}(T) \equiv f_{natrix} \cdot \sigma_{0.2matrix}(T) + f_{\lambda 1} \cdot \sigma_{\lambda 1}(T) + f_{\tau 1} \cdot \sigma_{\tau 1}(T)$$

kde f_n a $\sigma_{0.2n}$ jsou vztaženy k jednotlivým fázím. Realizace takového výpočtu $\sigma_{0.2}$ však i při použití dostupných hodnot $\sigma_{0.2}$ pro podobné matrice s ZrC karbidy [21] naráží na problém při stanovení $\sigma_{0.2}$ tvrdých, ale křehkých fází λ_1 a τ_1 [36].

Vliv obsahu uhlíku na creepové chování aluminidů železa legovaných Zr byl sledován v práci [P13]. Creepový experiment v ochranné argonové atmosféře byl realizován v tlaku s využitím zatěžování v krocích, tj. změna napětí následovala po dosažení ustálené creepové rychlosti pro dané zatížení. Z každého kroku byly vyhodnoceny creepové charakteristiky - napěťový exponent n a aktivační energie Q.

Hlavní dosažené výsledky:

- *Vliv poměru koncentrací Zr a C na creepovou odolnost aluminidů železa při vysokých teplotách*

Složení tří slitin pro creepový experiment je uvedeno v Tab. 4 (Table 1 v [P13]).

Tab. 4 Chemické složení testovaných slitin v at.%

Alloy	Al [at.%]	Zr [at.%]	C [at.%]
Fe-25Al-5Zr	25.4	5.0	0.06
Fe-25Al-5Zr-1C	25.3	5.65	0.92
Fe-25Al-5Zr-4C	24.7	5.42	3.46

Slitiny byly testovány v litém stavu a ve stavu po žíhání 50 h při 1000°C pro stabilizaci struktury. Mikrostruktura všech slitin v litém stavu byla tvořena matricí, eutektikem Lavesovy fáze a matrice a částicemi karbidů Zr v množství a velikosti korespondujícím s obsahem C v jednotlivých slitinách. Po žíhání došlo u slitin s nižším obsahem uhlíku ke koagulaci a zhrubnutí Lavesovy fáze [P12], Fig. 4a a [P13], Fig. 2, u slitiny Fe-25Al-5Zr-4C k rozpadu eutektika a koagulaci Lavesovy fáze v matrici [P13], Fig. 4. Ve struktuře žíhaných slitin Fe-25Al-5Zr-1C a Fe-25Al-5Zr-4C po creepových testech byly pomocí TEM zjištěny drobné částice (o velikosti 0,5 až 1 μm). Selektivní elektronová difrakce tyto částice identifikovala

jako fázi $Fe_{23}Zr_6$ s plošně centrovanou kubickou mřížkou typu $Mn_{23}Th_6$ s mřížkovým parametrem 1,18 nm), [P13], Fig. 5 a 6. Tyto částice odpovídají metastabilní fázi identifikované u Fe - Al - Zr ternárních slitin, která je stabilizována příměsemi [36].

K výpočtu creepových charakteristik jednotlivých slitin v litém a žíhaném stavu při teplotách 700°C a 900°C byly využity vztahy (1) a (2), kap. 1.2. Vliv přidaného uhlíku je výrazný zejména při teplotě 700°C, kdy rychlost creepu jednoznačně narůstá s rostoucím obsahem uhlíku ([P13], Fig. 9). Hodnoty aktivačních energií Q byly stanoveny ze vztahu (1) metodou vícenásobné lineární regrese za předpokladu, že aktivační energie je nezávislá na napětí. Hodnoty napěťového exponentu n byly vypočteny pro každou ze zkušebních teplot a jsou uvedeny v tabulce III, [P13]. Pro obě nízkouhlíkové slitiny, tedy Fe-25Al-5Zr a Fe-25Al-5Zr-1C, odpovídají hodnoty napěťového exponentu n hodnotám obvyklým pro aluminidy železa [40]. Korespondují s hodnotami popsanými pro slitiny na bázi Fe-28Al při vyšších napětích [41] a naznačují, že rozhodujícím mechanismem ovlivňujícím rychlost tečení je šplhání dislokací. Vyšší hodnoty n u slitiny Fe-25Al-5Zr-4C při teplotě 1173 K (900°C) lze odůvodnit v rámci koncepce prahového napětí [42].

Vliv kombinace aditiv Zr a C na creepovou odolnost aluminidů železa legovaných chromem byl již diskutován z hlediska jejich vzájemného poměru v komentované práci [P7]. Obr. 17, kde je napětí působící creepovou rychlost 10^{-7} s^{-1} prezentováno jako funkce poměru koncentrací aditiv c(Zr)/c(C), zahrnuje porovnání s výsledky [P7] (ref.[17] v Obr. 17).

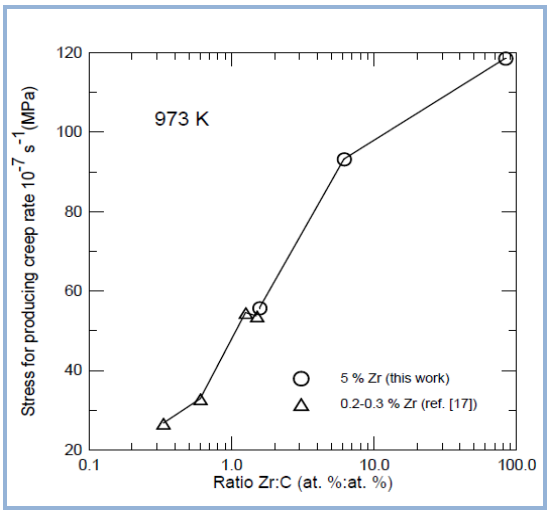

Obr. 17. Napětí působící creepovou rychlost 10^{-7} s^{-1} jako funkce poměru c(Zr)/c(C), porovnání výsledků o [P13] s výsledky Δ [P7] (Fig. 10, [P13])

Nárůst creepové odolnosti s rostoucím poměrem koncentrací c(Zr)/c(C) pro slitiny s vyšším obsahem Zr velmi dobře koresponduje s předchozím výzkumem [P7] a potvrzuje podstatnou roli vzájemného poměru koncentrací zirkonia a uhlíku pro vysokoteplotní creepové vlastnosti aluminidů železa na bázi Fe_3Al.

2.3 Analogie výsledků u aluminidů legovaných niobem

V návaznosti na výzkum optimálního poměru koncentrací přísadových prvků c(Zr)/c(C) se jeví jako perspektivní systém Fe-Al-Nb. U aluminidů železa legovaných niobem lze předpokládat podobný mechanismus zpevňování slitiny jako v případě přídavku zirkonia, neboť systémy Fe-Al-Zr a Fe-Al-Nb vykazují podobnosti v železem bohaté oblasti ternárních diagramů především co se týče tvorby Lavesových fází.

I přes relativně nízkou hodnotu je rozpustnost niobu v Fe_3Al matrici v ternárním systému Fe-Al-Nb vyšší než rozpustnost Zr v systému Fe-Al-Zr. Díky rozpouštění většího množství niobu v matrici zbývá (při podobných obsazích legujícího prvku) méně aditiva pro tvorbu zpevňující sekundární fáze, než v systému Fe-Al-Zr. Touto fází je nekoherentní Lavesova fáze $(Fe,Al)_2Nb$, o níž lze předpokládat, že může plnit ve slitinách s niobem podobnou zpevňující roli jako Lavesova fáze $(Fe,Al)_2Zr$ v systému Fe-Al-Zr. S tím rozdílem, že v Fe-Al-Nb systému je nutno zohlednit rovněž zpevňující vliv tuhého roztoku [43].
Pro legování niobem existuje řada dalších důvodů: přídavek niobu zvyšuje transformační teplotu B2-A2 přechodu (přechod od uspořádané k neuspořádané struktuře) a zvyšuje i teplotu přechodu $D0_3$-B2, čímž stabilizuje strukturu s vysokým stupněm uspořádání [44].

Proto byl v posledních letech souběžně s výzkumem aluminidů legovaných Zr zahájen intenzívní výzkum slitin legovaných Nb. Některé z jeho dosavadních výsledků jsou částečně prezentovány v publikacích, na kterých jsem se rovněž podílela, např. [45]. Podobně jako v případě aluminidů legovaných Zr jsou zkoumány slitiny legované jednak pouze Nb, „bez uhlíku“(tedy s minimálním obsahem C přítomným ve výchozí surovině - železe), jednak s uhlíkem jako záměrným aditivem. Na základě doposud získaných výsledků lze potvrdit, že hodnoty vysokoteplotní meze kluzu $\sigma_{0.2}$ u aluminidů v litém stavu legovaných 3, resp. 5 at.% niobu rostou se zvyšujícím se obsahem přidané legury stejně jako v případě aluminidů legovaných Zr.

U slitin legovaných niobem a uhlíkem probíhá studium vlivu vzájemného poměru koncentrací Nb/C na vysokoteplotní mechanické vlastnosti se stejnou motivací jako v případě zirkoniem dopovaných slitin. Ve shodě s výzkumem slitin se zirkoniem a uhlíkem vykazují i slitiny legované 1 a 5 at.% niobu a uhlíkem v množství 0.8 a 1.4 at.% lepší vysokoteplotní mechanické vlastnosti s rostoucím přebytkem niobu (slitina s vyšším poměrem koncentrací Nb/C vykazovala o 100 MPa vyšší mez kluzu při 600 a 700°C a o 50 MPa při 800°C). V důsledku vyšší rozpustnosti niobu v matrici Fe_3Al nevytváří Lavesova fáze s matricí eutektickou směs jako u slitin legovaných Zr a C, ale částice Lavesovy fáze a karbidů niobu

tvoří ve struktuře poměrně rovnoměrnou a hustou disperzi. Tento způsob distribuce částic sekundární fáze zřejmě významně přispívá ke zpevnění za vysokých teplot, jak ukazuje výzkum vlivu obsahu uhlíku na vysokoteplotní vlastnosti aluminidů legovaných Nb. Slitina legovaná Nb a C vykazuje při všech zkušebních teplotách vyšší hodnotu vysokoteplotní meze kluzu v tlaku než slitina bez uhlíku se stejným obsahem Nb.

I přes malé rozdíly dosavadní výzkum potvrzuje, že na vysokoteplotní chování aluminidů legovaných Nb a C lze nahlížet stejným způsobem jako v případě Zr a C, a tudíž při užití Zr a Nb jako aditiv aluminidů železa musí být vždy brána v úvahu přítomnost i malého množství uhlíku.

3 Shrnutí a závěry

- Výzkum aluminidů železa na bázi FeAl legovaných uhlíkem, resp. uhlíkem a křemíkem přispěl k upřesnění poznatků o vymezení oblastí existence fází (κ karbidu a grafitu) v rámci ternárního diagramu. Na základě studia fázového složení bylo navrženo posunutí fázových hranic v kvazibinárním diagramu a v odpovídající části diagramu ternárního. Ve slitinách s vyššími obsahy uhlíku byla potvrzena přítomnost karbidu Al_4C_3 ve struktuře slitin dopovaných křemíkem i ve slitinách bez křemíku v souladu s predikovanou oblastí jeho výskytu podle teoretických výpočtů.
- Byla popsána souvislost vysokoteplotních vlastností s velikostí a způsobem distribuce sekundární fáze a identifikovány creepové mechanismy uplatňující se u aluminidů železa na bázi FeAl legovaných uhlíkem, resp. uhlíkem a křemíkem při vysokoteplotní deformaci. Bylo prokázáno, že způsob distribuce karbidu hliníku Al_4C_3 ve slitinách s vyšším obsahem uhlíku a přídavkem křemíku - tj. tenké jehlice vyplňující prostor mezi dendrity tuhého roztoku α - velmi účinně brání pohybu dislokací v matrici a výrazně zvyšuje creepovou odolnost slitin.
- Na základě studia fázového složení aluminidů na bázi Fe_3Al s přídavkem Cr a dalšími aditivy (Zr, Zr+TiB_2, Zr+C) byla popsána role sekundárních fází při vysokoteplotní deformaci. Studium struktury vzorků po creepových testech pomocí transmisní elektronové mikroskopie ukázalo, že jak u aluminidů s aditivy Zr+TiB_2 tak u aluminidů dopovaných Zr a C při teplotách 600 a 650°C je proces vysokoteplotní deformace omezován především velmi jemnými precipitáty vznikajícími v průběhu deformace. Při vyšších teplotách creepové deformace dochází pak u obou typů slitin k výraznému hrubnutí těchto jemných precipitátů a nárůstu vzdáleností mezi nimi. Z toho důvodu již při vyšších teplotách nejsou jako překážky pro pohyb dislokací efektivní.
- Z porovnání získaných výsledků s výsledky dalších studií slitin na bázi Fe_3Al dopovaných pouze Zr nebo pouze TiB_2 bylo zjištěno, že kombinace aditiv Zr a TiB_2 nevede ke zvýšení creepové odolnosti ani vysokoteplotní pevnosti v tahu. Bylo prokázáno, že aditivem vhodným pro zvýšení vysokoteplotních vlastností je samotné Zr, případně v kombinaci s uhlíkem, a jako překážky pro pohyb dislokací se uplatňují jemné precipitáty ZrC.
- U aluminidů železa legovaných pouze Zr (a tedy s minimálním obsahem uhlíku z výrobního procesu) byl prostřednictvím testů vysokoteplotní pevnosti v tlaku

potvrzen zpevňující vliv Lavesovy fáze. Objemový podíl eutektika ve struktuře litého stavu slitin se zvyšuje lineárně s rostoucím obsahem Zr a tomu odpovídá i nárůst hodnot vysokoteplotní meze kluzu $\sigma_{0.2}$.

- Analýza fázového složení slitin na bázi Fe_3Al legovaných Zr a C ukázala význam vzájemného poměru C a Zr pro tvorbu Lavesovy fáze. S rostoucím rozdílem koncentrací c_{Zr} - c_C je k dispozici větší množství Zr pro vznik Lavesovy fáze $(Fe,Al)_2Zr$. S rostoucím objemovým podílem eutektika matrice a Lavesovy fáze $(Fe,Al)_2Zr$) ve struktuře slitin rostou hodnoty $\sigma_{0.2}$ pro všechny testovací teploty. Role vzájemného poměru koncentrací zirkonia a uhlíku je podstatná také pro vysokoteplotní creepové vlastnosti slitin na bázi Fe_3Al: přítomný uhlík vždy redukuje množství Zr dostupného pro vznik zpevňující Lavesovy fáze v těchto slitinách a tím omezuje jejich creepovou odolnost. Na vzájemném poměru koncentrací Zr a C závisí i množství Zr, které se může v průběhu vysokoteplotní creepové deformace podílet na vzniku jemné disperze částic dalších fází, plnících funkci překážek pro pohyb dislokací.
- Vzájemný poměr Zr a C ovlivňuje rovněž vysokoteplotní oxidační chování aluminidů železa. Jsou-li ve struktuře majoritní fází karbidy ZrC, proniká oxidace z povrchu do matrice přednostně přes tyto částice karbidů, a to pak vede u k mnohem vyššímu hmotnostnímu přírůstku a lineárnímu oxidačnímu chování. Naproti tomu u slitiny s převažující Lavesovou fází je oxidace omezena pouze na tuto fázi. Oxidy ZrO_2 vznikající u aluminidů dopovaných Zr plní funkci katalyzátoru pro nukleaci kompaktní pasivační vrstvy Al_2O_3.

4 Literatura

[1] Vyklický, M., Tůma H., Hutnické listy, 14, 1959, p. 118

[2] Palm, M., Inden, G., Intermetallics, 3, 1995, p. 443

[3] Palm, M., Intermetallics, 13, 2005, p. 1286

[4] Balasubramaniam,R., J Alloy Compd, 2002, p. 330

[5] Zhu, S.M. et al., in Hemker,K.J. et al., editors. Structural Intermetalics. The Minerals, Metals & Mater Soc,2001, p. 755

[6] Vogel, R., Mäder, H., Arch Eissenhütten, 1938, 11, p. 607

[7] Ohtani, H., Yamano, M., Hasebe, M., ISIJ Internat., 44, 2004, p. 1738

[8] Vyklický, M., Zpráva VÚMT Praha, Z-57-548, Praha 1957

[9] Sasaki, M.,Kaminaga, M., Tagami J., Jpn Foundry Eng Soc, 1999, 71, p. 455

[10] Sundar, R.S., Deevi, S.C., Metal Mater Trans, 2003, 34A, p. 2233

[11] Schneider, A., Falat, L., Sauthoff, G., Frommayer, G., Intermetallics, 13, 2005, p. 1322

[12] Zhang, W.J, Sundar, R.S., Deevi, S.C., Intermetallics, 12, 2004, p. 893

[13] Nagpal, P., Baker, I., 1990 Met Trans A21, p. 2281

[14] Liu, C.T., Sikka, V.K., McKamey, C.G., 1993, Alloy Development of FeAl Aluminide Alloys for Structural Use in Corrosive Environments. ORNL/TM-12199

[15] Palm, M., Intermetallics 2005, 13, p. 1286

[16] MorrisDG,Muñoz-Morris MA,BaudinC. ActaMater 2004, 52, p. 2827

[17] MorrisDG, Muñoz -Morris MA.MaterSciEng 2007, A462, p. 45

[18] MorrisDG, Muñoz -Morris MA,ChaoJ.Intermetallics 2004, 12, p. 821

[19] Stein F., Palm M., Sauthoff G., Intermetallics 2005,13, p. 1275

[20] McKamey, C.G.; Horton, J.A.; Liu, C.T. Journal of Materials Research 1989 (4), Issue 5, p. 1156

[21] Kratochvíl, P., Málek, P., Cieslar, M., Hanus, P., Hakl, J., Vlasák, T. Intermetallics 2007, 15, p. 333

[22] Kratochvíl, P., Málek, P., Pešička, J., Hakl, J., Vlasák, T., Hanus, P., Kovové Materiály 2006, 44, p. 185

[23] Cieslar M, Karlík M. Carbide formation in Zr-containing Fe3Al-based alloys, Mater Sci Eng A 2007, 462, p. 289

[24] M. Karlík, P. Kratochvíl, J. Pešička, T. Vlasák, Int. J. Mater. Res. 100, 2009, p. 806

[25] D.G. Morris, M.A. Muñoz-Morris, L.M. Requejo, Acta Mater. 54, 2006, p. 2335

[26] D.G. Morris, I. Gutierrez-Urrutia, M.A. Muñoz-Morris, Scr. Mater. 57, 2007, p. 449

[27] S. Khaple, R.G. Baligidad, S. Rao, Mater. Sci. Technol. 23, 2007, p. 930

[28] R. Krein, A. Schneider, G. Sauthoff, G. Frommeyer, Intermetallics 15, 2007, p. 1172

[29] C.G. McKamey, J.H. DeVan, P.F. Tortorelli, V.K.J. Sikka, *Mat. Res. 6*, 1991, p. 1779

[30] P.F. Tortorelli, K. Natesan, Mat. Sci. Eng. A258, 1998, p. 115

[31] R. Prescott, M.J. Graham, *Oxid. Met. 38,* 1992, p. 73

[32] S. Chevalier, P. Juzon, G. Borchardt, A. Galerie, K. Przybylski, J.P. Larpin, *Oxid. Met. 73*, 2010, p. 43

[33] B.A. Pint, P.F. Tortorelli, I.G. Wright, Long-term oxidation performance of ingot produced Fe3Al alloys, Mater. High Temp. 16, 1999, p. 1

[34] F. Stein, M. Palm, G. Sauthoff, Intermetallics 13, 2005, p. 1275

[35] B. A. Pint, Oxid. Met. 45, 1996, p. 1

[36] F. Stein, G. Sauthoff, M. Palm*: Z. Metallk.,* 2004, vol. 95, p. 469

[37] M. Palm: *J. Alloy Compd., 2009,* vol. 475, p. 173

[38] A. Schneider, L. Falat, G. Sauthoff, and G. Frommeyer, *Intermetallics,* 2003, vol. 11, p.443

[39] L. Falat, A. Schneider, G. Sauthoff, and G. Frommeyer, *Intermetallics*, 2003, vol. 13, p. 1256

[40] N.S. Stoloff, *Mater. Sci. Eng. A 258,* 1998, p. 1

[41] C.G. McKamey, P.J. Maziasz, and J.W. Jones*: J. Mater. Res.,* 1992, vol. 7, p. 2089

[42] J.D. Whittenberger: *Metall. Trans. A*, 1977, vol. 8A, pp. 1155

[43] Prymak O., Stein F., *Intermetallics 18,* 2010, p. 1322

[44] Morris, D. G., Requejo, L. M., Munoz – Morris, M. A. *Intermetallics 13*, 2005, p. 86

[45] Dobeš F.; Kratochvíl P.; Pešička J., Vodičková V., *Metallurgical and Materials Transaction* 46A, 2015, p. 1580

5 Soubor komentovaných publikací

[P1] Vodičková V., Kratochvíl P., Dobeš F., *The effect of carbon on the structure of Fe-40Al-xC (at.%) ternary alloys*, **Kovové materiály - Metallic Materials 45** (2007) 153-158

[P2] Kratochvíl P., Dobeš F., Vodičková V., *The effect of silicon on the structure of Fe-40at.%Al type alloys with high contents of carbon*. **Intermetallics 17** (2009) 39-45

[P3] Dobeš F., Kratochvíl P., Vodičková V., Milička K., Pešička J., *The effect of carbon on high temperature deformation of Fe-40Al-xC (at.%) ternary alloys*, **Kovové materiály - Metallic Materials 46** (2008) 97-103

[P4] Dobeš F., Kratochvíl P., Vodičková V., *The effect of carbon and silicon additions on the creep properties of Fe-40 at.% Al type alloys at elevated temperatures*, **Intermetallics 19** (2011) 1526 – 1532

[P5] Kratochvíl P., Vodičková V., Hanus P., Hakl J., Vlasák T., Pešička J., *High-temperature mechanical properties of Fe_3Al type alloy with combined additives TiB_2* and Zr, **Intermetallics 18** (2010) 1365-1368

[P6] Vodičková V., Hanus P., Kratochvíl P., Málek P., *Effect of Carbon addition on phase composition and high-temperature mechanical properties of Fe-Al-Zr ternary alloys*, **METAL 2010** - 19th International Conference on Metallurgy and Materials, Conference Proceedings, 765-769

[P7] Kratochvil P., Dobeš F., Pešička J., Málek P., Buršík J., Vodičková V., Hanus P., *Microstructure and high-temperature properties of Zr-alloyed Fe_3Al type aluminides: The effect of carbon*, **Materials Science and Engineering** Volume A 548 (2012) 175-182

[P8] Hotař, A., Palm, M., Kratochvil, P., Vodičková V., Daniš S., *High-temperature oxidation behaviour of Zr alloyed Fe3Al-type iron aluminide*, **CORROSION SCIENCE** Volume 63 (2012) 71-81

[P9] Vodičková V., Kratochvíl P., Daniš S., Švec M., *The Effect of Zirconium Content on the Phase Structure of Fe Al-xC type Intermetalic Alloys,* **METAL 2013** - 22nd International Conference on Metallurgy and Materials, Conference Proceedings, 1597-1602.

[P10] Kratochvíl P., Vodičková V., Král R., Švec M., *The Effect of Laves Phase (Fe,Al)(2)Zr on the High-Temperature Strength of Carbon-Alloyed Fe3Al Aluminide***, Metallurgical and Materials Transactions 47A** (2016) 1128-1131

[P11] Kratochvíl P., Kejzlar P., Král, R.,Vodičková, V., *The effect of Zr addition on the structure and high temperature strength of Fe-30 at.% Al type alloys,* **Intermetallics 20** (2012) 39-46

[P12] Kejzlar, P., Kratochvíl, P., Král, R., Vodičková, V., Phase *Structure and High-Temperature mechanical Properties of Two-Phase Fe-25Al-xZr Alloys Compared to Three-Phase Fe-30Al-xZr Alloys*, **Metallurgical and Materials Transactions 45** (2014), 335-342

[P13] Dobeš F., Vodičková V., Veselý J., Kratochvíl P.: *The effect of carbon additions on the creep resistance of Fe-25Al-5Zr Alloy,* přijato do **Metallurgical and Materials Transactions** (září 2016)

The effect of carbon on the structure of Fe-40Al-xC (at.%) ternary alloys

V. Vodičková [1]*, P. Kratochvíl[1], F. Dobeš[2]

[1] *Technical University of Liberec, Faculty of Engineering, Department of Material Science, Hálkova 6, CZ-46117 Liberec, Czech Republic*

[2] *Institute of Physical Metallurgy, Czech Academy of Sciences, Žižkova 22, CZ-61662 Brno, Czech Republic*

Received 27 November 2006, received in revised form 17 April 2007, accepted 24 April 2007

Abstract

The phase composition of Fe-40Al-xC (at.%) alloys depends on the content of C. The part of the quasibinary phase diagram is determined using light optical microscopy (LOM), Vickers hardness measurements (HV) and X-rays diffraction (XRD). The composition of the tested alloys approaches in succesive steps Pyroferal© alloy used in the fifties to replace the high chromium and nickel alloyed cast iron. The structural data are compared with those resulting from quasibinary Fe40Al-xC as well as ternary Fe-Al-C phase diagrams.

K e y w o r d s: iron aluminide (Fe-Al type), phase composition

1. Introduction

Special properties of Fe-40Al (at.%) intermetallics (low density, oxidation and sulfidation resistance) enable their use for high temperature (HT) applications [1]. The typical cases of applications are porous filtres for high sulphur contamined gases, e.g. heat exchangers in gas turbines, protecting sheets in vessels, tubes in power stations, incinerators, structural components in furnaces, etc. Carbon in the FeAl (B2) iron aluminide is used e.g. to enhance the mechanical properties and to improve machinability.

The following phases exist near the composition Fe-40Al (at.%) in the ternary Fe-Al-C system depending on content of C and temperature:

– solid solution of C in B2 lattice

– graphite (G)

– carbide $Fe_3AlC_{0.5}$ (perovskite), so called κ-phase (κ).

The presence of Si ($\sim$ 1 at.%) may iniciate the formation of aluminium carbide Al_4C_3.

A very complex study of the phase composition of alloys based on FeAl aluminide was performed by Vyklický and Tůma [2] who also determined pseudobinary phase diagrams for different contents of Al. That one corresponding to 40 at.% Al is shown in Fig. 1. This

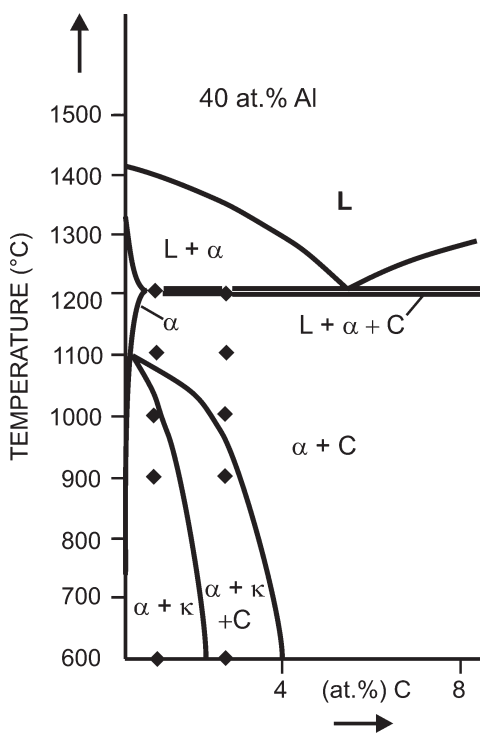

Fig. 1. Quasibinary diagram of Fe-40at.%Al-C according to data in [2].

*Corresponding author: tel.: +420 485 353 129; e-mail address: vera.vodickova@tul.cz

is the base material from which one can derive the series of alloys ending by Pyroferal© (ČSN 422484). Its composition is as follows: 44.4–46.5 at.% Al, 3.4–4.0 at.% C and max 0.5 at.% Mn, max 0.7 at.% Si. Maximum content of S, P is given by standard.

The mentioned Pyroferal© has a high resistance against thermal cycling, excellent resistance against chemical environments and also against abrasive wear. These properties enable to increase operating life time when compared to materials used before (Fe-Ni-Cr alloys). The reasons for favourable properties of Pyroferal© have never been fully understood and explained on the basis of structure (phase composition).

The aim of the present paper is to describe the structure of Fe-40Al (at.%) alloys with the increasing content of C. These results are used elsewhere to understand the mechanical properties at 600 ℃ [3].

2. Experimental technique

The nominal chemical compositions of alloy used for the experiment are summarized in Table 1. The alloys D-F were prepared by vacuum melting (10^{-1}–10^{-2} mbar). The induction furnace Leybold was used. The slabs (cross section 20 × 32–35 mm) were rolled at 1200 ℃ to 8 × 35–40 mm using 8–15 % reductions. After each reduction the slab was heated in the furnace to 1280 ℃.

Alloy H was prepared by sand casting.

Light optical microscopy (LOM), X-rays diffraction (XRD) and measurements of Vickers hardness (HV) were used to determine the phase composition of studied alloys. The phase structure, incl. grain boundaries was made visible using etching by emulsion OP-S (Struers). Also Nomarski contrast was applied to increase the resolution of phases. HV was measured using MICROMET 2100 – Buehler with image analyser. For XRD the system XRD7-FPM-Seifert was used.

Transmission electron microscopy (TEM) combined with the selected area diffraction (SAD) was used to identify the phases. The corresponding apparatus was JEOL FX2000. Phases were also identified by electron microanalysis.

3. Results

3.1. Structure of the alloy FA0.1C (D)

The size of equiaxed grains in the original material (after rolling at 1200 ℃ and free cooling) is larger than 500 μm. Only the B2 matrix without any other particles was identified (see Fig. 2) either inside the grains or along the grain boundaries. Carbon is fully soluble in the matrix. The average value of microhardness is 386 HV 0.05. The phase composition changed neither after 1100 ℃/8 h nor after 600 ℃/100 h annealing.

Table 1. Composition of the alloys (at.%/wt.%)

Alloy	Denoted	Al	C	Si
FA0.1C	D	41.05/25.2	0.07/0.02	
FA0.8C	E	40.5/24.9	0.75/0.19	
FA1.7C	F	40.05/24.8	1.7/0.44	
FA1.9C	H	41.3/26.08	1.9/0.52	1.2/0.8

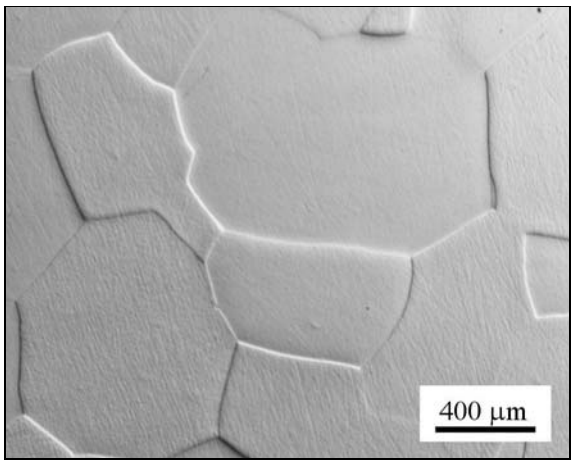

Fig. 2. Structure of alloy D, original state.

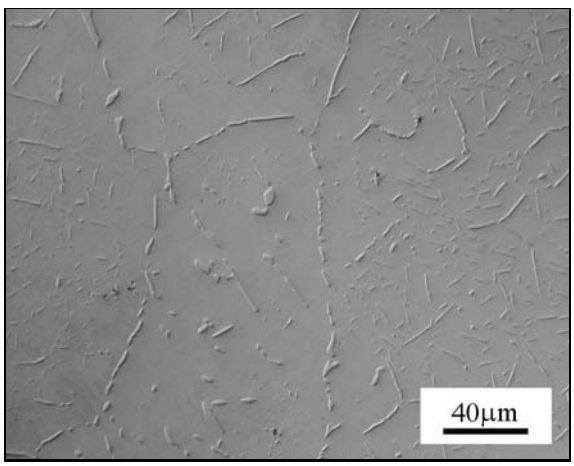

Fig. 3. κ-carbide in alloy E, original state.

3.2. Structure of alloy FA0.8C (E)

The original state: brighter rod-like particles are seen on the background situated along the grain boundaries and in the grains (Fig. 3). The values of

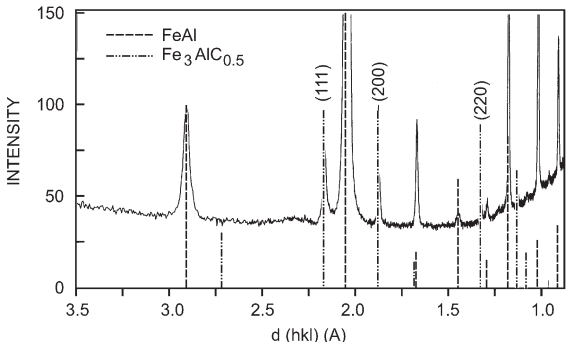

Fig. 4. XRD curve for sample E (annealed 600 °C/100 h).

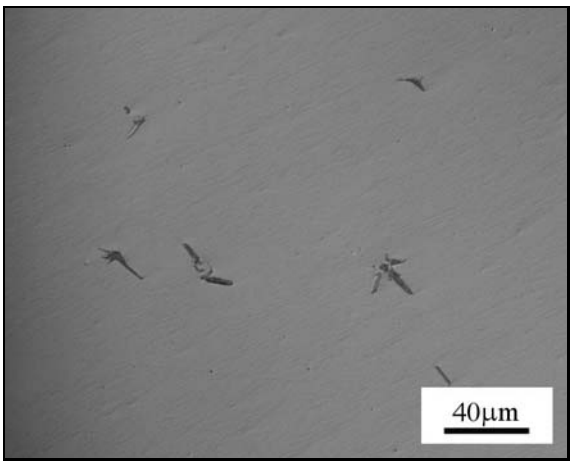

Fig. 5. Graphite in alloy E (annealed 1100 °C/8 h).

microhardness are 443 HV 0.05 for matrix and 575 HV 0.01 for the rod-like particles. For the given content of carbon and according to the rolling temperature graphite should be present in the matrix as supposed by the phase diagram shown in Fig. 1.

The observed bright phase corresponds to graphite neither morphologically nor by the value of HV. This relates to κ-phase. Using XRD κ-carbide was identified (see pronounced (111), (200) and (220) reflections of κ-phase in Fig. 4). The structure did not change after annealing at 600 and 800 °C.

The annealing at 1100 °C/8 h (oil quench) changes the structure. κ-phase is dissolved and particles of dark phase (graphite) with size of 10–40 μm are appearing within the grains and along the grain boundaries – see Fig. 5. The dissolution of κ-phase is in agreement with the situation in the phase diagram.

3.3. Structure of alloy FA1.7C (F)

It is possible to observe both the pieces of darker phase (little greater) and pieces of brighter phase (size

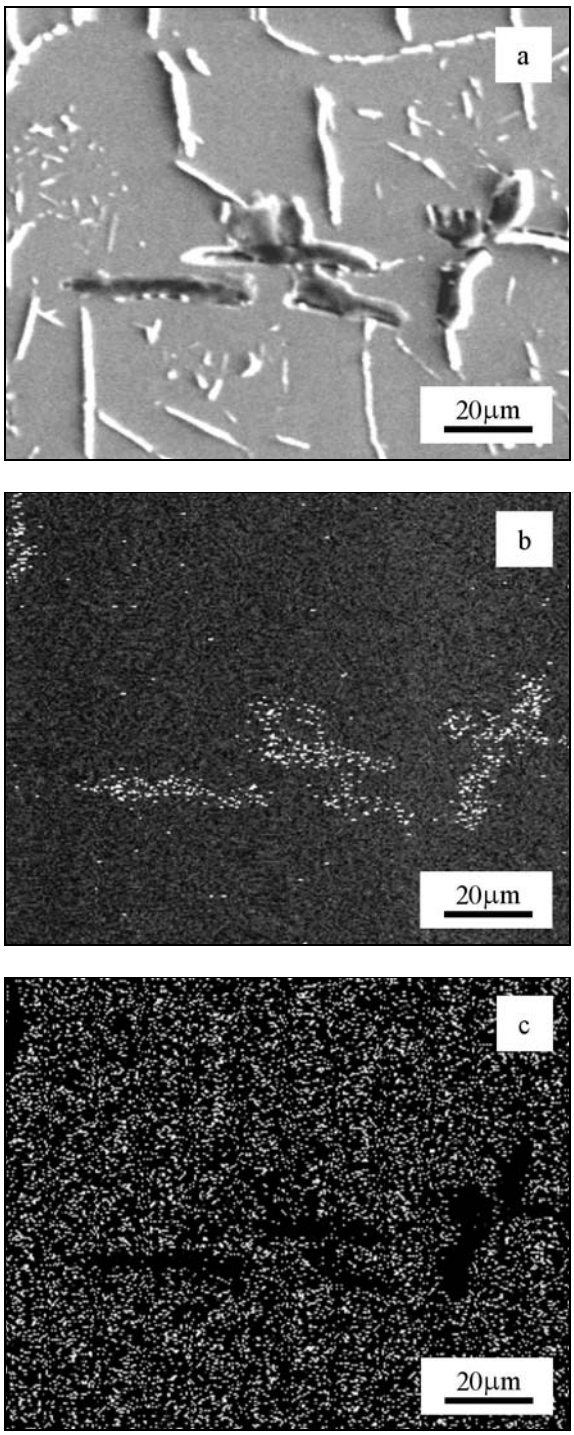

Fig. 6. (a) alloy F, original state, REM image, (b) alloy F, the same as in (a), image in $K_\alpha C$, (c) alloy F, the same as in (a), image in $K_\alpha Fe$.

20–50 μm) in the matrix (i.e. on the grey background), see Fig. 6a. The values of hardness are: matrix 357 HV 0.05, darker phase 140 HV 0.05, brighter phase 421 HV 0.01.

Using XRD the darker phase was identified to be graphite and brighter κ-phase. Also electron mi-

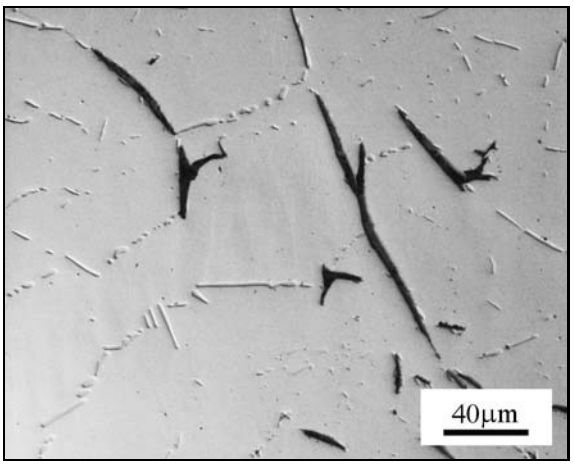

Fig. 7. Phases in alloy F are graphite (big dark phase) and κ-carbide (tiny bright phase), annealed 800 °C/8 h.

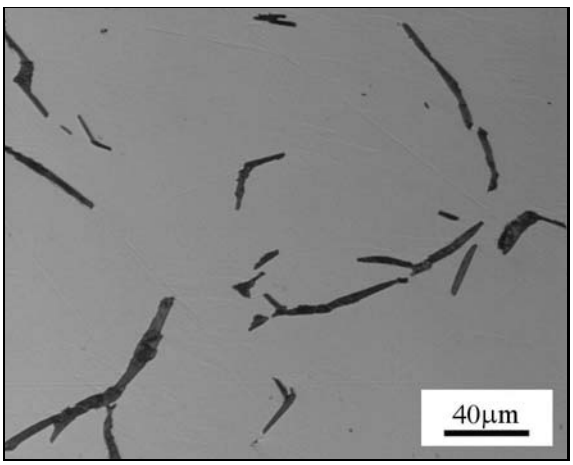

Fig. 8. Graphite in alloy F (annealed 1100 °C/8 h).

croanalysis was used to confirm graphite particles. Using $K_\alpha C$ line and $K_\alpha Fe$ (Figs. 6b,c), the increased content of C or zero content of Fe are obvious. It was not possible to identify carbon in bright particles (κ-phase) according to low sensitivity of the equipment. The phase composition at 600 °C/100 h and at 800 °C/8 h is characterized by the substantial contribution of κ-carbide existing together with graphite lamellae – Fig 7. The phases were identified by XRD. Microhardness values also support the presence of κ--carbides: matrix 413 HV 0.05, graphite 161 HV 0.05, κ-phase 503 HV 0.01.

On the other hand graphite (hardness 79 HV 0.01) is the only phase in matrix after annealing at 1100 °C/8 h. Lamellae up to 100 μm long (Fig. 8) are observed. The dissolution of κ-carbide increases the hardness of matrix to 478 HV 0.05.

XRD reveals weak but recognizable lines of κ--phase. The particles are probably very fine and cannot be identified by LOM.

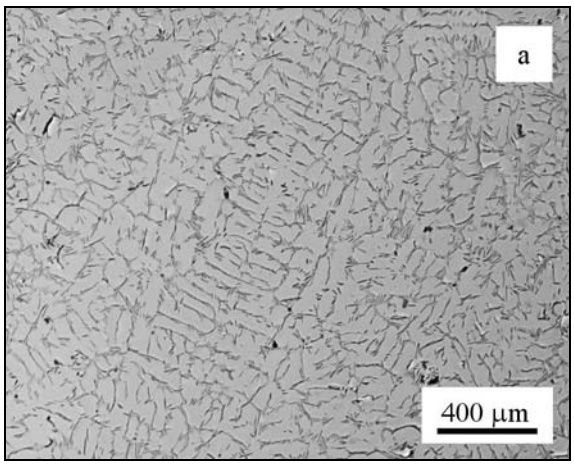

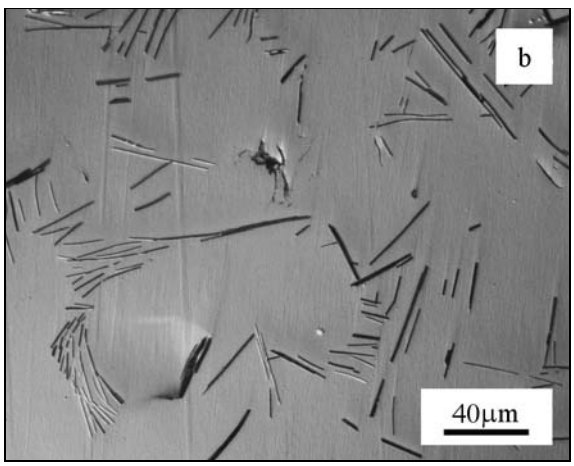

Fig. 9. (a) dendritic structure in alloy H, as cast, (b) dendritic structure in alloy H, detail.

3.4. Structure of alloy FA1.9C (H)

The composition of alloy FA1.9C is approaching to that of Pyroferal© (specially by the presence of Si). Dendrite structure is typical for the casting (hardness of the matrix 314 HV 0.1). Dendrites are formed by aluminium carbide Al_4C_3 (Fig. 9). The gradual dissolution of Al_4C_3 at 600 °C is obvious. Figure 10 describes the situation after 1000 hours.

During annealing at 1000 °C/8 h Al_4C_3 dissolves. Thus also the hardness of the matrix is enhanced: 495 HV 0.1. The phase composition was again verified by XRD.

3.5. Summary of experimental data

The knowledge about the presence of phases in the above studied alloys is summarized in Table 2. The summary obtains also the experimental methods used

Table 2. Table of observed phases and the art of identification

C (at.%)	Not annealed	Annealed at 600 °C/100 h	Annealed at 800 °C/8 h	Annealed at 1100 °C/8 h
0.1 (D)	C as soluted in B2 LOM, HV	C as soluted in B2 LOM, TEM, HV	C as soluted in B2	C as soluted in B2 LOM, HV
0.8 (E)	κ LOM, HV	κ LOM, TEM, HV	κ LOM	G LOM, XRD, HV
1.7 (F)	κ + G LOM, HV	κ + G LOM, XRD, TEM	κ + G LOM, HV	G + κ LOM, XRD, HV
1.9 (H)	Al_4C_3 + G LOM, XRD	Al_4C_3 + G LOM		Al_4C_3 + G LOM, XRD, HV

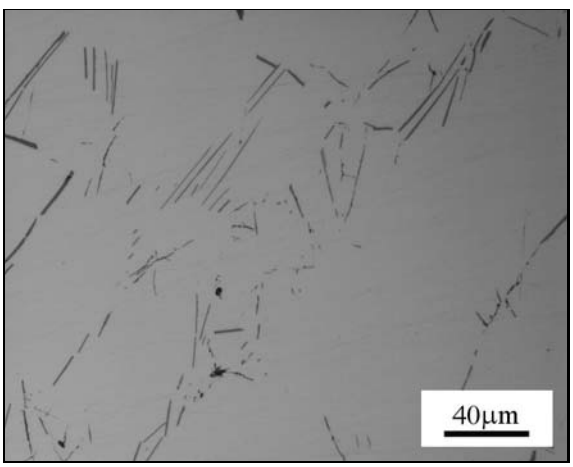

Fig. 10. Structure as in Fig. 9b after annealing at 600 °C.

in individual cases. The small deviations compared to quasibinary diagram in Fig. 1 are obvious in Fig. 11.

4. Discussion

There is discrepancy concerning the region of existence of κ-phase. Its complete dissolution [4] should take place approx. at 950 °C. In our experiment κ-phase is present both in the original state and after annealing at 1100 °C/8 h.

The fields of existence of κ-phase are uncertain even after intensive work in the past [5–9]. Mostly these studies have failed to determine the borders of the existence of κ-phase. The most reliable informations are due to Palm and Inden [7] at 800, 1000 and 1200 °C. They pointed out the difficulties in determining the exact position of κ-phase, which arise from the precipitation of graphite, that yields metastable phase equilibria in expected κ-single phase field.

The results obtained here can be situated also into

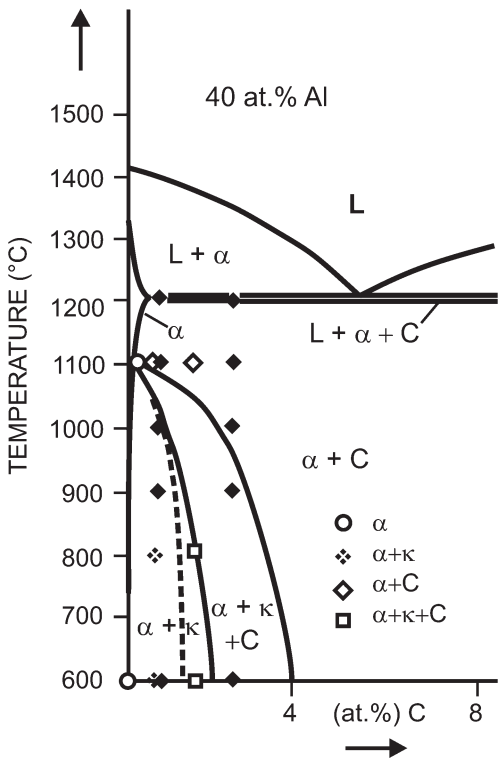

Fig. 11. Phase diagram Fe-40at.%Al-C as in Fig. 1 completed by data obtained in this paper.

isothermal cuts through Fe-Al-C data [6] at 800 °C and 1100 °C.

800 °C: Our data for alloys FA0.8C (E) and FA1.7C (F) do not fit into corresponding regions according to [6] – see Fig. 12. In both cases κ-phase was identified in a two-phase region α + C. This disagreement can be improved moving three phase $\alpha + \kappa$ + C boundary into the position marked by dashed line in Fig. 12.

1100 °C: The alloys E and F, i.e. FA0.8C and FA1.7C should be found in two-phase region α + C. This was the case only for alloy E. In the alloy F κ-

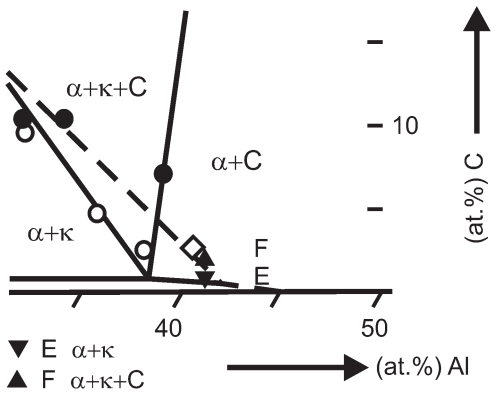

Fig. 12. Part of a ternary Fe-Al-C diagram at 800 °C according to [6]. The results with alloys E and F are included.

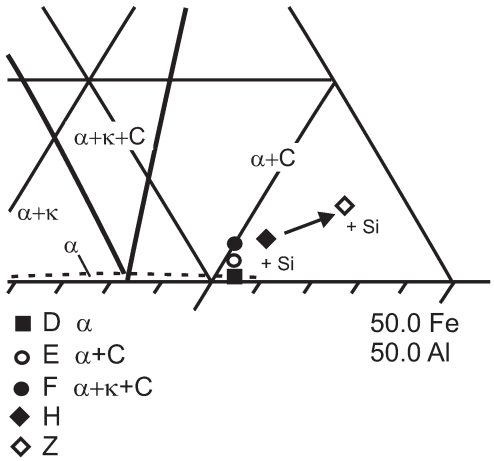

Fig. 13. Part of a ternary Fe-Al-C diagram at 1100 °C according to [6]. The results with alloys E, F and H are included together with the alloys to be studied in the future.

-phase was present in little extent. Figure 13 should illustrate this situation. Also future procedure is illustrated: from alloy H the two alloys will be approached having the composition nearly identical to Pyroferal (Z), the first one without Si, the other one the same one but with Si.

Very interesting is the appearing of aluminium carbide Al_4C_3 in alloy FA1.9C, which is probably caused by the presence of Si. The increase of the concentration of Al is a matter of further experiments. Al_4C_3 fully dissolves at temperatures higher than 1100 °C. Aluminium carbide is the phase observed in the binary system Al-C.

Very recently Ohtani et al. [10] calculated the ternary Fe-Al-C phase diagrams at 800, 1000 and 1200 °C introducing CALPHAD method combined with FLAPW (Full Potential Linearized Augmented Plane Wave) method. The results fit partly the investigation by Palm and Inden [7]. The very important point in the "story of κ-phase" is the chemical composition of κ-phase, which was reported [6] between $Fe_{3.2}Al_{0.8}C_{0.71}$ and $Fe_{2.8}Al_{1.2}C_{0.42}$.

5. Conclusions

The attempt was made to determine the phase composition of the Fe-Al-xC (at.%) alloys and to determine regions of existence for $Fe_3AlC_{0.5}$ (κ-carbide) and graphite phase as function of C content.

The methods used for such procedure were LOM, XRD, HV, and TEM combined with SAD.

As a result, small corrections both in the quasibinary Fe40Al-xC (at.%) diagram and in ternary Fe-Al-C phase diagrams are proposed.

Acknowledgements

The authors would like to dedicate this paper to Prof. RNDr. Zuzanka Trojanová, DrSc., on the occasion of her 65^{th} birthday.

The authors acknowledge the support both by the Ministry of Education of the Czech Republic, project No. MSM 46788501, and by the Grant Agency of the Czech Republic, project No. 106/06/0019.

References

[1] SIKKA, V. K.: In: Proceedings of a symposium sponsored by the ASM/MSD held at the Annual Meeting of the TMS in San Francisco 1994. Eds.: Schneibel, J. H., Crimp, M. A. Warrendale, TMS 2001, p. 3.
[2] VYKLICKÝ, M.—TŮMA, H.: Hutnické Listy, *14*, 1959, p. 118.
[3] VODIČKOVÁ, V.: Fyzikálně metalurgické postupy při úpravě mechanických vlastností slitin na bázi FeAl. [PhD. Thesis]. Liberec, Technical University in Liberec 2006.
[4] KUMAR, K. S.—PANG, L.: Mat. Sci. Eng., *A258*, 1998, p. 153.
[5] HERRMANN, J.—INDEN, G.—SAUTHOFF, G.: Steel Res. Int., *75*, 2004, p. 343.
[6] PALM, M.: Intermetallics, *13*, 2005, p. 1286.
[7] PALM, M.—INDEN, G.: Intermetallics, *3*, 1995, p. 443.
[8] SWAN, P. R.—DUFF, W. R.—FISHER, R. M.: Metal. Trans., *3*, 1972, p. 409.
[9] OKAMOTO, H.—BECK, P. A.: Metal. Trans., *2*, 1971, p. 569.
[10] OHTANI, H.—YAMANO, M.—HASEBE, M.: ISIJ Internat., *44*, 2004, p. 1738.

Intermetallics 17 (2009) 39–45

Contents lists available at ScienceDirect

Intermetallics

journal homepage: www.elsevier.com/locate/intermet

The effect of silicon on the structure of Fe-40 at.% Al type alloys with high contents of carbon (1.9–3.8 at.%)

P. Kratochvíl [a,*], F. Dobeš [b], V. Vodičková [c]

[a] Department of Physics of Materials, Charles University, CZ 121 16 Prague 2, Czech Republic
[b] Institute of Physics of Materials, Academy of Sciences of the Czech Republic, Brno, Czech Republic
[c] Department of Material Science, Technical University, Liberec, Czech Republic

ARTICLE INFO

Article history:
Received 4 August 2008
Received in revised form
16 September 2008
Accepted 19 September 2008
Available online 7 November 2008

Keywords:
A. Iron aluminides, based on FeAl
B. Phase identification
F. Microscopy, various

ABSTRACT

The phase compositions of alloys based on Fe-40 at.% Al with additions of carbon ranging from 1.9 to 3.8 at.% and with and without the addition of 1.2 at.% Si were studied by light optical and transmission electron microscopies, X-ray diffraction and electron probe microanalysis. The structure of the matrix of all alloys is a B2 lattice, inherent to the intermetallic compound FeAl. Two main precipitating phases are observed: graphite and aluminium carbide Al_4C_3. The quantity of the phases depends in detail on the chemical composition and the heat treatment. The presence of Al_4C_3 in the alloys with the highest carbon content is in agreement with the recent theoretical prediction of a Fe–Al–C ternary phase diagram by Ohtani et al., as well as with older experiments of Vyklický and Tůma. The occurrence of Al_4C_3 is supported by the addition of silicon. Small traces of carbide κ of perovskite-type Fe_3AlC are observed only in the alloys with the lowest aluminium and carbon contents.

1. Introduction

Successful application of Fe–Al-based intermetallics at elevated temperatures is critically dependent on improvement of their creep resistance [1,2]. Strengthening by second-phase particles represents a potential method in this direction [3,4]. One of the cheapest available alloying elements is carbon, with its low solubility in iron and a negligible solubility in aluminium. The strengthening may be achieved by the presence of either graphite or carbide particles (cementite Fe_3C, carbide κ of perovskite-type Fe_3AlC and Al_4C_3). The ternary phase diagram Fe–Al–C at target temperatures (i.e., from approx. 600 °C to 1000 °C) is known in detail only for concentrations up to 40 at.% Al (atomic percentage used throughout) [5,6]. On the other hand, alloys with aluminium concentrations above this limit may be useful in specific industrial applications. An example of such an alloy is the heat-resistant alloy Pyroferal, with about 45% aluminium and 3.4–4% carbon [7]. It may be important to know the phase diagram, especially the nature of second-phase particles in the respective concentration region. An exact knowledge of the precipitating phases may contribute to optimizing its mechanical properties. The aim of the present paper is to describe the structure of FeAl-based alloys with aluminium and carbon contents approaching that of Pyroferal. The results are used elsewhere to understand the mechanical properties at elevated temperatures [8].

2. Experimental technique

The list of alloys used to study the above-mentioned problem is shown in Table 1. Two types of alloys denoted H–J can be distinguished:

(a) the ternary Fe–40Al–*x*C type,
(b) the same type of alloy as (a) with the addition of Si.

The similarity of the concentration of alloys with that of Pyroferal is obvious. The points representing the studied alloys are indicated in all ternary Fe–Al–C phase diagrams presented below. The B2 structure is denoted as α-phase in the diagrams as well as in further text. Three isothermal sections were published by Palm and Inden [6]: at 800 °C, 1000 °C and 1200 °C (Fig. 1 gives details at 800 °C and 1200 °C). The sections at 800 °C and 1000 °C do not differ significantly in the relevant part of the diagram. Therefore, it can be expected that the 800 °C section may also be representative for a temperature of 600 °C, i.e., the lowest annealing temperature investigated in the present study. At 1200 °C, the occurrence of an $\alpha+\kappa$ phase field is restricted and the phase boundaries are shifted towards lower Al concentrations. All experimental alloys, including the above-mentioned industrial alloy Pyroferal are positioned within the $(\alpha+C)$ phase field according to available isothermal sections of diagram by Palm and Inden [6]. It should be mentioned that the maximum aluminium concentration in the experimental heats prepared by Palm and Inden was about 40 at.%. Consequently,

* Corresponding author. Tel.: +420 221 911 364; fax: +420 221 911 490.
E-mail address: pekrat@met.mff.cuni.cz (P. Kratochvíl).

0966-9795/$ – see front matter © 2008 Elsevier Ltd. All rights reserved.
doi:10.1016/j.intermet.2008.09.004

Table 1
Alloy compositions (at.%).

Alloy	Denoted	Al	C	Si
FA 1.9C Si	H	41.3	1.9	1.2
FA 2.2C	K	39.9	2.2	0.06
FA 2.9C	L	38.9	2.9	0.05
FA 3.8C	M	42.1	3.8	0.04
FA 3.6C Si	J	42.6	3.6	1.14

the right-hand sides of the diagrams in Fig. 1 should be studied with caution.

All alloys (with the exception of alloy H) were prepared by vacuum melting (1–10 Pa) in the induction furnace. The purities of iron and aluminium were 3 N and 4 N, respectively. The master alloy Fe–C containing 9.8 at.% C was used for the addition of carbon. Silicon was alloyed as a pure element. Alloy H was prepared as cylinders of 13 mm in diameter and of 70 mm in length and was available only as a cast. The samples of alloy H were taken from product prepared by one of the procedures applied for Pyroferal [7]. The raw used materials were cast iron and aluminium with substantitial content of Si. Carbon was added to adjust the composition in the induction furnace. The casting took place by using the tea-pot investment casting in air.

The cast slabs (cross-section 20×32–35 mm) were rolled at 1200 °C to 8×35–40 mm using several passes of 8–12% reductions. Such samples are taken as in an initial state. The chemical compositions of all alloys were determined using spectral analysis (optical emission spectrometer LECO GDS 750a).

The phase structure was studied using

(a) etching by emulsion OP–S (Struers) for light optical microscopy (LOM) and application of Nomarski contrast,
(b) X-ray diffraction (XRD) with XRD7–FPM (Seifert in Bragg–Brentano geometry) with Cu Kα radiation.
(c) Vickers microhardness (HV) measured by MICROMET 2100 (Buehler) with image analyser. Different loads on the hardness tester were used according to the size of the particles of the phase in question. This does not influence the value of HV.

The phase identification was also supported by analysis of LOM images (software LUCIA was used for determination of volume fractions of phases), by electron probe microanalysis (EPMA) with energy dispersive X-ray spectroscopy and by transmission electron microscopy (TEM) at 200 kV with selected area diffraction (SAD).

The heat treatment took place in air and it was followed by quenching into the oil. The cooling rate was not measured. The size of samples was $\sim 7 \times 7 \times 12$ mm and the cooling rate could be assessed as greater than 10 K/s.

Table 2
Observed secondary phases and identification techniques.

Alloy	Not annealed	Annealed at 600 °C/100 h	Annealed at 1100 °C/8 h
H	Al_4C_3 + (G) LOM, XRD	Al_4C_3 + (G) LOM	(G) + (Al_4C_3) LOM, XRD
K	G LOM, XRD, EPMA	G + (κ) LOM, TEM, EPMA	G LOM
L	***G*** LOM, XRD, EPMA	G + (κ) LOM, TEM, EPMA	***G*** LOM
J	Al_4C_3 + (G) LOM, XRD, EPMA		Al_4C_3 + (G) LOM, XRD
M	Al_4C_3 + (G) LOM, EPMA		G + (Al_4C_3) LOM, EPMA, XRD

(): For minor phase; G: for graphite.

3. Results

The phases observed in the α matrix and the respective experimental methods used for their identification are summarized in Table 2.

3.1. Alloys without Si

3.1.1. Structure of alloys FA 2.2C (K) and FA 2.9C (L)

The structures of both alloys FA2.2C and FA2.9C are characterized by the presence of a large volume fraction of graphite (elongated particles up to 50 μm long), see Fig. 2a and b. The corresponding XRD with identification of the lines is given in Fig. 3. The volume fraction of graphite is greater in the alloy FA2.9C than in the alloy FA2.2C.

A small volume fraction of κ-carbide (perovskite Fe_3AlC), which was visible only using TEM (no peaks of κ-carbide in XRD) was identified by means of SAD. The κ precipitates are oval shaped, approximately 200 nm in diameter (see Fig. 4). Particles of both phases (i.e., graphite and κ-carbide) are situated inside the grains. The phase composition does not change in either of the two alloys after annealing (see Fig. 5a and b). On the other hand, the microhardness of the matrix of the alloy K increases from 335 HV0.01 (initial state) to 484 HV0.01 (after 1100 °C/8 h annealing), and from 367 HV0.01 (initial state) to 484 HV0.01 (after 1100 °C/8 h annealing) for the alloy L. This can be ascribed to the dissolution of carbon into the lattice that is fixed by rapid cooling.

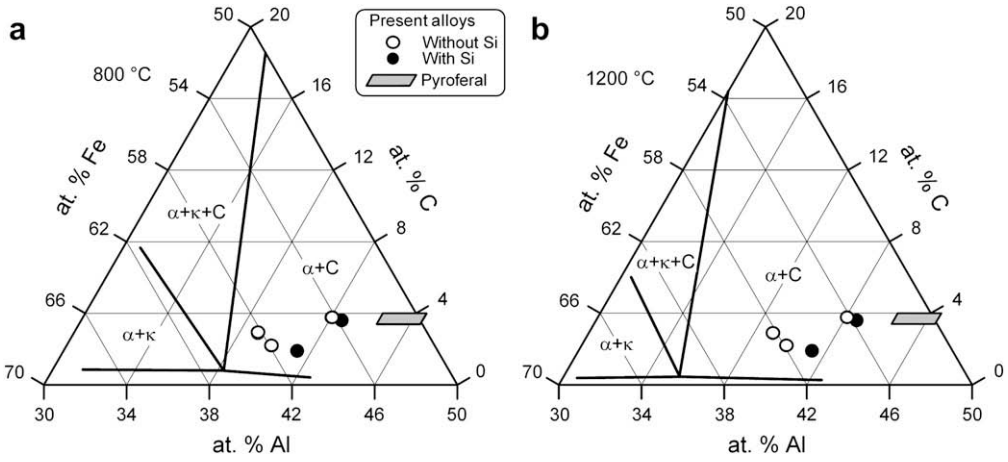

Fig. 1. The part of the ternary Fe–Al–C phase diagram corresponding to the alloys studied in the present paper according to [6] (a) for 800 °C, (b) for 1200 °C.

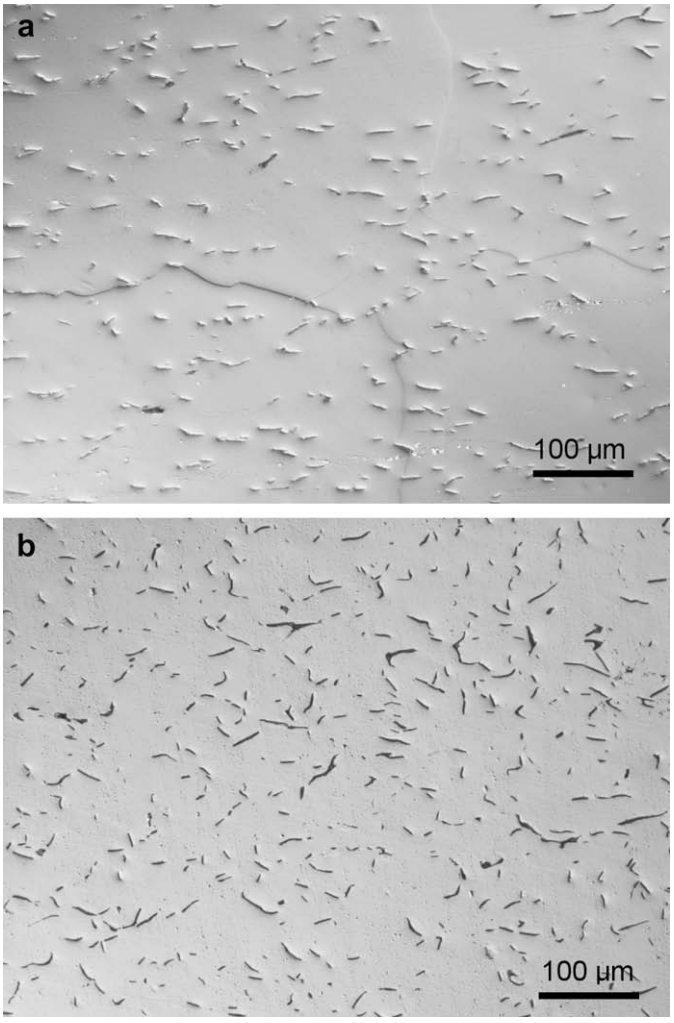

Fig. 2. Microtructure of as-received alloys (a) K, (b) L. using LOM.

3.1.2. Structure of alloy FA 3.8C (M)

The as-cast alloy FA3.8C (without Si) exhibited a hypoeutectic solidification structure consisting of FeAl dendrites outlined by aluminium carbide Al_4C_3 in interdendritic spaces. The presence of Al_4C_3 was proven by XRD. Occasionally, small particles are observed that could be identified as graphite in this alloy (Fig. 6a).

The dendritic structure dissolves during annealing at 1100 °C/8 h (Fig. 6b). The majority of second-phase particles are graphite flakes. Nevertheless, a small amount of Al_4C_3 was identified by XRD even

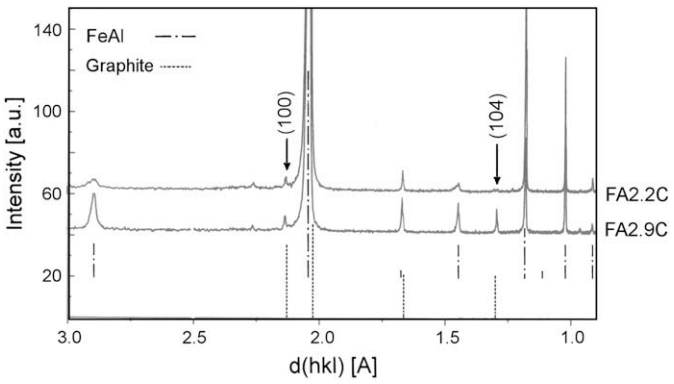

Fig. 3. X-ray diffraction curves for as-received alloys K and L.

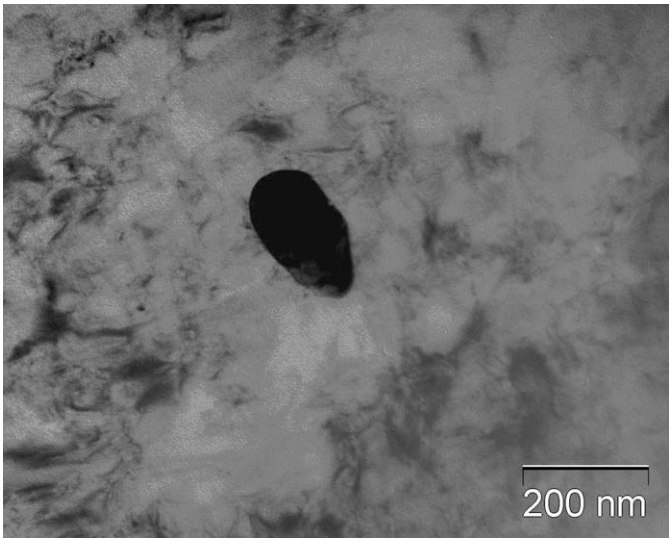

Fig. 4. TEM image of the particle of κ-carbide (Fe_3AlC) in alloy K.

after this annealing. The microhardness value of the matrix increased from 351 HV0.05 for the as-received state to 506 HV0.05 for the annealed state at 1100 °C. This is due to the dissolution of carbon in the matrix.

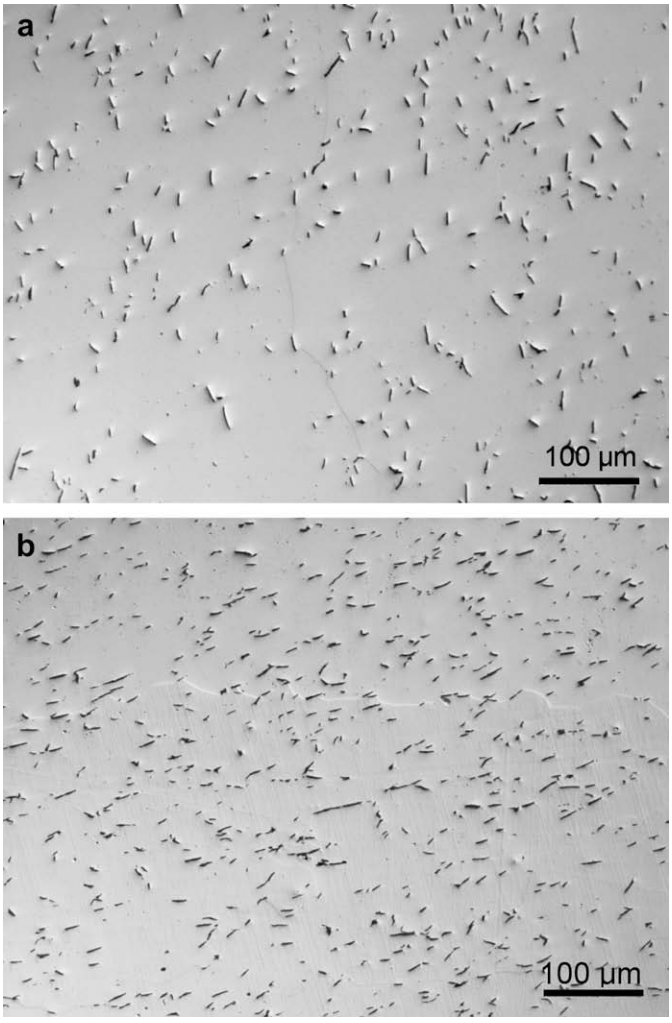

Fig. 5. Microstructure of annealed alloys (a) K, 8 h at 1100 °C, (b) L, 100 h at 600 °C using LOM.

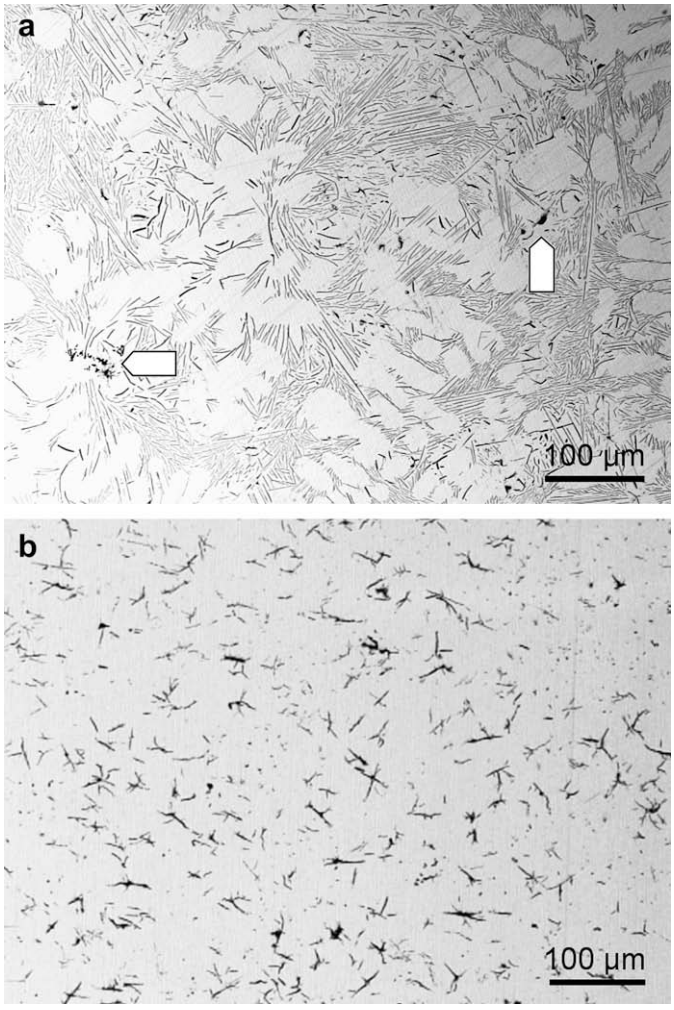

Fig. 6. Microstructure of alloy M (a) as-received, (b) annealed 8 h at 1100 °C using LOM (some of the graphite particles are marked by arrows).

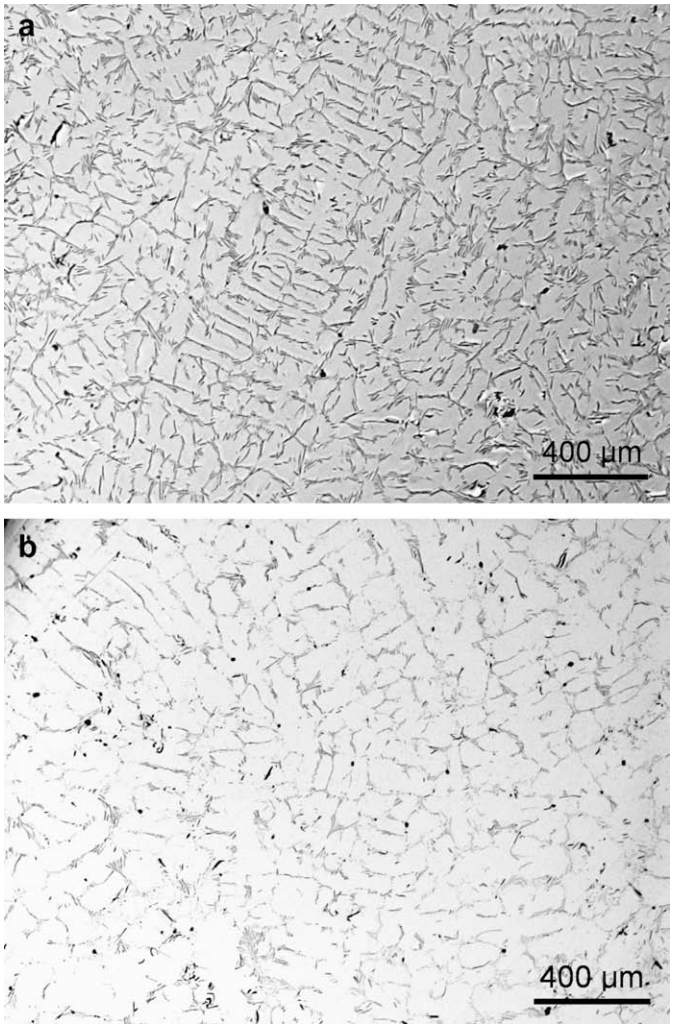

Fig. 7. Microstructure of alloy H (a) as-cast, (b) annealed 100 h at 600 °C using LOM.

3.2. Alloys with Si

3.2.1. Structure of alloy FA 1.9C Si (H)

The composition of the alloy FA1.9CSi approaches that of Pyroferal (especially by the presence of Si and as far as its production technology is considered). The appearance of the microstructure closely resembles type E flake structures typically found in grey iron when undercooling of melt is large. Dendrites are similarly to those in the alloy M formed by α and outlined by the aluminium carbide Al_4C_3 phase (Fig. 7a). The phase composition was controlled by XRD. The diffraction lines of Al_4C_3 are visible as well as their disappearance after annealing at 1100 °C/8 h (see Fig. 8). The gradual dissolution of Al_4C_3 was also observed after annealing for 100 h at 600 °C, which is obvious from Fig. 7b. The existence of a small amount of graphite was proved both prior to and after annealing, but no traces of κ-carbide were found.

The hardness of the matrix in the as-cast state is equal to 314 HV0.1. Annealing of the alloy enhances this hardness to a value of 495 HV0.1 due to the dissolution of Al_4C_3 and the increase in the amount of carbon solved in the FeAl matrix.

3.2.2. Structure of alloy FA 3.6CSi (J)

White dendritic areas of first solidified FeAl are typical for the alloy in the as-cast state. Interdendritic spaces are filled by Al_4C_3 needles. A small volume fraction of graphite particles can also be observed. Stability of the needle-like structure of Al_4C_3 is very good: lamellae of carbide are only partly dissolved, but the apparent character of the microstructure is retained even after annealing at 1100 °C for 8 h, see Fig. 9a and b and in detail Fig. 10a and b, respectively. The hardness of the as-received matrix is 423 HV0.05 which increased to 580 HV0.05 after annealing at 1100 °C/8 h due to partial dissolution of Al_4C_3.

4. Discussion

The discussion is related to the part of the ternary diagram where the investigated alloys are situated. The available experimental

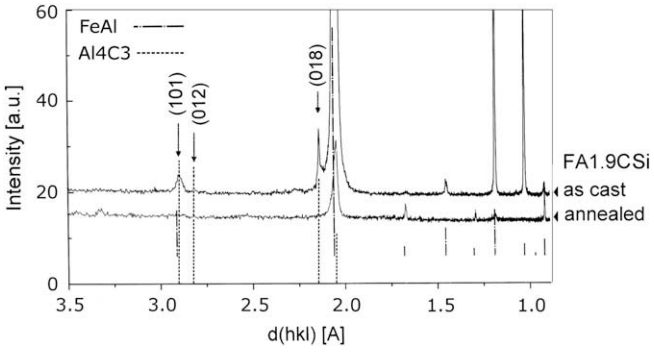

Fig. 8. X-ray diffraction curve for alloy H.

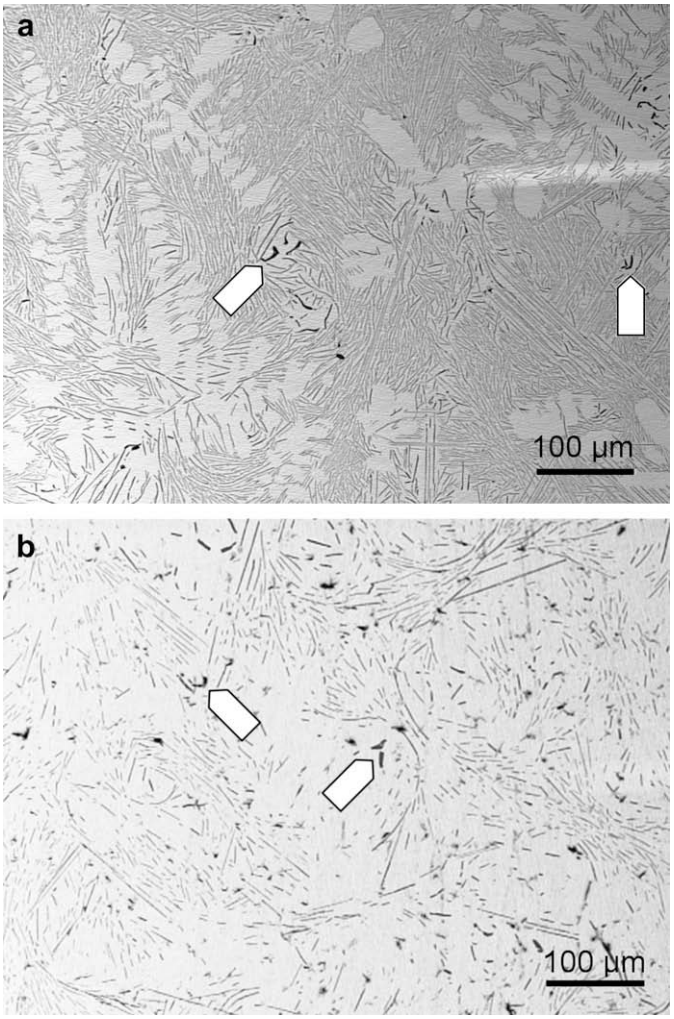

Fig. 9. Microstructure of alloy J (a) as-received, (b) annealed 8 h at 1100 °C using LOM (some of the graphite particles are marked by arrows).

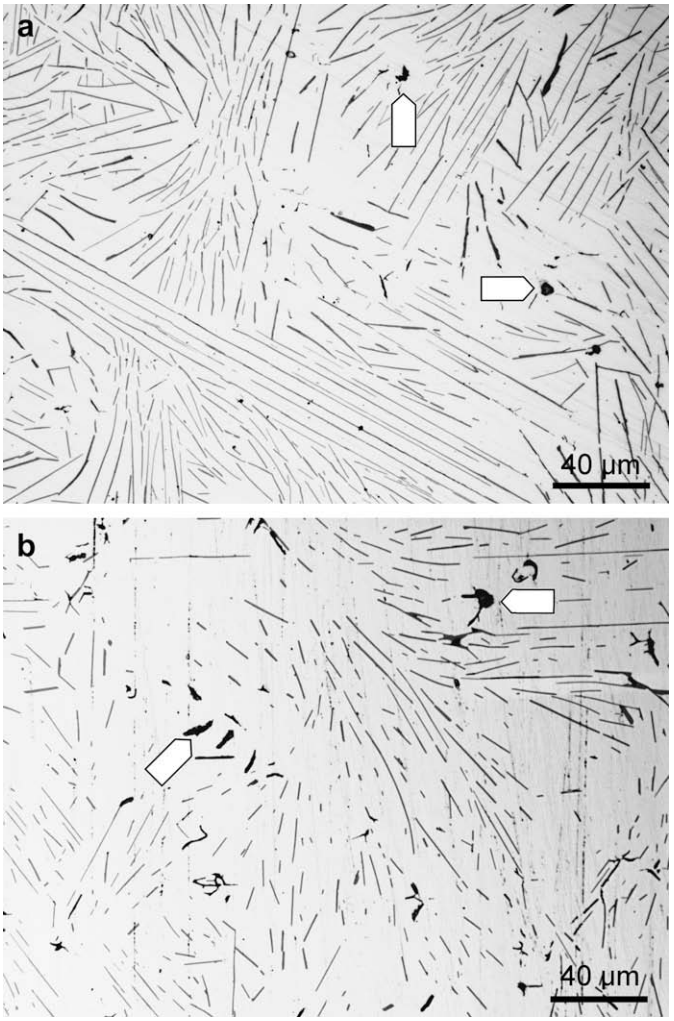

Fig. 10. Detail of Al_4C_3 lamellae in alloy J as in Fig. 9: (a) as-received, (b) annealed 8 h at 1100 °C using LOM (some of the graphite particles are marked by arrows).

ternary diagrams [5,6] do not describe the respective range of concentrations in detail. A quantitative view can be obtained from the theoretical paper by Ohtani et al. [9]. They calculated the diagram by incorporating *ab initio* energetic calculations into the CALPHAD approach and presented isothermal sections for 800 °C, 1000 °C and 1200 °C. Similarly to Ref. [6], diagrams for 800 °C and 1000 °C do not differ much and it may be again expected that the diagram for 600 °C is also similar. The sections for temperatures 800 °C and 1200 °C are illustrated in Fig. 11.

Various Fe–Al–C alloys were studied by Vyklický and Tůma [10,11] within the development of the alloy Pyroferal. The research was focused on concentrations from 15 to 30 wt.% of Al (from about 27 to 47 at.%) and from 0 to 3 wt.% of C (from 0 to about 9.75 at.%). The isopleths at 25 and 30 wt.% Al (about 41 and 47 at.%) can be found in Ref. [7].

4.1. The presence of κ-carbide

Both alloys K and L contain residua (small volume fractions) of κ-carbide that probably appeared during the thermal treatment of the alloys and did not dissolve. Though the presence of κ-carbide is in agreement with Nishida [5], it should not occur according to diagrams of Palm and Inden [6] and Vyklický and Tůma [10,11]. The differences in observation of κ-carbide may be ascribed to differences in annealing of experimental alloys: the longest time of annealing in the present experiments was 100 h at 600 °C, while Palm and Inden applied annealing for 240 h at 800 °C and Vyklický and Tůma up to 400 h at 1000 °C.

4.2. The presence of graphite in alloys K and L

Both of the alloys contain graphite, in agreement with the corresponding area of the diagram determined by Palm and Inden [6], and their relative position is the same in both diagrams (800 °C and 1200 °C sections). The same area (α + C) by Ohtani et al. [9] does not include alloys K and L in the isothermal section at temperature of 800 °C (Fig. 11a). On the other hand, the alloys are well located within the (α + C) phase field of 1200 °C section (Fig. 11b).

The difference between Ohtani et al. [9] and other references is the solubility of carbon in α in dependence of temperature. While Ohtani et al. [9] assume that in this specific composition range the carbon content increases markedly with decreasing temperature most other references assume that the carbon content decreases with decreasing temperature. This is the reason why the compositions of the alloys lie within different phase fields according to the different references.

4.3. The presence of carbide Al_4C_3

The carbide Al_4C_3 is given explicitly in one of the oldest versions of the Fe–Al–C ternary diagram by Vogel and Mäder [12]. It is not mentioned in the latter improvements of this diagram by Löberg

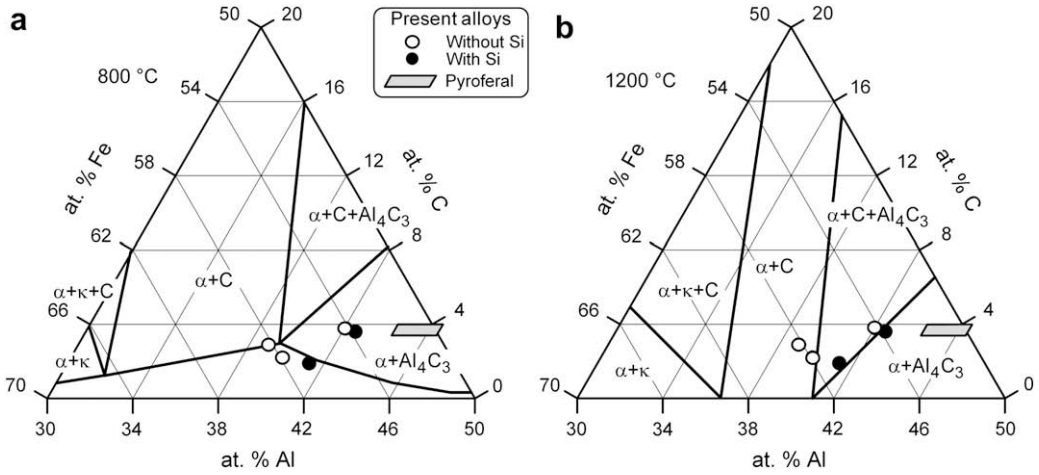

Fig. 11. The part of the ternary Fe–Al–C phase diagram corresponding to the alloys studied in the present paper according to [9], (a) for 800 °C, (b) for 1200 °C.

and Schmidt [13], Nishida [5] and Palm and Inden [6], since their experiments are limited to the iron-rich corner only. Vogel and Mäder indicated the existence of Al_4C_3 at concentrations of Al and C as low as 44.22% and 1.06%, respectively. The isothermal sections corresponding to those in Fig. 1 can hardly be constructed from their data. Such sections calculated by Ohtani et al. [9] clearly define the concentration and temperature conditions of the occurrence of Al_4C_3 (Fig. 11). Observations of Al_4C_3 in the alloys M and J are in agreement with the prediction at both temperatures. On the other hand, the occurrence of Al_4C_3 in the alloy H is not confirmed by the calculated diagrams at temperatures below 1000 °C.

The same conclusions concerning the observation of Al_4C_3 in the present experiments can also be confirmed by comparison with the results of Vyklický and Tůma [10,11] (Fig. 12). The occurrence of aluminium carbide is predicted in the alloys M and J, in agreement with the calculated diagram by Ohtani et al. [9], as well as its absence in the alloy H. The phase boundary $(\alpha + C)/(\alpha + C + Al_4C_3)$ shifts slightly towards greater aluminium concentrations with decreasing temperature. The alloys M and J (and of course the alloy H) preserve their positions relative to phase boundary at 800 °C. It has to be mentioned that the alloys H and J have additions of silicon and their plotting onto the ternary Fe–Al–C isothermal sections should be taken as the approximation only.

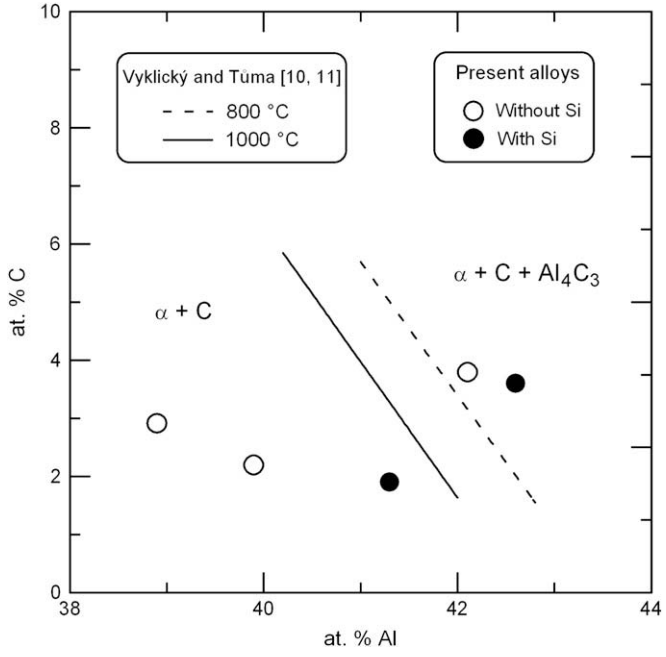

Fig. 12. The boundary of the first appearance of Al_4C_3 at 800 and 1000 °C according to [10,11].

4.4. The influence of silicon

It is worth to notice, that the stability of Al_4C_3 during annealing is greater in the alloys with silicon additions (see data on alloys H and J). It seems, therefore, that the addition of silicon supports the formation of Al_4C_3. The defect corrosion resistance of Fe–Al-based alloys in aqueous environments is connected with the presence of Al_4C_3. This is due to the great volume change accompanying the reaction of aluminium carbide with water [14,15]. The formation of undesirable Al_4C_3 may be prevented by additions of proper elements. It was shown that titanium additions greater than about 4.5 wt.% can totally remove Al_4C_3 [16]. In this respect, an investigation of the influence of silicon on Al_4C_3 formation may be important. The quaternary Fe–Al–C–Si diagram is known only partially in the Fe-rich corner [17]. It follows from Figs. 11 and 12 that, in the alloy H (with the addition of silicon), the aluminium carbide is observed at concentrations outside the predicted phase field of its occurrence in the pure ternary Fe–Al–C diagram.

The effect of silicon may be realized through the following mechanism: The solubility of Si in FeAl is high (contrary to low solubility in other Fe–Al intermetallics) [18] and the Si atoms replace Al atoms in this compound. It can be supposed that the effects of Al and Si add together. In the presence of Si, the phase boundary $(\alpha + C)/(\alpha + C + Al_4C_3)$, etc. is then shifted towards lower Al content. The observed effect of silicon is in agreement with the observation that low silicon content promotes Al_4C_3 formation in Al/SiC composites [19].

5. Conclusions

1. Two main precipitating phases are observed within the FeAl (B2) matrix: graphite and aluminium carbide Al_4C_3. The quantity of phases depends in detail on the chemical composition and the heat treatment.
2. The presence of Al_4C_3 in the alloys with the highest carbon contents is in agreement with the recent theoretical prediction of the Fe–Al–C ternary phase diagram by Ohtani et al. [9] as well as with older experiments of Vyklický and Tůma [10,11].

3. The occurrence of Al_4C_3 is supported by the addition of silicon.
4. Small traces of κ-carbide (perovskite Fe_3AlC) are observed only in the alloys with the lowest aluminium and carbon contents.

Acknowledgements

This research was supported by the Grant Agency of the Czech Republic through the projects 106/06/0019 and 106/08/1238, as well as by the Research Intents of the Ministry of Education of the Czech Republic under numbers MSM 0021620834 and MSM 4674788501.

References

[1] Deevi SC, Sikka VK. Intermetallics 1996;4:357.
[2] Stoloff NS. Mater Sci Eng A 1998;258:1.
[3] Palm M. Intermetallics 2005;13:1286.
[4] Morris DG, Munoz-Morris MA. Mater Sci Eng A 2007;462:45.
[5] Nishida K. Technical reports of the Hokaido university, vol. 48; 1968. p. 79.
[6] Palm M, Inden G. Intermetallics 1995;3:443.
[7] Kratochvíl P. Intermetallics 2008;16:587.
[8] Dobeš F, Kratochvíl P, Vodičková V, Milička K, Pesička J. Kovove Mater 2008;46:1.
[9] Ohtani H, Yamano M, Hasebe M. ISIJ Int 2004;44:1738.
[10] Vyklický M, Tůma H. Hutnické Listy 1959;14:118 (in Czech).
[11] Vyklický M. Report of VÚMT Praha, No. Z-57-548, Praha; 1957, in Czech.
[12] Vogel R, Mäder H. Arch Eisenhüttenw 1936;9:333.
[13] Löberg K, Schmidt W. Arch Eisenhüttenw 1938;11:607.
[14] Binczyk F. The factors which determine the structure of the Fe–Al–C alloys with high content of aluminium and the analysis of the phenomena leading to their self-disintegration, Ph.D. thesis, Silesian Technical University, Katowice; 1992.
[15] Binczyk F, Skrzypek SJ. Powder Technol 2001;120:159.
[16] Fras E, Kopycinski D, Lopez HF. Int J Cast Met Res 2002;15:9.
[17] Ueberschaer A. Die stabilen Phasengleichgewichte in eisenreichen, nahezu kohlenstoffgesättigten Fe–C–Si–Al Legierungen, Ph.D. thesis, TU Berlin; 1968.
[18] Maitra T, Gupta SP. Mater Charact 2003;49:293.
[19] Sasaki M, Kaminaga M, Tagami M. J Jpn Foundry Eng Soc 1999;71:455.

The effect of carbon on high temperature deformation of Fe-40Al-xC (at.%) ternary alloys

F. Dobeš[1*], P. Kratochvíl[2], V. Vodičková[3], K. Milička[1], J. Pešička[2]

[1] *Institute of Physics of Materials, Academy of Sciences of the Czech Republic, Žižkova 22, 616 62 Brno, Czech Republic*
[2] *Department of Metal Physics, Faculty of Mathematics and Physics, Charles University, Ke Karlovu 5, 121 16 Prague 2, Czech Republic*
[3] *Department of Material Science, Faculty of Mechanical Engineering, Technical University of Liberec, Hálkova 6, 461 17 Liberec 1, Czech Republic*

Received 20 September 2007, received in revised form 14 January 2008, accepted 14 January 2008

Abstract

Mechanical properties of Fe-40Al alloys with C contents of 0.07–1.9 at.% were studied by uniaxial compressive creep and constant strain rate tests at temperatures from 600 °C to 750 °C. The dependence of both the creep resistance and the constant strain rate characteristics on the carbon content is not monotonous; the worst mechanical properties are observed in the alloys with 0.75 and 1.7 at.% C. The final heat treatment consisting in annealing at 1100 °C for 8 hours with quenching to oil has only a small influence on the creep rate. The stress and temperature dependence of the creep rate was determined by stepwise loading and evaluated in terms of the stress exponent n and the activation energy Q, respectively. These quantities can be interpreted by means of dislocation motion controlled by climb and by the presence of second phase particles. Deformation in the alloys with 0.75 and 1.7 at.% C occurs by the dislocation motion as in the single-phase FeAl matrix, eventually modified by the presence of dissolved carbon atoms (solid solution hardening). The dislocation motion is obstructed by tiny precipitates, probably of carbide κ, in the alloy with 0.07 at.% C and by particles of Al_4C_3 in the alloy with 1.9 at.%. Precipitates of carbide κ do not improve creep resistance efficiently at moderate carbon additions.

K e y w o r d s: iron aluminides, creep, high temperature deformation

1. Introduction

The Fe-Al based alloys with 40 to 45 at.% of aluminium were studied extensively in the early fifties of the last century in the former Czechoslovakia [1, 2]. The research resulted in the development of the alloy with commercial name Pyroferal. The alloy was frequently used to replace deficient heat-resistant nickel-chromium steels in many industrial applications (blades in roasting furnaces, cementation pots, annealing boxes, fire-grate bars etc. [3]). Its composition is given in Table 1. Note that the composition reminds that of the recently studied FeAl-based alloys with different additions of carbon [4-6]. The main task of present experiments is to approach step by step the composition of the "old intermetallic". Using this procedure, the effect of individual additives should be understood. The effect of carbon content in the ternary Fe-40Al-xC is the first we decided to investigate. The results of the phase analyses and of microstructure observations were published in the preceding paper [7]. In the present paper, the results of high temperature mechanical tests (constant strain-rate test and creep test) are summarized.

T a b l e 1. The composition of Pyroferal

	Al	C	Si	Mn
wt.%	29.0–31.0	1.0–1.2	max. 0.5	max. 0.7
at.%	44.4–46.5	3.4–4.0	max. 0.7	max. 0.5

*Corresponding author: tel.: +420 532 290 408; e-mail address: dobes@ipm.cz

Table 2. Composition of the alloys used (at.%/wt.%)

Alloy	Denoted	Al	C	Si
Fe-40Al-0.1C	D	41.05/25.2	0.07/0.02	
Fe-40Al-0.8C	E	40.5/24.9	0.75/0.19	
Fe-40Al-1.7C	F	40.05/24.8	1.7/0.44	
Fe-40Al-1.9C	H	41.3/26.08	1.9/0.52	1.2/0.8

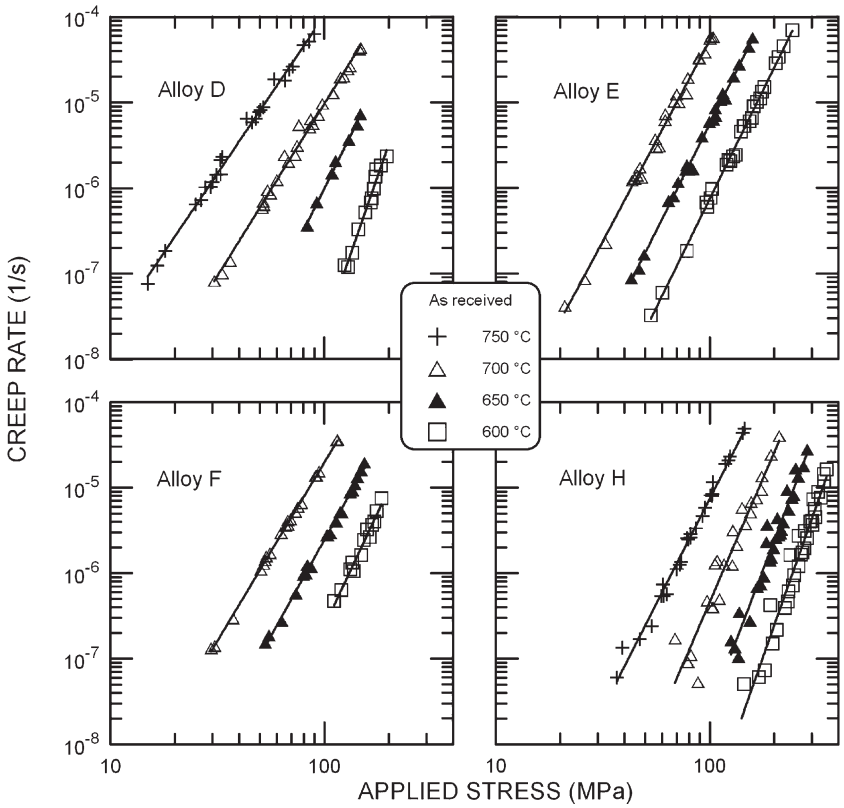

Fig. 1. Dependence of creep rate on applied stress in alloys D to H at different temperatures.

2. Experimental procedure

The alloys D to F were melted and cast as slabs 30 × 50 × 100 mm in a vacuum furnace at the Institute of Modelling and Control of Forming Processes, Technical University, Ostrava, Czech Republic. The slabs were hot rolled at 1200 ℃ in several steps (20 % deformation in each step) to obtain sheets 8 mm thick. Alloy H was cast in the foundry Kdynium, Strakonice, Czech Republic. It is available as casting only (the rolling is impossible) and in an annealed form (see below). The composition of tested materials is in Table 2.

Specimens for mechanical tests were spark machined cylinders (diameter 5 mm for constant strain rate tests, diameter 6 mm for creep tests, height 12 mm). Constant strain rate tests were performed in uniaxial compression at temperature 600 ℃ and (engineering) strain rate 6×10^{-5} s^{-1}. Two types of uniaxial compressive creep tests were performed: (i) at constant stress on a special cantilever machine with load compensation by Hofman's principle [8] and (ii) at constant load at simple cantilever machine. The former type was performed at 600 ℃ and 120 MPa. The step-wise loading was used in the latter type of tests: in each step, the load was changed to a new value after stationary creep rate had been established. The terminal values of the true stress and the true strain rate were evaluated for the respective step. This type of testing was primarily intended to estimate the stress sensitivity of the creep rate and its temperature dependence. All tests were performed in protective argon atmosphere. The temperature was kept constant within 1 K. The specimens were tested in two different states: (a) as received after casting and rolling (alloys D, E and F) or after casting (alloy H), respectively, and (b) after annealing at 1100 ℃ for 8 hours with quenching to oil.

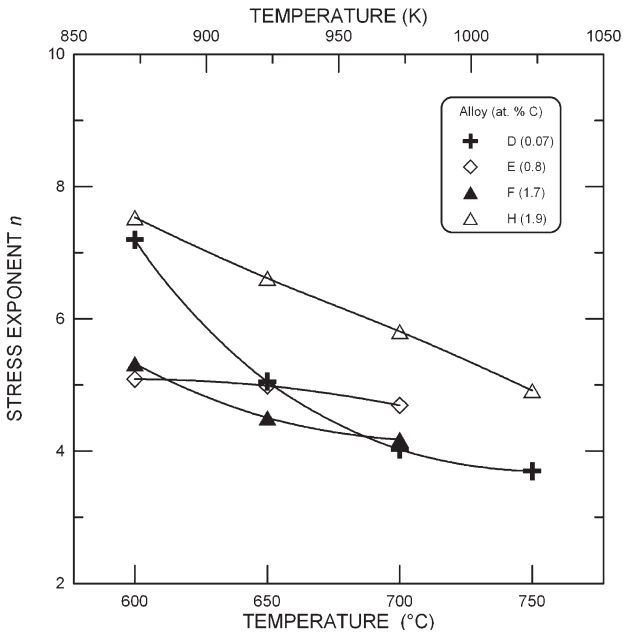

Fig. 2. Temperature dependence of stress exponent n in as-received state.

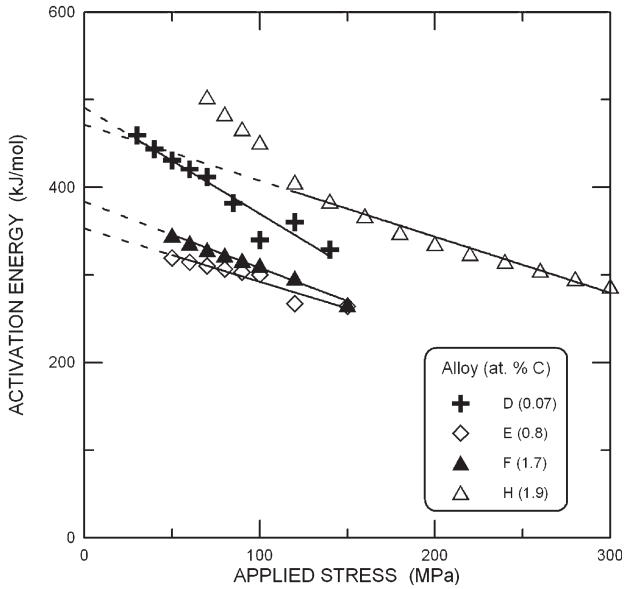

Fig. 3. Applied stress dependence of activation energy of creep rate in as-received state.

3. Results

The applied stress dependences of the creep rate in the as-received materials are given in Fig. 1. The dependence can be described at a given temperature by the power function

$$\dot{\varepsilon} = A\sigma^n, \tag{1}$$

where $\dot{\varepsilon}$ is the creep rate, σ is the applied stress and A is a temperature dependent constant. The power n is decreasing with increasing temperature in all studied alloys. Its values are given in Fig. 2.

Values of logarithm of creep rate found by fitting by means of Eq. (1) were plotted as function of reciprocal temperature. The apparent activation energy of creep

$$Q = -R\left(\frac{\partial \ln \dot{\varepsilon}}{\partial \frac{1}{T}}\right)_{\sigma} \tag{2}$$

was then calculated by linear regression (R is the universal gas constant and T is the absolute temperature). The results are given in Fig. 3. The activation energy is decreasing with the increasing applied stress. This observation is connected with the above-shown decrease of the stress exponent with the increasing temperature. The activation energy extrapolated linearly to zero applied stress can be separated to two different groups: (i) it is equal to 350 kJ mol^{-1} and 383 kJ mol^{-1} in the alloys E and F, respectively, and

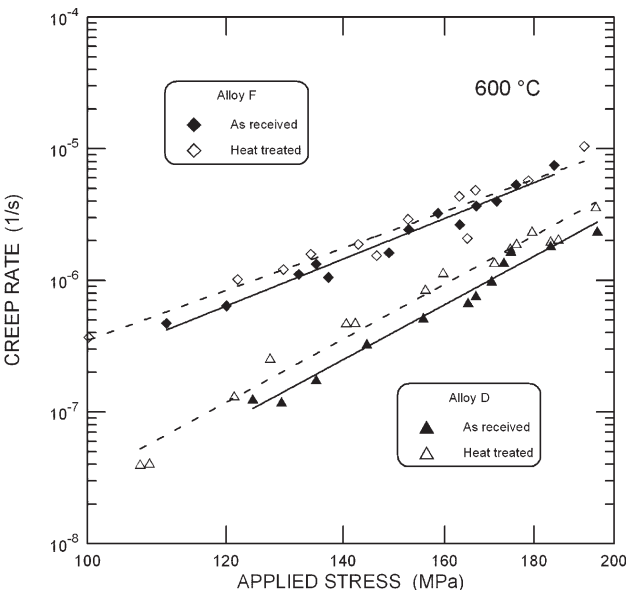

Fig. 4. Applied stress dependence of creep rate in alloys D and F in as-received and heat-treated states.

(ii) it is equal to about 490 kJ mol^{-1} and 470 kJ mol^{-1} in the alloys D and H, respectively. (The data for the applied stress greater than 120 MPa were taken into account for this linear extrapolation in the alloy H. The values of the activation energy about 700 kJ mol^{-1} can be obtained by the extrapolation of low stress data in this alloy.)

The effect of heat treatment on creep properties is illustrated in Fig. 4. The applied heat treatment has only a small influence on the minimum creep rate.

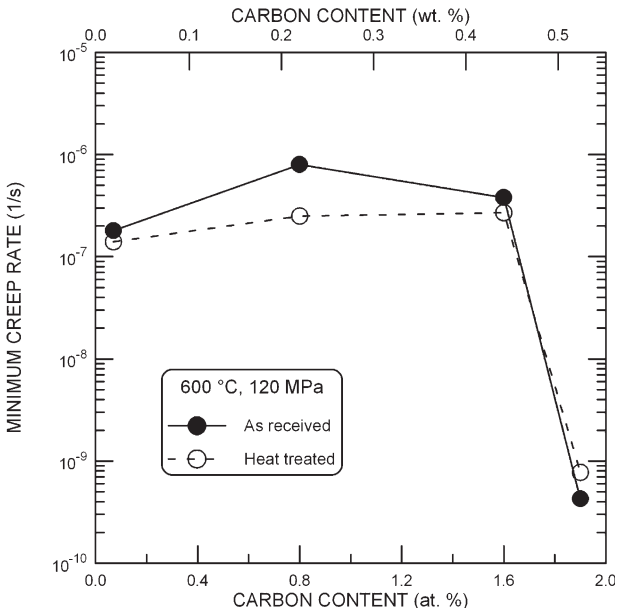

Fig. 5. Dependence of minimum creep rate in constant--stress tests on carbon content.

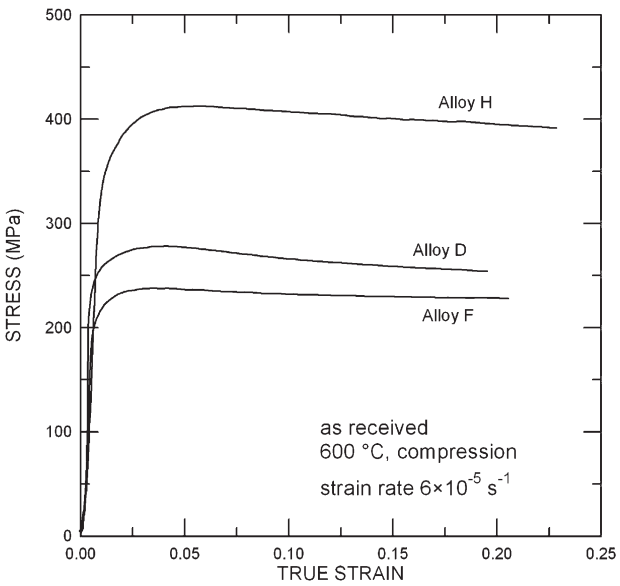

Fig. 6. Examples of constant strain rate tests.

The dependence of the minimum creep rate obtained in constant-stress tests on the carbon contents is given in Fig. 5. The dependence is not monotonous, note a lower creep resistance with the increasing carbon content in the alloys E and F.

The examples of stress vs. strain dependence obtained in constant strain rate test are given in Fig. 6. Two important quantities can be determined from the constant-rate tests: (i) the yield stress and (ii) the maximum value of stress. The yield stress was evaluated as stress causing a permanent strain of 0.002. The maximum value of the stress is equivalent to the ultimate tensile strength (UTS) measured usually in the tensile variant of the test. It will be designated as ultimate strength in what follows. The dependences of both the yield stress and the ultimate strength on the carbon content are given in Fig. 7. They follow the same pattern as the creep resistance depicted in Fig. 5.

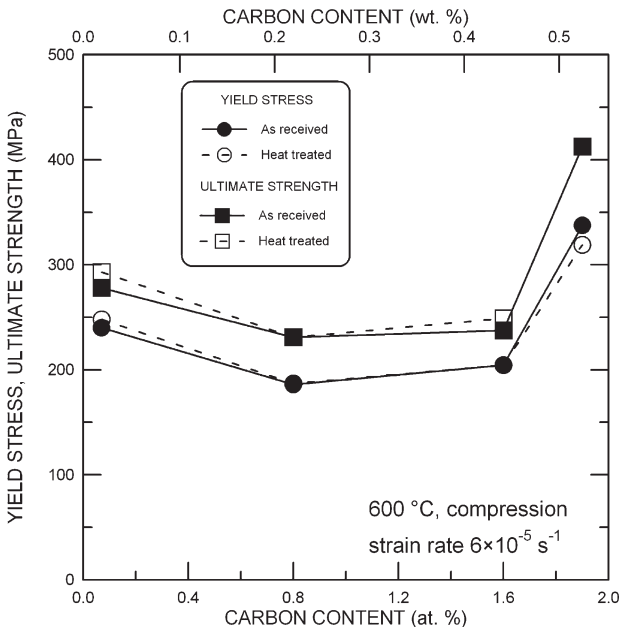

Fig. 7. Dependence of yield stress and ultimate strength on carbon content.

4. Discussion

The stress exponents in the alloys E and F (and in the alloy D at higher temperatures) varied between 4 and 5. This is usually taken as an indication that the recovery processes during creep are controlled by dislocation climb in single-phase matrix. On the other hand, the greater values of the stress exponent in the alloy H and in the alloy D at 600 °C suggest that the dislocation motion is impeded by dispersed second-phase particles. The observed great values of the activation energy can be explained by the same argumentation: The volume fraction of secondary particles is expected to be temperature dependent and the measured activation energy is thus greater than the value corresponding to the volume diffusion of both Fe and Al in FeAl matrix. This interpretation can be supported by following microstructural observations.

Tiny precipitates are formed in the alloy D as suggested by an appearance of dislocation network (cf. Figs. 8a,b). It is evident that the dislocations are

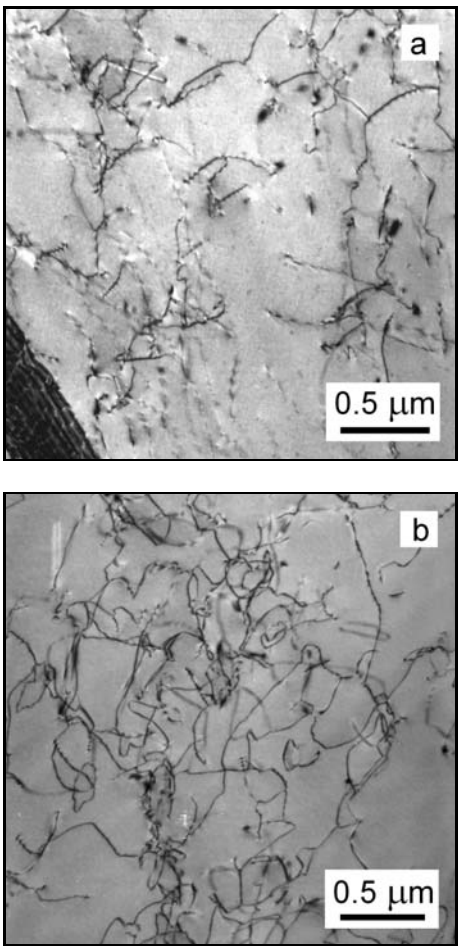

Fig. 8. Dislocation structure after creep at 600 °C in alloy D in (a) as received state and (b) heat-treated state.

pinned down by very small particles that obstruct their motion. The type of particles and/or their composition was not possible to determine. It seems probable that they can be assigned as iron carbides.

In alloys E and F, particles of carbide κ (Fig. 9) are formed and the matrix is depleted of dissolved carbon. Though the dislocations react with particles of diameter up to 500 nm, the density of such particles is too low to prevent dislocation motion. The fraction of small particles that react with dislocations is unsatisfactory.

The alloy H with great proportion of carbide Al_4C_3 is characterized by an outstanding creep resistance and in this point it differs from the other investigated alloys. Dendritic structure of this alloy that is formed by needles of Al_4C_3 carbide is dissolved only partially at 600 °C (cf. Figs. 10a,b) and it constitutes obstacle to dislocation motion in creep deformation.

It could be concluded, that the deformation in the alloys E and F occurs by the dislocation motion as in the single-phase FeAl matrix, eventually modified by the presence of dissolved carbon atoms (solid solution hardening). The dislocation motion is obstructed by tiny precipitates, probably of carbide κ, in the alloy D and by particles of Al_4C_3 in the alloy H.

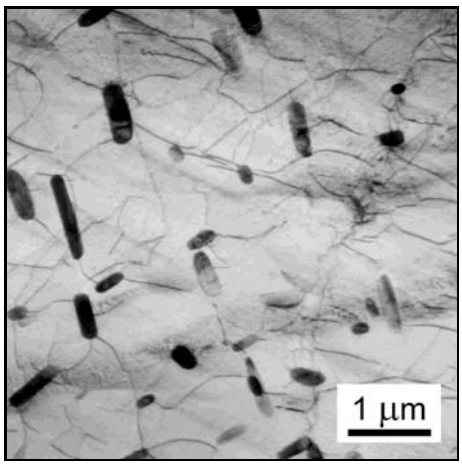

Fig. 9. Dislocation structure after creep at 600 °C in alloy E in as received state.

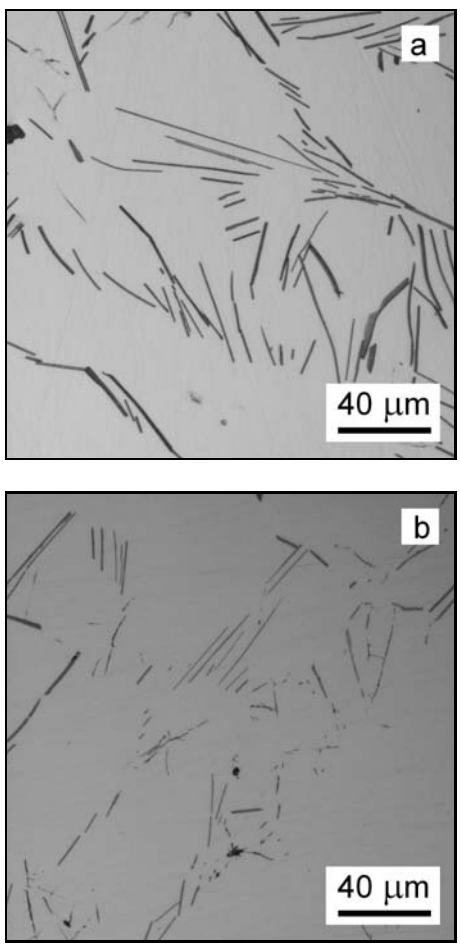

Fig. 10. Dendritic structure in alloy H in (a) as cast state and (b) after creep at 600 °C.

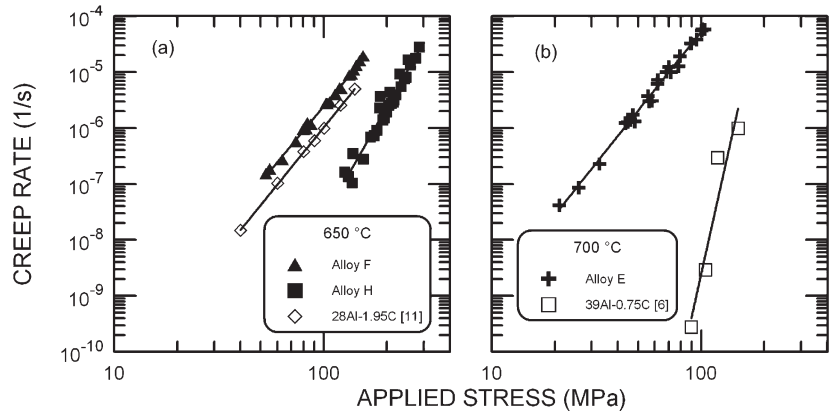

Fig. 11. Comparison of stress dependence of creep rate in present alloys and in Fe-Al alloys with carbon additions published in Refs. [11] (a) and [6] (b).

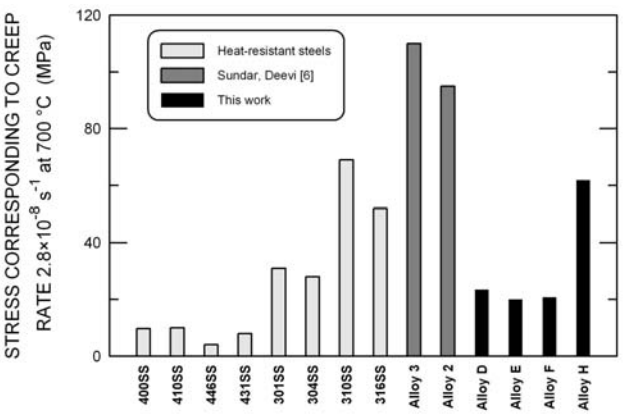

Fig. 12. Comparison of the creep resistance of present alloys with that of several grades of commercial steels and of Fe-Al-C alloys by Sundar and Deevi [6].

A decrease of elevated temperature mechanical properties with increasing carbon content was reported by Baligidad et al. [9, 10] also in Fe_3Al-based alloys. The reduction in creep resistance with an increase in carbon addition from 0.27 to 1.3 wt.% was attributed to the precipitation of carbon as soft graphite [9]. The amount of carbon in the alloys studied in the present contribution is too low to accept this explanation and in fact the graphite phase is not observed here. On the other hand, the decrease of the ultimate tensile strength and of the yield strength at 600 ℃ with the increase of carbon addition from 0.27 to 0.50 wt.% [10] may be related to the same reasons that worsen mechanical properties of the alloys E and F with respect to the alloy D.

A quantitative comparison of the present results with the data reported by the Baligidad's group can be done for the results of compressive creep tests at 650 ℃ given in Ref. [11] (cf. Fig. 11a). Creep rate of the reported alloy with 0.5 wt.% of C (about 1.95 at.%) is comparable with the creep rate in the present alloy F with 1.7 at.% of C and is faster than the creep rate in the present alloy H with 1.9 at.% of C but the difference in aluminium content should be also noted.

Comparison with the literature data of carbon-alloyed iron aluminides of the same class of aluminium content can be done for the data given by Sundar and Deevi [6] for the alloy with 39.33 at.% of Al and 0.75 at.% of C at 700 ℃, Fig. 11b. Creep resistance of the alloy of Sundar and Deevi is substantially superior to that observed in the comparable alloy E of the present paper. This is certainly due to the additions of carbides-forming elements as Mo, Zr and Ti in the alloy of Sundar and Deevi. The excellent creep resistance of this alloy – comparable with or better than that of various superalloys (cf. Fig. 12b in [6]) – confirms the effectiveness of alloying of FeAl-based alloys with carbon. The Sundar's and Deevi's comparison with several grades of commercial heat-resistant steels at 700 ℃ (Fig. 12a in [6]) can also be extended to the present results. Though the stress that results in a creep rate of 2.8×10^{-8} s^{-1} in the alloy H of the present study (60 MPa) is lower than that in Sundar's and Deevi's FeAl-based alloys, it is surpassed by the steel 310 SS only of the selected eight heat-resistant steels (Fig. 12).

5. Conclusions

– The values of the stress exponent and of the activation energy of creep can be explained by dislocation motion controlled by climb and by the presence of second-phase particles.

– Deformation in the alloys E and F occurs by the dislocation motion as in the single-phase FeAl matrix, eventually modified by the presence of dissolved carbon atoms (solid solution hardening).

– The dislocation motion is obstructed by tiny precipitates, probably of carbide κ, in the alloy D and by particles of Al_4C_3 in the alloy H.

– Precipitates of carbide κ do not improve creep resistance efficiently at moderate carbon additions.

– Creep resistance of the present alloy H is better than that of several grades of austenitic, ferritic and martensitic stainless steels and it is surpassed by the steel 310 SS only.

Acknowledgements

The paper is based on work supported by the Grant Agency of the Czech Republic within the project 106/05/0409.

References

[1] PLUHAŘ, J.—VYKLICKÝ, M.: Slévárenství, *2*, 1954, p. 9.
[2] VYKLICKÝ, M.—TUMA, H.: Hutnické Listy, *14*, 1959, p. 118.
[3] PLUHAŘ, J.—VYKLICKÝ, M.: Properties of heat-resistant alloy ČSN 42 2484 (Pyroferal) and its application. Technical report No. 189. Ministry of Heavy Industry, Praha 1959 (in Czech).
[4] KUMAR, K. S.—PANG, L.: Mater. Sci. Engng., *A258*, 1998, p. 153.
[5] GARCIA OCA, C.—MORRIS, D. G.—MUÑOZ-MORRIS, M. A.: Scripta Mater., *44*, 2001, p. 561.
[6] SUNDAR, R. S.—DEEVI, S. C.: Metal. Mater. Trans., *34A*, 2003, p. 2233.
[7] VODIČKOVÁ, V.—KRATOCHVÍL, P.—DOBEŠ, F.: Kovove Mater., *45*, 2007, p. 153.
[8] DOBEŠ, F.—ZVĚŘINA, O.—ČADEK, J.: J. Test. Eval., *14*, 1986, p. 271.
[9] BALIGIDAD, R. G.—RADHAKRISHNA, A.—SARMA, D. S.: J. Mater. Sci., *40*, 2005, p. 5537.
[10] BALIGIDAD, R. G.—PRAKASH, U.—RADHAKRISHNA, A.—RAMAKRISHNA RAO, V.—RAO, P. K.—BALLAL, N. B.: Scripta Mater., *36*, 1997, p. 105.
[11] KOLLURU, D. V.—BALIGIDAD, R. G.: Mater. Sci. Engng., *A328*, 2002, p. 58.

Intermetallics 19 (2011) 1526–1532

Contents lists available at ScienceDirect

Intermetallics

journal homepage: www.elsevier.com/locate/intermet

The effect of carbon and silicon additions on the creep properties of Fe-40 at. % Al type alloys at elevated temperatures

F. Dobeš [a,*], P. Kratochvíl [b], V. Vodičková [c]

[a] Institute of Physics of Materials, Academy of Sciences of the Czech Republic, Žižkova 22, 616 62 Brno, Czech Republic
[b] Department of Physics of Materials, Faculty of Mathematics and Physics, Charles University, Ke Karlovu 5, 121 16 Prague 2, Czech Republic
[c] Department of Material Science, Faculty of Mechanical Engineering, Technical University of Liberec, Hálkova 6, 461 17, Liberec 1, Czech Republic

ARTICLE INFO

Article history:
Received 23 March 2011
Received in revised form
27 May 2011
Accepted 28 May 2011
Available online 22 June 2011

Keywords:
A. Iron aluminides
B. Creep
B. Mechanical properties at high temperatures

ABSTRACT

The mechanical properties of Fe–Al alloys with 39–43 at.% Al, C contents up to 4.9 at.% and Si contents up to 1.2 at.% were studied using uniaxial compressive creep at temperatures from 600 to 800 °C. The stress and temperature dependence of the creep rate were determined by stepwise loading and evaluated in terms of the stress exponent n and the activation energy Q, respectively. These quantities can be interpreted by means of dislocation motion controlled by climb and by the presence of second-phase particles. The dislocation motion is obstructed by precipitates of carbide κ in alloys E and F and by particles of Al_4C_3 in the alloys with either higher content of C or of C and Si. Both carbon and silicon improved the creep resistance, but the effect of silicon was more significant.

1. Introduction

The Fe–Al based alloys with 40 to 45 at. % aluminium were studied extensively in the early 1950s in Czechoslovakia [1,2] with the aim to replace heat-resistant steels alloyed with deficient nickel and chromium. The research resulted in the development of the alloy with the commercial name Pyroferal, which contains 44.4–46.5 at. % Al and 3.4–4.0 at. % C. The composition is similar to that of recently studied FeAl-based alloys with different additions of carbon [3–5]. The creep properties were reported by Sundar and Deevi [5]. They showed that increasing the carbon content from 0.2 to 0.75 at. % led to a decrease in the minimum creep rate and increased the time to rupture. The observed improvement in creep resistance was ascribed to the presence of fine carbide precipitates and dislocation loops formed by the condensation of vacancies in the alloy. Nevertheless, the presence of carbide-forming elements Zr, Ti and Mo has to be taken into account for an exact description of the carbon effect in the study of FeAl alloys.

The influence of carbon was also studied in Fe–Al alloys with aluminium contents ranging from 24 to 28 at. % [6,7]. Baligidad et al. [6] attributed the improvement in the elevated temperature mechanical properties to the presence of the Fe_3AlC phase (carbide κ) as well as the interstitial carbon in the matrix. On the other hand, according to Schneider et al. [7], the carbide κ does not improve the high temperature strength efficiently due to fast coarsening.

The improved mechanical properties of Pyroferal, in comparison with those of single-phase intermetallic FeAl, were ascribed to the effect of carbon addition. That is why a set of FeAl-based alloys with different amounts of carbon was prepared. The composition of the alloys was designed to be approximately within the (i) (Fe–40Al)–C and (ii) (Fe–40Al)––Al_4C_3 vertical sections of the ternary Fe–Al–C system. The selection of the initial point i.e. binary Fe–40Al was motivated by the fact that the majority of available experimental data for B2–FeAl aluminide was obtained for this composition [8–10]. A potential choice of stoichiometric composition Fe–50Al as the starting point of our investigation and thus preparation of alloys of pseudobinary systems FeAl–C and FeAl–Al_4C_3 would miss the targeted alloy Pyroferal.

It should be noted that the original alloy Pyroferal also contained silicon in amounts of about 0.5 at. %. This amount of silicon resulted from alloying with scrap aluminium of electrotechnical quality. The silicon was thus another element included in the present search for the origin of the properties of Pyroferal. It was quite obviously added only to selected alloys of the Section (ii), i.e. (Fe–40Al)–Al_4C_3. In the present paper, the results of creep tests are summarized.

* Corresponding author. Tel.: +420 532290408; fax: +420 541218657.
E-mail address: dobes@ipm.cz (F. Dobeš).

0966-9795/$ – see front matter © 2011 Elsevier Ltd. All rights reserved.
doi:10.1016/j.intermet.2011.05.024

2. Experimental procedure

The compositions of the alloys investigated are listed in Table 1. The experimental techniques used for the preparation of the alloys are described in the previous papers (D to H in [11], H to J in [12]). The additional alloys N and O were processed by vacuum induction melting and rolled under the same conditions as the majority of the previous alloys (with the exception of the alloy H that was available in the cast state only). The chemical compositions were checked by spectral analysis (optical emission spectrometer LECO GDS 750a). Small deviations from the intended compositions were found; these were caused by the problems with simultaneous alloying by aluminium and carbon. The resulting alloys can thus be better described by sections (Fe–41Al)–C (alloys D, E, F, K and L) and (Fe–41Al)–Al_4C_3 (alloys D, H, J, M, N and O) of the ternary diagram Fe–Al–C. The positions of alloys and of respective sections are depicted in Fig. 1.

The phase composition and structure were studied using light optical microscopy (LOM) with Nomarski contrast application. The phase structure was visualized using polishing and etching by Struers emulsion OP-S or by Buehler emulsion Mastermet 2. The X-ray diffraction (XRD) diffractometer XRD-7 (Seifert-FPM) with Cu Kα radiation was used for determination of phases. Phases were also identified by electron probe microanalysis (scanning electron microscope TESCAN equipped with an energy-dispersive X-ray spectrometer Bruker (EDS)). A transmission electron microscope (TEM) JEOL 2000FX with selected area electron diffraction (SAD) was used to study the dislocation structure. The samples for TEM were electrolytically twin-jet polished in 20% solution of HNO_3 in methanol at −30 °C.

Cylindrical specimens for creep tests were prepared by electro-discharge machining (diameter 6 mm, height 12 mm). Uniaxial compressive creep tests were performed at constant load. Stepwise loading was used at temperatures from 600 to 800 °C: at each step, the load was changed to a new value after a steady level of the creep rate was established. The terminal values of the true stress and the true strain rate were evaluated for the step. This type of testing was used to estimate the stress sensitivity of the creep rate and its temperature dependence. All tests were performed in a protective argon atmosphere.

The specimens were tested in two different states: (a) as-received after casting and rolling or after casting (alloy H) and (b) after annealing at 1100 °C for 8 h with quenching in oil. The annealing was expected to form the best basis for the potential hardening treatment by carbide κ.

3. Results and discussion

The structure of the matrix of all alloys is a B2 lattice, inherent to the intermetallic compound FeAl. Three phases containing carbon are observed: carbide κ, graphite and aluminium carbide Al_4C_3. The occurrence of secondary phases, identified by X-ray diffraction and electron probe microanalysis is summarized in Table 2. The results of microstructure observations in alloys D to J were published in the preceding papers [11,12]. The microstructure of the additionally prepared alloys N and O is illustrated in Figs. 2 and 3, respectively. The microstructure of alloy N in the as-received state is characterized by fine lamellae of Al_4C_3 carbide and large lamellae of graphite. In the annealed state graphite flakes can be identified. Alloy O in the as-received state contains fine lamellae of Al_4C_3 carbide, very coarse lamellae of Al_4C_3 and graphite lamellae. In the annealed state fine needles of Al_4C_3, very coarse lamellae of Al_4C_3 and fine graphite flakes are observed. The hardness measurement can also be used for phase identification in these alloys. The Vickers hardness of carbide lamellae is ~1500 HV0.1, while graphite lamellae hardness is ~200 HV0.01 compared to matrix hardness ~350 HV0.1.

The applied stress dependences of the creep rate in the as-received materials are given in Fig. 4a–c. The data for silicon-alloyed materials are placed in the lower right corners of figures a and b and the data for medium silicon-alloyed materials are

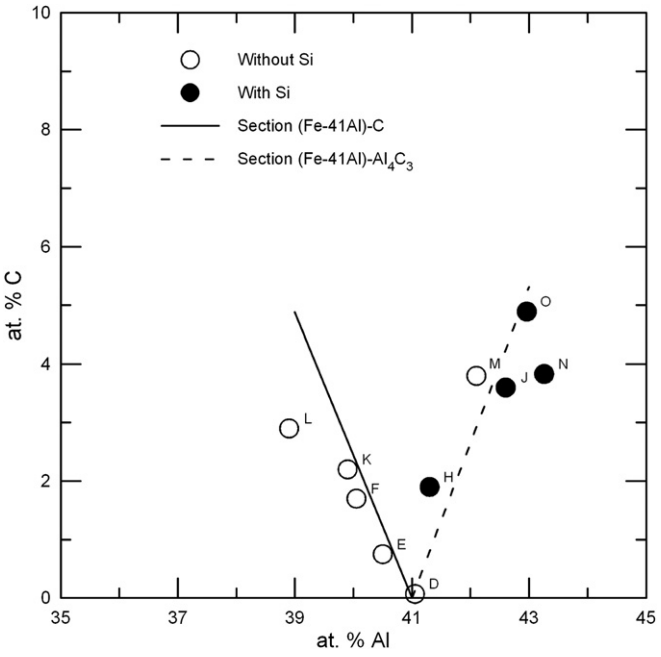

Fig. 1. Composition of the studied alloys with respect to idealized sections (i) (Fe–41Al)–C and (ii) (Fe–41Al)–Al_4C_3.

Table 1
Measured composition of the alloys used (at. %). Alloys are sorted according to their carbon content.

Alloy	Denoted	Al	C	Si	Section
FA 0.1C	D	41.05	0.07	0.05	1, 2
FA 0.8C	E	40.5	0.75	0.05	1
FA 1.7C	F	40.05	1.7	0.05	1
FA 1.9C Si	H	41.3	1.9	1.2	2
FA 2.2C	K	39.9	2.2	0.06	1
FA 2.9C	L	38.9	2.9	0.05	1
FA 3.6C Si	J	42.6	3.6	1.14	2
FA 3.8C	M	42.1	3.8	0.04	2
FA 3.8C Si	N	43.26	3.83	0.78	2
FA 4.9C Si	O	42.96	4.89	0.69	2

Table 2
Observed secondary phases.

Alloy	Not annealed	Annealed at 1100 °C/8 h
Section (Fe–41Al)–C		
D	(κ?)	(κ?)
E	κ	G
F	κ + G	G + κ
K	G	G
L	G	G
Section (Fe-41Al)-Al_4C_3		
D	(κ?)	(κ?)
H	Al_4C_3 + (G)	(G) + (Al_4C_3)
J	Al_4C_3 + (G)	Al_4C_3 + (G)
M	Al_4C_3 + (G)	G + (Al_4C_3)
N	Al_4C_3 + (G)	Al_4C_3 + (G)
O	Al_4C_3 + (G)	Al_4C_3 + (G)

( ), Minor phase; G, graphite.

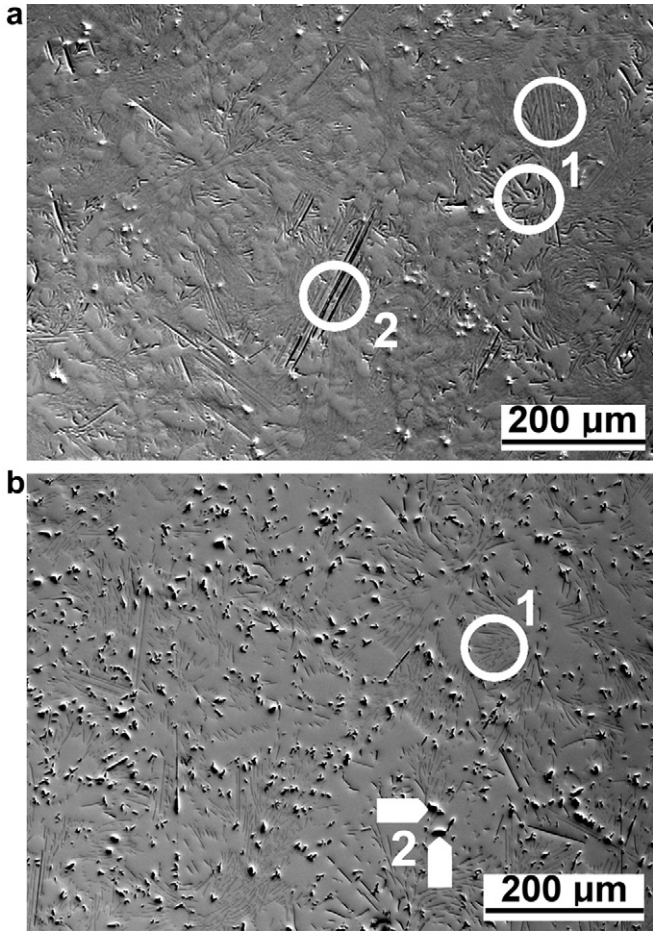

Fig. 2. Microstructure of alloy N: (a) as-received - fine lamellae of Al_4C_3 carbide (marker 1) and large lamellae of graphite (marker 2), (b) annealed at 1100 °C 24 h – fine lamellae of Al_4C_3 (marker 1) and graphite flakes (marker 2).

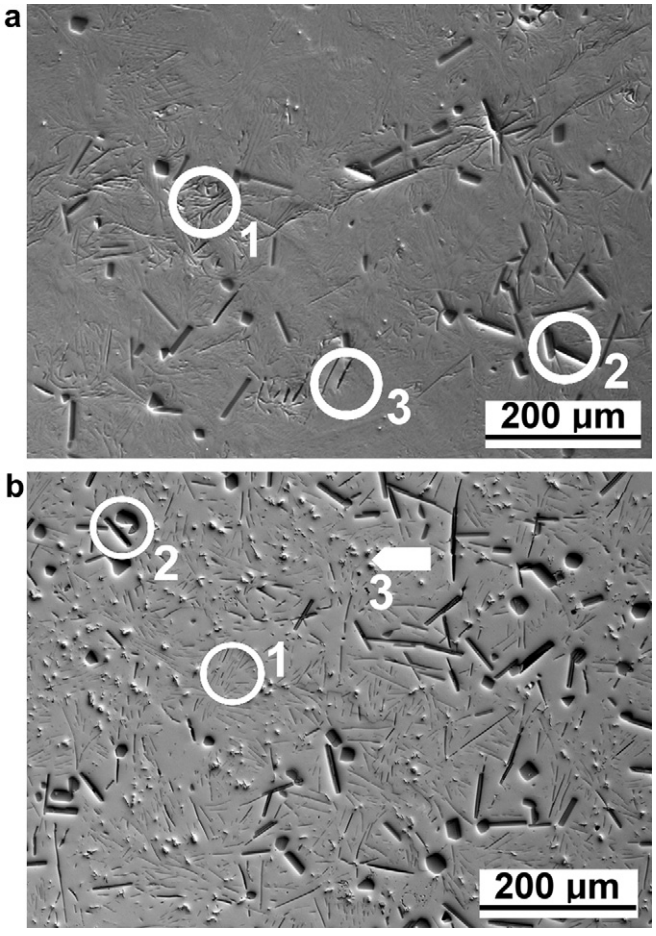

Fig. 3. Microstructure of alloy O: (a) as-received - fine lamellae of Al_4C_3 carbide (marker 1), very coarse lamellae of Al_4C_3 (marker 2) and graphite lamellae (marker 3), (b) annealed at 1100 °C 24 h – fine needles of Al_4C_3 (marker 1), very coarse lamellae of Al_4C_3 (marker 2) and fine graphite flakes (marker 3).

in Fig. 4c. Both positive and negative load changes were applied. By this procedure, it was possible to obtain approximately the same creep rate/stress values at different creep strains and thus different testing times. The values measured within initial load steps, characterized by lower true stress and thus corresponding to primary creep stage, were omitted. It is supposed that the influence of possible changes of microstructure, i.e. additional precipitation and/or particle coarsening, was eliminated by this procedure. The dependence can be described at a given temperature by the power function

$$\dot{\varepsilon} = A\sigma^n \tag{1}$$

where $\dot{\varepsilon}$ is the creep rate, σ is the applied stress and A is a temperature dependent constant. The values of the power n are given in Table 3. The power n increased with increasing carbon content (in alloys without silicon about 0.7 per at. % C) and decreased with increasing temperature (about 1.4 per 100 K). The influence of Si on n was probably less significant.

A decrease in the exponent n with the increasing temperature was predicted by the deformation mechanism controlled by double-kink nucleation and propagation on dislocations. The respective temperature dependence can be deduced from Eq. (10) in Ref. [13] (in both the low and high stress regimes)

$$\frac{\partial n}{\partial T} = \frac{1}{2k}\sqrt{\frac{(bh)^3\sigma}{2\pi}}\left(\frac{1}{2T\sqrt{\mu}}\frac{\mathrm{d}\mu}{\mathrm{d}T} - \frac{\sqrt{\mu}}{T^2}\right) \tag{2}$$

where μ is the shear modulus, k is the Boltzmann constant, T the absolute temperature, b is the magnitude of the Burgers vector of the dislocation and h is the periodicity of the Peierls barriers in the glide plane. It was assumed that b and h are equal, as it is true for edge dislocations. The results of these calculations for $b = h = 0.25$ nm (i.e. $b = 1/2a\langle 111\rangle$ in B2 [14,15] with a lattice parameter $a = 0.289$ nm) and $\mu = 100{,}180 - 37.44 \times T$ MPa [16] are given in Fig. 5. The calculated values of the derivative $\mathrm{d}n/\mathrm{d}T$ are more than an order of magnitude greater than the experimentally estimated values. A change to $\langle 100\rangle$ slip occurs in FeAl at temperatures above 0.45 of melting point and both $\langle 100\rangle$ and $\langle 111\rangle$ dislocations can be observed at intermediate temperatures [17]. The substitution of the $\langle 100\rangle$ Burgers vector length into the above calculations reduces the value of $\mathrm{d}n/\mathrm{d}T$ by a factor of 1.5 and only slightly improves the discrepancy of the theory and the present experiments. This comparison does not support the double-kink model as the rate-controlling mechanism. It should be pointed out that the present method of comparison of derivatives is more advantageous than a direct comparison of measured and calculated exponents n since it is independent of the actual level of the critical stress, and it is not influenced by neglecting the stress dependence of the dislocation density [13].

The lower values of the stress exponent n, i.e., the values about 4 to 5, are usually taken as an indication that the recovery processes during creep are controlled by dislocation climb in the single-phase matrix. This was the case for low-carbon alloys (with the exception

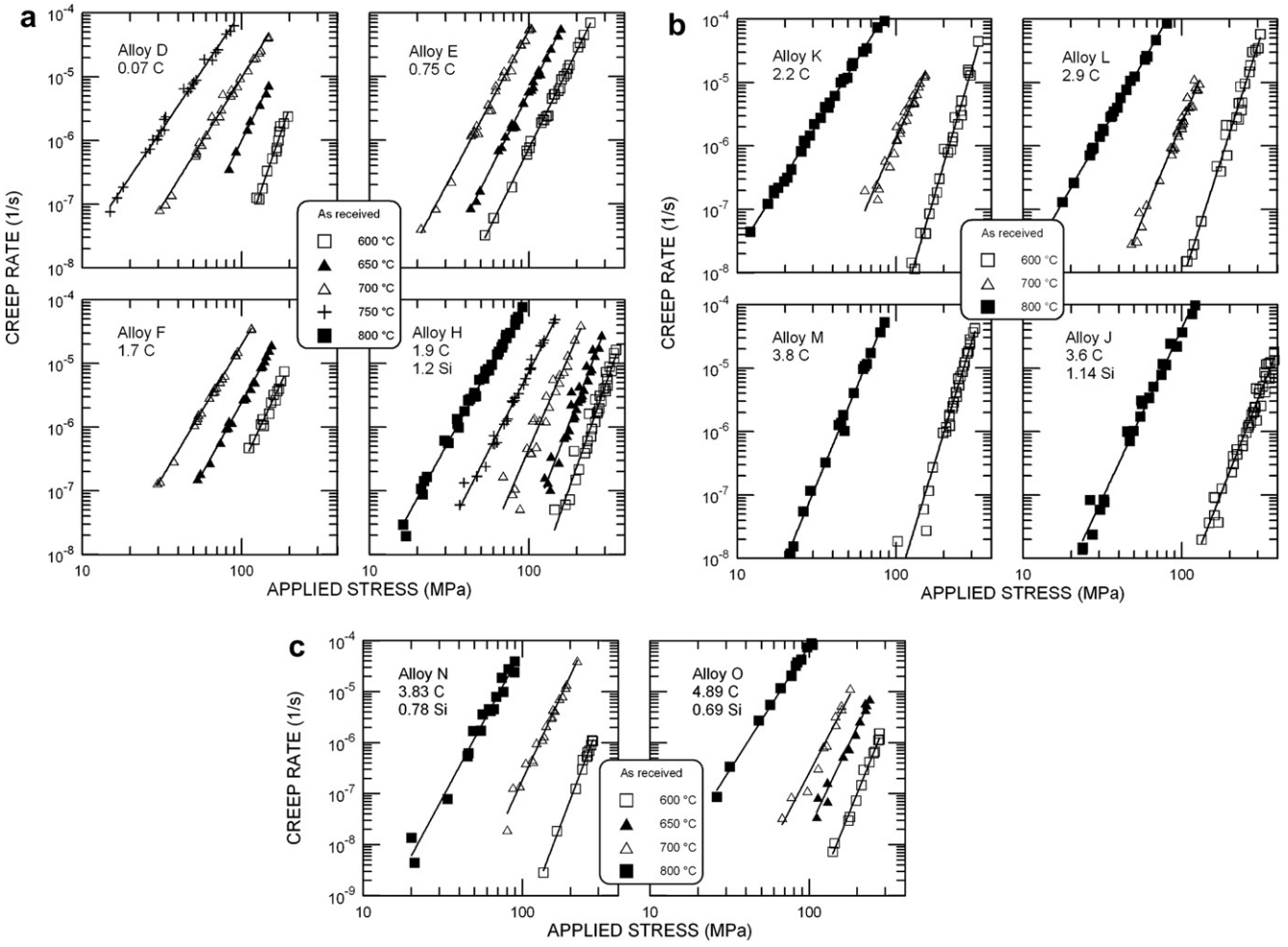

Fig. 4. The dependence of the creep rate on the applied stress.

of the alloy D) and for higher temperatures. On the other hand, the greater values of the stress exponent in the alloys with the greater additions of carbon and with silicon suggested that the dislocation motion is impeded by dispersed second-phase particles.

Since the stress exponent n is dependent on temperature, the apparent activation energy Q defined as

$$Q = -R\left(\frac{\partial \ln \dot{\varepsilon}}{\partial(1/T)}\right)_{\sigma} \tag{3}$$

Table 3
Stress exponents n measured in the as-received state

Alloy	Temperature (°C)				
	600	650	700	750	800
Section (Fe–41Al)–C					
D	7.2	5.1	4.0	3.7	
E	5.1	5.0	4.7		
F	5.3	4.5	4.2		
K	8.5		5.7	4.9	4.5
L	7.8		6.1		4.3
Section (Fe–41Al)–Al_4C_3					
D	7.2	5.1	4.0	3.7	
H	7.1	6.6	5.9	4.9	4.5
M	8.2				6.0
J	6.4				5.3
N	8.3		6.8		5.8
O	7.7	6.7	6.0		4.9

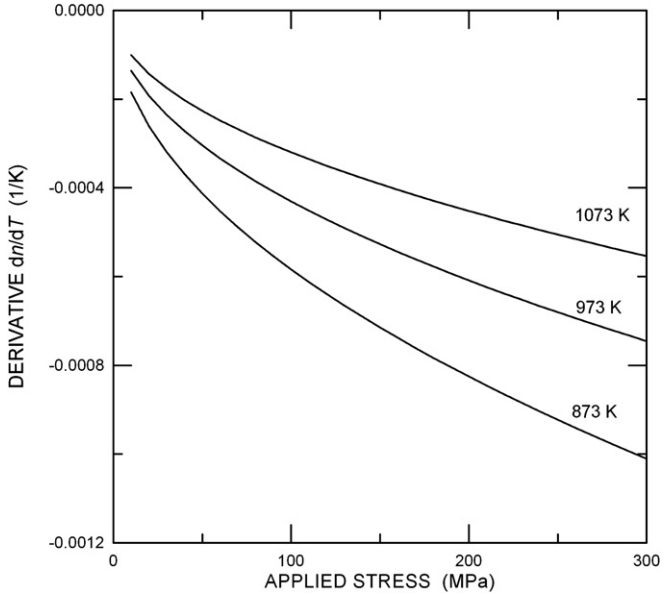

Fig. 5. The calculated dependence of the temperature derivative of power n on the applied stress in the applied-kink model.

Table 4
Activation energy Q measured in the as-received state.

Alloy	Activation energy (kJ/mol)	
	600–700 °C	600–800 °C
Section (Fe–41Al)–C		
D	429	
E	301	
F	311	
H	392	432
K	478	465
L	406	407
Section (Fe–41Al)–Al_4C_3		
D	429	
H	392	432
M		419
J		375
N	466	486
O	446	463

is dependent on the applied stress; it increases with decreasing applied stress. Consequently, it is rather problematic to estimate the value at zero stress as an important characteristic of the deformation process. Therefore, the activation energy was assessed from creep rates found at 100 MPa (eventually estimated by extrapolation) and at temperatures of 600 °C and 700 °C (800 °C, respectively). The values are given in Table 4. In analogy to the interpretation of stress power n, the values of Q could also be explained in terms of two activation mechanisms: (i) dislocation climb controlled in single-phase matrix with $Q \approx 310$ kJ/mol and (ii) mechanism controlled by the presence of second-phase particles with $Q \approx 450–500$ kJ/mol.

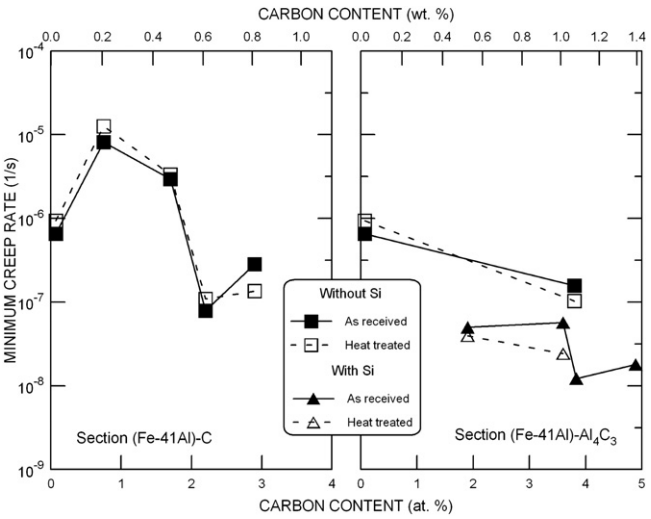

Fig. 7. The dependence of the creep rate at 600 °C and applied stress 160 MPa on the carbon content.

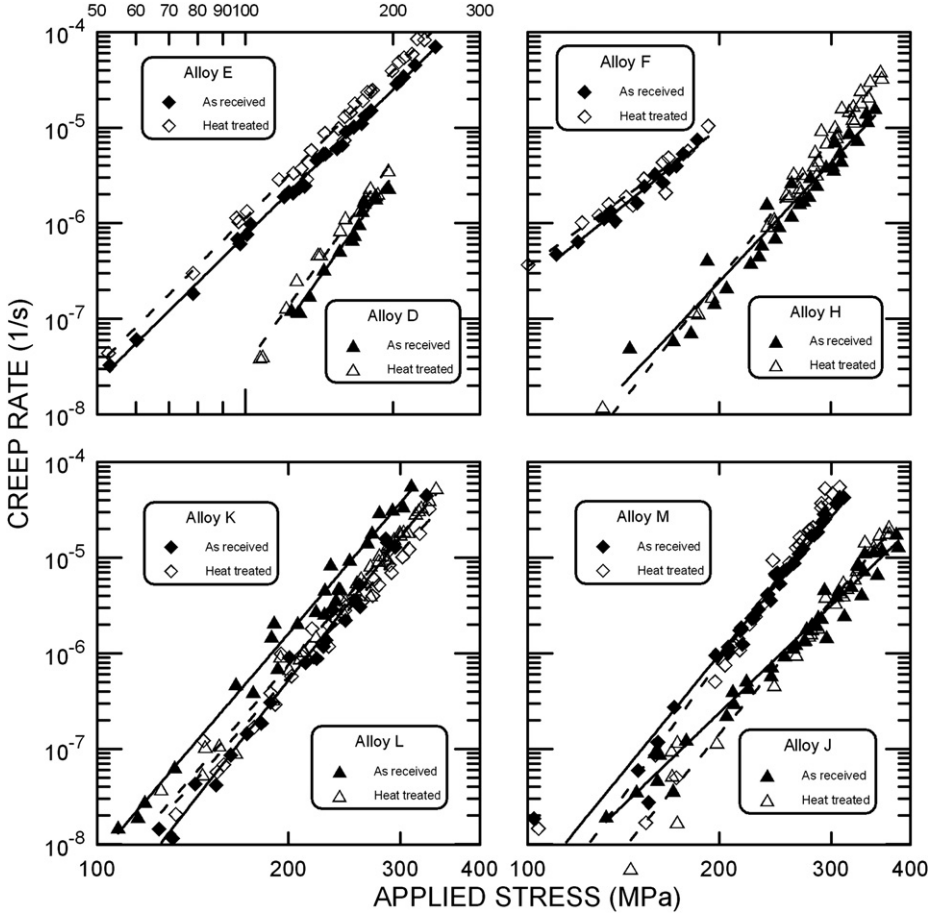

Fig. 6. The applied stress dependence of the creep rate in the as-received and heat-treated states at 600 °C.

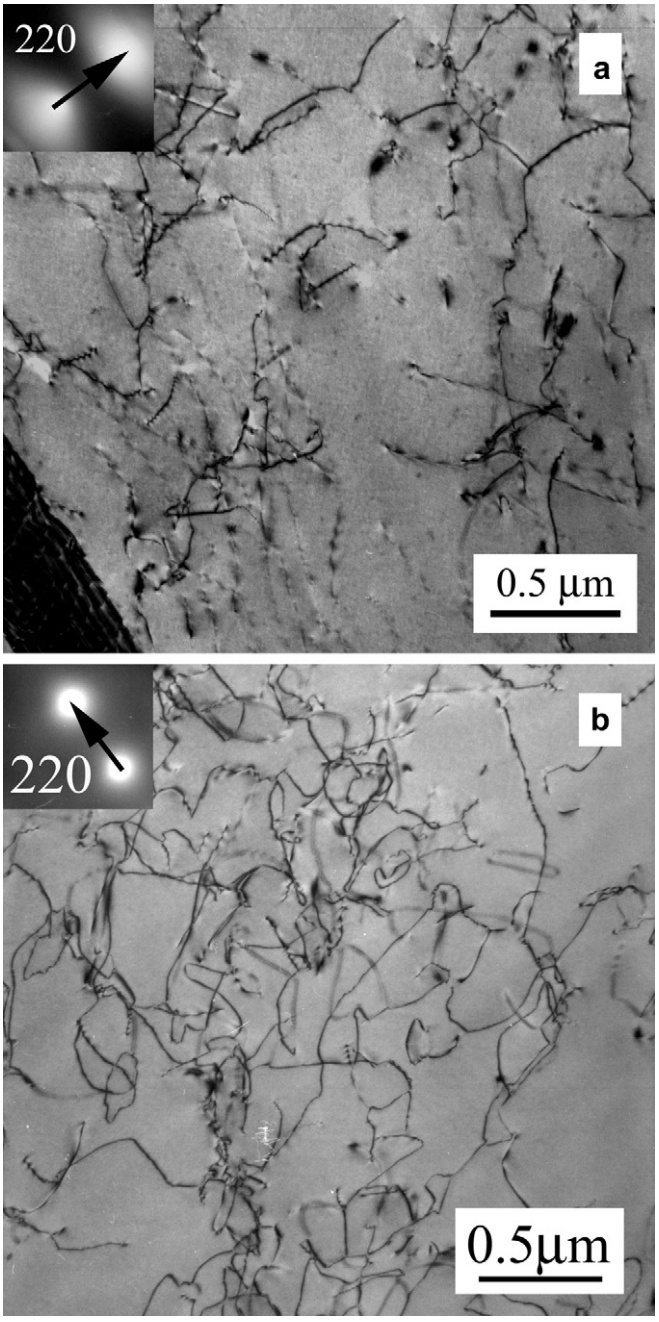

Fig. 8. TEM micrographs of the dislocation structures after creep at 600 °C in alloy D in (a) the as-received state and (b) the heat-treated state.

The effect of heat treatment on the creep properties is illustrated in Fig. 6. The applied heat treatment had only a small influence on the minimum creep rate. The influence of additions of carbon on the creep rate at 873 K and applied stress 160 MPa is illustrated in Fig. 7. The initial increase of the creep rate in the Section (Fe–41Al)–C might be identical to a similar decrease in the tensile strength at 800 °C, reported by Sundar and Deevi [5], when the carbon content was increased from 0.2 to 0.45%. From the appearance of dislocation networks observed after deformation of the alloy D (Fig. 8), it is evident that there exist obstacles which impede the motion of dislocations or their configurations. It was impossible to determine the type of obstacles. These might be either carbides κ or the sessile configurations of dislocations.

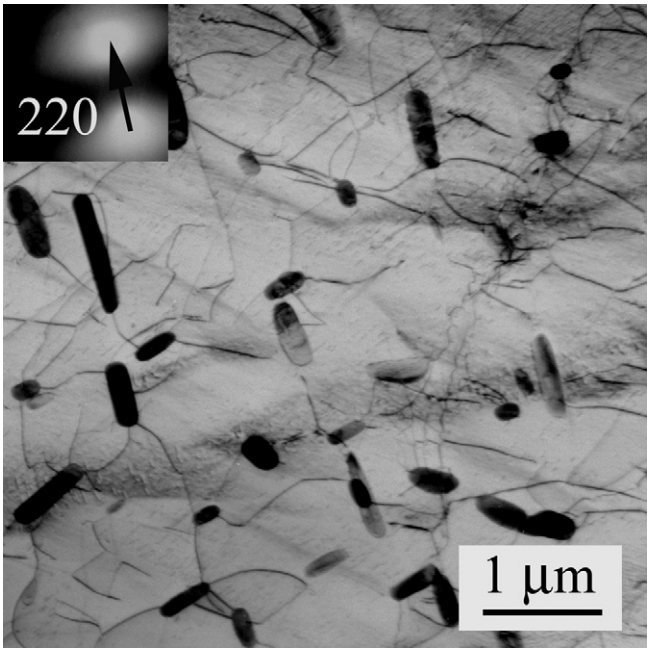

Fig. 9. TEM micrographs of the dislocation structure after creep at 600 °C in alloy E in the as-received state. The particles were identified as carbide κ.

On the other hand, in the alloys E and F, relatively greater particles identified as carbide κ (Fig. 9) were formed and the matrix was depleted of dissolved carbon. Though the dislocations react to particles with diameters up to 500 nm, the density of such particles was too low to prevent dislocation motion. The fraction of small particles that reacted with dislocations was unsatisfactory, and consequently, the strength of these alloys was lower than that of the alloy D.

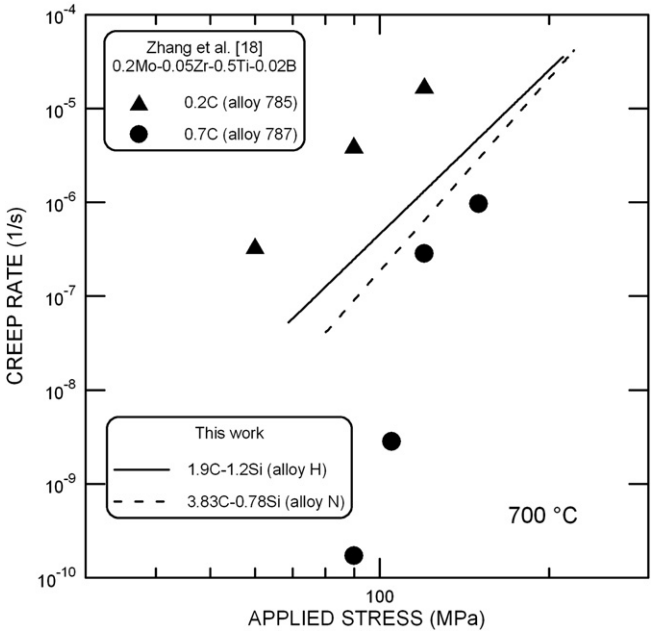

Fig. 10. Comparison of creep rate variation with applied stress at 700 °C for the present alloys H and N and two FeAl-based alloys containing C additions (concentrations are given in at. %) [18].

The increase in the creep resistance with increasing carbon content (beyond the alloy D) matched roughly with the expected increase in the amount of secondary phases, i.e. carbide κ, Al_4C_3 and graphite in the alloys of Section (i) and Al_4C_3 in the Section (ii). The creep rate in the alloy L is faster than in the alloy K. This may be caused by a slightly less amount of aluminium in the alloy L: The solubility of carbon in B2 lattice is increasing with the decreasing concentration of aluminium and consequently, less amount of carbon is available for graphite precipitation in the alloy L.

It is clear that both carbon and silicon improved the creep resistance, but the effect of silicon was evidently more significant. It follows from optical observations [12] that the microstructure of the silicon-enriched alloys consists of dendritic needles of Al_4C_3. These needles represent effective obstacles to dislocation motion. Thus, the positive effect of silicon addition was due to the fact that silicon promoted the formation of this type of carbide.

Both phases fine lamellae of Al_4C_3 and large of graphite strengthen the material. The creep resistance may be understood as the strength of composite material for which the volume fractions of the phases must be available. The other contribution to the strength is connected to the blocking of grain boundary and dislocation motion within the grains by the mentioned phases, which have in the individual alloys their special size and shapes. The incoherent particles can be overcome by different mechanisms, generally by the Orowan mechanism and, at elevated temperatures, by climb or by cross slip. The influence of particles on creep resistance is usually described by including the back-stress term, i.e. the threshold stress, into Eq. (1). This can explain the values of the observed stress exponents and their temperature dependence [15]. An exact physical nature of the back stress and its proper interpretation is not yet clear.

Comparison of the present results with the above-mentioned literature data on the creep behaviour of Fe–40Al alloys with carbon additions is given in Fig. 10 [5,18]. The present silicon-enriched alloys have lower creep resistance than the alloy 787 with 0.7% of C. The superiority of the alloy 787 can be attributed to the presence of the carbide-forming elements Mo, Zr and Ti. It should be noted that the creep resistance of this alloy also surpasses the resistance of Fe_3Al-based alloys (cf. Fig. 4 in Ref. [19]), but the ductility of the alloys with reduced aluminium content is generally better.

4. Conclusions

- The values of the stress exponent n and of the activation energy Q can be explained by dislocation motion controlled by climb and by the presence of second-phase particles.
- Deformation in alloys E and F occurred by dislocation motion as in the single-phase FeAl matrix, eventually modified by the presence of dissolved carbon atoms (solid solution hardening).
- The dislocation motion was hindered by particles of carbide κ and graphite and by particles of Al_4C_3 in the alloys with silicon additions.
- Precipitates of carbide κ did not improve creep resistance efficiently at moderate carbon additions.

Acknowledgements

The paper is based on work supported by the Grant Agency of the Czech Republic within the project 106/08/1238 and by the Ministry of Education, Youth and Sports within the project MSM 4674788501.

References

[1] Vyklický M, Tůma H. Hutnické Listy 1959;14:118.
[2] Kratochvil P. Intermetallics 2008;16:587.
[3] Kumar KS, Pang L. Mater Sci Eng 1998;A258:153.
[4] Garcia Oca C, Morris DG, Muñoz-Morris MA. Scripta Mater 2001;44:561.
[5] Sundar RS, Deevi SC. Metal Mater Trans 2003;34A:2233.
[6] Baligidad RG, Prakash U, Radha Krishna A. Mater Sci Eng 1997;A230:188.
[7] Schneider A, Falat L, Sauthoff G, Frommeyer G. Intermetallics 2005;13:1322.
[8] Morris MA, Morris DG. Acta Metal Mater 1990;38:551.
[9] Whittenberger JD, Nathal MV, Gaydosh DJ. Intermetallics 1994;2:193.
[10] Morris DG, Gutierrez-Urrutia I, Muñoz-Morris MA. Int J Plasticity 2008;24:1205.
[11] Vodičková V, Kratochvíl P, Dobeš F. Kovove Mater 2007;45:153.
[12] Kratochvíl P, Dobeš F, Vodičková V. Intermetallics 2009;17:39.
[13] Mitchell TE, Hirth JP, Misra A. Acta Mater 2002;50:1087.
[14] Kad BK, Horton JA. Mater Sci Eng 1997;A239–240:118.
[15] Morris DG, Gutierrez-Urrutia I, Muñoz-Morris MA. Scripta Mater 2007;57:449.
[16] Deevi SC, Swindeman RW. Mater Sci Eng 1998;A258:203.
[17] Baker I. Mater Sci Eng 1995;A192–193:1.
[18] Zhang WJ, Sundar RS, Deevi SC. Intermetallics 2004;12:893.
[19] Morris DG, Muñoz-Morris MA, Requejo LM. Acta Mater 2006;54:2335.

Intermetallics 18 (2010) 1365–1368

Contents lists available at ScienceDirect

Intermetallics

journal homepage: www.elsevier.com/locate/intermet

High temperature mechanical properties of Fe28Al4Cr alloy with additives TiB_2 and Zr

Petr Kratochvíl [a,*], Věra Vodičková [b], Jan Hakl [c], Tomáš Vlasák [c], Pavel Hanus [b], Josef Pešička [a]

[a] Charles University, Department of Physics of Materials, Prague, Czech Republic
[b] Technical University, Department of Material Science, Liberec, Czech Republic
[c] Research Institute SVÚM a.s., Prague-Běchovice, Czech Republic

ARTICLE INFO

Article history:
Received 5 October 2009
Received in revised form
14 December 2009
Accepted 25 January 2010
Available online 25 February 2010

Keywords:
A. Iron aluminides based on Fe_3Al
B. Mechanical properties at high temperature
B. Precipitates

ABSTRACT

The research of the high temperature mechanical properties of Fe28Al4Cr with additives Ce, TiB_2 and Zr is completed using as additive Zr combined with TiB_2. The alloy was prepared using vacuum induction melting and rolling at 1200 °C and finally applying annealing at 1150°C for 2 hours. During alloying the majority of Ti in TiB_2 was replaced by Zr. The majority of $(Zr,Ti)B_2$ particles is situated along the grain boundaries. Fine ZrC carbide particles appear mainly on dislocations. Tensile and creep tests were performed at 600, 650, 700, 800 and 900 °C. Transmission electron microscopy showed precipitation of fine particles on dislocations, subgrain boundaries and also in the matrix. Coarsening of these particles during creep at 800 °C and 900 °C takes place. The high temperature mechanical properties of alloys with additives Ce, TiB_2, Zr and Zr combined with TiB_2 are compared. The Larson–Miller parameter is used to describe the creep strength.

1. Introduction

Fe_3Al-type iron aluminides exhibit good strength at moderate temperatures and have low density. The interest in these materials is growing due to their high temperature (H.T.) environmental resistance. Current research is focused on improving H.T. tensile and creep properties in order to enable applications up to temperatures in the range of 800 °C–1000 °C. The general task to enhance the H.T. mechanical properties of Fe_3Al iron aluminides may be handled by using different methods (for overview see e.g. [1]):

i) Strengthening by solid solution hardening which is useful forsmall ternary additions such as Cr, V, Mo and Ti,
ii) strengthening by incoherent precipitates which may be either formed due to ternary additions of Zr, Ta, Nb or Ti in higher concentrations (diverse phases originate according to high temperature isothermal section of phase diagrams) or carbide and boride precipitates, which need additions of C or B (also as quaternary to the above mentioned elements),
iii) strengthening by coherent precipitates as one of the most effective methods (B2 in A2 and vice versa for Fe–Al–Ni–Cr alloys or B2 + $L2_1$ in Fe–Al–Ta system),
iv) strengthening by increased crystallographic order which stabilizes the $D0_3$ structure to higher temperatures (e.g. Fe–Al–Ti).

In all cases, the strengthening effect depends on the temperature and on the stress at which the material is used. The crucial point of the technological procedure, which determines the phase structure of the alloy, is the heat treatment to produce the microstructure. The determining factor for the use of the material is the stability of the microstructure at H.T.

Zirconium was found to be a noticeable alloying addition to the Fe_3Al matrix. Even small amounts of Zr result in the precipitation of Laves-phase $(Fe,Al)_2Zr$ or τ_1-phase $(Fe,Al)_{12}Zr$ particles hindering the motion of dislocations [2–5]. If the alloy contains carbon or boron, zirconium carbides or borides can be formed [6,7]. The existence and the type of Zr-rich particles depend on the ratio of zirconium, carbon, and boron concentrations. Recent experiments to improve Fe_3Al–type ordered alloys with Zr addition of the order of 1 at.% are due to Alven and Stolloff [8,9], Morris et al. [7,10], Kratochvíl et al. [11] and to Karlík et al. [12].The phases identified by these authors were ZrC, $(Fe,Al)_2Zr$, $Fe_3(Al,Zr)$ and ZrB_2. The material with TiB_2 was tested by Kratochvíl et al. [13] and by Krein et al. [14].

It is the purpose of the present paper to investigate the possibility to apply the combined effect of Zr and TiB_2 to enhance the HT mechanical properties (creep and tension tests).

* Corresponding author. Tel.: +420 221 911 364; fax: +420 221 911 490.
E-mail address: pekrat@met.mff.cuni.cz (P. Kratochvíl).

0966-9795/$ – see front matter © 2010 Elsevier Ltd. All rights reserved.
doi:10.1016/j.intermet.2010.01.038

Table 1

	Al	Cr	TiB_2	Zr	C	Fe
at.%	27.6	3.5	1.57	0.48	0.12	bal

2. Experimental techniques

The alloy was prepared by vacuum induction melting and casting. TiB_2 was added as a powder composed of 10 μm long rods and Zr in metallic form. The result of the chemical analysis is in Table 1. The composition of the tested alloy Prismatic casts (29 × 40 × 400 mm) were annealed at 1200 °C for 2 h and then were rolled at 1200 °C from 29 mm thickness to 13 mm in several steps with 15% thickness reduction in one pass. After each pass between the rolls, the material was reheated to 1200 °C and at the final thickness it was rapidly cooled in mineral oil. The samples for tensile and creep tests (5 mm in diameter, 25 mm gauge length, and M12-threaded heads) have the axis parallel to the rolling direction. After machining the samples were additionally annealed at 1150 °C for 2 h and slowly cooled in air.

Deformation tests were carried out at 600, 650, 700, 800 and 900 °C. Tensile tests were performed at a strain rate of 1.5×10^{-4} s^{-1} and creep tests under constant load. During both tests, the temperature was kept with the accuracy of 3 K.

The phase composition and structure were studied using light optical microscopy (LOM) and X-ray diffraction (XRD). The phase structure and grain boundaries were visualized using Mastermet 2 (Buehler) emulsion and subsequent chemical etching by Rollason solution (100 ml H_2O + 50 ml 38%HCl + 5 g $FeCl_3$). Phases were also identified by electron probe microanalysis (scanning electron microscope TESCAN equipped with an energy-dispersive X-ray spectrometer (EDS) Bruker). A transmission electron microscope (TEM) JEOL 2000FX with selected area electron diffraction (SAD) was used to study the dislocation structure. The samples for TEM were electrolytically twin-jet polished in 20% solution of HNO_3 in methanol at −30 °C.

3. Results

3.1. Structure

The typical structure prior to the deformation, i.e. after hot rolling at 1200 °C and additional annealing at 1150 °C for 2 h, are grains slightly elongated in the rolling direction. The coarse particles (~5 μm) are observed along the grain boundaries, Fig. 1. These were identified as (Zr,Ti)B_2. Ti is present as a minor substitute (the shift of the positions of the corresponding X-ray diffraction maxima) and is present also dissolved in the lattice. It can be concluded that the chemical affinity of Zr to B is higher than that of Ti and the conversion of TiB_2 to ZrB_2 takes place during alloying (Fig. 1).

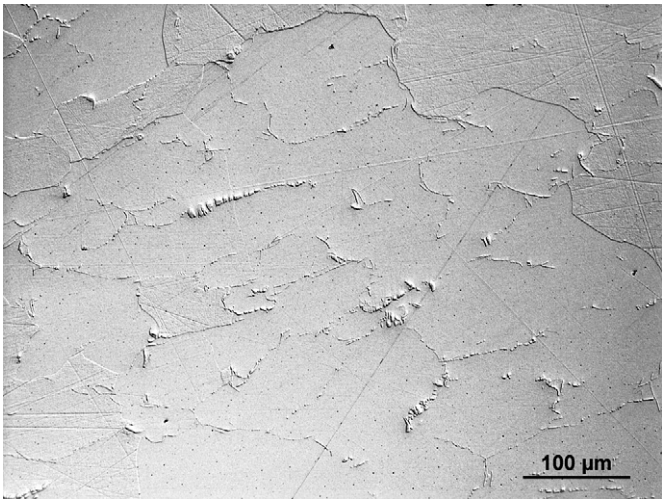

Fig. 1. LOM of particles along the grain boundaries after hot rolling at 1200 °C and annealing at 1150 °C.

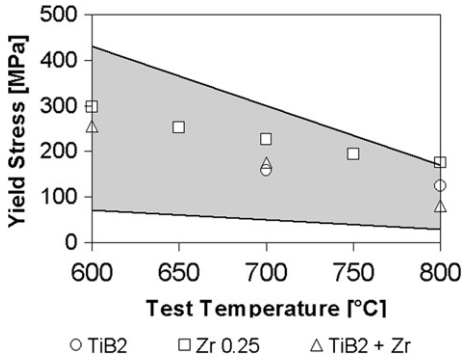

Fig. 2. The HT $\sigma_{0.2}$ for the tested alloy compared with previous results.

3.2. Mechanical properties

The HT 0.2% yield strength $\sigma_{0.2}$ was measured at 600, 700 and 800 °C (Fig. 2) and compared to the results, which the authors obtained for materials with Zr [11] (the data completed by not yet published values for 650 °C and 750 °C) and TiB_2 [13]. The grey area represents schematically the range of results related to dispersion strengthened iron aluminides [2].

The creep properties of the investigated iron aluminide for 600 °C–900 °C are summarized in Figs. 3 and 4, where the values of minimum creep rate (MCR) and of time to rupture (TTR) are given.

3.3. Microstructure after creep

TEM observations show a clear difference between the particles and dislocation structure of the samples crept at 600 °C and 700 °C and those crept at 800 °C and 900 °C. Tiny particles (~10 nm) are ZrC and are formed both during creep at 600 °C and also after annealing at 1150 °C/2 h before testing particles (Fig. 5a). The type of the particles and their coarsening fully corresponds to that described in [6]. These authors determined their composition as ZrC. The microstructure is characterized by coarsening of the

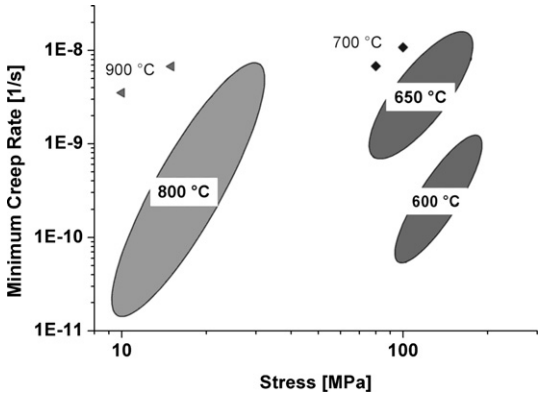

Fig. 3. The values of MCR at 600–900 °C.

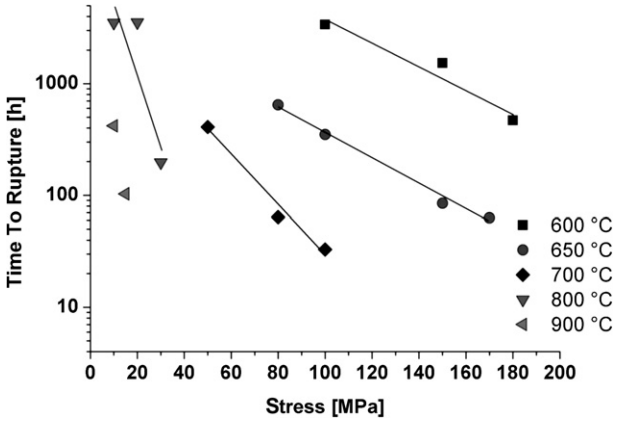

Fig. 4. The values of TTR at 600–900 °C.

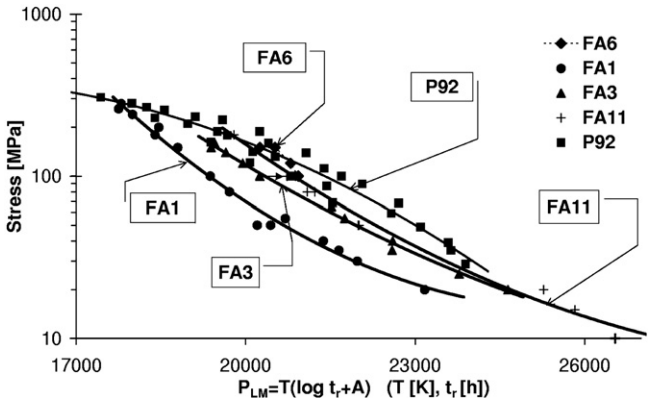

Fig. 6. Creep strength as a function of Larson–Miller parameter.

particles at 800 °C and 900 °C (Fig. 5b and c). SAD pattern of large particles is in Fig. 5b. The exact determination of the structure is not available [6]. ZrC particles are observed not only on dislocation lines but also in sub-boundaries.

The few large particles observed in the lattice or situated along the grain boundaries are apparently (Zr,Ti)B_2 (determined by XRD, SAD and EDS) have no influence on the movement of dislocations during creep.

4. Discussion

The creep experiments were performed using constant load experiments. The detailed analysis of creep data (determination of the stress exponent n) is not possible according to small number of experimental data available for each of the creep temperatures. The creep in this alloy is inhibited by particles at the temperatures of 600 and 650 °C. At temperatures 800 and 900 °C the particle strengthening gives way to matrix solute control of creep. To summarize the role of the phases appearing in the material:

a) the most efficient for the strength at 600 and 650 °C is the fine dispersion of Zr carbide particles having the cubic structure [6]. The hardening effect of Zr carbide deteriorates at high temperatures (800 °C and 900 °C) at which the phase coarsens.
b) Zr boride (or combined Ti, Zr boride), which originate due to the rebuilding of the Ti boride already during the alloying process, appears on grain boundaries. The contribution to the strength of the alloy due the Hall–Petsch relation is rather small [16].
c) There exists only minor evidence of the presence of $Al_{0.4}Fe_{1.6}Zr$ Laves-phase [5,7,10,11,15], which appears if no C or B atoms are available and Zr atoms react with Fe and Al neighbors.

The characteristics of the creep properties of different iron aluminides was compared. The dependence of TTR, t_r[h], at different temperatures T[K] is related to the stress σ [MPa] using the so called Larson–Miller parameter $P_{LM} = T\,(\log t_r + A)$, see e.g. [16]. The creep properties of the studied materials (Fe_3Al–type alloys with Ce, TiB_2 and Zr) [11,13] are compared in Fig. 6, where also the

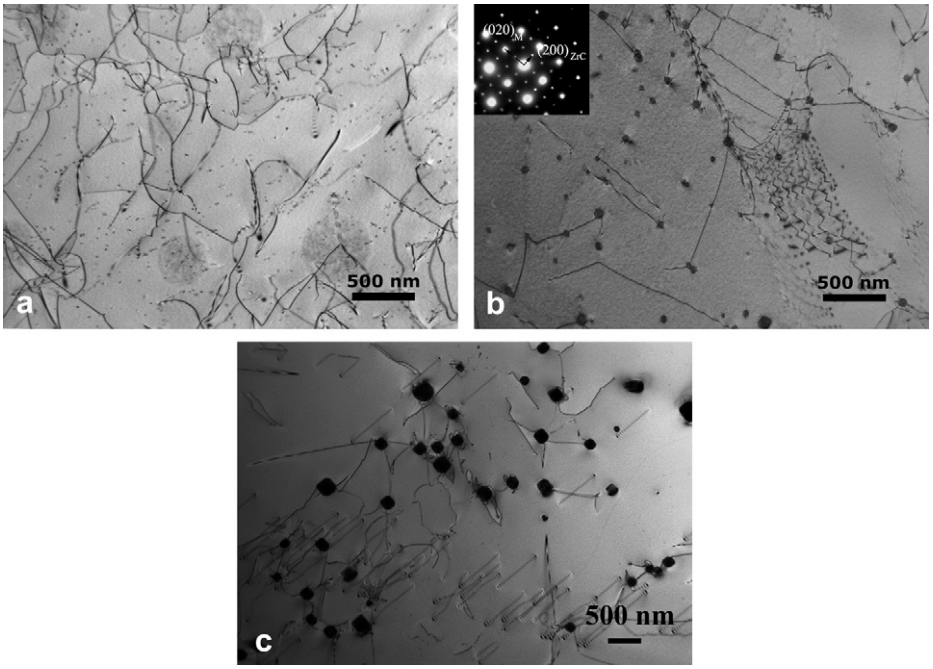

Fig. 5. a) Dislocations with fine ZrC precipitates after creep at 600 °C, 100 MPa, 5000 h; b) Dislocations with coarsened ZrC precipitates after creep at 800 °C, 20 MPa, 200 h; c) Dislocations with very coarse ZrC precipitates after creep at 900 °C,10 MPa, 400 h.

Table 2
The summary of additives in the recent experiments [11,13].

at.%	TiB_2	Zr	Ce	C
FA1	–	–	0.02	0.16
FA3	2.84	–	–	0.16
FA6	–	0.25	–	0.19

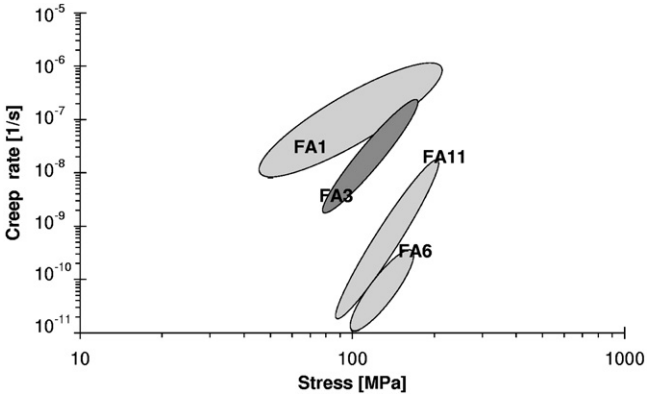

Fig. 7. The comparison of MCR at 600 °C for materials as in Fig. 6.

values for P92 (high chromium steel with ferrite matrix) are presented. The important alloying additions that can lead to particle strengthening are listed in Table 2.

For comparison of the values of MCR at 600 °C see Fig. 7. The material slightly alloyed with Zr with fine dispersion of ZrC particles is obviously the best of the compared iron aluminides. For this material also high value for TTR and for the time to 1% deformation were obtained [13].

5. Summary

- The combination of additives Zr + TiB_2 in the tested alloy does not enhance the strength.
- The strengthening by Zr appearing as ZrC fine precipitate is the determining one in the alloys denoted here as F6 and F11.
- The rest of Zr, which did not take part in the formation of the fine ZrC precipitate forms ZrB_2 phase, which segregates along the grain boundaries with zero contribution to the creep strength. The similar conclusion is valid for the HT tensile properties.
- The creep strength of both alloys (FA6 and FA11) can be compared with the chromium ferritic steel P92 up to 650 °C. The Fe28Al4Cr alloy with 0.25 Zr is recommended for the use up to 650 °C.

Acknowledgement

Financial support from the Czech Ministry of Education, Youth and Sports (projects MSM 4674788501 and MSM 0021620834) is gratefully acknowledged.

References

[1] Palm M. Intermetallics 2005;13:1286.
[2] Morris DG, Muñoz-Morris MA, Baudin C. Acta Mater 2004;52:2827.
[3] Morris DG, Muñoz-Morris MA. Mater Sci Eng 2007;A462:45.
[4] Morris DG, Muñoz-Morris MA, Chao J. Intermetallics 2004;12:821.
[5] Stein F, Palm M, Sauthoff G. Intermetallics 2005;13:1275.
[6] Cieslar M, Karlík M. Mater Sci Eng A 2007;462:289.
[7] Morris DG, Muñoz-Morris MA, Requejo LM. Acta Mater 2006;54:2335.
[8] Alven DA, Stoloff NS. Scripta Mater 1996;34:1937.
[9] Alven DA, Stoloff NS. Mater Sci Eng 1997;A239–240:362.
[10] Morris DG, Guiterrez-Urrutia MA, Muñoz-Morris MA. Scripta Mater 2007;57:449.
[11] Kratochvíl P, Málek P, Cieslar M, Hanus P, Hakl J, Vlasák T. Intermetallics 2007;15:333.
[12] Karlík M, Kratochvíl P, Pešička J, Vlasák T. Int J Mat Res 2009;100:6.
[13] Kratochvíl P, Málek P, Pešička J, Hakl J, Vlasák T, Hanus P. Kovove Mater 2006;44:185.
[14] Krein R, Schneider A, Sauthoff G, Frommeyer G. Intermetallics 2007;14:1172.
[15] Wasilkowska A, Bartsch M, Stein F, Palm M, Sauthoff G, Messerschmidt U. Mat Sci Eng 2004;A381:1.
[16] Bína V, Hakl J. Mat Sci Eng 1997;A234–236:583.

EFFECT OF CARBON ADDITION ON PHASE COMPOSITION AND HIGH TEMPERATURE STRENGTH OF Fe_3Al-TYPE IRON ALUMINIDE WITH Zr.

VODIČKOVÁ V.[1)], HANUS P.[1)], KRATOCHVÍL P.[2)], MÁLEK P.[2)]

[1)] *Department of Material Science, Faculty of Mechanical Engineering, Technical University of Liberec, Hálkova 6, 461 17 Liberec, Czech Republic, vera.vodickova@tul.cz*

[2)] *Department of Material Physics, Faculty of Mathematics and Physics, Charles University, Ke Karlovu 5, 121 16 Prague 2, Czech Republic*

Abstract

Iron aluminides of Fe_3Al type with Zr addition are studied as good high-temperature resistant materials for structural applications. Generally, Zr addition leads to formation of Laves phase in the structure of ternary alloys. Presence of these phase enhances high-temperature mechanical properties. The effect of carbon addition on the phase composition of these ternary alloys was studied. Two ordered alloys with the similar Fe, Al and Zr content and different carbon content were compared. The phase composition was studied by light optical microscopy (LOM), scanning electron microscopy (SEM) with energy dispersive analysis (EDA) and X-ray diffraction analysis (XRD). High-temperature mechanical properties are tested in tension.

Keywords: Fe_3Al type aluminides, Zr and C addition, phase structure, high-temperature mechanical properties.

1. Introduction

Ordered Fe_3Al-type iron aluminides have generally good high-temperature properties: enviromental resistance, creep resistance and H.T. strength.

The general task to enhance the H.T. mechanical properties of Fe_3Al iron aluminides may be handled by using different methods (for overview see e.g. [1]):

i) Strengthening by solid solution hardening which is useful for small ternary additions such as Cr, V, Mo and Ti,

ii) strengthening by incoherent precipitates which may be either formed due to ternary additions of Zr, Ta, Nb or Ti in higher concentrations (diverse phases originate according to high-temperature isothermal section of phase diagrams) or carbide and boride precipitates, which need additions of C or B (also as quaternary to the above mentioned elements),

iii) strengthening by coherent precipitates as one of the most effective methods (B2 in A2 and vice versa for Fe-Al-Ni-Cr alloys or $B2+L2_1$ in Fe-Al-Ta system),

iv) strengthening by increased crystallographic order which stabilizes the $D0_3$ structure to higher temperatures (e.g. Fe-Al-Ti).

In all cases, the strengthening effect depends on the temperature and on the stress at which the material is used. The determining factor for the use of the material is the stability of the microstructure at H.T.

Incoherent phases in iron aluminides are typical for the ternary Fe-Al-Zr systém. The most important phases for the hardening of iron aluminides are [2-7] phases λ_1 $(Fe,Al)_2Zr$, and, τ_1 $(Fe,Al)_{12}Zr$, see the ternary diagram in Fig. 1. Hardening effect of the mentioned phases was reported in [8,9].

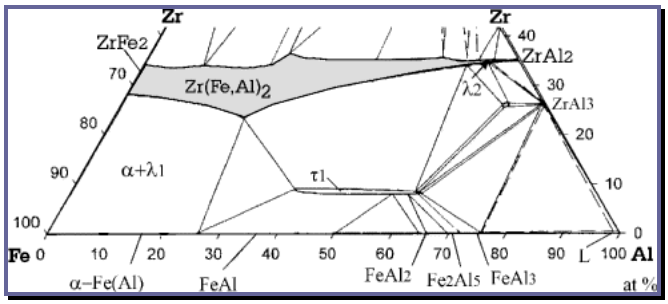

Fig. 1. Isotermal section at 800℃ of Fe-Al-Zr syst em according to [7]

If the alloy contains carbon, zirconium carbides can be formed [10]. It is the purpose of the present paper to study the effect of carbon on the hardening of the Zr alloyed iron aluminides.

2. Experimental technique

The alloy was prepared by vacuum induction melting and casting. The result of the chemical analysis is in Table 1. The structure of ingots (29x40x400 mm) was studied in as cast state and also the structure of before tension tests. For this purpose the casts were annealed at 1200℃ for 2 hours and then rolled at 1200℃ from 29 mm thickness to 13 mm in several steps with 15 % thickness reduction in one pass. After each pass between the rolls, the material was reheated to 1200℃. After machining the samples were additionally annealed at 1150℃ fo r 2h and slowly cooled in air. The samples for tensile tests (5mm in diameter, 25mm gauge length, and M12-threaded heads) have the axis parallel to the rolling direction.

Table 1.

	C	Al	Cr	Zr	Fe
GA1 [wt.%]	**0.05**	17.02	4.12	0.57	bal
GA1 [at.%]	0.2	29.74	3.74	0.3	bal
GA2 [wt.%]	**0.12**	14.90	3.88	0.51	bal
GA2 [at.%]	0.5	26.48	3.58	0.27	bal

Deformation tests were carried out at 600, 650, 700 and 800℃. Tensile tests were performed at a strain rate of 1.5 $\times 10^{-4}$ s^{-1}. During test the temperature was kept with the accuracy of 3 K.

The phase composition and structure were studied using light optical microscopy (LOM) and X-ray diffraction (XRD). The phase structure and grain boundaries were visualized using Mastermet 2 (Buehler) emulsion and subsequent chemical etching by solution (100 ml H_2O + 15 ml 38%HCl + 40 ml 63% HNO_3). Phases were also identified by electron probe microanalysis (scanning electron microscope TESCAN equipped with an energy-dispersive X-ray spectrometer (EDX) Bruker. The phases were identified by XRD (XRD7-FPM Seifert).

3. Results and discussion

3.1 The characterisation of the structure

The typical as cast structure of alloy GA1 are non equiaxed grains with second phase along the grain bounderies, see Fig. 2. SEM image in BSE mode provided better imaging of this phase, Fig. 3. The phase was identified by X-ray diffraction (Fig. 5) as Laves phase $Zr(Fe,Al)_2$ /white area/ and eutecticum mixture of Laves phase $Zr(Fe,Al)_2$ and matrix (solid solution α) respectively /white-gray area/ - see the detail of phase in Fig. 4. (Note to Fig. 5: The peaks are slightly shifted due to Al presence.)

The structure of GA1 alloy prior to deformation is characterized by second phase particles inside of grain and along boundaries, see Fig. 6. The eutectic configurations disappeared during the annealing and rolling.

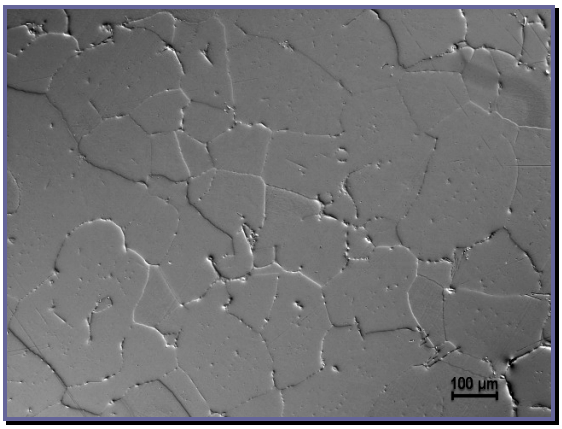

Fig. 2. The structure of alloy GA1, as cast state (LOM)

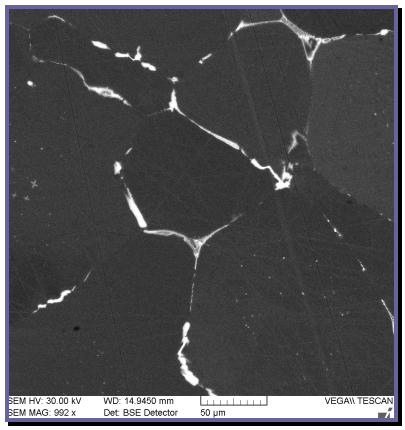

Fig. 3. The distribution of Laves phase $Zr(Fe,Al)_2$ in GA1 along grain boundaries (BSE)

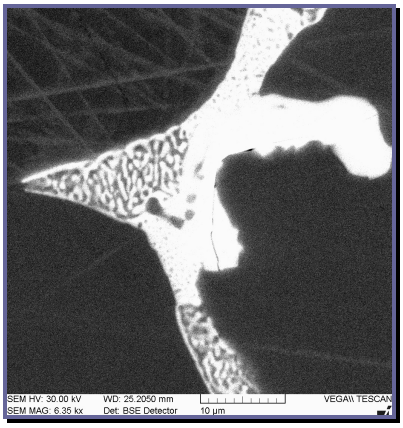

Fig. 4. Laves phase $Zr(Fe,Al)_2$ detail, (SEM, BSE image)

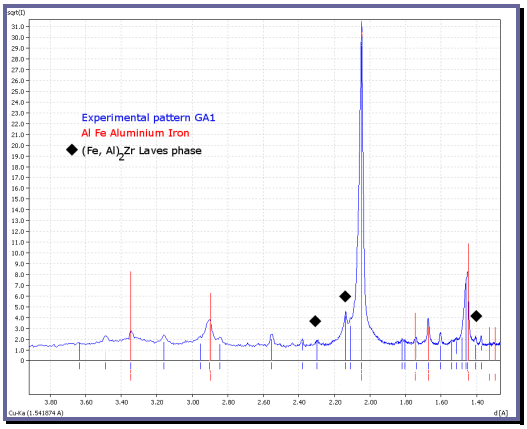

Fig. 5. The diffraction curve of alloy GA1 as cast state

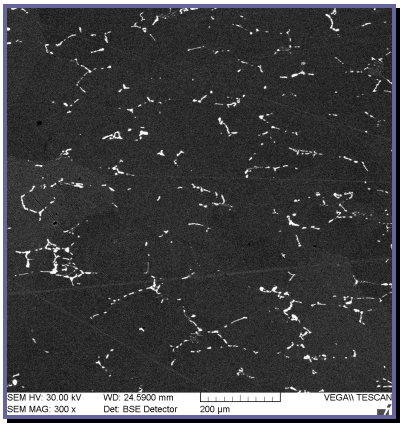

Fig 6. The distribution of particles in GA1 prepared for deformation (SEM, BSE image)

The as cast structure of alloy GA2 is in Fig. 7, 8. The particles are distributed inside of grains and along of grain bounderies too. There are two types of particles in the matrix (Fig. 9 a,b) - rod like (length about 8-20 µm) and cubic particles (diagonal > 10 µm). EDX analysis determined both types as zirconium carbide ZrC. This result was confirmed by XRD – Fig.10. Particles are uniformly distributed inside of grains after rolling and annealing at 1150℃/2h. The type of particles (ZrC) after rolling and annealing is the same as in the as cast material.

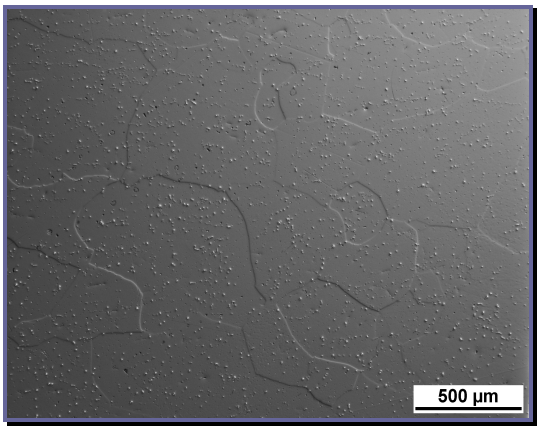

Fig. 7. Structure of the as cast GA2 (LOM)

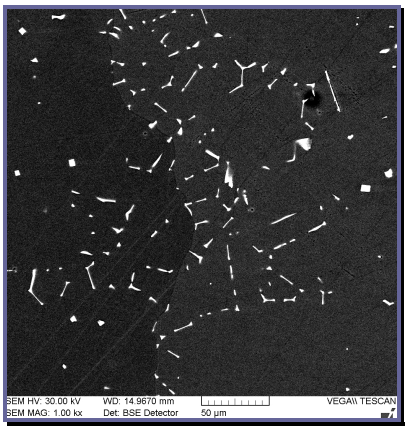

Fig. 8. Structure of the as cast GA2 (BSE)

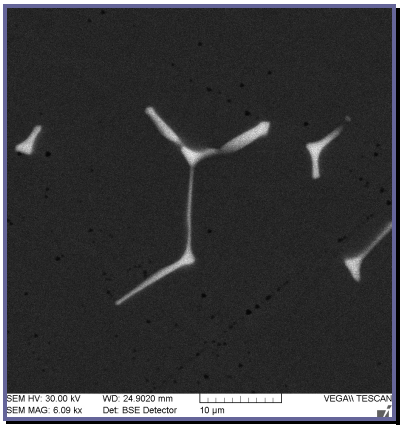

Fig. 9a. The rod type particles in as cast GA2 (BSE)

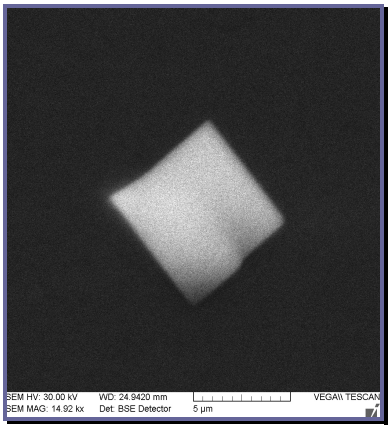

Fig. 9b. The cubic particle in as cast GA2 (BSE)

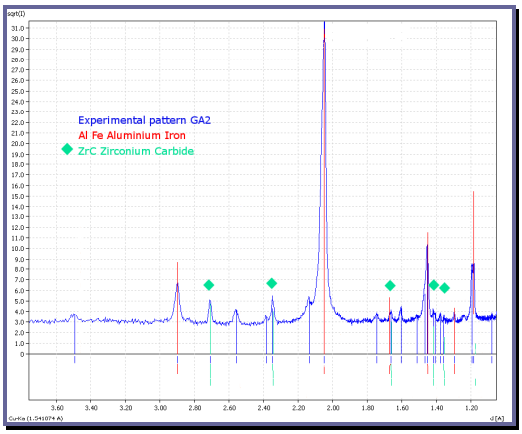

Fig. 10. The diffraction curve of alloy GA2 as cast state

3.2 Yield stress 0.2 at high temperatures

The high temperature yield stress $R_{p0,2}$ was measured in range 600 - 800°C. The values are compared for both materiále in Table 2 and in Fig.11.

Table 2. Temperature dependence of $R_{p0,2}$ for tested materials

	GA1	GA2
Temperature	**Rp0.2**	**Rp0.2**
[℃]	**[MPa]**	**[MPa]**
600	298	288
650	252	232
700	227	186
800	175	68

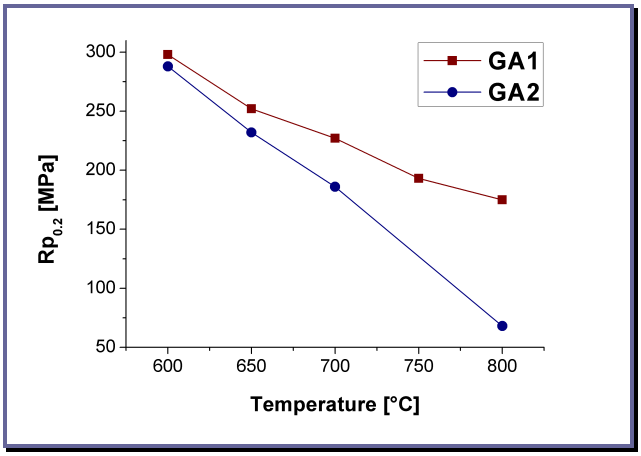

Fig. 11. The temperature dependence of yield stress $R_{p0,2}$

The values of the yield stress $R_{p0,2}$ for the material with lower carbon content (GA1) are in the whole temperature interval higher. The carbon present in alloy GA1 corresponds to the low content of carbon in the pure iron, which was used for preparing the alloys. The behaviour of Zr during melting corresponds to the chemical afinity to C. The a very fine dispersion of tiny ZrC precipitates originates as obstacle to dislocation motion. Appearing of such obstacles was already described in a material

with very simmilar composition [11] and very similar values of the yield stress. Large particles of the Laves phase $Zr(Fe,Al)_2$ have no influence on the strentgh: a) the contribution to Hall-Petsch stress is small due to the great size of the grains (more than 100 μm), b) the distance between the great particles within the grains is high to contribute by the Orowan stress.

The situation in material G2 is different: There is more carbon available for the formation of ZrC, starting at 700°C the fine particles of ZrC phase coarsen. The distribution of wide spread coarse particles makes not an efficient obstacle for the dislocation motion. The strength of this material fall down more quickly with the further decreasing temperature.

Conclusion

1. The carbon iniciates the formation of ZrC. If the any Zr remains, it forms λ_1 $(Fe,Al)_2Zr$, while Zr is not soluble in α-FeAl. If sufficient amount of carbon is available no λ_1 $(Fe,Al)_2Zr$ is appearing.
2. The distribution of fine ZrC precipitite is very efficient in enhancing the mechanical properties at H.T. Coarsening of ZrC precipitate at H.T. leads to the softening of the material.
3. λ_1 $(Fe,Al)_2Zr$ does not contribute to the hardening in the configuration and amount present in the tested alloys. It is supposed the fine ZrC precipitate determines the H.T. mechanical properties of material GA1.

Acknowledgements

This research was supported by Grant Agency of the Czech Republic through the project No. 106/08/P005 and by Ministry of Education of the czech Republic under numbers MSM 4674788501.

References

[1] M. Palm, *Intermetallics* 13 (2005), p. 1286-1295

[2] V.V. Burnashova, V.Ya. Markiv, Dopov. Akad. Nauk RSR Ser A 69 (1969) 351

[3] V. Raghavan, Phase Diagrams of Ternary Iron Alloys, Part 6, Indian Institute of Metals, Calcutta, India, 1992, p.224

[4] F. Stein, M. Palm, G. Sauthoff, in: R. Kopp (Ed.), Werkstoffwoche ´98, bandVI, Met. Symp. 14,Simul. Met.Wiley-VCH Verlag Gmbh, Weinhein, Germany

[5] G. Sauthoff. *Intermetallics* 8 (2000), p. 1101

[6] F. Stein, G. Sauthoff and M. Palm. *J. Phase Equilib.* 23 6 (2002), pp. 480–494.

[7] A. Wasilkowska, M. Bartsch, F. Stein, M. Palm, K. Sztwiertnia, G. Sauthoff, U. Messerschmidt, *Mat. Sci. Eng.* A 380 (2004), p. 9-19

[8] A. Wasilkowska, M. Bartsch, F. Stein, M. Palm, K. Sauthoff, U. Messerschmidt, *Mat. Sci. Eng.* A 381 (2004), p. 1-15

[9] F. Stein, M. Palm, G. Sauthoff, Intermetallics 13 (2005), p. 1275-1285

[10] Cieslar M, Karlík M. *Mater Sci Eng A 2007;462:289*.

[11] P. Kratochvíl, P.Málek, M.Cieslar, P.Hanus, J.Hakl, T.Vlasák,. *Intermetallics 15 (2007), p.333*

Materials Science and Engineering A 548 (2012) 175–182

Contents lists available at SciVerse ScienceDirect

Materials Science and Engineering A

journal homepage: www.elsevier.com/locate/msea

Microstructure and high temperature mechanical properties of Zr-alloyed Fe_3Al-type aluminides: The effect of carbon

P. Kratochvíl[a], F. Dobeš[b,*], J. Pešička[a], P. Málek[a], J. Buršík[b], V. Vodičková[c], P. Hanus[c]

[a] Department of Physics of Materials, Faculty of Mathematics and Physics, Charles University, Ke Karlovu 5, 121 16 Prague 2, Czech Republic
[b] Institute of Physics of Materials, Academy of Science of the Czech Republic, Žižkova 22, 616 62 Brno, Czech Republic
[c] Department of Material Science, Faculty of Mechanical Engineering, Technical University of Liberec, Hálkova 6, 461 17 Liberec, Czech Republic

ARTICLE INFO

Article history:
Received 21 November 2011
Received in revised form 20 March 2012
Accepted 26 March 2012
Available online 12 April 2012

Keywords:
Electron microscopy
Mechanical characterization
Intermetallics
Precipitation

ABSTRACT

The effect of the additives Zr and C on the phase composition and high temperature (H.T.) mechanical properties of Fe_3Al-type alloys is investigated. The presence of phases is related to the ratio of zirconium and carbon in the alloy. The presence of Laves phase λ_1 $(Fe,Al)_2Zr$ particles is governed by the relationships seen in the ternary phase diagram for Fe–Al–Zr, while the appearance of ZrC carbide particles is due to the affinity of Zr for C. The presence of tiny metastable phase particles, identified as $(Fe_{1-x}Al_x)_3Zr$ and Fe_2Zr, affects the H.T. tensile and creep properties of the alloys.

1. Introduction

Enhancing the good H.T. mechanical properties of Fe_3Al-type alloys can be achieved using a variety of methods (for an overview, see e.g. [1,2]). An especially effective method is based on the addition of elements with a low solubility in the Fe_3Al-matrix. From this point of view, the alloying by zirconium may be of interest because nearly no solid solubility for Zr exists in the Fe–Al phases. This idea initiated several investigations of the influence of Zr-additions to Fe–Al alloys. We will leave aside the large additions of Zr (i.e. up to 30% [3–5]) as well as additions to alloys based on FeAl with B2 lattice [6–9] or to ferritic Fe–Al alloys [10]. The beneficial effect of zirconium addition on creep resistance was first reported in a series of papers by McKamey and Maziasz [11–13]. The results obtained in a complex alloy FA-180 containing 28Al, 5Nb, 0.8Mo, 0.025Zr, 0.05C, 0.005B (atomic percent is given throughout) are summarized in [13]. The annealing for 1 h at 1150 °C followed by quenching was successfully used to obtain the longest creep rupture live and the slowest minimum creep rate in creep tests at 593 °C. The microstructural analysis revealed that the strengthening was due to a dispersion of fine Nb- and Zr-rich carbides in the matrix and along grain boundaries.

Zirconium was tested as an additive to Fe_3Al-type iron aluminide to enhance the high temperature tensile and creep properties by Kratochvíl et al. [14,15] (the alloy was 31.5Al, 0.25Zr, 3.5Cr, 0.2C). The tensile strength at 600 °C was determined by solid solution hardening. The formation of Zr–C particles, which contributed to improvement of tensile creep properties, was described. After creep at 600 °C, the material contained coarse Zr-rich particles with a cubic structure, which were identified as Zr-carbides [16]. The dislocations were locked by tiny precipitates. These precipitates were not identified due to their small size (~10 nm). The crystal structure of the Zr–C particles in this material was further investigated by Cieslar and Karlík [16]. Addition of Zr suppressed the precipitation of hexagonal Cr–Fe–C carbides. Instead, cubic Zr carbides were formed during hot rolling. Two types of particles were observed, with the same crystal structure but different sizes. The smaller ones having the diameter around 50 nm were stable up to 1150 °C. At this temperature they dissolved or transformed into coarser particles with the same structure. Coarse Zr-carbides were very stable and did not dissolve, even at 1350 °C. Analysis of the creep results by means of the threshold stress [15] and the internal stress concepts [17] did not indicate the efficiency of second-phase particles as obstacles against dislocation motion at temperatures above 650 °C.

Karlík et al. [18] studied the creep of the Fe_3Al-type aluminide with 29.5Al, 2.35Cr, 0.63Zr and 0.2C at temperatures up to 800 °C. The large Laves phase particles composed of λ_1 $(Fe,Al)_2Zr$ and of ZrC (2–5 μm) were identified, together with a dispersion of tiny particles (~10 nm). These tiny particles contained Zr and were assumed to be zirconium carbides. If the amount of carbon in Fe_3Al-type aluminide alloyed by Zr is great, κ-carbide $Fe_3AlC_{0.5}$ is observed [19].

For the alloys without carbon, i.e. pure Fe–Al–Zr alloy, incoherent phases in iron aluminides are typical. The most important

* Corresponding author. Tel.: +420 532290408; fax: +420 541218657.
E-mail address: dobes@ipm.cz (F. Dobeš).

0921-5093/$ – see front matter © 2012 Elsevier B.V. All rights reserved.
http://dx.doi.org/10.1016/j.msea.2012.03.103

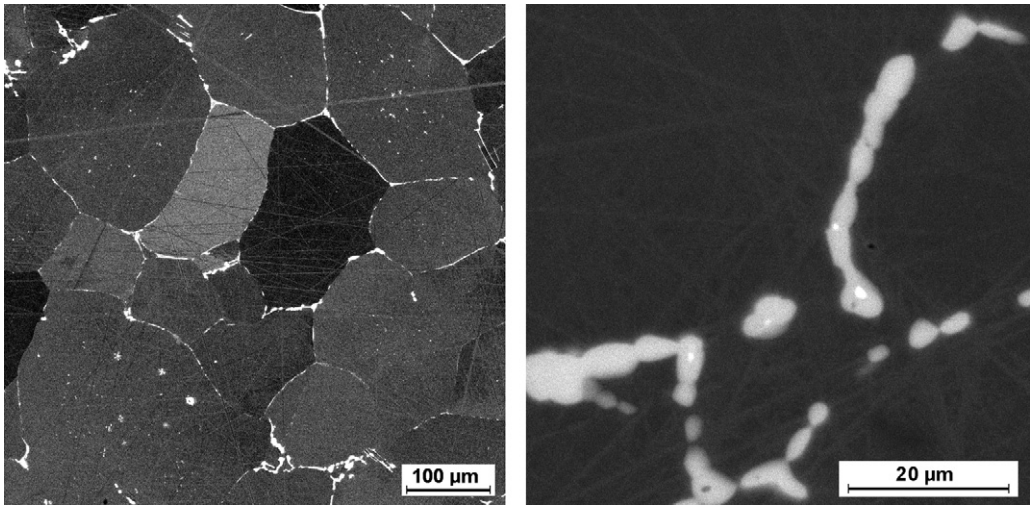

Fig. 1. Microstructure of alloy 1A after rolling and annealing. SEM using back scattered electrons. ZrC nuclei in the Laves phase are presented in the right part.

phases for the strengthening of Fe_3Al-type alloys are λ_1 $(Fe,Al)_2Zr$ and τ_1 $(Fe,Al)_{12}Zr$ (see the ternary diagram in [5]). Recently Kratochvíl et al. [20] studied the microstructure and strength of Fe–30Al–*x*Zr alloys ($x = 0.4$–5.0). The alloys contained both λ_1 and τ_1 phases in comparison to the alloys tested in [3–5], which were the two-phase alloys either with λ_1 or with τ_1.

Zr-containing Fe–Al alloys without carbon were also studied by Morris et al. [21,22]. The ferritic alloy (20 at.%Al) [21] contained 0.5 at.%Zr and 5.0 at.%Cr (the presence of carbon was not reported). $Fe_3(Al,Zr)$ precipitates with small amount of dissolved Cr were identified after mechanical testing at temperatures up to 900 °C. Two Fe_3Al-type aluminides were alloyed with Zr and B [22]. After creep and compression tests at 700 °C the phases were ZrB_2, Laves phase λ_1 $(Fe,Al)_2Zr$ and $Fe_3(Al,Zr)$.

The present research investigated only low-level alloying (up to 1.0% Zr, but at least one order of magnitude greater than in [13]) to induce the formation of a fine dispersion of particles within the alloy matrix. This paper studies the effect of the $c(Zr)/c(C)$ ratio on the microstructure and high-temperature mechanical properties of Fe_3Al-type aluminides. Two cases are distinguished: materials with excess Zr and those with excess C. An exact knowledge of the nature of the particles can contribute to the improvement of creep resistance at high temperatures.

2. Experimental

The composition of the studied alloys is given in Table 1. The Zr and C contents in alloy 1A are very similar to the alloy tested in [14], with $c(Zr)/c(C) > 1$. Alloys 2A and 4A have higher C content and hence, a $c(Zr)/c(C) < 1$. Because of the very good H.T. tensile and creep properties of the material in [14], the hypothesis was that an increase in the $c(C)$ would enhance the H.T. mechanical properties of this type of iron aluminide.

The effect of Al on the strength at high temperatures (600–800 °C) is negligible [23]. Since also the high-temperature creep strength of iron aluminides had been found to be independent of aluminium concentration [24], the deviation in concentration of Al in the alloy 1A was not corrected. The Cr addition was made since this may improve room-temperature ductility [25] and its presence is important for the application of investigated materials. The influence on the creep resistance is probably only marginal.

Table 1
Composition of alloys (at.%).

Alloy	Al	Zr	Cr	C	$c(Zr)/c(C)$
1A	29.7	0.3	3.7	0.2	1.5
2A	26.5	0.3	3.6	0.5	0.6
4A	26.5	0.2	2.8	0.6	0.3
Ref. [14]	31.5	0.25	3.5	0.2	1.25
Ref. [18]	29.5	0.63	2.35	0.2	3.15

The alloys were prepared by vacuum induction melting and casting. The casts (29 mm thick) were rolled at 1200 °C to 13 mm in several steps, with a 15% thickness reduction in one pass. After each pass, the material was reheated to 1200 °C. The tensile test samples (5 mm in diameter, 25 mm gauge length, and M12-threaded heads) had a parallel axis to the rolling direction. After machining, the samples were annealed at 1150 °C for 2 h and subsequently cooled in the air before deformation testing.

Deformation tests were carried out at 600, 650, 700 and 800 °C. Tensile tests were performed at a strain rate of $1.5 \times 10^{-4}\ s^{-1}$. During the test, the temperature was maintained within 3 K of the set temperature. Creep tests were performed in uniaxial compression on spark-machined samples of dimension 12 mm × 5 mm × 5 mm. Tests were performed under a constant load in a protective atmosphere of dry purified argon. The test temperature was held constant within ±1 K for each individual test. Specimen shortening was measured using a linear variable displacement transducer. The samples were subjected to stepwise loading, where the load changed to a new value after the steady-state creep rate had been established for a given load. The terminal values of the true stress and strain rate were evaluated for each respective step.

The phase composition and microstructure were studied using light optical microscopy (LOM) and X-ray diffraction (XRD). The phase structure and grain boundaries were visualized using Mastermet 2 (Buehler) emulsion. Phases were also identified by electron probe microanalysis (scanning electron microscope (TESCAN) equipped with an energy-dispersive X-ray spectrometer Bruker (EDS)). A transmission electron microscope (TEM) (JEOL 2000FX) with selected area electron diffraction (SAD) was used to study the dislocation structure. The samples for TEM were electrolytically twin-jet polished in 20% HNO_3 in methanol at −30 °C.

3. Experimental results

3.1. Microstructure of alloys

3.1.1. Alloy 1A

Laves phase λ_1 $(Fe,Al)_2Zr$ particles are observed mainly along grain boundaries and inside the grains as elongated particles of the

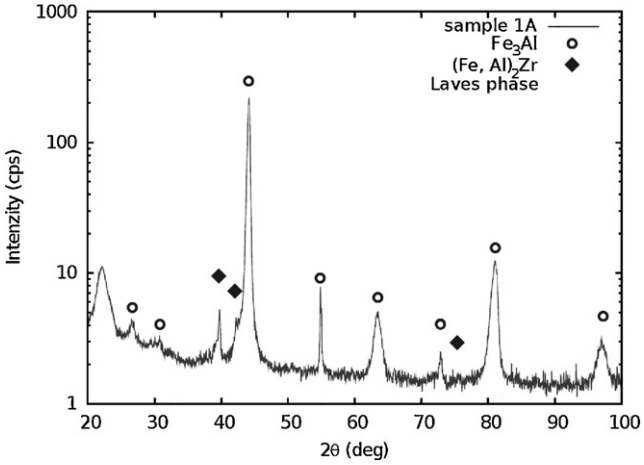

Fig. 2. XRD diffraction line for alloy 1A.

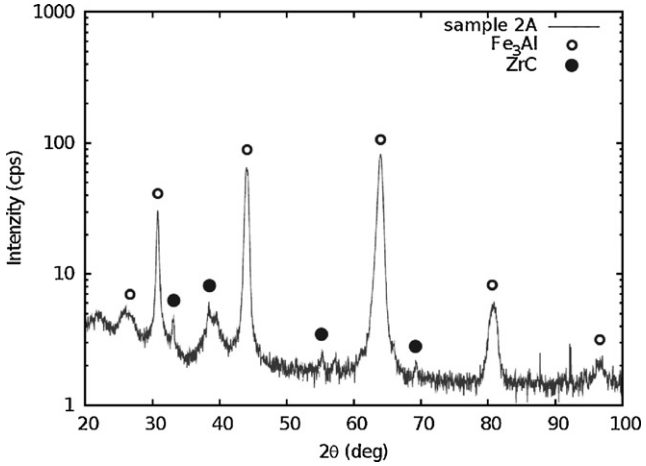

Fig. 4. XRD diffraction line for alloy 2A.

cross section ~5 μm (Fig. 1). The ZrC particles were identified using EDS as nuclei that start the formation of the Laves phase λ_1 (see Fig. 1). The structure of the Laves phase λ_1 was confirmed by XRD (Fig. 2). The volume fraction of ZrC is too small to be detected by XRD.

3.1.2. Alloys 2A and 4A

The composition of alloys 2A and 4A is nearly the same. As a result of the increase of the concentration of carbon, no Laves phase λ_1 appears in these alloys. ZrC particles are distributed inside grains and along the grain boundaries. Two types of large ZrC particles are observed: rodlike particles (length about 8–15 μm) and cubic (edge length > 10 μm) particles (Fig. 3). The type of the particles was verified by XRD (Fig. 4).

3.1.3. Overview

The ratio of $c(Zr)/c(C)$, see Table 1, determined the phase composition of the studied alloys. This was valid for both undeformed and deformed alloys. Zirconium, which is not soluble in Fe–Al alloys (see ternary phase diagram for Fe–Al–Zr [5]), either reacts with C to form carbide ZrC [18] or forms a Laves phase λ_1 $(Fe,Al)_2Zr$. In alloys with a ratio of $c(Zr)/c(C) > 1$, the major phase is the Laves phase λ_1 $(Fe,Al)_2Zr$ and the minor phase is ZrC. The low carbon concentration is due to the iron used to prepare the alloys. Therefore the amount of ZrC is very small. In alloys with $c(Zr)/c(C) < 1$, ZrC is the dominant phase. In both types of studied alloys zirconium left after the formation $(Fe,Al)_2Zr$ and/or ZrC takes part in the formation of other, sometimes metastable, phases, observed by TEM after the deformation, see below.

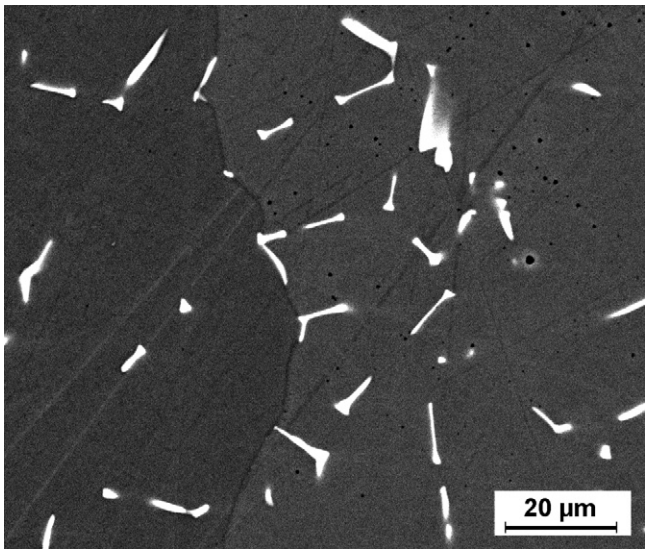

Fig. 3. Microstructure of alloy 4A after rolling and annealing. SEM using back scattered electrons.

3.2. High temperature deformation and microstructure of deformed alloys

3.2.1. Yield stress

The values of the yield stress obtained for the materials tested at H.T. are summarized in Table 2, together with the data from [14,18]. A dispersion of fine ZrC precipitates appeared as dislocation obstacles, as was previously described [14,16]. The yield stresses of the tested alloy 1A and the material in [14] (compositionally similar to alloy 1A) were very similar for temperatures between 600 and 800 °C.

3.2.2. Creep

Fig. 5 summarizes the dependence of the creep rate on stress for heat treated (annealed) alloys 1A, 2A and 4A. At all temperatures, alloy 1A was the most creep-resistant compared to the other tested materials. The behavior of alloys 2A and 4A was very similar at 600 °C and 650 °C. At 700 °C and 800 °C, the creep rate of alloy 2A was lower than that of alloy 4A. The apparent activation energy, which characterizes the dependence of the creep rate on temperature (Table 3), is about 400 kJ/mol for temperatures of 700–800 °C in all alloys and increases to almost 900 kJ/mol for temperatures of 600–650 °C in alloys 1A and 4A. The activation energy in alloy 2A at low temperatures was distinctly lower. The values of the stress exponent, n, for the series of tests are shown in Table 4. The results point to a decreasing role of particle strengthening with an increasing temperature for alloys 1A and 4A. However, the increasing role of particle strengthening may exist in alloy 2A.

Table 2
Yield stress $\sigma_{0.2}$ (MPa) at high temperatures.

T (°C)	1A	2A	4A	[14]	[18]
600	298	288	332	300	
650	252	232	284		
700	227	186	230	220	230
800	175	68	84		129

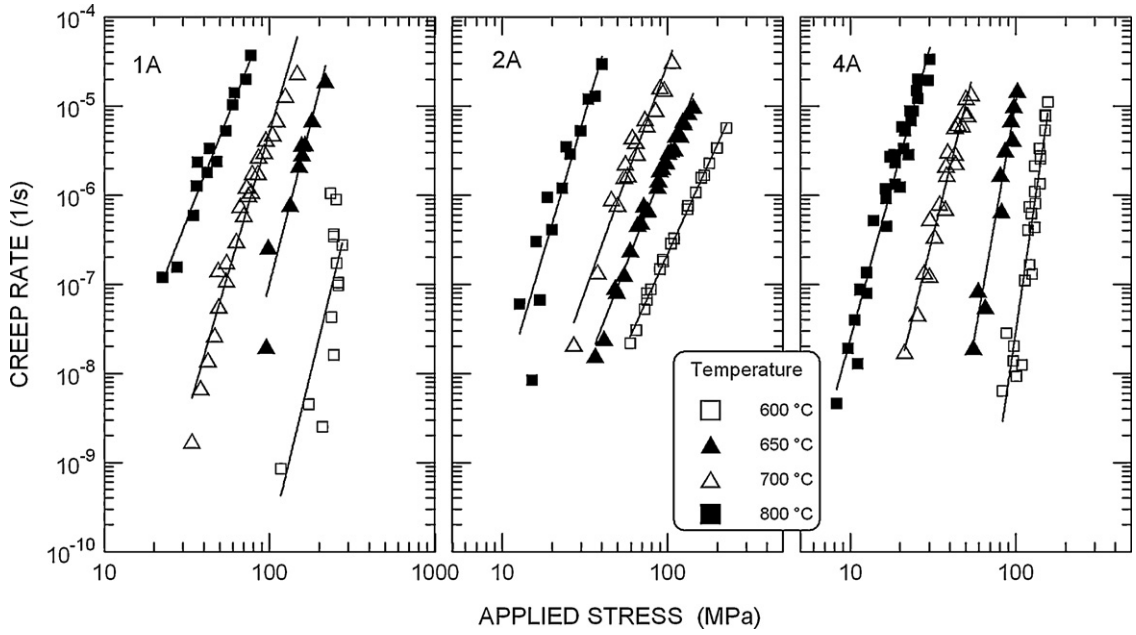

Fig. 5. Dependence of the creep rate on the applied stress separately for each tested alloy at temperatures of 600 °C, 650 °C, 700 °C and 800 °C.

Table 3
Activation energy of creep measured in annealed alloys.

Stress (MPa)	Activation energy (kJ/mol)		
	Alloy 1A	Alloy 2A	Alloy 4A
600–650 °C			
50		270	
80		310	855
100	895	330	795
150	873	365	
200	857		
700–800 °C			
30	445	394	450
50	370		
80	303		

3.2.3. Microstructure

The microstructure of deformed samples was studied at higher resolution by TEM and SAD. The microstructure of the alloy 2A after deformation was not studied extensively, since it is very similar to that of the alloy 4A. Even more phases than those described in Section 3.1 were observed. The size of the particles of these phases can be divided into two groups: large particles, which probably do not take part in the strengthening processes (obstacles for the dislocation motion) and small ones, which hinder the dislocation motion and can enhance the H.T. mechanical properties.

The character of the dislocation obstacles (size and density) controlled by diffusion processes changes at a slower rate at 600 °C than at 800 °C. Nevertheless, the particle character was not influenced by the time that the tested sample spends at the deformation temperature (approx. 2–4 h for the tensile test, and 100–900 h for the creep experiments). The phases and dislocation structures do not differ for either case of deformation in this study: H.T. tensile tests and H.T. creep tests.

Table 4
Stress exponent of creep rate in annealed alloys.

Temperature (°C)	Alloy		
	1A	2A	4A
600	7.6	4.1	12.6
650	7.2	4.8	10.6
700	6.3	5.1	7.5
800	4.7	6.2	6.8

After testing alloy samples at 600 °C and 800 °C, particles with diameters of several micrometers were observed in both alloys 1A and 4A. Their structure was found to be $Fe_{23}Zr_6$ (space group $Fm\bar{3}m$, lattice parameter 1.169 nm) (Fig. 6). The alloy 1A showed a few rodlike particles after deformation at 800 °C, which were probably metastable $(Fe_{1-x}Al_x)_3Zr$ particles (space group $Fd\bar{3}m$, lattice parameter 1.21 nm) (Fig. 7). The pure binary Fe_3Zr phase is described by the lattice parameter $a = 1.166$ nm [26]. The difference 0.044 nm is believed to be due to the presence of Al in the phase.

After deforming alloy 1A at 600 °C, no small particles were found. The dislocation structure consisted also of superdislocation partials ½⟨1 1 1⟩ pairs (Fig. 8). The type of strengthening is most

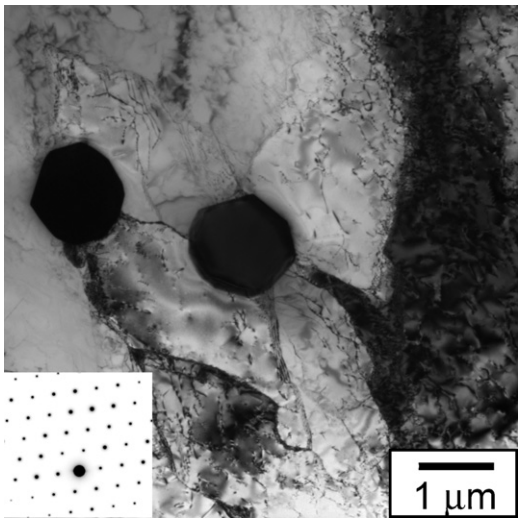

Fig. 6. Microstructure observed by TEM after creep, bright-field image. Big $Fe_{23}Zr_6$ particles were rarely observed in alloys 1A and 4A; in the left bottom corner is the diffraction pattern of these particles, identified as a pole [1 1 0].

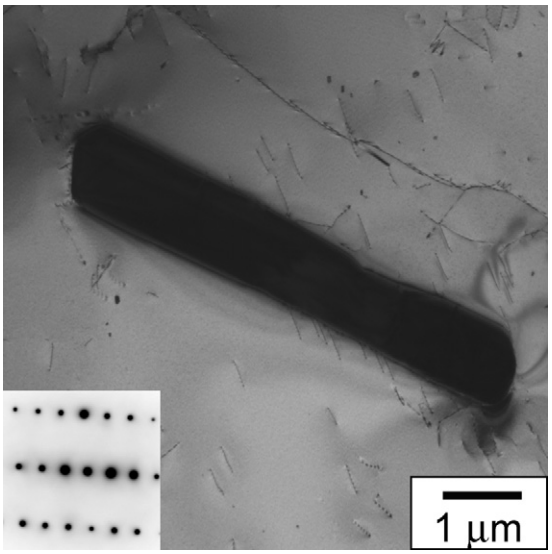

Fig. 7. $(Fe_{1-x}Al_x)Zr$ rod-like big particles were observed in alloy 1A after creep testing at 800 °C; in the left bottom corner is the diffraction pattern taken from this particle – pole [1 2 3].

likely solid solution strengthening, which is consistent with the strengthening for the nearly identical material in [14].

Two types of small particles were observed in alloy 4A after deformation at 600 °C (Fig. 9). (i) The particles' size ranged from 40 to 80 nm and they were distributed homogeneously. The particles were Fe_2Zr. Details are described below. (ii) The coherent particles (max. size of 40 nm) comprised the majority of particles in alloy 4A characterized by typical coffee-bean contrast (Fig. 9). These coherent particles contained Zr, but the corresponding diffractions were not detectable by SAD.

After deformation at 800 °C, both alloy 1A (Fig. 10) and alloy 4A (Figs. 11 and 12) had two types of detectable particles. The first one, Fe_2Zr, was only of a minor occurrence, while the second one, $(Fe_{1-x}Al)_3Zr$, was the prevailing particle type. The particle size clearly grew during deformation at 800 °C, up to 30–60 nm in alloy 1A, and even up to 0.3–0.6 μm for alloy 4A. The particles that are aligned along the dislocation (Fig. 11) had apparently nucleated on the dislocation beforehand, as the dislocation could

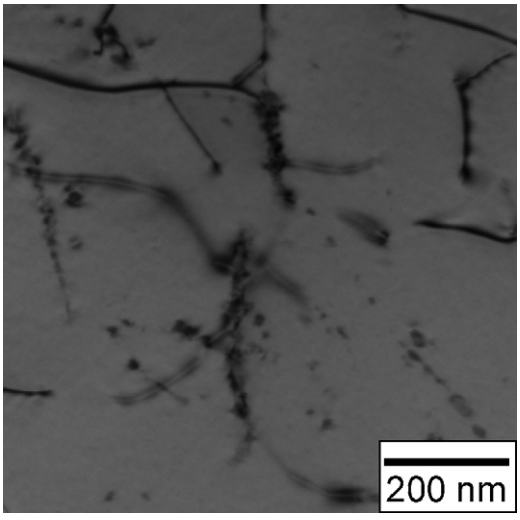

Fig. 8. Dislocations in alloy 1A crept at 600 °C. Example of dissociated superdislocations, i.e. partials ½a ⟨1 1 1⟩.

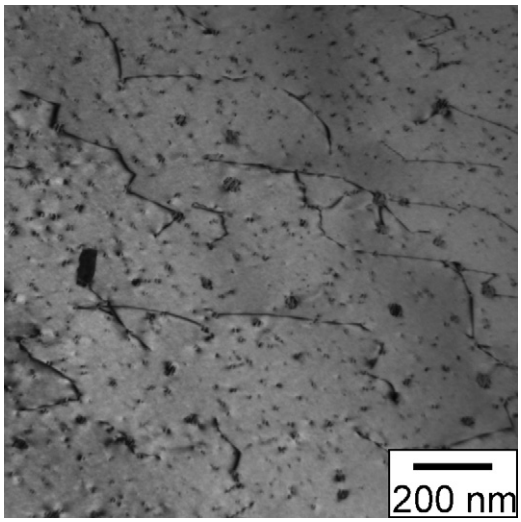

Fig. 9. Particles in alloy 4A after creep testing at 600 °C: (i) a small number of the Fe_2Zr particles and (ii) prevailing tiny coherent particles with coffee-bean contrast.

have taken part in the deformation process. The dislocation density and the density of the obstacles is lowered, meaning less particle strengthening and an increased proportion of solid solution strengthening, which corresponds to the values of the stress exponent in Table 4.

3.2.4. Overview

The following statements summarize the characteristics of the particles after deformation:

600 °C:
Alloy 1A – No small particles visible by TEM.
Alloy 4A – Rectangular particles with slightly bent sides are Fe_2Zr, a = 0.701 nm, $Fd\bar{3}m$.
Tiny coherent particles with coffee-bean contrast were not identified by SAD.
800 °C:
Alloys 1A and 4A – Two types of rectangular particles – ones with slightly bent sides are Fe_2Zr, $a = 0.701$ nm, $Fd\bar{3}m$, while the square particles with straight sides are most probably $(Fe_{1-x}Al_x)_3Zr$, estimated $a = 1.21$ nm, $Fd\bar{3}m$. The Fe_2Zr particles make up approximately 10% of all particles.

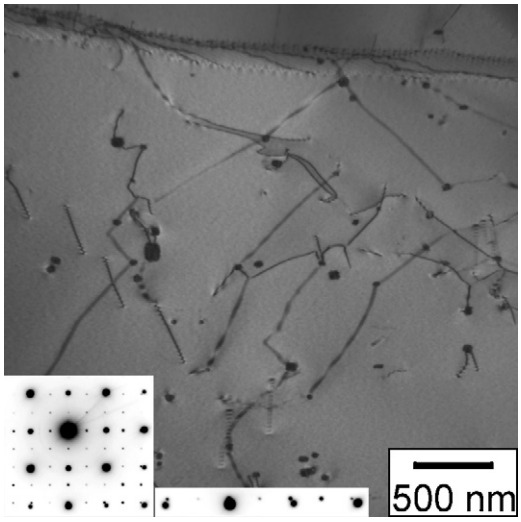

Fig. 10. Small particles in alloy 1A after creep testing at 800 °C. Two types of particles were seen: $(Fe_{1-x}Al_x)_3Zr$ and Fe_2Zr. The diffraction pattern in the left bottom corner corresponds to the $(Fe_{1-x}Al_x)_3Zr$ particle – pole [1 0 0]. The lowest row of the diffraction spots shows that positions of particle spots do not match with matrix spots.

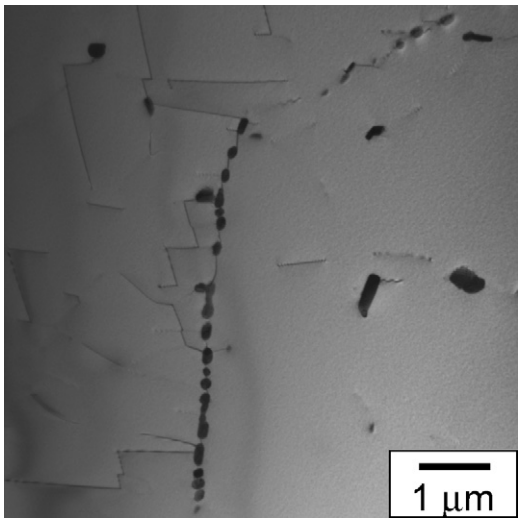

Fig. 11. Small particles in alloy 4A after creep testing at 800 °C; two type of small particles – $(Fe_{1-x}Al_x)_3Zr$ particles and Fe_2Zr particles – were sometimes aligned along dislocation lines.

4. Discussion

The phase structure of the investigated alloys was studied in two levels: first, using the LOM, SEM and XRD; and secondly, using TEM and SAD, in order to introduce two different views of the alloys' microstructure.

- The ratio of zirconium to carbon additives influences the phase structure that is predicted by the Fe–Al–Zr ternary phase diagram, as seen by SEM combined with XRD of both as-cast and hot rolled/annealed alloys. Laves phase λ_1 $(Fe,Al)_2Zr$ and ZrC large particles are situated mostly along grain boundaries, with some contained in the grains. Their strengthening role is limited to blocking both the grain boundary sliding and migration. The effect on the dislocation motion inside the grains is small owing to a large distance between these large particles.
- Investigating the H.T. deformed alloys by TEM and SAD reveals that the very small particles act as obstacles for dislocations during the H.T. deformation process. These particles are most likely formed from Zr left after generation of the carbide ZrC and Laves phase λ_1 $(Fe,Al)_2Zr$ particles. It implies that – contrary to zero solubility suggested by the phase diagram – some amount of Zr atoms remains dissolved in the lattice after casting and rolling process or after annealing at 1000 °C.

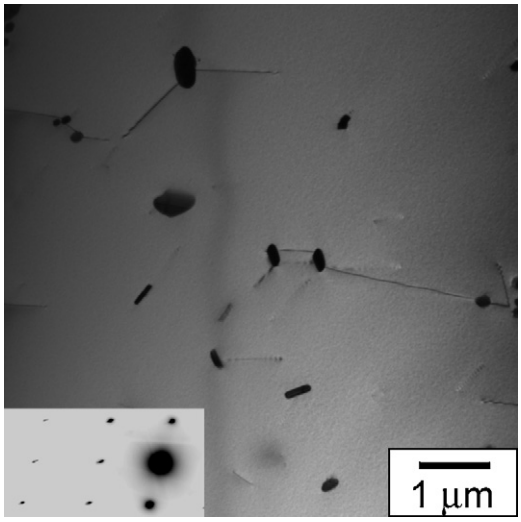

Fig. 12. Small particles in alloy 4A after creep testing at 800 °C; the diffraction pattern in the left bottom corner corresponds to the Fe_2Zr particle – pole [3 4 5].

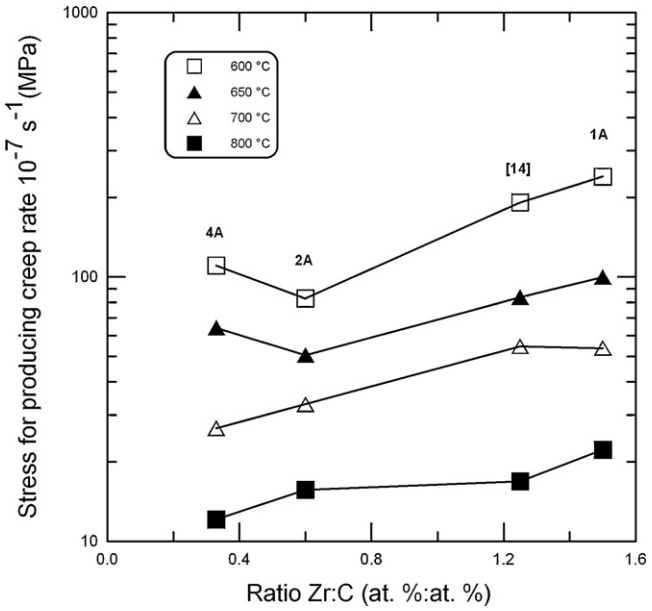

Fig. 13. The stress necessary to produce a creep rate of 10^{-7} s^{-1} as a function of c(Zr):c(C). The creep data of the similar previous alloy [14] were published in Ref. [17].

Evidence of the particles acting as the obstacles to dislocation motion was obtained by TEM and SAD. The values of $\sigma_{0.2}$ at respective temperatures correspond well to this observation. However, the values of creep stress exponent n are difficult to interpret in the same way. For example the values of n for alloy 1A at 600 °C and 650 °C correspond well to high values of $\sigma_{0.2}$ for the same material (Table 2) but are not supported by a direct observation of small particles hindering the dislocation motion. A possible explanation for this phenomenon may be that (together with the solid solution hardening expected on the base of TEM results) the very small coherent and incoherent particles were not able to be resolved during TEM observation.

The main task of the present investigation was to study the influence of combined C and Zr additives on the Fe_3Al-type alloy. The effect of concentration for both additives is clear, governed by the relationships shown in the ternary Fe–Al–Zr phase diagram: the formation of Laves phase λ_1 $(Fe,Al)_2Zr$ particles is due to the near zero solubility of Zr in Fe–Al alloys, which is the case for alloy 1A. Carbide ZrC forms either before or during the formation of Laves phase, due to the very high affinity of Zr for C. This explains alloys 2A and 4A, as well as the appearance of ZrC nuclei in particles of λ_1 $(Fe,Al)_2Zr$ in alloy 1A (see Fig. 1).

The effect of combined C and Zr additives on H.T. mechanical properties can be assessed using the ratio of c(Zr):c(C). In Fig. 13, the stress for producing a creep rate of 10^{-7} s^{-1} is presented as a function of this ratio. A slight increase of the stress in alloys with c(Zr):c(C) > 1 is in agreement with the above documented appearance of the Laves phase and its contribution to creep resistance. The effect of large particles situated along the grain boundaries or even inside the grains to the overall strengthening of the material must be taken in account. The ratio determines also the amount of Zr available for the formation of observed metastable phases constituting the small obstacles for dislocation motion.

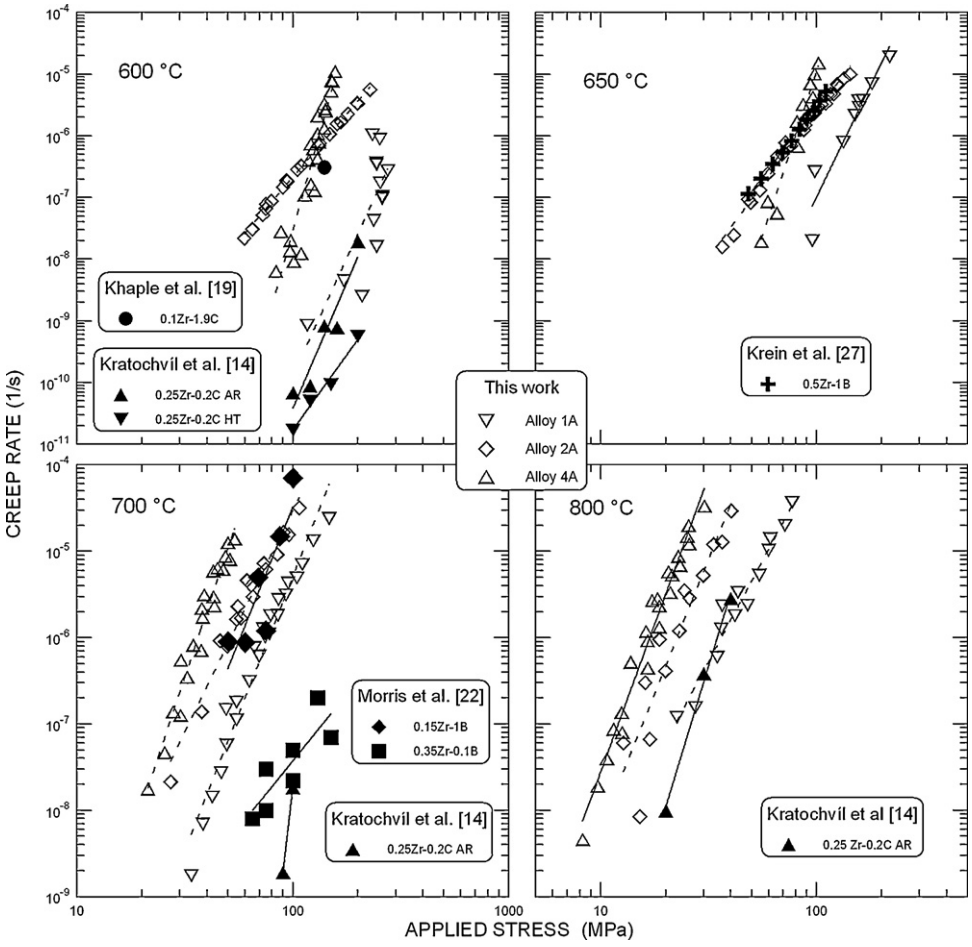

Fig. 14. The comparison, of measured creep rates for alloys 1A, 2A and 4A at temperatures of 600 °C, 650 °C, 700 °C and 800 °C, with corresponding data from the literature.

The small particles observed by TEM determine the H.T. deformation behavior of the studied alloys. The general decrease of the creep resistance and tensile strength at 800 °C compared to 600 °C (i.e. beyond that ascribed to the temperature dependence of lattice diffusion) coincides well with a pronounced increase in the size of the dislocation obstacles and their average distance. The role of solid solution hardening in creep deformation (cf. values of the stress exponent n in Table 4) and in tensile testing (Table 2) is more pronounced. The phase composition of obstacles does not agree with the phases observed on a macroscopic scale, i.e. Laves phase λ_1 $(Fe,Al)_2Zr$ and carbide ZrC. This observation most likely results from the concentration fluctuations that may originate in the alloys after the formation of equilibrium phases (Laves phase λ_1 $(Fe,Al)_2Zr$ in alloy 1A and carbide ZrC in alloy 4A). Similarly, Morris et al. [21,22] observed nonequilibrium, metastable particles that were identified as $Fe_3(Al,Zr)$ in a ferritic alloy. From the two phases that formed obstacles in the present investigation, the first one, $(Fe_{1-x}Al_x)_3Zr$, must be assumed to be metastable, while the other, Fe_2Zr, may be understood as the limit concentration of Laves phase λ_1 $(Fe,Al)_2Zr$.

It may be useful to compare the studied alloys, both to each other and with previously reported creep data of zirconium-alloyed iron aluminides [14,19,22,27] (see Fig. 14). For comparison, only alloys with similar aluminium content, i.e. between 26.5 and 30 at.% containing carbon or boron additives, respectively, were taken into account. Because different research groups use different testing temperatures, the comparison is presented accordingly.

In spite of differences in the respective investigations – i.e. tensile vs. compressive creep, alloying by carbon vs. alloying by boron, different amounts of aluminium, different heat treatment – it is clear that the creep resistance of alloys with a Zr:C or Zr:B ratio greater than 1 is superior to that of alloys with a ratio smaller than 1.

5. Conclusions

This research showed that the ratio of two additives (zirconium and carbon) influenced the phase structure of the investigated undeformed alloys in agreement with the relationships in the Fe–Al–Zr ternary phase diagram. Laves phase λ_1 $(Fe,Al)_2Zr$ and ZrC particles are found primarily along grain boundaries, with some distribution in the grains as well. Their strengthening role is limited to blocking the grain boundaries' motion because the effect of these particles inside the grains (owing to large distance between the particles) is very small.

Small particles made of two different metastable phases $(Fe_{1-x}Al_x)_3Zr$ and Fe_2Zr, which originate during the H.T. deformation, interact with dislocations and affect the mechanical properties of the alloys. The changing density and size of these obstacles with temperature explains the observed change in the materials' mechanical properties. Their effect combines with solid solution hardening and hardening by coherent particles to influence the overall mechanical properties of these alloys at high temperatures.

Acknowledgments

This work was financed by the Ministry of Education, Youth and Sport of the Czech Republic (MSM 0021620834), by the Grant

Agency of the Czech Republic (project No. 106/08/1238) and by the IMPULS project, financed by the Ministry of Industry and Commerce (FI-IM5/099).

References

[1] M. Palm, Intermetallics 13 (2005) 1286–1295.
[2] D.G. Morris, M.A. Muñoz-Morris, Mater. Sci. Eng. A462 (2007) 45–52.
[3] A. Wasilkowska, M. Bartsch, F. Stein, M. Palm, K. Sztwiertnia, G. Sauthoff, U. Messerschmidt, Mater. Sci. Eng. A380 (2004) 9–19.
[4] A. Wasilkowska, M. Bartsch, F. Stein, M. Palm, G. Sauthoff, U. Messerschmidt, Mater. Sci. Eng. A381 (2004) 1–15.
[5] F. Stein, M. Palm, G. Sauthoff, Intermetallics 13 (2005) 1275–1285.
[6] J.D. Whittenberger, M.V. Nathal, D.J. Gaydosh, Intermetallics 2 (1994) 193–200.
[7] J.H. Schneibel, E.P. George, I.M. Anderson, Intermetallics 5 (1997) 185–193.
[8] C.T. Liu, E.P. George, P.J. Maziasz, J.H. Schneibel, Mater. Sci. Eng. A258 (1998) 84–98.
[9] J. Machida, S. Kobayashi, Y. Kaneno, T. Takasugi, Mater. Sci. Forum 561–565 (2007) 399–402.
[10] R.G. Baligidad, A. Radhakrishna, J. Mater. Sci. Lett. 21 (2002) 1231–1235.
[11] C.G. McKamey, P.J. Maziasz, J.W. Jones, J. Mater. Res. 7 (1992) 2089–2106.
[12] C.G. McKamey, P.J. Maziasz, G.M. Goodwin, T. Zacharia, Mater. Sci. Eng. A174 (1994) 59–70.
[13] C.G. McKamey, P.J. Maziasz, Intermetallics 6 (1998) 303–314.
[14] P. Kratochvíl, P. Málek, M. Cieslar, P. Hanus, J. Hakl, T. Vlasák, Intermetallics 15 (2007) 333–337.
[15] F. Dobeš, P. Kratochvíl, K. Milička, Strength Mater. 40 (2008) 106–109.
[16] M. Cieslar, M. Karlík, Mater. Sci. Eng. A462 (2007) 289–293.
[17] F. Dobeš, Scr. Mater. 59 (2008) 59–62.
[18] M. Karlík, P. Kratochvíl, J. Pešička, T. Vlasák, Int. J. Mater. Res. 100 (2009) 806–810.
[19] S. Khaple, R.G. Baligidad, S. Rao, Mater. Sci. Technol. 23 (2007) 930–936.
[20] P. Kratochvíl, P. Kejzlar, R. Král, V. Vodičková, Intermetallics 20 (2012) 39–46.
[21] D.G. Morris, M.A. Muñoz-Morris, L.M. Requejo, Acta Mater. 54 (2006) 2335–2341.
[22] D.G. Morris, I. Gutierrez-Urrutia, M.A. Muñoz-Morris, Scr. Mater. 57 (2007) 449–452.
[23] C.T. Liu, V.K. Sikka, C.G. McKamey, Alloy development of FeAl aluminide alloys for structural use in corrosive environments, Oak Ridge National Laboratory Report, ORNL/TM-12199, Oak Ridge, Tennessee, 1993.
[24] J.D. Whittenberger, Mater. Sci. Eng. 77 (1986) 103–113.
[25] C.G. McKamey, C.T. Liu, Scripta Metal. Mater. 24 (1990) 2119–2122.
[26] Y. Liu, S.M. Allen, J.D. Livingson, Scripta Metal. Mater. 32 (1995) 1129–1132.
[27] R. Krein, A. Schneider, G. Sauthoff, G. Frommeyer, Intermetallics 15 (2007) 1172–1182.

Corrosion Science 63 (2012) 71–81

Contents lists available at SciVerse ScienceDirect

Corrosion Science

journal homepage: www.elsevier.com/locate/corsci

High-temperature oxidation behaviour of Zr alloyed Fe_3Al-type iron aluminide

A. Hotař [a,*], M. Palm [b], P. Kratochvíl [c], V. Vodičková [a], S. Daniš [c]

[a] Technical University of Liberec, Faculty of Engineering, Department of Material Science, Studentská 2, CZ 46117 Liberec, Czech Republic
[b] Max-Planck-Institut für Eisenforschung GmbH, Max-Planck-Strasse 1, D-40237 Düsseldorf, Germany
[c] Charles University of Prague, Faculty of Mathematics and Physic, Ke Karlovu 5, CZ 12116 Prague 2, Czech Republic

ARTICLE INFO

Article history:
Received 6 January 2012
Accepted 26 May 2012
Available online 9 June 2012

Keywords:
A. Intermetallics (based on Fe_3Al)
B. XRD
B. SEM
B. EPMA
C. Oxidation
C. Kinetic parameters

ABSTRACT

The oxidation behaviour of two Fe_3Al-based Fe–Al–Cr–Zr–C alloys has been evaluated between 900 and 1200 °C. The alloys contained either $(Fe,Al)_2Zr$ Laves phase or ZrC carbide. The alloys were oxidised for up to 1000 h in synthetic air using thermogravimetric analysis (TGA). Scales that formed on the surfaces of the sample as well as cross sections were analysed by light optical microscopy (LOM), X-ray diffraction (XRD), scanning electron microscopy (SEM), and energy-dispersive X-ray spectrometry (EDS).

At 900 °C parabolic growth and low weight gains for both tested alloys were observed. The scales are predominantly formed by Al_2O_3 with minor amounts of ZrO_2. Some Fe_2O_3 was observed after oxidation at 900 °C. At 1000 °C oxidation ingresses into the samples along grain boundaries due to preferential oxidation of the Zr-rich precipitates, becoming more severe at higher temperatures. Ingress of oxidation into the sample is more pronounced for the alloy containing ZrC where at 1200 °C it is not any longer limited to the carbide but extends markedly into the Fe_3Al matrix.

1. Introduction

Fe_3Al-based alloys have been studied as materials for high-temperature structural applications because they have low material costs (compared with corrosion and heat resistant steels), low density (5.8–6.3 g/cm^3) and a very good corrosion resistance at high temperatures in a variety of aggressive environments [1,2]. The good corrosion resistance of Fe–Al-based alloys is caused by the formation of protective α-Al_2O_3 (alumina) scales in oxidising environments [1,2]. However, depending on alloy composition (especially the Al content in the base Fe–Al), exposure time and temperature, iron oxides and metastable γ-, δ- and θ-Al_2O_3 can form. All these oxides grow faster and are more voluminous and porous than α-Al_2O_3 and are therefore less protective [3–6].

Additions of ternary alloying elements influence the mechanical properties and corrosion resistance of Fe–Al-based alloys. The addition of Cr increases ductility and ultimate strength but also increases the oxidation rate [1,7,8]. On the other hand, the oxidation resistance can be improved by addition of small Zr levels [2,9–11]. Doping of Fe_3Al with Zr results in flatter scales and the outward diffusion of Al through the scale is suppressed (for details see [12] and references therein). Specifically, it has been shown that addition of Zr in the range 0.05–0.1 at.% to Fe_3Al–Cr alloys improves the adherence of the α-Al_2O_3 scale [11,13–17]. Apparently, doping with Zr inhibits the formation of voids at the metal/scale interface [16].

The purpose of the present paper is to investigate the high-temperature oxidation behaviour of two Fe–Al–Cr–Zr–C alloys. Their composition is similar to the composition of an alloy tested in [18], which in view of its strength is promising for high-temperature applications.

2. Experimental

Two Fe–Al–Cr–Zr–C alloys were molten in a vacuum furnace and ingots were produced by investment casting. The composition of the alloys (in at.%) is given in Table 1. The ingots with dimension $30 \times 40 \times 350$ mm^3 were rolled at 1200 °C to sheets with a final thickness of 13 mm. For oxidation tests as-rolled samples with dimension $10 \times 10 \times 1$ mm^3 were cut by electrical discharge machining (EDM). The surfaces of the samples were ground to 1200 grit. The oxidation behaviour was investigated using a Setaram SETSYS 16/18 thermobalance with continuous recording of the mass gains and with a mass sensitivity of 1 μg. Samples of both alloys were oxidised in synthetic air (20.5% O_2, 79.5% N_2) at a flow rate of 1.54×10^{-6} m^3/s at temperatures from 900 to 1200 °C.

All scales and microstructures were inspected by light optical microscopy (LOM) and scanning electron microscopy (SEM). For observation of the ingress of the oxidation and the microstructures, cross sections of the samples were prepared by cutting with a precision saw and embedding them in a conductive resin. Metallographic samples were ground by diamond suspensions and

* Corresponding author. Tel.: +420 485 353 136; fax: +420 485 353 631.
E-mail address: adam.hotar@tul.cz (A. Hotař).

0010-938X/$ - see front matter © 2012 Elsevier Ltd. All rights reserved.
http://dx.doi.org/10.1016/j.corsci.2012.05.027

Table 1
Chemical composition of alloys in at.%.

Alloy	Al	Zr	Cr	C	Fe
A	29.7	0.3	3.8	0.2	Bal.
B	26.4	0.2	2.8	0.6	Bal.

subsequently polished by a suspension of non-crystallising colloidal silica. The phases in the oxide scales were determined by X-ray diffraction (XRD) and grazing incidence X-ray diffraction (GI-XRD). Measurements were performed on a Seifert XRD 7 diffractometer with Bragg–Brentano geometry using Cu Kα radiation. The compositions of the phases of the scales were evaluated

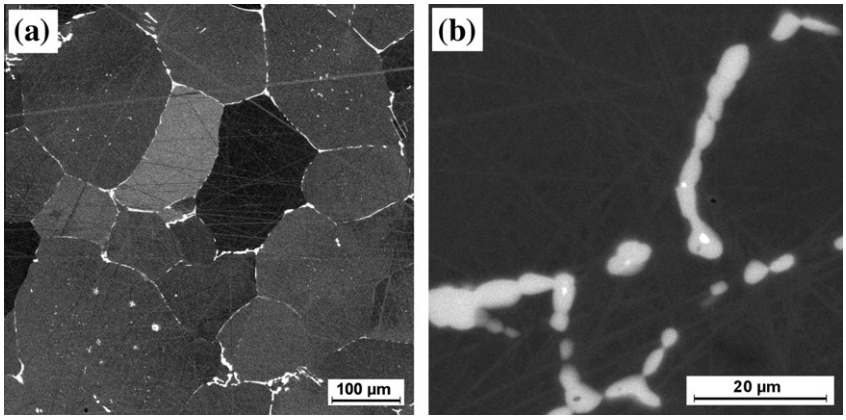

Fig. 1. SEM micrograph (backscatter electron (BSE) contrast) of alloy A (Fe–29.7Al–3.8Cr–0.3Zr–0.2C) in the as rolled condition. (a) Overview showing the Fe_3Al matrix (black) and $(Fe,Al)_2Zr$ Laves phase particles (light phase); (b) Magnification of (a) showing small ZrC nuclei (white) within the Laves phase (grey).

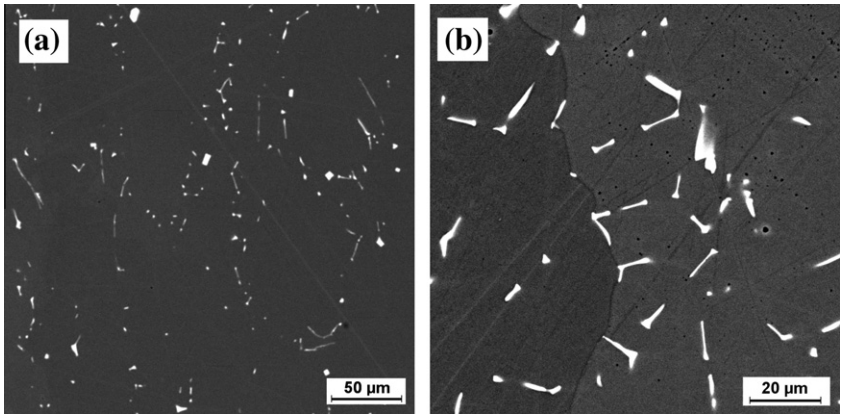

Fig. 2. SEM-BSE micrograph of alloy B (Fe-26.4Al-2.8Cr-0.2Zr-0.6C) in the as rolled condition. (a) Overview showing the Fe_3Al matrix (black) and ZrC particles (light phase) (b) Detail of ZrC particles on the grain's boundary.

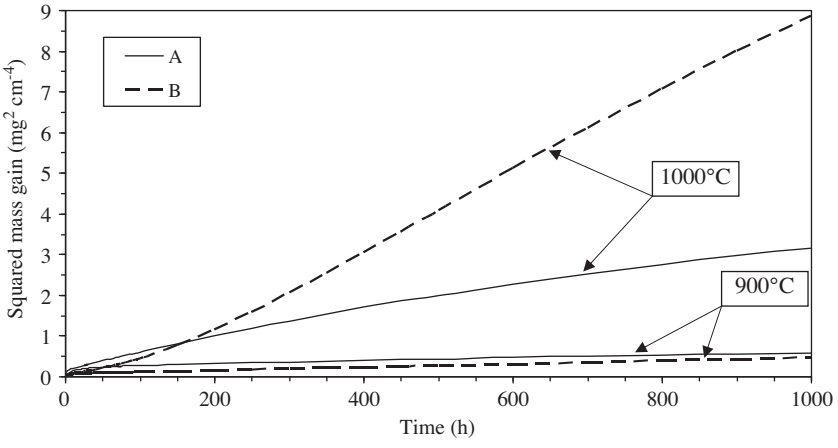

Fig. 3. Squared mass gain versus exposure time for alloys A and B at 900 and 1000 °C in synthetic air.

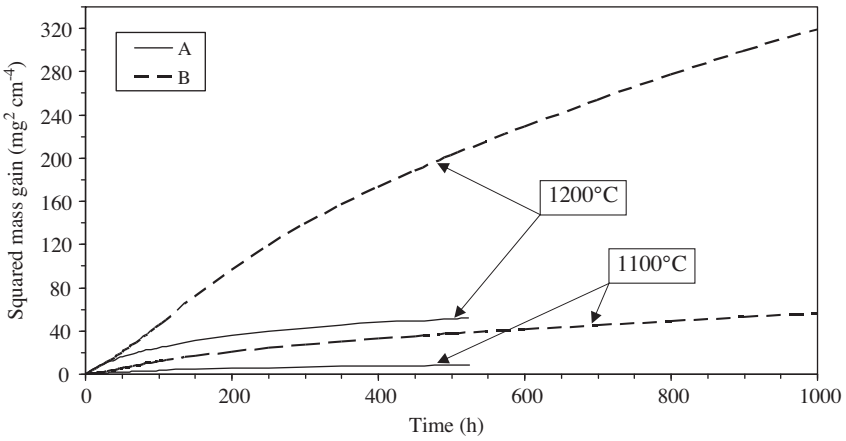

Fig. 4. Squared mass gain versus exposure time for alloys A and B at 1100 and 1200 °C in synthetic air.

Table 2
Apparent parabolic rate constants k_p of selected Fe–Al alloys oxidised in air. The current data for k_p were calculated from the TGA curves omitting the initial 200 h.

Alloy (at.%)	k_p (g^2 cm^{-4} s^{-1})				Reference
	900 °C	1000 °C	1100 °C	1200 °C	
A Fe–29.7Al–3.8Cr–0.3Zr–0.2C	8.3×10^{-14}	7.5×10^{-13}	2.7×10^{-12}	1.3×10^{-11}	This work
B Fe–26.4Al–2.8Cr–0.2Zr–0.6C	1.1×10^{-13}	[c]	1.2×10^{-11}	7.6×10^{-11}	This work
Fe–27.2Al–5.1Cr–0.1Zr[a]				6.0×10^{-12}7.4 $\times 10^{-12}$	[12][12]
Fe–28Al–5Cr–0.05Zr–0.03C[b]	–	3.3×10^{-15}	1.6×10^{-13}	6.1×10^{-12}	[11]
Fe–28Al–5Cr–0.03C[b]	–	1.4×10^{-13}	1.5×10^{-11}	3.8×10^{-11}	[11]
Fe–20Al–0.1Zr	9×10^{-14}				[20]
Fe–32Al–0.8Zr	4×10^{-13}	–	–	–	[20]
Fe–28Al–3Cr–0.02Ce	4.2×10^{-13}	–	[c]	–	[23]
Fe–30Al–4Cr–2.7TiB2	6.9×10^{-13}	–	4.3×10^{-12}	–	[23]
Fe–25Al	1.0×10^{-13}	–	–	–	[24]
Fe–27Al–15Ti	1.4×10^{-13}	–	–	–	[22]

[a] Oxidation in dry O_2.
[b] Short term oxidation for 100 h.
[c] No parabolic oxidation behaviour.

through energy-dispersive X-ray spectrometry (EDS; Bruker) on a TESCAN SEM.

3. Results and discussion

The two selected alloys have been designed for applications at high temperatures. They differ in that two different phases have been related to their corrosion behaviour. After hot rolling at 1200 °C, the microstructure of alloy A (Fe–29.7Al–3.8Cr–0.3Zr–0.2C) consists of a Fe_3Al matrix with a grain size of about 500 μm with elongated particles of the Laves phase $(Fe,Al)_2Zr$ (Fig. 1) which has been identified by EDS and XRD. The Laves phase is mostly observed along grain boundaries. Within the Laves phase light nuclei are observed which have been identified as ZrC by SEM-EDS (Fig. 1b).

The main difference in the composition of alloy B (Fe–26.4Al–2.8Cr–0.2Zr–0.6C) is a considerably higher carbon content. While the Fe_3Al matrix has about the same grain size than alloy A, alloy B does not any longer contain Laves phase but instead ZrC particles are observed. They are distributed inside the grains as well as along grain boundaries (Fig. 2).

The results of the oxidation tests performed in synthetic air at 900, 1000, 1100 and 1200 °C are summarised in Figs. 3 and 4. After an initial transition period parabolic mass gains are observed with

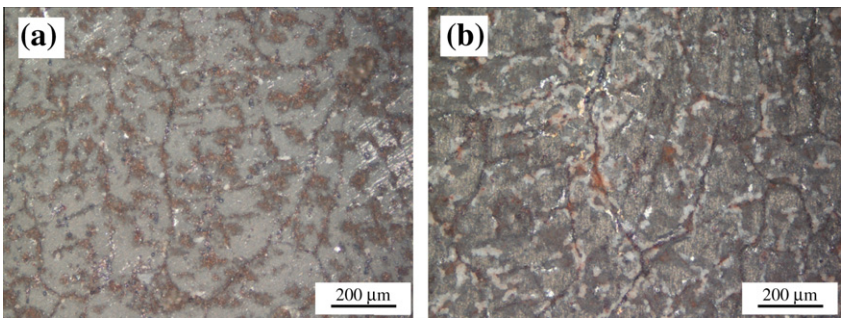

Fig. 5. LOM micrographs of scales formed on alloy A at 900 °C (a) and 1000 °C (b).

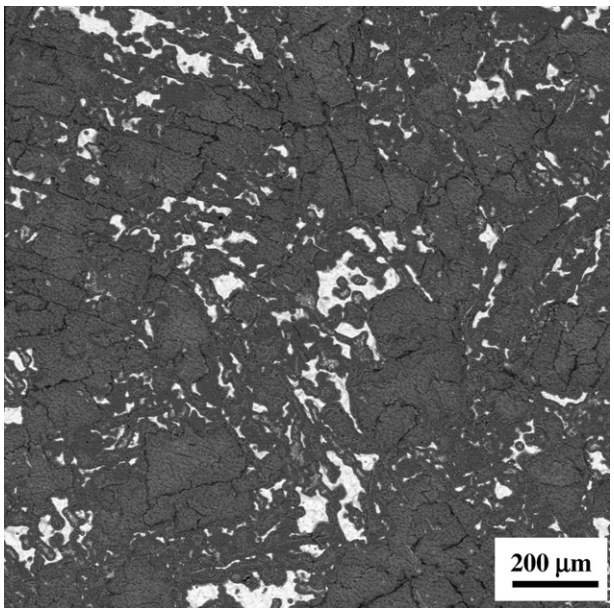

Fig. 6. SEM-BSE micrograph of the surface of alloy A oxidised at 1200 °C/500 h. The oxide scale (grey) has spalled markedly during cooling (light areas).

the exception of alloy B, where linear or even hyperbolic growth is observed at 1000 °C. With increasing temperature the mass gain increases for both alloys. However, for alloy B the increase with time is markedly higher above 900 °C than for alloy A. No drops in the mass gain curves (Figs. 3 and 4) are observed which indicates that no spallation took place during isothermal oxidation. The initial transition period, which is characterised by a higher oxidation rate, is due to the formation of transient Al_2O_3 phases [3–6]. Their transformation to α-Al_2O_3 and the effect of Zr on that is discussed in [11,19].

Parabolic rate constants (k_p) evaluated from the parabolic rate law

$$(\Delta m/A)^2 = k_p t \quad (1)$$

where $\Delta m/A$ is the weight gain per unit area (mg/cm^2) and t is the time (s) are usually employed to compare the oxidation behaviour of different alloys. Strictly, not only parabolic growth but also the formation of an even scale is a prerequisite for the determination of k_p. Because of the ingress of oxidation into the sample, determination of k_p in its true sense is not possible for the present alloys. However, in cases where no true parabolic growth of the scales has been observed but where the weight gains show a parabolic curve shape, "apparent" parabolic rate constants have been determined in order to judge the oxidation behaviour [20–22]. At 900 °C alloys A and B both have low apparent parabolic rate constants (Table 2) comparable to those of binary Fe_3Al [24] and lower than those of other Fe_3Al-type iron aluminides [20,22,23]. At higher temperatures k_p values seem to be at the high side of reported data, possibly due to increasing ingress of oxidation of the present alloys. However, data are scarce as these temperatures are already quite high for the application of Fe–Al alloys and also difficult to compare because of varying experimental conditions (Table 2).

The inspection of the scales by LOM and SEM revealed that thin adherent oxide scales formed on the surfaces of alloys A and B at 900 °C. Scales formed on alloy B at higher temperatures are dense and adherent. In contrast, scales formed on alloy A between 1000 and 1200 °C were porous and spalled easily during or after cooling to room temperature (22 °C). Fig. 5 shows LOM micrographs of the scales formed on alloy A at 900 and 1000 °C. They are dense and adherent though cooling from 1000 °C lead to the formation of cracks. In contrast, scales on alloy A oxidised at 1100 and 1200 °C spalled during cooling (Figs. 6 and 7). The element mappings in Fig. 7b–f) show that the scale mainly consists out of Al_2O_3 with small amounts of ZrO_2 scattered on top of the Al_2O_3 scale. It also reveals that Cr is only present in the matrix and does not enter into the scale in any detectable amounts.

The scales formed on alloy B during oxidation at 900–1200 °C did not spall during cooling and also they did not show cracking as was observed in case of alloy A (Fig. 5b). Fig. 8 shows the intact scale on alloy B after oxidation and cooling from 1200 °C. In contrast to the scale formed on alloy A at the same temperature (Fig. 6) the oxide scale has not spalled during cooling. SEM-EDS revealed that the scale mainly consist out of Al_2O_3 with small amounts of ZrO_2 scattered on the surface (Fig. 9), i.e. comparable to the scale that formed on alloy A at the same temperature.

Specifically the scales formed on alloy A at 900 and 1000 °C showed brown patches indicative of the presence of iron oxides (Fig. 5).

In order to characterise further the oxide scales they were analysed in detail by XRD and GI-XRD (Table 3). Scales formed on both alloys at 900 °C consisted of Al_2O_3 and minor amounts of ZrO_2 and Fe_2O_3 while at 1200 °C scales are formed by Al_2O_3 and ZrO_2 (Figs. 10 and 11). In general, while the amount of Fe_2O_3 decreases with increasing temperature the volume fraction of ZrO_2 increases (Ta-

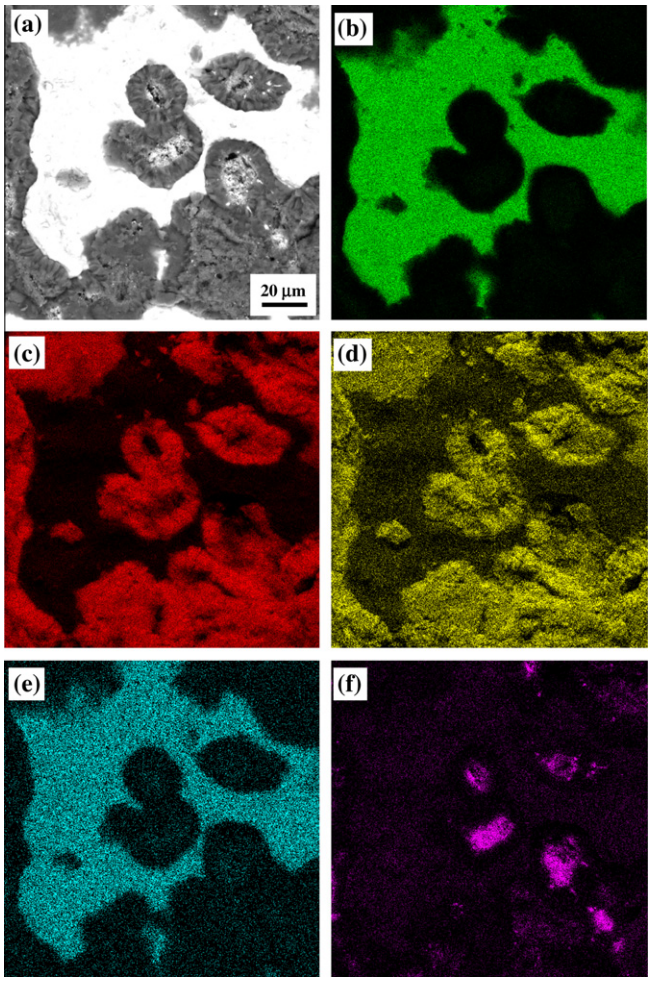

Fig. 7. SEM-BSE micrograph of the surface of alloy A oxidised at 1200 °C (a) and mappings of elements: Fe (b), Al (c), O (d), Cr (e) and Zr (f).

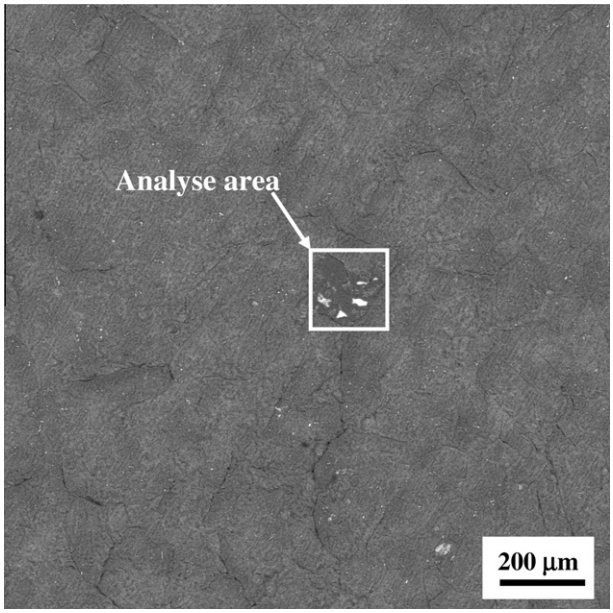

Fig. 8. SEM-BSE micrograph of the scale on alloy B oxidised at 1200 °C/1000 h. Fig. 9 shows SEM-EDS analysis of the marked area.

Table 3
Phases detected by GI-XRD (or XRD) and EDS in the oxide scales of alloys A and B after isothermal oxidation between 900 and 1200 °C.

Temperature (°C)	A	B
900	Al_2O_3, few ZrO_2, minor amounts of Fe_2O_3	Al_2O_3, few Fe_2O_3, minor amounts of ZrO_2
1000	Al_2O_3, few ZrO_2, Fe_2O_3?	Al_2O_3, ZrO_2
1100	Al_2O_3, ZrO_2	Al_2O_3, ZrO_2
1200	Al_2O_3, ZrO_2	Al_2O_3, ZrO_2

ble 3). The formation of iron oxides is typical for the initial stage of the oxidation before the thermodynamically stable Al_2O_3 can develop a continuous scale and therefore these transient iron oxides are specifically observed at lower temperatures [6,25]. It is noteworthy, that ZrO_2 is present in two polymorphs, the monoclinic and the tetragonal one. Below about 1170 °C tetragonal ZrO_2 should transform into the monoclinic polymorph by a martensitic reaction. However, it is well known that tetragonal ZrO_2 can be stabilised at lower temperatures by impurities, particle size or strain energies [26–29].

The formation of ZrO_2 maybe partly associated with enrichment in Zr at the metal/scale interface during oxidation. For Fe–28Al–5Cr–0.1Zr (at.%) Alexander et al. [30] observed such enrichment after isothermal oxidation at 1000 °C for 96 h. For an alloy of nominally the same composition oxidised at 1100 °C for 100 h Chevalier et al. [11,19] established the presence of nm-sized ZrO_2 particles located close to the scale/alloy interface through transmission electron microscopy (TEM) which hints to ZrO_2 formation by Zr enrichment at the metal/scale interface. On the other hand they also detected ZrO_2 particles near the scale/gas interface [19] which should have formed by active diffusion of Zr toward the gas interface (see [12] and Refs. therein). The present results also show the presence of ZrO_2 on the surface of the scales, i.e. at the scale/gas interface (Fig. 7).

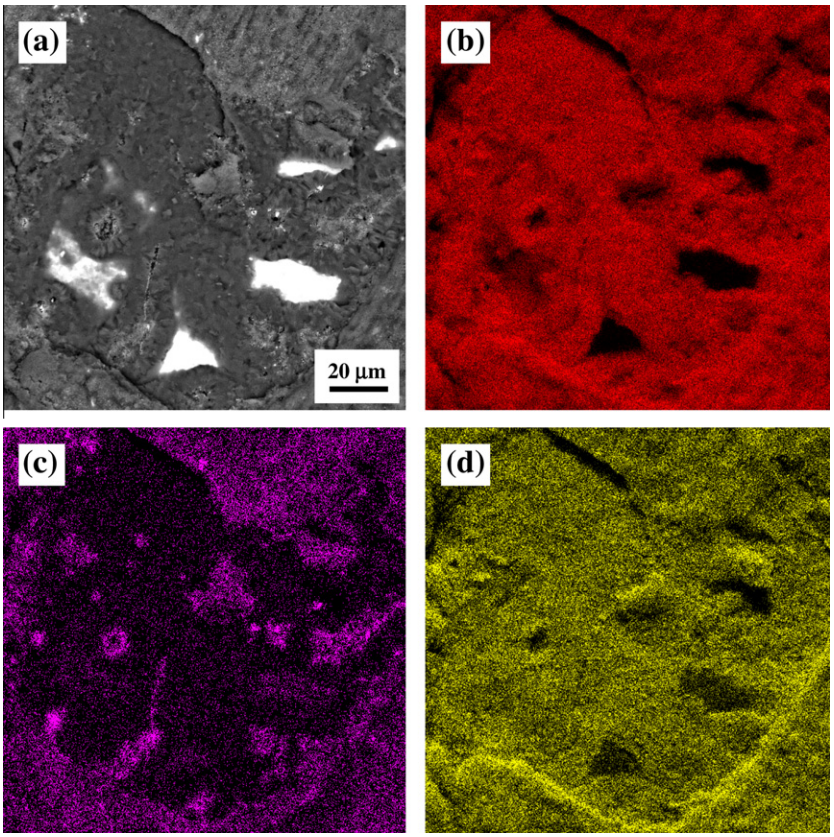

Fig. 9. SEM-BSE micrograph of the surface of alloy B oxidised at 1200 °C (a) and mappings of elements: Al (b), Zr (c) and O (d). The analysed area is marked in Fig. 8.

For alloys with low Zr contents usually only the presence Al_2O_3 in the scales has been reported, e.g. for Fe–28Al–5Cr–0.05Zr–0.03C (at.%) after cyclic oxidation at 1000 °C and cooling to RT for 500 h [15] only scales consisting out of Al_2O_3 were observed. However, in scales formed on Fe–27.2Al–5.1Cr–0.1Zr–0.04C (at.%) during cyclic oxidation between upper 1000–1300 °C and RT for up to 5000 h Pint et al. [16] observed Al_2O_3 scales with frequent ZrO_2 particles on the surface of the scales, i.e. at the gas interface. Fe–Al alloys with higher Zr contents of 0.3 and 0.8 at.% showed even larger volume fractions of zirconium oxide in the scales [31]. Therefore it is reasonable that the present alloys also show a larger volume fraction of ZrO_2 in the scales as they contain 0.2 and 0.3 at.% Zr compared to Fe–28Al–5Cr (at.%) alloys with 0.05–0.1 at.% Zr which may show scales only consisting out of Al_2O_3.

Inspection of cross sections of the oxidised samples revealed that after oxidation at 900 °C only oxide scales on the surfaces have formed while all samples oxidised at or above 1000 °C show ingress of the oxidation into the samples. For alloy A the oxidation after 1000 h at 1000 °C is limited to oxidation of Laves phase particles along grain boundaries (Fig. 12a) while after oxidation for 500 h at 1200 °C oxides protrude more frequently from the surface into the sample (Fig. 12c). Ingress of oxidation into the sample is even more pronounced in case of alloy B. Already after oxidation for 1000 h at 1000 °C oxides penetrate into the sample (Fig. 12b) and presumably this is the reason for the increased weight gain of alloy B compared to that of alloy A at the same temperature (Fig. 3). The oxides are not limited to former ZrC particles, but propagate into the Fe_3Al matrix. After oxidation at 1200 °C for 1000 h massive oxidation is observed in alloy B (Fig. 12d) where not only ZrC particles but also a large volume of the Fe_3Al matrix has already been oxidised.

The chemical composition of the oxides was analysed using SEM-EDS mappings and line scans. The EDS mapping of alloy A oxidised at 1000 °C reveals that the Zr-rich Laves phase particles at the grain boundaries are preferentially oxidised (Fig. 13). The majority of the oxide is Al_2O_3 but also some ZrO_2 is always present in the core of the oxides (Fig. 13c and d). The EDS mapping of alloy B also oxidised at 1000 °C shows the formation of Al_2O_3 and ZrO_2 as well (Fig. 14). The Zr oxide is more spread within the oxidised area, i.e. not limited to the core as observed in case of alloy A, and the oxidised areas are also larger compared to alloy A (Fig. 13). However, after oxidation at 1200 °C for 1000 h the EDS line scan (Fig. 15) reveals that also in alloy B oxidised areas are Zr rich in the core and more Al rich in the outer rim.

It has been shown before that apparently the presence of the Laves phase $(Fe,Al)_2Zr$ and the phase $(Fe,Al)_{12}Zr$ (τ_1) have a detrimental effect on the oxidation behaviour of Fe–Al–Zr alloys [20]. The current results suggest that also ZrC deteriorates the oxidation

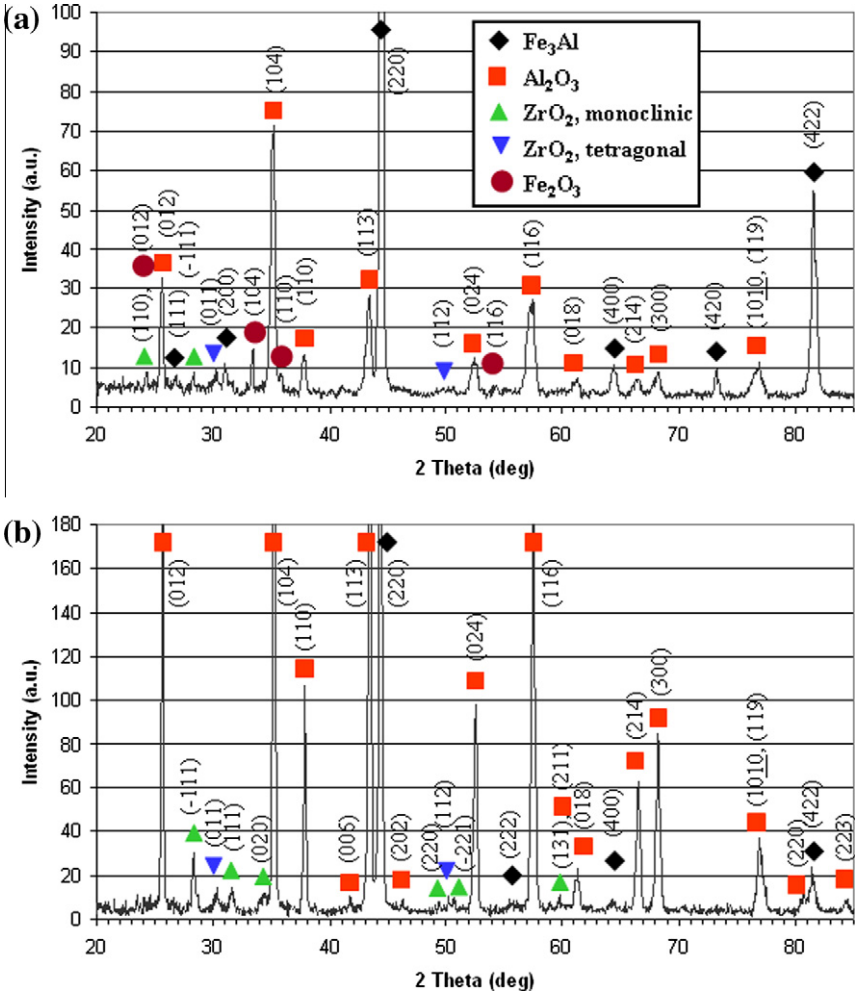

Fig. 10. XRD patterns of the oxidised surface of alloy A after oxidation at 900 °C/1000 h (a) and 1200 °C/500 h (b).

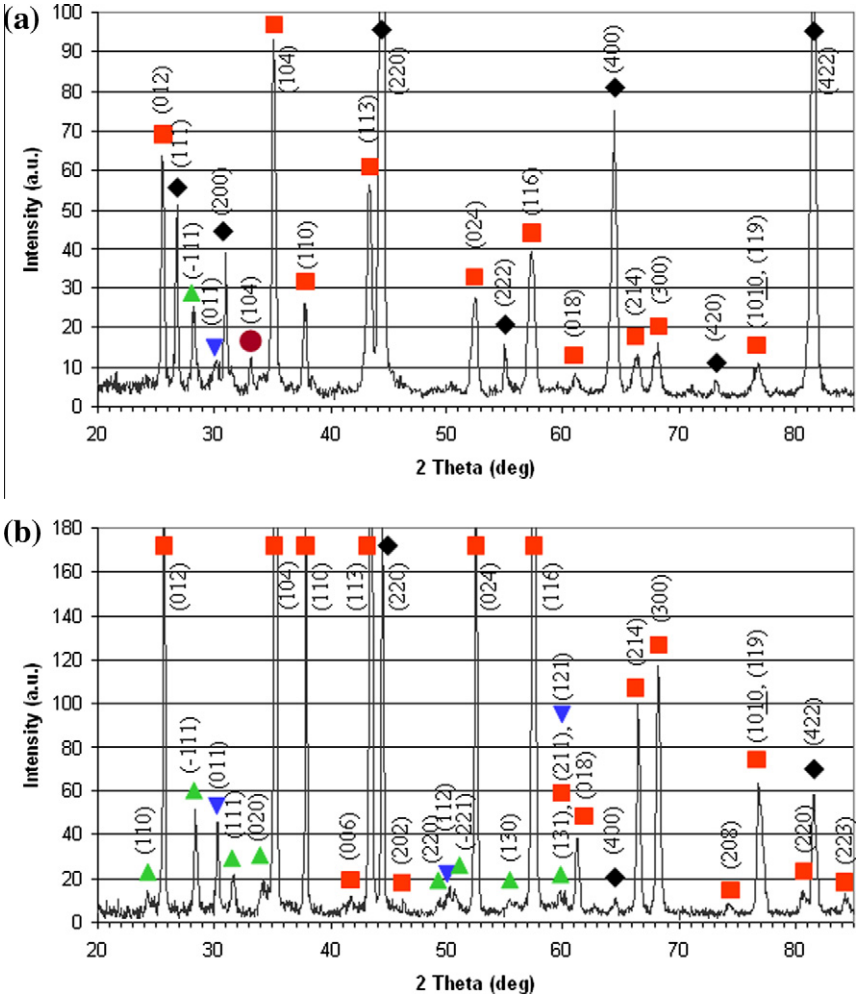

Fig. 11. XRD patterns of the oxidised surface of alloy B after oxidation at 900 °C/1000 h (a) and 1200 °C/1000 h (b).

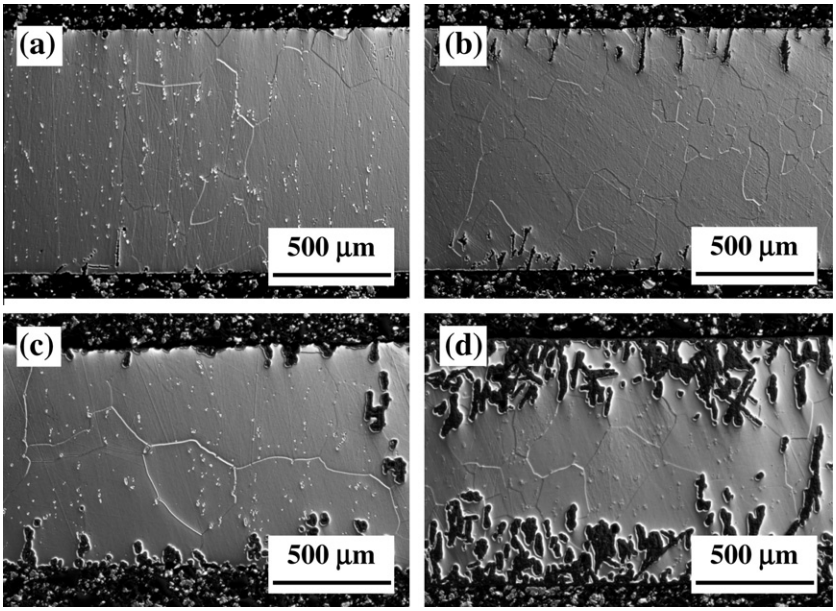

Fig. 12. LOM micrographs of cross sections showing the amount of oxide protrusions into the samples after oxidation at 1000 °C for 1000 h (a and b) and 1200 °C for 500 h (c), for 1000 h (d) of alloys A (left) and B (right).

behaviour of Fe–Al alloys, at least above 900 °C. It is well known that ZrC oxidises rapidly above about 500 °C by the reactions [32–35].

$$ZrC + O_2 \leftrightarrow ZrO_2 + C \quad (2)$$

or

$$ZrC + 2O_2 \leftrightarrow ZrO_2 + CO_2 \quad (3)$$

Actually, the EDS mapping of carbon reveals that carbon is enriched within the oxide (Fig. 13e), i.e. as expected according to Reaction (2). The volume of CO_2 generated by Reaction (3) is rather large and it has been suggested that therefore it should lead to the formation of spherical pores within the oxide [33,35]. That no gas pores are observed within the oxides also suggests that oxidation of ZrC happened according to Eq. (2).

From oxidation experiments carried out by other groups only in one case oxide penetration into a Fe–Al–Cr–Zr alloy has been reported. While no protrusions of oxides into the sample were observed for Fe–28Al–5Cr–0.1Zr–0.05B (at.%) after isothermal oxidation for 96 h at 1000 °C [30], an alloy of nominally the same composition showed deep oxide penetrations after cyclic oxidation between upper 1100–1300 °C and RT [16].

However, for explanation of some of the current results observations by Nourbakhsh et al. [35] are of great relevance. During pressure casting of a zirconia-toughened alumina (Al_2O_3) fibre-reinforced Fe_3Al-based intermetallic composite double layers of ZrC and $(Fe,Al)_2Zr$ Laves phase (denoted as Fe_2AlZr in [35]) formed at the fibre/matrix interface. These double layers were unintentionally oxidised when the composite was annealed at 1100 °C for 24 or 240 h in air. From an elaborate TEM study of the oxidised ZrC/Laves phase double layers the authors found that ZrC is more

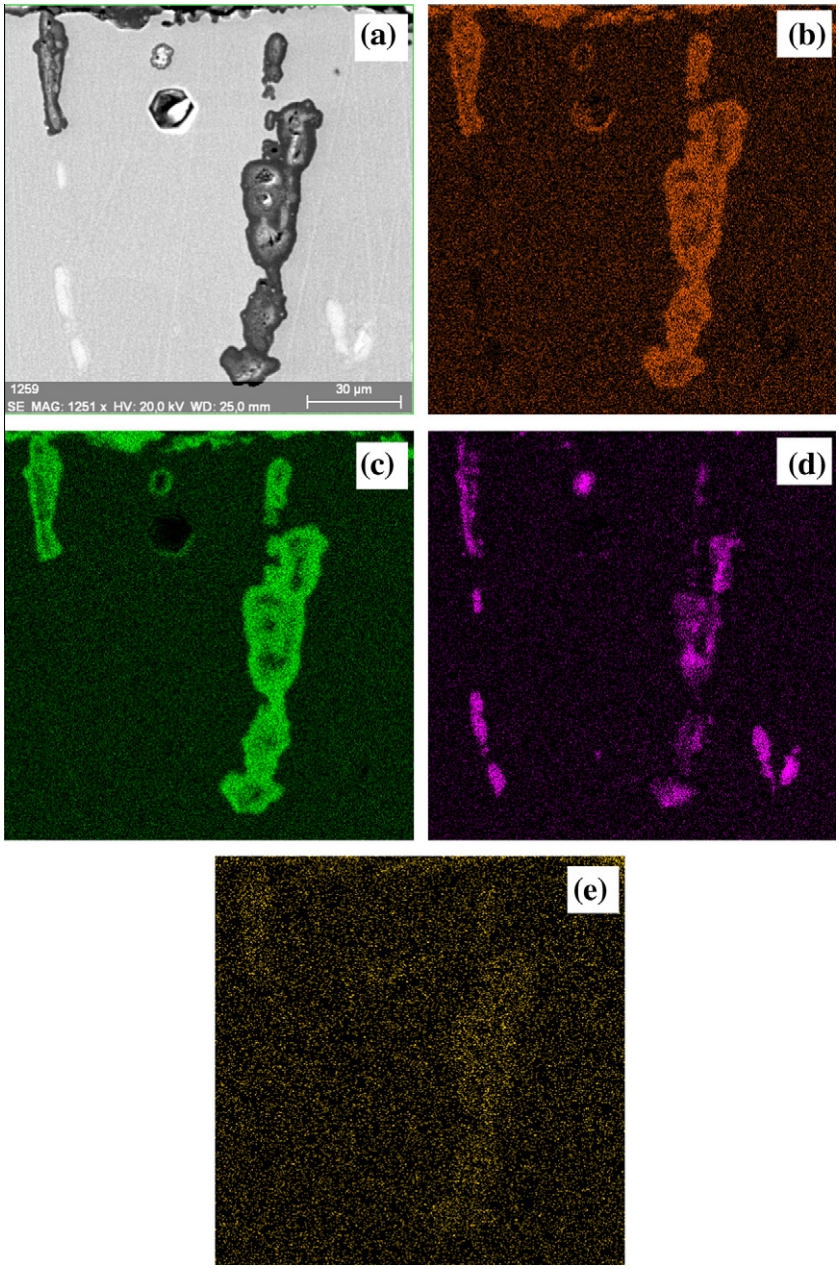

Fig. 13. SEM (secondary electron (SE) contrast) micrograph of the cross section of alloy A after oxidation at 1000 °C for 1000 h (a) and mappings of elements: O (b), Al (c), Zr (d), and C (e).

readily oxidised than the Laves phase $(Fe,Al)_2Zr$ and that Al_2O_3 grew preferentially where ZrO_2 had formed, enveloping the ZrO_2. From the latter observation the authors inferred that Al_2O_3 may have difficulty in nucleating on its own and that ZrO_2 may have a catalytic effect in enhancing Al_2O_3 formation [35].

The above observations are inline with the present results. Comparison of the cross sections of the oxidised samples reveals that at temperatures above 900 °C alloy B, which contains ZrC, is more readily oxidised than alloy A, which contains the Laves phase $(Fe,Al)_2Zr$ (Fig. 12). Also the pronounced zoning of the oxidised areas is observed for the present alloys (Figs. 13 and 15). That the initial formation of ZrO_2, by preferential oxidation of ZrC, may promote the formation Al_2O_3 would explain, why at 1100 and 1200 °C a massive ingress of oxidation into the sample takes place, which is not any longer limited to the phases richer in Zr than the matrix, but which markedly affects the otherwise much more oxidation resistant matrix (Fig. 12). It is noted that the presence of Zr in the alloys has an influence on the grain structure of Al_2O_3 in that columnar grains of Al_2O_3 are formed instead of equiaxed grains [2,12,14,16]. In case of the present alloys, comparable columnar grain structures of Al_2O_3 were observed around Zr-particles (Fig. 16).

Precipitates like Laves phases or carbides are frequently employed for strengthening Fe–Al-based alloys. The oxidation behav-

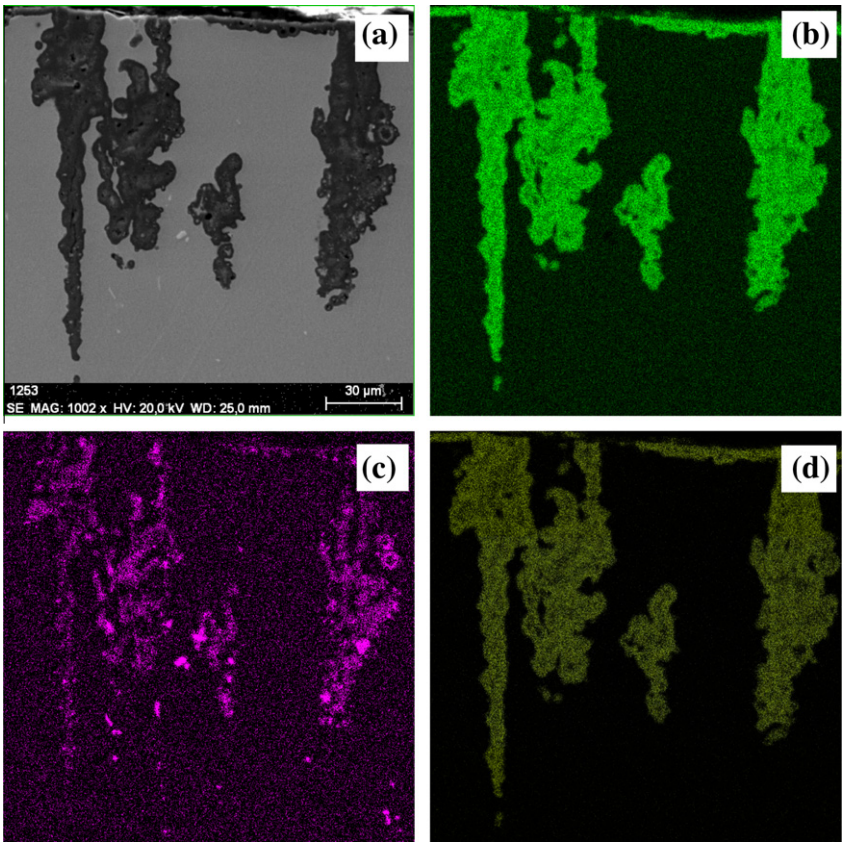

Fig. 14. SEM-SE micrograph of the cross section of alloy B after oxidation at 1000 °C for 1000 h (a) and mappings of elements: Al (b), Zr (c) and O (d) showing the distribution of Al_2O_3 and ZrO_2.

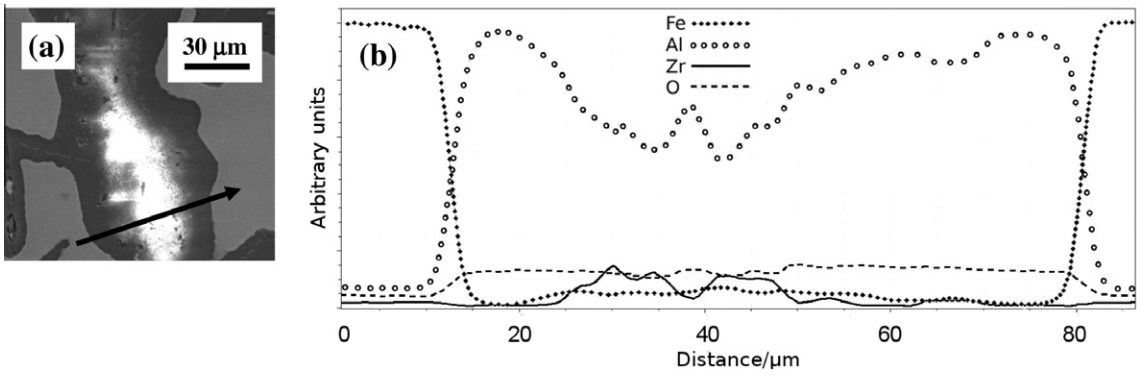

Fig. 15. SEM-SE micrograph of the cross section of alloy B after oxidation at 1200 °C for 1000 h (a); light phase: ZrO_2, dark: Al_2O_3, grey: Fe_3Al. The phases were identified through EDS line scans (b).

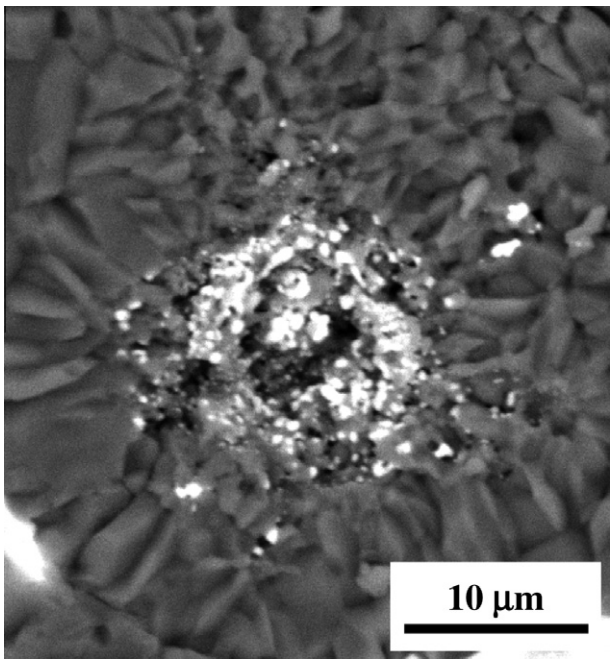

Fig. 16. SEM-BSE micrograph of the columnar grain microstructure of Al_2O_3 (grey) around the Zr-particles (white); the surface detail of alloy A oxidised at 1200 °C was observed at the metal/scale interface.

iour of the present alloys is therefore compared with other Fe–Al-based alloys designed for applications at high temperature. Recently, Janda et al. [36] reported the cyclic oxidation behaviour between upper 750–1050 °C and RT of a series of alloys including Fe–27Al–0.4Nb–0.19Zr (at.%). The alloy showed parabolic oxidation behaviour at 750 and 900 °C but spallation of the scales at 1050 °C. However, preferential oxidation of carbides and borides was already observed at 900 °C.

In Fig. 17 the squared mass gains versus exposure time for various iron aluminides at 900 °C in synthetic air are shown. It can be seen that the present alloys compare favourably to the other alloys in that they show lower mass gains.

In case of Fe–28Al–3Cr–0.02Ce and Fe–30Al–4Cr–2.7TiB_2 (at.%) thin and homogeneous oxide scales formed at 900 °C resulting in a parabolic growth of the scales [23]. In contrast, oxidation at 1100 °C resulted in a hyperbolic growth of the scales. Investigation of cross sections revealed marked intergranular oxidation in case of Fe–28Al–3Cr–0.02Ce.

A quite different oxidation behaviour was observed for Fe–Al–Ta alloys [21]. Under isothermal conditions they only showed parabolic oxidation behaviour between 600 and 800 °C. Above 800 °C scales cracked or spalled due to the formation of Laves phase precipitates at the sample/scale interface. On the other hand, isothermal oxidation tests on Fe–Al–Ti alloys with and without Laves phase precipitates as a strengthening phase revealed that the presence of a Laves phase itself a priori does not have a detrimental effect on the oxidation behaviour [22].

4. Summary and conclusions

The oxidation behaviour of two Fe–Al–Cr–Zr–C alloys designed for applications at high temperatures has been evaluated between 900 and 1200 °C. While both alloys showed a very good oxidation resistance at 900 °C, which compared favourably to those of other Fe_3Al-based alloys, they show increasing weight gains at higher temperatures due to ingress of the oxidation into the sample. While the alloy with $(Fe,Al)_2Zr$ Laves phase (alloy A) showed limited oxide protrusions at 1000 °C the alloy with zirconium carbide ZrC (alloy B) showed a marked ingress of oxidation already at this temperature, which led to a much higher weight gain and a linear oxidation behaviour. Above 1000 °C both alloys showed extensive oxide protrusions due to preferential attack of the strengthening precipitates but while for alloy A oxidation is limited to the Laves phase, oxidation in alloy B is not limited to the ZrC precipitates but extends into the matrix.

The oxidation behaviour of Fe–Al–Cr–(C) alloys with Zr and containing second phases such as carbides or Laves phase mainly along grain boundaries is compared to Fe–Al–Zr alloys with higher Al contents. The oxidation behaviour of the present alloys is less favourable as all other alloys do not show ingress of oxidation into the sample or only under cyclic conditions.

It may therefore be concluded that the present Fe_3Al-based Fe–Al–Cr–Zr–C alloys which have been prepared for application at high temperatures do have an excellent oxidation resistance up to 900–1000 °C. However, starting at 1000 °C the Zr-rich precipitates are preferentially oxidised, ZrC more readily than the Laves phase $(Fe,Al)_2Zr$.

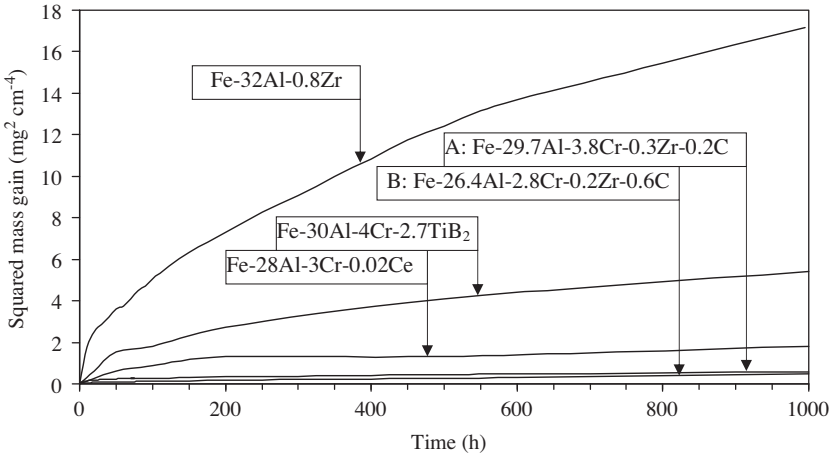

Fig. 17. Squared mass gain versus exposure time for various iron aluminides at 900 °C in synthetic air. Fe–28Al–3Cr–0.02Ce and Fe–30Al–4Cr–2.7TiB_2 (at.%): [35]; Fe–32Al–0.8Zr (at.%): [27].

Acknowledgements

The authors would like to thank Mr T. Schildheuer for help with oxidation testing and Mr G. Bialkowski for sample preparation. This research was supported by The Czech Science Foundation GACR (P 108/12/1452).

References

[1] C.G. McKamey, J.H. DeVan, P.F. Tortorelli, V.K.J. Sikka, A review of recent developments in Fe_3Al-based alloys, Mat. Res. 6 (1991) 1779–1805.
[2] P.F. Tortorelli, K. Natesan, Critical factors affecting the high-temperature corrosion performance of iron aluminides, Mat. Sci. Eng. A258 (1998) 115–125.
[3] R. Prescott, M.J. Graham, The oxidation of iron–aluminum alloys, Oxid. Met. 38 (1992) 73–87.
[4] I. Rommerskirchen, B. Eltester, H.J. Grabke, Oxidation of β-FeAl and Fe–Al alloys, Mat. Corros. 47 (1996) 646–649.
[5] A. Velon, I. Olefjord, Oxidation behavior of Ni_3Al and Fe_3Al: II early stage oxide growth, Oxid. Met. 56 (2001) 425–451.
[6] B. Pöter, F. Stein, R. Wirth, M. Spiegel, Early stages of protective oxide layer growth of binary iron aluminides, Z. Phys. Chem. 219 (2005) 1489–1503.
[7] P.F. Tortorelli, J.H. DeVan, Behavior of iron aluminides in oxidizing and oxidizing/sulfidizing environments, Mat. Sci. Eng. A153 (1992) 573–577.
[8] D.B. Lee, G.Y. Kim, G.J. Kim, The oxidation of Fe_3Al–(0%, 2%, 4%, 6%)Cr alloys at 1000 °C, Mat. Sci. Eng. A339 (2003) 109–114.
[9] J.H. DeVan, P.F. Tortorelli, Environmental effects on iron aluminides, Proc. 7th Annual Conf. on Fossil Energy Materials, Department of Energy DOE (1993) 277–288.
[10] K. Natesan, Corrosion performance of iron aluminides in mixed-oxidant environments, Mat. Sci. Eng. A258 (1998) 126–134.
[11] S. Chevalier, P. Juzon, G. Borchardt, A. Galerie, K. Przybylski, J.P. Larpin, High-temperature oxidation of Fe_3Al and Fe_3Al-Zr, Oxid. Met. 73 (2010) 43–64.
[12] B.A. Pint, Experimental observations in support of the dynamic-segregation theory to explain the reactive-element-effect, Oxid. Met. 45 (1996) 1–37.
[13] B.A. Pint, J.R. Regina, K. Prüßner, L.D. Chitwood, K.B. Alexander, P.F. Tortorelli, Effect of environment on the oxidation of ingot-processed iron aluminides, Intermetallics 9 (2001) 735–739.
[14] B.A. Pint, P.F. Tortorelli, I.G. Wright, The oxidation behavior of ODS iron aluminides, Mat. Corros. 47 (1996) 663–674.
[15] J. Ni, X.J. Wan, Q. Wang, X.Y. Cheng, W.M. Liu, X.Y. Zhang, The cyclic oxidation behaviors of Fe_3(Al, Cr, Zr) and Fe_3(Al, Cr, Nb) intermetallic compound at high temperature, J. Shanghai Univ. 1 (1997) 79–82.
[16] B.A. Pint, P.F. Tortorelli, I.G. Wright, Long-term oxidation performance of ingot produced Fe_3Al alloys, Mater. High Temp. 16 (1999) 1–13.
[17] B.A. Pint, K.L. More, P.F. Tortorelli, W.D. Porter, I.G. Wright, Optimizing the imperfect oxidation performance of iron aluminides, Mater. Sci. Forum 369–372 (2001) 411–418.
[18] P. Kratochvil, P. Malek, M. Cieslar, P. Hanus, J. Hakl, T. Vlasak, High-temperature mechanical properties of Zr alloyed Fe_3Al-type iron aluminide, Intermetallics 15 (2007) 333–337.
[19] K. Przybylski, S. Chevalier, P. Juzon, Effect of Zr on the oxidation properties of Fe_3Al intermetallic compound, J. Chin. Soc. Corros. Prot. 29 (2009) 286–292.
[20] F. Stein, M. Palm, G. Sauthoff, Mechanical properties and oxidation behaviour of two-phase iron aluminium alloys with Zr(Fe, Al)2 Laves phase or Zr(Fe, Al)12 τ_1 phase, Intermetallics 13 (2005) 1275–1285.
[21] A. Hotař, M. Palm, Oxidation resistance of Fe–25Al–2Ta (at.%) in air, Intermetallics 18 (2010) 1390–1395.
[22] M. Palm, G. Sauthoff, Deformation behaviour and oxidation resistance of single-phase and two-phase $L2_1$-ordered Fe–Al–Ti alloys, Intermetallics 12 (2004) 1345–1359.
[23] A. Hotař, P. Kratochvíl, J. Cizner, Oxidation resistance of Fe28Al3Cr0.02Ce and Fe30Al4Cr2.7TiB_2 (at.%) in air, Proc. 19th Int. Conf. on Metallurgy and Materials, METAL 2010, (2010), paper no. 127, online available at http://www.nanocon.cz/data/metal2010/sbornik/lists/papers/337.pdf.
[24] B. Pöter, F. Stein, M. Spiegel, reported in S. Milenkovic, M. Palm, Microstructure and mechanical properties of directionally solidified Fe–Al–Nb eutectic, Intermetallics 16 (2008) 1212-18.
[25] K. Natesan, P.F. Tortorelli, High-temperature corrosion and applications of nickel and iron aluminides in coal-conversion power systems, in: S.C. Deevi, P.J. Maziasz, V.K. Sikka, R.W. Cahn (Eds.), Int. Symp. on Nickel and Iron aluminides: Processing, Properties, and Applications, ASM, International, 1997, pp. 265.
[26] T. Mitsuhashi, M. Ichihara, U. Tatsuke, Characterization and stabilization of metastable ZrO2, J. Am. Ceram. Soc. 57 (1974) 97–104.
[27] R.C. Garvie, Stabilization of the tetragonal structure in zirconia microcrystals, J. Phys. Chem. 82 (1978) 218–224.
[28] J.R. Kelly, I. Denry, Stabilized zirconia as a structural ceramic: an overview, Dental Mat. 24 (2008) 289–298.
[29] J. Chevalier, L. Gremillard, The tetragonal-monoclinic transformation in zirconia: Lessons learned and future trends, J. Am. Ceram. Soc. 92 (2009) 1901–1920.
[30] K.B. Alexander, K. Prüssner, P.Y. Hou, P.F. Tortorelli, Microstructure of alumina scales and coatings on zirconium-containing iron aluminide alloys, in: J.A. Little, S.B. Newcomb (Eds.), Microscopy of Oxidation 3, Maney, 1997, p. 246.
[31] C.H. Xu, W. Gao, H. Gong, Oxidation behaviour of FeAl Intermetallics. The effects of Y and/or Zr on isothermal oxidation kinetics, Intermetallics 8 (2000) 769–779.
[32] R.W. Bartlett, M.E. Wadsworth, I.B. Cutler, The oxidation kinetics of zirconium carbide, Trans. Met. Soc. AIME 227 (1963) 467–472.
[33] R.F. Voitich, E.A. Pugach, High-temperature oxidation of ZrC and HfC, Powder Met. Met. Ceram. 12 (1973) 916–922.
[34] S. Shimada, A thermoanalytical study on the oxidation of ZrC and HfC powders with formation of carbon, Solid State Ionics 149 (2002) 319–326.
[35] S. Nourbakhsh, O. Sahin, W.H. Rhee, H. Margolin, A structural study of oxidation in a zirconia-toughened alumina fibre-reinforced Fe_3Al composite, Metall. Trans. A24 (1993) 435–443.
[36] D. Janda, M. Galetz, M. Schütze, M. Heilmaier, The effect of micro-alloying with Zr and Nb on the oxidation behavior of Fe_3Al and FeAl alloys, in: Proc. Sixth Discussion Meeting on the Development of Innovative Iron Aluminium Alloys FEAL2011, (2011) 133–136.

THE EFFECT OF ZIRCONIUM CONTENT ON THE PHASE STRUCTURE OF Fe_3Al-xC TYPE INTERMETALLIC ALLOYS

Věra VODIČKOVÁ [1], Petr KRATOCHVÍL [2], Stanislav DANIŠ [2], Martin ŠVEC [1]

[1] *Technical University of Liberec, Faculty of Engineering, Department of Material Science, Studentská 2, 46117 Liberec, Czech Republic*

[2] *Charles University of Prague, Faculty of Mathematics and Physic, Ke Karlovu 5, 12116 Prague 2, Czech Republic*

Abstract

The iron aluminides with Fe_3Al matrix are promising materials for structural applications. The addition of Nb, Cr, Zr, Ti, Ta, Mo to the matrix can improve their high-temperature mechanical properties.

The zirconium and carbon addition to the Fe-Al leads to the formation of zirconium carbide ZrC and other phases (e.g. Laves phase $(Fe,Al)_2Zr$, Fe_2Zr). These phases could enhance high-temperature mechanical properties, if they are formed in an appropriate shape.

Two alloys with different zirconium and carbon contents were prepared . The influence of the heat treatment on the structure of the alloys was studied. The phase composition was determined using scanning electron microscopy (SEM) with energy dispersive analysis (EDX) and XRD phase analysis.

Keywords: Fe_3Al type aluminides, Zr and C addition, phase structure, heat treatment

1. INTRODUCTION

The iron aluminides are one of the most promising materials with many advantages, but their mass extension has impeded some of their problematic properties. It is primarily a sharp drop in strength above 600°C or limited ductility at room temperature [1]. These disadvantages can be improved f. e. by alloying of binary alloy [2].

The alloying by zirconium may be one of the method to enhance high-temperature mechanical properties of Fe_3Al type iron aluminides. Zirconium has a very low solubility in the base binary alloy Fe–Al. Therefore Zr easily makes the particles, that can reinforce the matrix and improve the mechanical properties of the alloy. The beneficial effect of zirconium addition on creep resistance was first reported by McKamey and Maziasz [3, 4, 5].

It is important to monitor not only the effect of Zr addition to Fe–Al alloy, but also the effect of C addition to Fe–Al–Zr system. Carbon is present in the raw iron, which is used for the preparation of iron aluminides, or may be added to the alloy to improve some properties. Very important effect of carbon on the formation of phases in the mentioned alloys have recently been described by several authors [6, 7, 8, 9].

It is the purpose of the present paper to study the effect of the ratio c(C)/c(Zr) or respectively of the diference c(C) - c(Zr) on the phase structure of Fe_3Al-type alloys. Two cases are distinguished: material with excess Zr and that with excess C.

2. MATERIALS AND EXPERIMENTAL METHODS

The alloys were prepared by vacuum induction melting and casting. Ingots (20x40x150 mm) were hot rolled to final thickness at 1200°C in several steps with 15% thickness reduction in one pass. The chemical composition is given in Table 1. Concentrations of technical impurities (coming from the metals used for the preparation of the alloys) were: 0.1 at. % Cr, 0.01 at.% B, 0.1 at.% Mn. The alloys composition was selected so that one of them had higher carbon content than zirconium content (FA1143) and the second had the opposite ratio (FA1144). Also the effects of long term annealing (1000^{o}C/200 hours) and short term (1150^{o}C/1 hour) were tested.

The samples for study of microstructure were oxide-polishing by suspension OP-S only. The structure was observed by the light optical microscope Nikon Epiphot 200 (with use Differential interference contrast – DIC). The microstructural details and the phase composition were studied by the scanning electron microscope (SEM) Tescan Vega XMU equipped by Bruker detector for energy dispersive analysis (EDX) and SEM Zeiss ULTRA Plus equipped by Oxford detector for EDX. Also the X-ray diffraction (XRD) was performed.

Table 1 – The chemical composition of the samples

Sample	Chemical composition (at. %)			
	Fe	Al	C	Zr
FA1143	balance	25.7	1.7	1.1
FA1144	balance	25.2	1.6	2.1

3. RESULTS

3.1 The characterization of phase structure of FA1143

The typical phase structure of the as received alloy FA1143 is shown in Fig. 1. The grains have an irregular shape and their dimensions are in orders of hunderds of microns. The particles of phases are distributed inside the grains and along the grain bounderies. SEM image in BSE mode allows to recognize

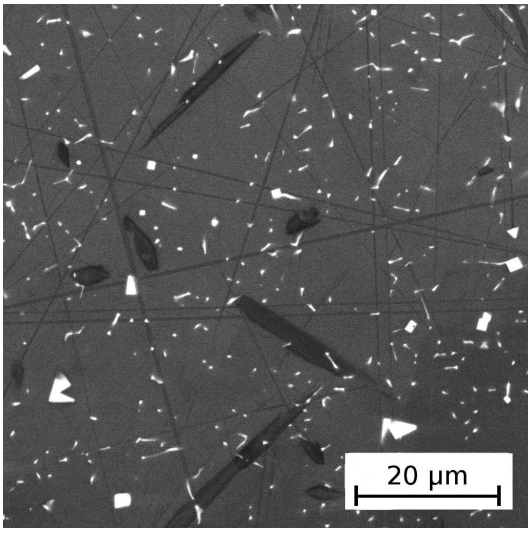

Fig. 1 – The structure of alloy FA1143 as received

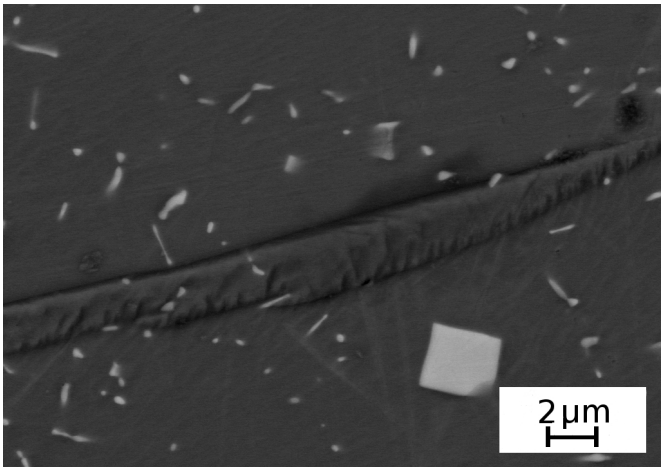

Fig. 2 – The detail of particles in alloy 1143 (1150^{o}C/1h)

two phases in the matrix: a) white particles with different morphology – rod like (length about 1-4 μm) and cubic particles (diagonal 2-5 μm) and b) great dark particles, see Fig. 1.

The white phase was identified as zirconium carbide ZrC using both the EDX and XRD, see Fig.3. The dark phase (dark elongated areas, 4 to 40 μm long or smaller oval areas diameter 4 to 8 μm), detail in Fig. 2, was determined as perovskite type ε-carbide Fe_3AlC_x (the result of EDX and XRD analysis), see Fig. 3.

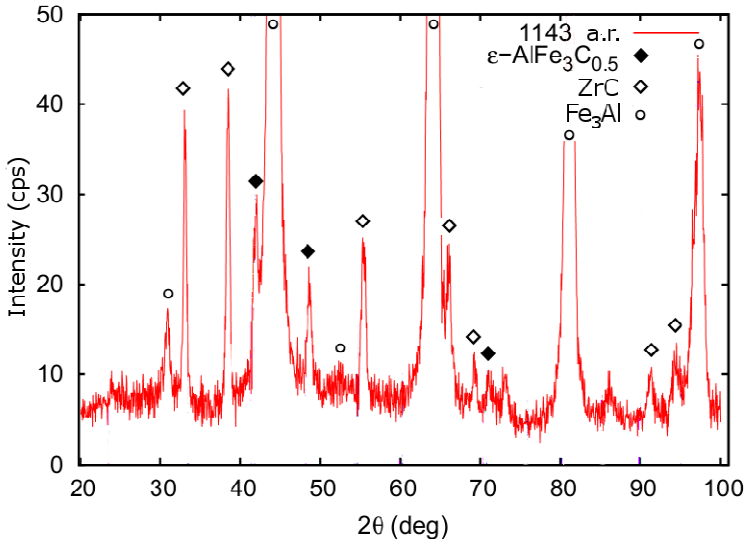

Fig. 3 – The XRD results of alloy FA1143 as received

Phase composition is the same after annealing 1150°C/1h. The long-time annealing (1000°C/200h) effect on the phase stability is evident in Fig. 4a. ZrC carbide rod-like particles are partly dissolved, cubic particles are distributed not homogeneously in clusters. The perovskite type carbide Fe_3AlC_x is partly dissolved too. Dark perovskite needles are much smaller (lenght up 10 μm, 1μm wide) than before annealing – section in Fig. 4b.

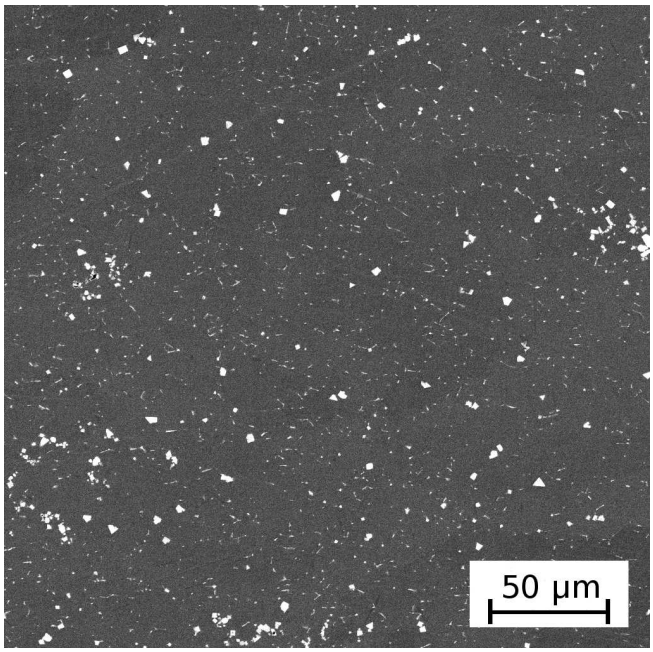

Fig. 4a – The structure of alloy FA1143 after annealing (1000°C/200h)

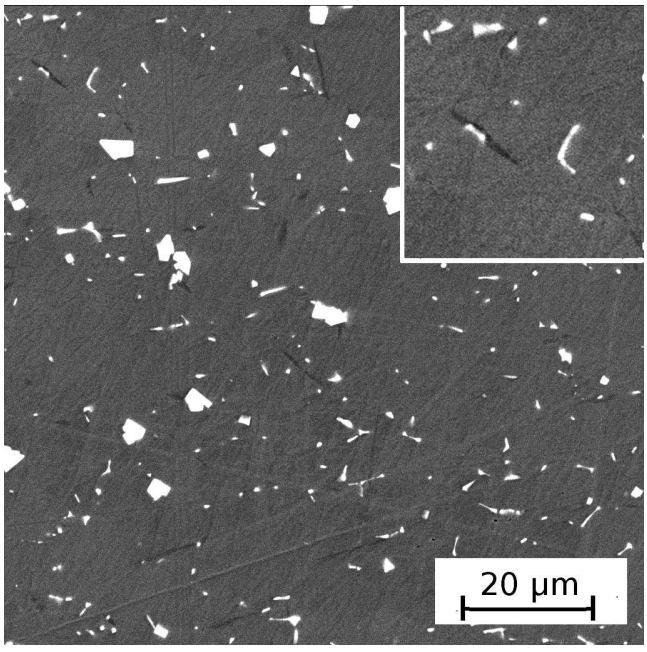

Fig. 4b – The detail of small dark perovskite particles (like – needle) – magnified in the section

3.2 The characterization of phase structure of FA1144

The structure of FA1144 alloy is characterized by several types of particles inside of grain and along grain boundaries. SEM image in BSE mode provided better imaging of this phase, Fig. 5a. The phase was identified by EDX analysis and by X-ray diffraction as ZrC (white cubic particles) and Laves phase λ_1 $(Fe,Al)_2Zr$ (bright-gray oval-shape fine particles arranged in a necklace configuration – see the detail of phase in Fig. 5b). Also Laves phase λ_1 $(Fe,Al)_2Zr$ particles with ZrC core was observed (Fig. 5b).

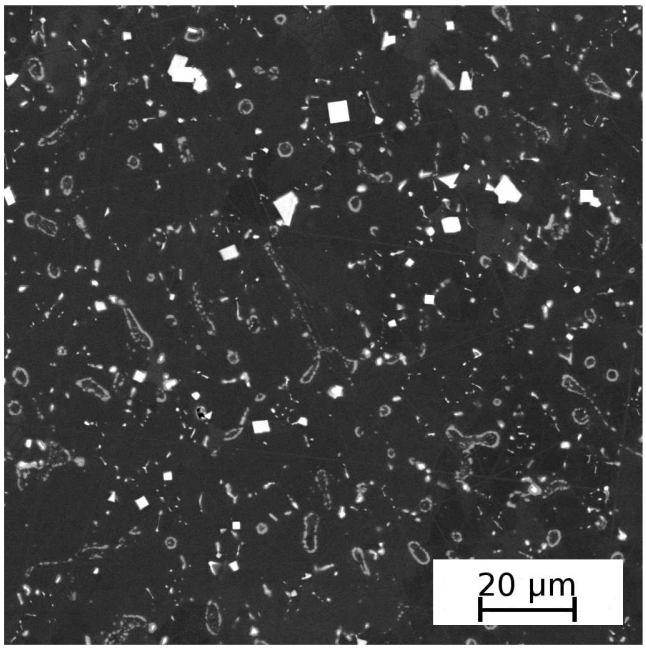

Fig. 5a – The structure of alloy FA1144 as received

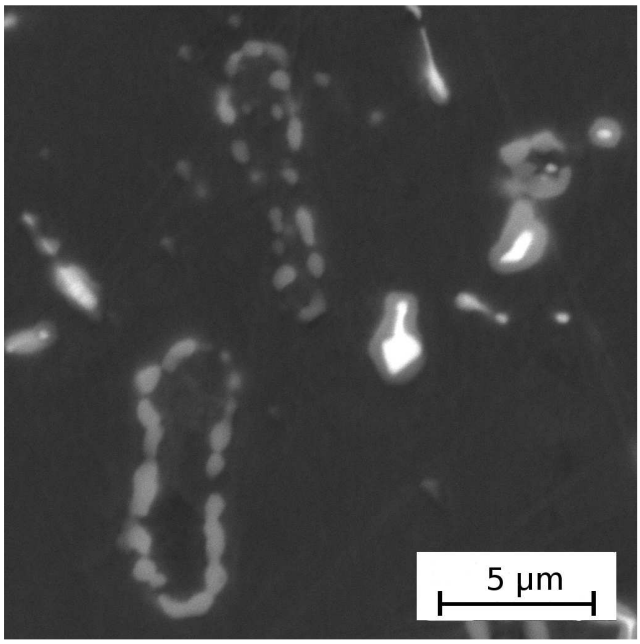

Fig. 5b – The detail of chain particles and particles with ZrC core in alloy FA1144 as received

Phase composition and its configuration is the same after annealing 1150°C/1h. The effect of the annealing for 200 hours at 1000°C is more evident. There are the clusters of cubic ZrC particles in the structure, see Fig. 6a. Fine particles of λ_1 $(Fe,Al)_2Zr$ with ZrC core appeared most frequently in the structure, Fig. 6b. Phase determination was verified by EDX analysis, the comparing of matrix, Laves phase and ZrC spectra is given in Fig. 7a, b.

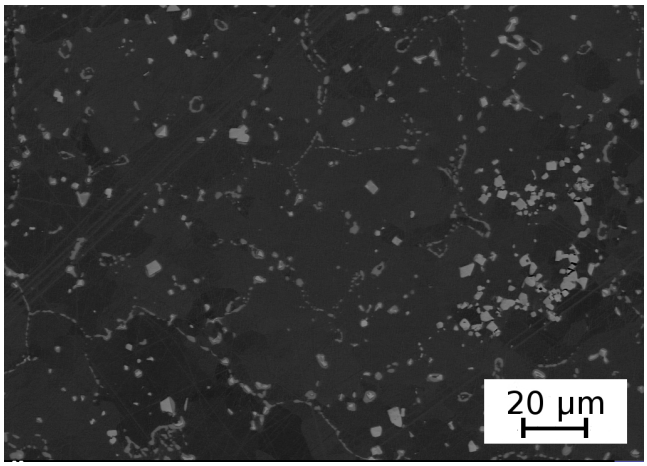

Fig. 6a – The structure of alloy FA1144 (1000°C/200 hours)

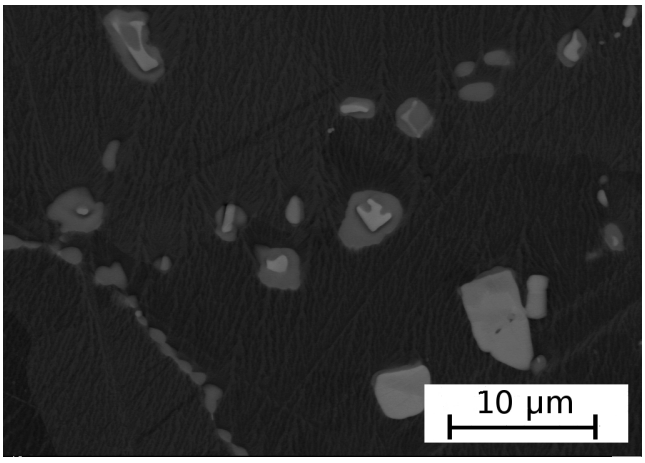

Fig. 6b – The detail of fine λ_1 particles with ZrC core in alloy FA1144 (1000°C/200 hours)

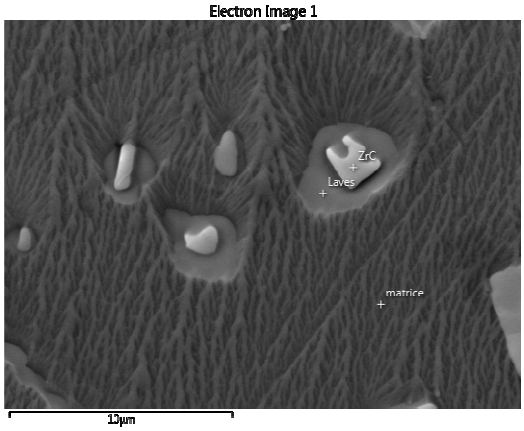

Fig. 7a – Localities of point spectra

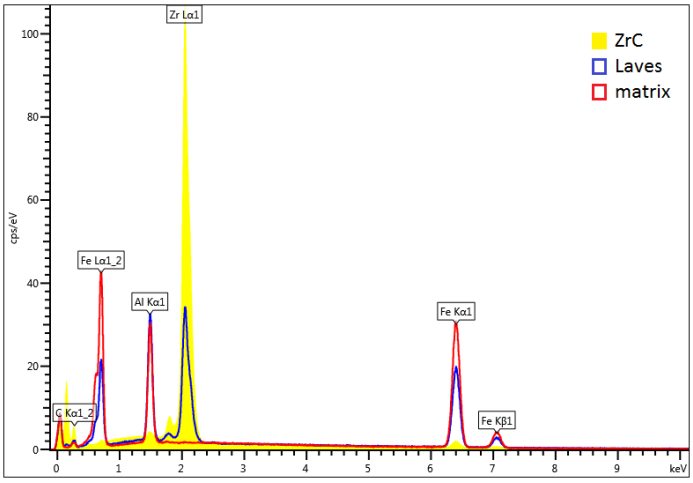

Fig. 7b – Point spectra of matrix (red line), Laves phase (blue) and ZrC (yellow) particles in comparison

4. DISCUSSION AND CONCLUSIONS

Structure of the tested alloys 1143 and 1144 can be summarized as follows: The prevailing phase , i.e. the higher volume fraction in both alloys depends on value of the ratio c(C)/c(Zr). For values > 1, based on he afinity of Zr to C ZrC is the prevailing phase. The rest of C forms the ε – carbide. On the other hand for ratio c(C)/c(Zr) <1 Zr left (over Zr/C = 1) forms λ_1 $(Fe,Al)_2Zr$.

Very important effect of C on the formation of phases in the mentioned alloys was recently noticed [3-9]. It is interesting that even small concentrations of carbon (e.g. in raw iron) can be important. Kratochvíl et al. [6,9] tested Zr as an additive to Fe_3Al-type alloy to enhance the high temperature tensile and creep properties.. The particles both of Laves phase λ_1 $(Fe,Al)_2Zr$ and of ZrC were identified.

Recently Kratochvíl et al. [10] mentioned the presence of ZrC also in the structure of Fe–30Al–xZr alloys (x = 0.4–5.0) together with λ_1 $(Fe,Al)_2Zr$ and with τ_1 $(Fe,Al)_{12}Zr$.

The presence of particles of both phases ZrC and λ_1 $(Fe,Al)_2Zr$ in both alloys of the size described in the present paper influences the hardening Fe_3Al iron aluminide very little. It is but well known that the presence of small size precipitates of the mentioned phases [6,9] do exist in the alloys of very similar composition. It will be the future task to verify the presence of tiny precipitates of both phases also in the high temperature deformed alloys 1143 and 1144.

It was also the purpose of the present investigation to confirm the same phase composition as it was observed in alloys with the addition of chromium (~ 4-5 at.%), which is the corrosion reducing and room ductility enhancing additive. It was also shown that the carbon as an additive can lower the influence of Zr (by the formation of ZrC) on the corrosion resistance of iron aluminides [11].

The high temperature annealing is the contribution to the testing of the long term stability of the phases for the use alloys of the tested type as a structural material for high temperature use (see also the not about corrosion above).

ACKNOWLEDGMENT

This research was supported by Grant Agency of the Czech Republic through the project No. P108/12/1452. The authors acknowledge the assistance during the testing of the phase structure by ing. Pavel Hanus, PhD. and ing. Pavel Kejzlar of the Department of Material Science of the Technical university in Liberec. Also the help the Faculty of Metallurgy and Material Engineering (Prof. Ivo Schindler) of the Technical University in Ostrava, where the alloys were prepared, is acknowledged.

REFERENCES

[1] MC KAMEY, C. G. Iron Aluminides. In Physical Metalurgy and processing of Intermetallic Compounds, eds. STOLOFF N. S. – SIKKA V. K., 1994, 351 – 391.

[2] MORRIS, D. G. Possibilities for high – temperature strengthening in iron aluminides. In Intermetallics 6 (1998), 753 – 758.

[3] MC KAMEY, C. G., MAZIASZ, P. J. Heat treatment effect for improved creep-rupture resistance of a Fe_3Al based alloy. In Intermetallics 6 (1998), 303 – 314.

[4] MC KAMEY, C. G., MAZIASZ, P. J., JONES, J. W. Effect of Addition of Molybdenum or Niobium on Creep Rupture Properties of Fe_3Al. In Mater. Res. 7 (1992), 2089 – 2106.

[5] MC KAMEY, C. G., MAZIASZ, P. J., GOODWIN, G. M., ZACHARIA, T. Effects of Alloying Additions on the Microstructures, Mechanical Properties and Weldability of Fe_3Al-based Alloys. In Materials Science and Engineering A174 (1994), 59 – 70.

[6] KRATOCHVÍL, P. at al. High-temperature mechanical properties of Zr alloyed Fe_3Al type iron aluminide. In Intermetallics 15 (2007), 333 – 337.

[7] DOBEŠ, F., KRATOCHVÍL, P., MILIČKA, K. Compressive creep of Fe_3Al-type iron aluminide with Zr additions. In Strength of Materials Vol. 40 (2008), 106 – 109.

[8] CIESLAR, M., KARLÍK, M. Carbide formation in Zr-containing Fe_3Al-based alloys. In Mater. Sci. Eng. A462 (2007), 289 – 293.

[9] KRATOCHVÍL, et al. Microstructure and high temperature mechanical properties of Zr-alloyed Fe_3Al-type aluminides. The effect of carbon. Mat. Sci. Eng. A 548 (2012), 175-182

[10] KRATOCHVÍL, et al. The effect of Zr addition on the structure and high temperature strength of Fe-30at. % Al type alloys. Intermetallics 20 (2012), 39-46

[11] HOTAŘ, A. et al. High-temperature oxidation behaviour of Zr alloyed Fe3Al-type iron aluminide. Corr. Sci. 63 (2012), 71-81

The Effect of Laves Phase $(Fe,Al)_2Zr$ on the High-Temperature Strength of Carbon-Alloyed Fe_3Al Aluminide

PETR KRATOCHVÍL, VĚRA VODIČKOVÁ, ROBERT KRÁL, and MARTIN ŠVEC

The effects of carbon on the phase structure and on the yield stress $\sigma_{0.2}$ in the temperature range from 873 K to 1073 K (600 °C to 800 °C) of the Fe_3Al type aluminides alloyed by Zr are analyzed. Four alloys with Zr and C in ranging from 1.0 to 5.0 at. pct of additives were used. The appearing of either Laves phase $(Fe,Al)_2Zr$ and/or carbides depend on the difference in concentrations, $c_{Zr} - c_C$. This parameter $(c_{Zr} - c_C)$ has been selected instead of the concentration ratio c_{Zr}/c_C used in previous works since it exhibits a significantly better correlation with the Laves phase concentration which influences the high-temperature yield stress, $\sigma_{0.2}$, of the tested alloys. The presence of Laves phase or eutectic (matrix—Laves phase), respectively, enhances the value of the yield stress $\sigma_{0.2}$. The amount of Laves phase is decreased by the presence of C due to the affinity of carbon to Zr.

DOI: 10.1007/s11661-015-3309-2

I. INTRODUCTION

THE alloying by zirconium is a method to enhance HT mechanical properties of Fe_3Al alloys. Very low solid solubility of Zr in the Fe-Al initiated investigations of the influence of Zr addition to Fe_3Al and FeAl alloys. The beneficial effect of zirconium and niobium addition on *e.g.* creep resistance was first reported in papers by McKamey and Maziasz.[1–3] Significant attention was payed to the effect of Zr on the phase structure and high-temperature (HT) mechanical properties of iron aluminides. Especially the formation of Laves phase (Fe, $Al)_2$ Zr and (Fe, $Al)_2$ Nb was referred.[4–10]

Aside are left the large additions of Zr (*i.e.*, up to 30 at. pct[4,5]). It is important to determine the effect of carbon (present in the raw iron used for the preparation of iron aluminides for structural uses). This may modify the mechanical properties, corrosion process, *etc.*, by the influence of, *e.g.,* the Laves phase. The presence of carbon in iron aluminides with zirconium modifies the formation of Laves phase in the Fe corner of the ternary equilibrium diagram.[6] Low solubility of Zr in $D0_3$/B2 Fe-Al results in the formation of Laves phase $(Fe,Al)_2Zr$.

Recently, Kratochvil *et al.*[11] showed in iron aluminides alloyed by Cr that the ratio of zirconium and carbon influences the phase structure of Fe_3Al-type alloys. This was documented by the effects of the ratio c_{Zr}/c_C on both the yield stress 0.2 and the creep rate at high temperatures.

Laves phase λ_1 $(Fe,Al)_2Zr$ and ZrC particles were found primarily along grain boundaries, with some distribution in the grains as well. Their strengthening role is limited to blocking the grain boundaries' motion because the effect of these particles inside the grains (owing to large distance between the particles) was very small. Partly such effects of low concentrations of Zr and C have been mentioned by Kejzlar *et al.*[12] The appearing of metastable phases, $(Fe_{1-x}Al_x)_3Zr$ and Fe_2Zr, which originate during the HT deformation[10] was also detected in the iron aluminides alloyed by Cr.

It is therefore the purpose of the present paper to verify the effect of the ratio of zirconium and carbon—described by the difference $c_{Zr} - c_C$—in an alloy without chromium on the structures of Fe_3Al alloys and on their HT yield strengths. The difference $c_{Zr} - c_C$ was chosen as it better describes the amount of Zr left for the formation of Laves phase, if any, compared with the ratio of both concentrations. This fact is obvious from a significantly better correlation with eutectic (matrix—Laves phase) in case of $c_{Zr} - c_C$ compared with c_{Zr}/c_C.

II. EXPERIMENTAL PROCEDURE

The alloys were prepared by a vacuum melting and casting under argon. The chemical compositions are given in Table I. The actual compositions of the alloys were established by wet chemical analysis at the Research and Testing Centre, Plzen. The concentrations were chosen to get alloys with different values of $c_{Zr} - c_C$. The alloys contain (25.6 to 26.2) at. pct Al. Concentrations of impurities (from the metals used for

PETR KRATOCHVÍL, Professor, and ROBERT KRÁL, Associate Professor, are with the Department of Physics of Materials, Charles University, Ke Karlovu 5, 121 16 Prague, Czech Republic. Contact e-mail: pekrat@met.mff.cuni.cz VĚRA VODIČKOVÁ, Associate Professor, and MARTIN ŠVEC, Ph.D. Student, are with the Department of Materials Science, Faculty of Engineering, Technical University of Liberec, Studentská 2, 46117 Liberec, Czech Republic.
Manuscript submitted September 10, 2015.
Article published online December 30, 2015

the preparation of the alloys) were: 0.1 at. pct Cr, 0.01 at. pct B, 0.1 at. pct Mn.

All alloys were tested in the as-cast state. Samples (parallelepipeds 6 × 6 × 10 mm) for compression test at temperatures ranging from 873 K to 1073 K (600 °C to 800 °C) were prepared from the alloys via electrical discharge machining (EDM). The compressive yield stress was evaluated using a digitally controlled testing machine (INSTRON 1186R). The deformation rate was 1.2×10^{-4} s^{-1}.

The temperatures ranging from 873 K to 1073 K (600 °C to 800 °C) were chosen because these temperatures are mostly above the yield strength anomaly. This is an increase in the strength with the increasing temperature, typically observed for Fe-Al-based alloys with a maximum at about 823 K (550 °C). All the investigated alloys are at these temperatures, B2-ordered, which allows direct comparison of their yield strengths.

Microstructural phase compositions were studied using a field emission-scanning electron microscope (FE-SEM)—Zeiss Ultra Plus—equipped with energy-dispersive spectrometer (EDS)—OXFORD X-MAX 20—and with a detector for electron backscatter diffraction (EBSD)—OXFORD NordlysNano. For the characterization of the carbides, EDS combined with analysis of Kikuchi patterns was used. Analyses were carried out at an accelerating voltage of 20 kV, and the typical primary electron beam diameter was 2 nm.

III. EXPERIMENTAL RESULTS AND DISCUSSION

The sizes of the grains of all the investigated as-cast alloys were ranging from 100 to 400 μm. The phase structures of the alloys are summarized in Table I. In alloy 1143 ($c_{Zr} - c_C = -0.67$ at. pct), the volume fraction f_v of ZrC is 1.9 pct. ZrC are plates partly seen edgeways. The rest of the carbon forms perovskite $AlFe_3C_{0.5}$ ($f_v = 4.5$ pct) as documented in Figure 1 or is dissolved in the lattice. Porovskite is forming also plates, contrast of which is not excellent. In alloy 1144 ($c_{Zr} - c_C = 0.53$ at. pct), ZrC particles ($f_v = 2.3$ pct) and Laves phase $(Fe,Al)_2Zr$ ($f_v = 4.2$ pct) appear. The Laves phase is a part of an eutectic with matrix, Figure 2.

The structures of alloys 1181 and 1182 are characterized by a dendritic arrangement of eutectic (matrix plus Laves phase) immersed in the matrix, Figures 3 and 4. ZrC carbide particles are seen inhomogeneously dispersed, and its volume fraction $f_v = 1.2$ pct in 1181 alloy. In 1182 alloy, f_v reaches the value of 3.9 pct. The values of f_v of the eutectic Laves phase plus matrix are 41.7 and 34.7 pct, respectively, in the both the alloys. The basic point of the above observations is that the eutectic strengthens the tested alloys.

The compression 0.2 yield stresses as a function of temperature was used to describe HT mechanical properties of the tested iron aluminides, which are summarized in Table II. Experimental errors are 3 pct (valid also for yield stress 0.2 values in Table II). The increasing value of HT yield stress 0.2 with the increasing volume fraction of the eutectic (Laves phase λ_1 $(Fe,Al)_2$ Zr with matrix) is obvious as seen in Figure 5. Due to the fact that carbon forms ZrC, it lowers the amount of Zr available for the formation of Laves phase λ_1 $(Fe,Al)_2$ Zr. Figure 5 shows the comparison of the

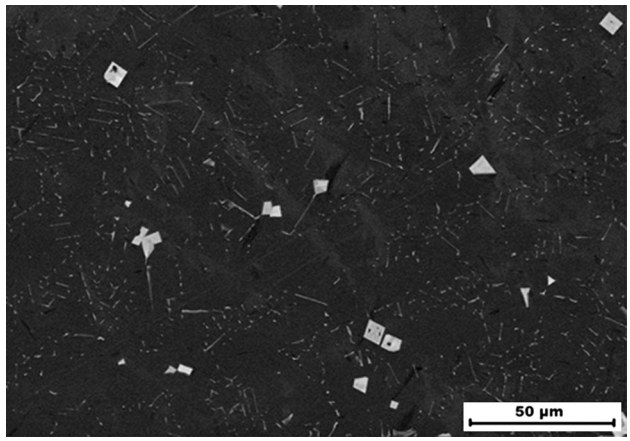

Fig. 1—The structure of the as-cast 1143 alloy (SEM): perovskite black (dark needle like), carbide—white, matrix—gray.

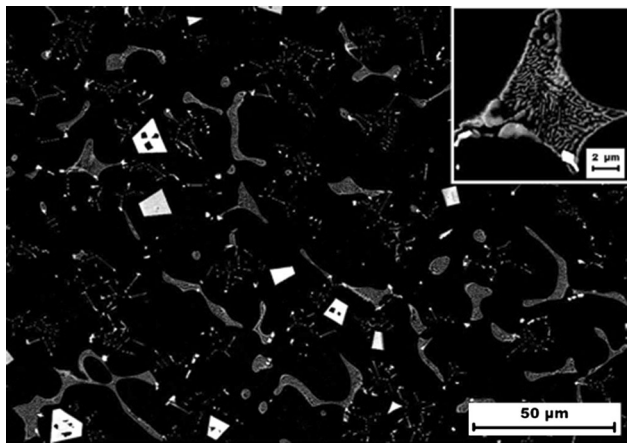

Fig. 2—The structure of the as-cast 1144 alloy (SEM): carbide—white (polygonal, partly rod like), multiform eutectic of Laves phase and matrix—gray, matrix—dark.

Table I. The Compositions of Alloys

	Zr	C	$c_{Zr} - c_C$ (at. pct)	f_v (pct) ZrC	f_v (pct) Eutectic
1143	1.05	1.72	−0.67	1.9 + 4.5 (perovskite)	—
1144	2.11	1.58	0.53	2.3	4.2
1181	4.9	1.4	3.5	1.2	41.7
1182	4.8	2.1	2.6	3.9	34.9

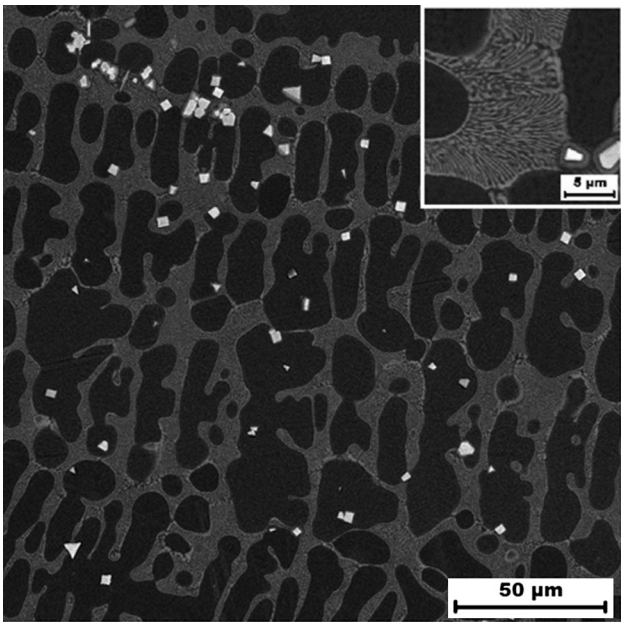

Fig. 3—The phases in the as-cast alloy 1181 (SEM): eutectic of Laves phase, and matrix—gray, ZrC carbide—white, matrix—dark, with the details shown in the upper right corner.

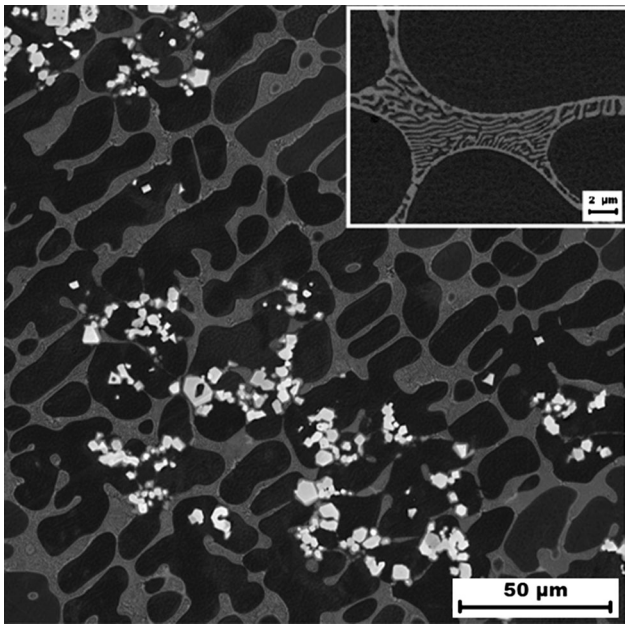

Fig. 4—The phases in the as-cast alloy 1182 (SEM): eutectic of Laves phase and matrix seen as gray, ZrC carbide as white, matrix as dark, the detail in the upper right corner.

curves (1144, 1181, and 1182) with $c_{Zr} - c_C > 0$ with the curve of alloy 1143 with $c_{Zr} - c_C < 0$. This relationship (the influence of concentration of zirconium and carbon) between the four alloys studied is kept even during further deformation, *i.e.,* up to the maximum stress (given also for all alloys and temperatures in Table II). Maximum stress is reached between 5 and 10 pct. compressive strain. The lengths of error bars are comparable with the sizes of symbols, and the bars in Figure 5 are not plotted. The effect is less pronounced at 1073 K (800 °C) probably due to the softness of the matrix. The main effect of softening by the exhaustion of Zr in the aluminide by formation of the ZrC remains.

The solubility of Nb in iron aluminide Fe_3Al is low compared with Zr. For the similarity of ternary diagrams in respect of Fe-Al-Zr and Fe-Al-Nb with Laves phase in Fe corners, see References 13 and 14. The phase structure and the HT strength of the Fe-26Al-4Nb-1C and Fe-26Al-2Nb-1C alloys are compared in References 15 and 16. The structures of both alloys include NbC carbide and $(FeAl)_2Nb$ Laves phase. Only nominal values of $c_{Nb} - c_C$ for the mentioned alloys are available. Thus, it correlates to the above reasoning that the presence of the Laves phase is reported only in the Fe-26Al-4Nb-1C alloy, for which higher values of yield stress 0.2 at HT were observed.

IV. CONCLUSIONS

The amount of the Laves phase λ_1 $(Fe,Al)_2$ Zr in Fe_3Al aluminides is influenced by the presence of carbon (great

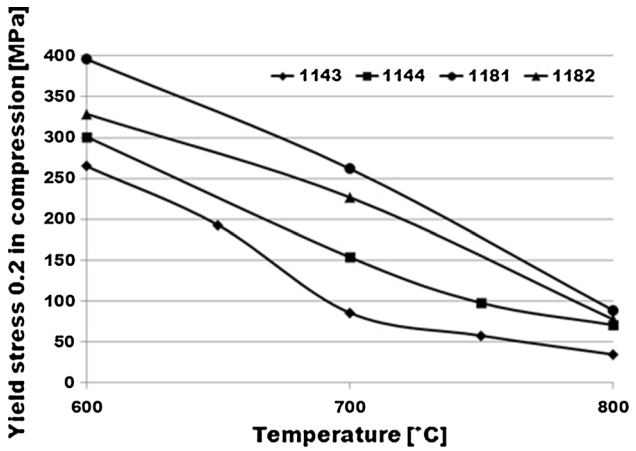

Fig. 5—The dependence of the yield stress 0.2 on temperatures ranging from 873 K to 1073 K (600 °C to 800 °C) for as-cast alloys 1143, 1144, 1181, and 1182.

Table II. Yield Stress 0.2/Maximum Stress of the Tested Alloys (in MPa)

Temperature [K (°C)]	1143	1144	1181	1182
873 (600)	265/408	301/453	396/576	329/518
923 (650)	193/239	—	—	—
973 (700)	86/151	154/202	262/348	227/309
1023 (750)	58/90	98/135	—	—
1073 (800)	35/58	71/82	89/118	78/111

affinity of C to Zr). The formation of ZrC carbides has a negative effect on the HT strength of Fe_3Al type aluminides, while it lowers the amount of Zr available for the formation of the Laves phase, strengthening the aluminide. The eutectic of Laves phase plus matrix enhances the yield stress 0.2 at high temperatures.

The behaviors of Nb-and C-alloyed iron aluminides reported elsewhere can be understood in the same way. For the use Zr or Nb as an additive to iron aluminides in structural materials, the presence of even small concentrations of carbon must be taken in account.

ACKNOWLEDGMENT

The paper is based on the work supported by the Grant Agency of the Czech Republic within the Project 108/12/1452.

REFERENCES

1. C.G. McKamey, P.J. Maziasz, and J.W. Jones: *J. Mater. Res.*, 1992, vol. 7, pp. 2089–2106.
2. C.G. McKamey, P.J. Maziasz, G.M. Goodwin, and T. Zacharia: *Mater. Sci. Eng. A*, 1994, vol. 174, pp. 59–70.
3. C.G. McKamey and P.J. Maziasz: *Intermetallics*, 1998, vol. 6, pp. 303–14.
4. A. Wasilkowska, M. Bartsch, F. Stein, M. Palm, K. Sztwiertnia, G. Sauthoff, and U. Messerschmidt: *Mater. Sci. Eng. A*, 2004, vol. 380, pp. 9–19.
5. A. Wasilkowska, M. Bartsch, F. Stein, M. Palm, G. Sauthoff, and U. Messerschmidt: *Mater. Sci. Eng. A*, 2004, vol. 381, pp. 1–15.
6. F. Stein, M. Palm, and G. Sauthoff: *Intermetallics*, 2005, vol. 13, pp. 1275–85.
7. D.G. Morris, M.A. Muñoz-Morris, and L.M. Requejo: *Acta Mater.*, 2006, vol. 54, pp. 2335–41.
8. D.G. Morris, I. Gutierrez-Urrutia, and M.A. Muñoz-Morris: *Scripta Mater.*, 2007, vol. 57, pp. 449–52.
9. D.G. Morris and M.A. Muñoz-Morris: *Mater. Sci. Eng. A*, 2012, vol. 552, pp. 134–44.
10. D.G. Morris, L.M. Requejo, and M.A. Muñoz-Morris: *Intermetallics*, 2012, vol. 13, pp. 862–71.
11. P. Kratochvil, F. Dobeš, J. Pešička, P. Málek, J. Buršík, V. Vodičková, and P. Hanus: *Mater. Sci. Eng. A*, 2012, vol. 548, pp. 175–82.
12. P. Kejzlar, P. Kratochvíl, R. Král, and V. Vodičková: *Metall. Mater. Trans. A*, 2014, vol. 45A, pp. 335–43.
13. F. Stein, G. Sauthoff, and M. Palm: *Z. Metallk.*, 2004, vol. 95, pp. 469–76.
14. M. Palm: *J. Alloy Compd.*, 2009, vol. 475, pp. 173–77.
15. A. Schneider, L. Falat, G. Sauthoff, and G. Frommeyer: *Intermetallics*, 2003, vol. 11, pp. 443–50.
16. L. Falat, A. Schneider, G. Sauthoff, and G. Frommeyer: *Intermetallics*, 2003, vol. 13, pp. 1256–62.

Intermetallics 20 (2012) 39–46

Contents lists available at SciVerse ScienceDirect

Intermetallics

journal homepage: www.elsevier.com/locate/intermet

The effect of Zr addition on the structure and high temperature strength of Fe-30 at.% Al type alloys

Petr Kratochvíl[a,*], Pavel Kejzlar[b], Robert Král[a], Věra Vodičková[b]

[a] Charles University, Faculty of Mathematics and Physics, Department of Metal Physics, Ke Karlovu 5, Prague 2, CZ-12116, Czech Republic
[b] Technical University of Liberec, Faculty of Mechanical Engineering, Department of Material Science, Studentska 2,460 01 Liberec, Czech Republic

ARTICLE INFO

Article history:
Received 2 May 2011
Received in revised form
19 August 2011
Accepted 21 August 2011
Available online 1 October 2011

Keywords:
A. Iron aluminides based on Fe_3Al
B. Mechanical properties at high temperature

ABSTRACT

The structure of four Fe–30Al alloys with different contents of Zr has been studied. Light optical microscopy (LOM), scanning electron microscopy (SEM) with EDX module, measurement of microhardness as well as X-ray diffraction (XRD) was used to determine the structure and phase composition. Addition of Zr to Fe–30Al leads, in the cast state, to the formation of a Fe–Al matrix with a hard lamellar eutectic skeleton. The eutectic is composed of thin lamellae of λ_1-Laves phase $Zr(Fe,Al)_2$ and Fe–Al ($B2/DO_3$). Annealing at 1000 °C for 200 h results in the formation of the equilibrium phase τ_1 $Zr(Fe,Al)_{12}$. The presence of these phases in the matrix leads to increase of high temperature yield stress and strength.

1. Introduction

Fe_3Al type intermetallics are promising candidates for replacing expensive Ni–Cr-based stainless steel as materials for structural applications due to their outstanding high temperature (H.T.) oxidation resistance, good mechanical strength and relatively low density ($\sim$ 6.0 g/cm^3), good wear resistance and low raw material costs. These materials have high specific moduli (E/ρ) which allows the weight reduction of rotating parts. However, the H.T. mechanical strength and creep properties of Fe_3Al type alloys are not optimal for structural application.

Interest in these materials is growing due to their H.T. environmental resistance. Current research is focused on improvement of H.T. mechanical properties to enable applications up to temperatures in the range of 600 °C–900 °C. The general task, to enhance the H.T. mechanical properties of Fe–Al alloys with 30 at. % Al in temperature range 600–900 °C, i.e. above the DO_3 stability limit may be handled using different methods (for overview see e.g [1–5].):

i) Strengthening by solid solution hardening which is useful for small ternary additions such as Cr, V, Mo and Ti,
ii) strengthening by incoherent precipitates which may be either formed due to ternary additions of Zr, Ta or Nb in higher concentrations (different phases form according to the high temperature isothermal section of phase diagrams), or carbide and boride precipitates, which need additions of C or B (also as quaternary to the above mentioned elements),
iii) strengthening by coherent precipitates which is one of the most effective methods (B2 in A2 and vice versa for Fe–Al–Ni–Cr alloys or $B2+L2_1$ in the Fe–Al–Ta system),
iv) strengthening by increased crystallographic order which stabilises the DO_3 structure to higher temperatures (e.g. Fe–Al–Ti).

The crucial point in the technological procedure is the heat treatment which produces the microstructure. The determining factor for the application of the material is the stability of the microstructure at H.T.

Zirconium was found as a useful alloying element for the Fe_3Al matrix. If the alloy contains carbon or boron, zirconium carbides or borides can be formed [6]. The structure and stability of Laves phases are described in [7,8].

It is known that Zr solid solubility in all phases in Fe–Al alloys is independent of the temperature [8–10] near zero. Even small amounts of Zr lead to the formation of Laves-phase $Zr(Fe,Al)_2$ and/or τ_1-phase $Zr(Fe,Al)_{12}$ [11–13]. The phase relation and equilibrium are obvious from the part of isothermal section of Fe–Al–Zr

* Corresponding author. Tel.: +420 221 911 364; fax: +420 221911 490.
E-mail address: pekrat@met.mff.cuni.cz (P. Kratochvíl).

0966-9795/$ – see front matter © 2011 Elsevier Ltd. All rights reserved.
doi:10.1016/j.intermet.2011.08.007

Table 1
The crystal structures of phases in Fe–Al–Zr diagram [9].

Phase	Composition [at.%]	Lattice type	Prototype
$Zr(Fe,Al)_2$ (λ_1)	20–51.7 Al 23.2–35.2 Zr	Hexagonal	$MgZn_2$
$Zr(Fe,Al)_{12}$ (τ_1)	37.4–61.6 Al 7.9–8.5 Zr	Tetragonal	$ThMn_{12}$

Table 2
Chemical composition of investigated materials.

Alloy	Al [at.%]	Zr[at.%]	Fe[at.%]
30_0	29.3	0.4	Bal.
30_1	29.2	0.9	Bal.
30_2	28.9	1.9	Bal.
30_5	30.1	5.2	Bal.

diagram at 1000 °C [8]. The excess or inhomogeneous distribution of Zr can cause formation of nonequilibria $Fe_3(Al,Zr)$ referred to by Morris et al. [14] and impurity stabilised $(Fe,Al,X)_{23}Zr_6$ described by Stein et al. [8]. These phases are not included in ternary diagrams. The presence of these phases can enhance the mechanical properties [5,9–13]. It is known that very small addition of Zr to Fe–Al alloys with low Al content have a benefical effect on the formation of the protective α-Al_2O_3 scale, improves its adherence and for this reason increases the oxidation resistance at elevated temperatures. Large amounts of Zr proved to have a detrimental effect on the oxidation behaviour [3,11–13]. The moisture-induced hydrogen embrittlement of Fe_3Al can be reduced by addition of small amounts of Zr. The room temperature (R.T.) ductility of Fe_3Al was found to be decreased by alloying with 5 at.% Zr [3,13]. The deformation behaviour of Fe–10Al–2.5Zr and Fe–20Al–2.5Zr was studied and described in [12]. The effect of different Zr content on the structure, mechanical properties and oxidation behaviour of some Fe–10Al, Fe–20Al and Fe–40Al was studied in [13]. It was shown, that 0.2% yield stress continuously decreases with increasing temperature for each composition and it increases with increasing amounts of Laves phase and of τ_1-phase at all temperatures.

Five ternary phases are known in the Fe–Al–Zr system. The phases occurring in the Fe-rich corner of the Fe–Al–Zr are in

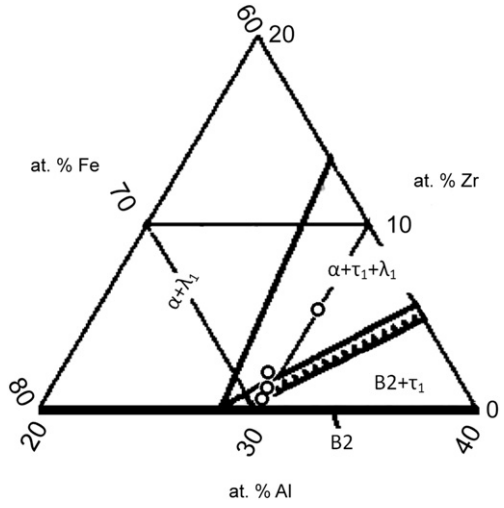

Fig. 1. A part of the ternary Fe–Al–Zr diagram at 1000 °C [9]. The compositions of the investigated alloys are marked by circles.

Table 3
Composition, microstructure and R.T. bulk Vickers hardness of the as-cast alloys.

Alloy	Microstructure of the cast	Volume fraction of the eutectic [%]	Bulk hardness HV0.5
30_0	$B2/D0_3$ + eut ($B2/D0_3+\lambda_1$)	3.4	284 ± 11
30_1	$B2/D0_3$ + eut ($B2/D0_3+\lambda_1$)	8.7	320 ± 6
30_2	$B2/D0_3$ + eut ($B2/D0_3+\lambda_1$)	20.9	325 ± 7
30_5	$B2/D0_3$ + eut ($B2/D0_3+\lambda_1$)	55.2	445 ± 13

Table 1. The lattice parameters of the Laves phase increase linearly with increasing Al and Zr content [8].

The purpose of this paper is to describe the effects of Zr-additions on the structure, phase composition and on the H.T. mechanical properties of Fe_3Al type alloys with 30 at.% Al – a system only rarely investigated previously [11–13]. Both λ_1 Laves phase Zr $(Fe,Al)_2$ and τ_1-phase $Zr(Fe,Al)_{12}$ appear in the Fe–Al ($D0_3$/B2) matrix after proper annealing.

2. Experimental

The samples were prepared by melting and casting in a vacuum induction furnace. Four casts with dimensions of 20 × 40 × 150 mm were prepared. Zr was added in metallic form. The composition is given in Table 2. and in Fig. 1. The mean concentrations of technological impurities (coming from the metals used for the preparation of the alloys) were: 0.1 at.% Cr, 0.01 at.% B, 0.1 at.% Mn, 0.06 at.% C. The alloys (slices 20 × 40 × 10 mm) were also annealed at

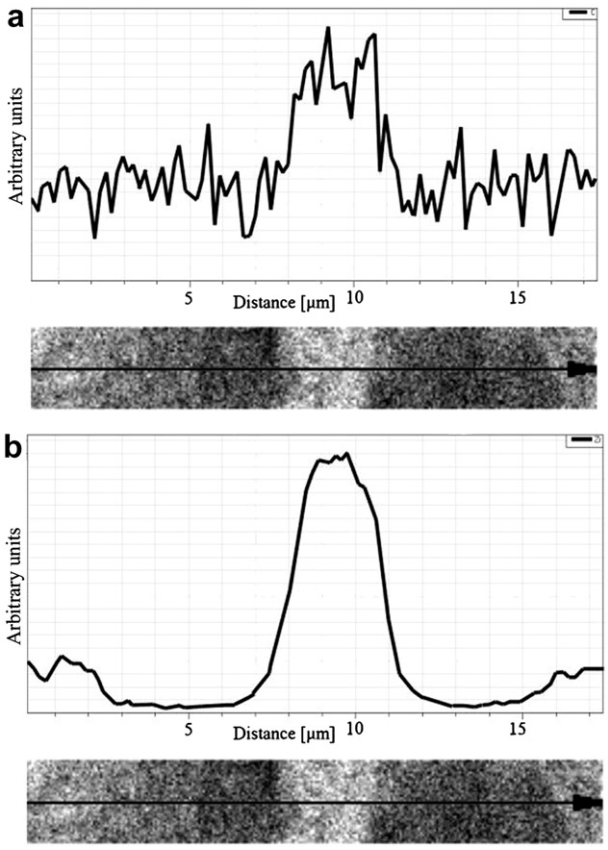

Fig. 2. Line EDX analysis of ZrC particle. Signal received during line profiling from a) carbon (the value of K_α of carbon is limiting for the detection ability of used detector and it causes low signal intensity and higher signal noise), b) zirconium.

1000 °C for 200 h. The annealing was followed by quick cooling in the air outside the furnace.

The samples for light optical microscopy (LOM) were prepared by standard methods. The phase structure and grain boundaries were visualised using mechanical-chemical polishing with the OP-S emulsion (Struers). Nomarski differential interference contrast (NDIC) in LOM was used for better visibility of each phase. The phase composition and the structure were studied using LOM, by a scanning electron microscope (SEM) equipped with an energy-dispersive X-ray analysis system (EDX). X-ray diffraction (XRD) was also applied. The radiation Cu Kα (wavelength $\lambda = 0.1544$ nm) was used. The reflections corresponding to phases identified in the samples are marked on the rocking curves by special symbols. The volume fractions of the observed phases were evaluated by an image analysis of SEM images which were taken in the chemical contrast mode.

The samples for H.T. compression tests were cut from the bulk by spark machining. The surface of samples sized 6 × 6 × 10 mm was polished. Deformations were carried out by digitally controlled testing machine (INSTRON 1186) at temperatures of 600, 700, 800 and 880 °C. Compression tests were performed with a strain rate of 1.5 x 10^{-4} s^{-1}, the temperature was kept with the accuracy of 3 K.

3. Experimental results

3.1. Structure of cast alloys

Volume fractions of the eutectic: matrix Fe–Al + Laves phase $Zr(Fe,Al)_2$ λ_1 see Table 3 and of ZrC were determined. Also the bulk hardness HV0.5 at R.T. is given in Table 3. The volume fraction of the eutectic grows linearly with increasing Zr content from 3.4% at 0.4 at.% Zr to 55.2% at 5.2 at.% Zr.

ZrC particles with dimension of ~ 2 μm appear also in all samples. These particles were formed due to the presence of a small amount of carbon (max 0.06 at.%) as an impurity in the raw Fe-material and due to high affinity of C to Zr [6]. The presence of ZrC cannot be detected by XRD because of its small volume fraction, therefore ZrC particles were identified by EDX (Fig. 2). The volume fraction of ZrC does not exceed 0.02% in all four types of as cast alloys.

3.1.1. Alloy 30_0

Two types of particles (dimensions of 1–5 μm) are visible in the BSE image from the SEM (Fig. 3a): The bright ones are the ZrC particles. Grey particles were identified by EDX as $Zr(Fe,Al)_2$ forming a lamellar eutectic with the Fe–Al (DO_3/B2) matrix. The detailed view of the lamellar eutectic is shown in Fig. 3a.

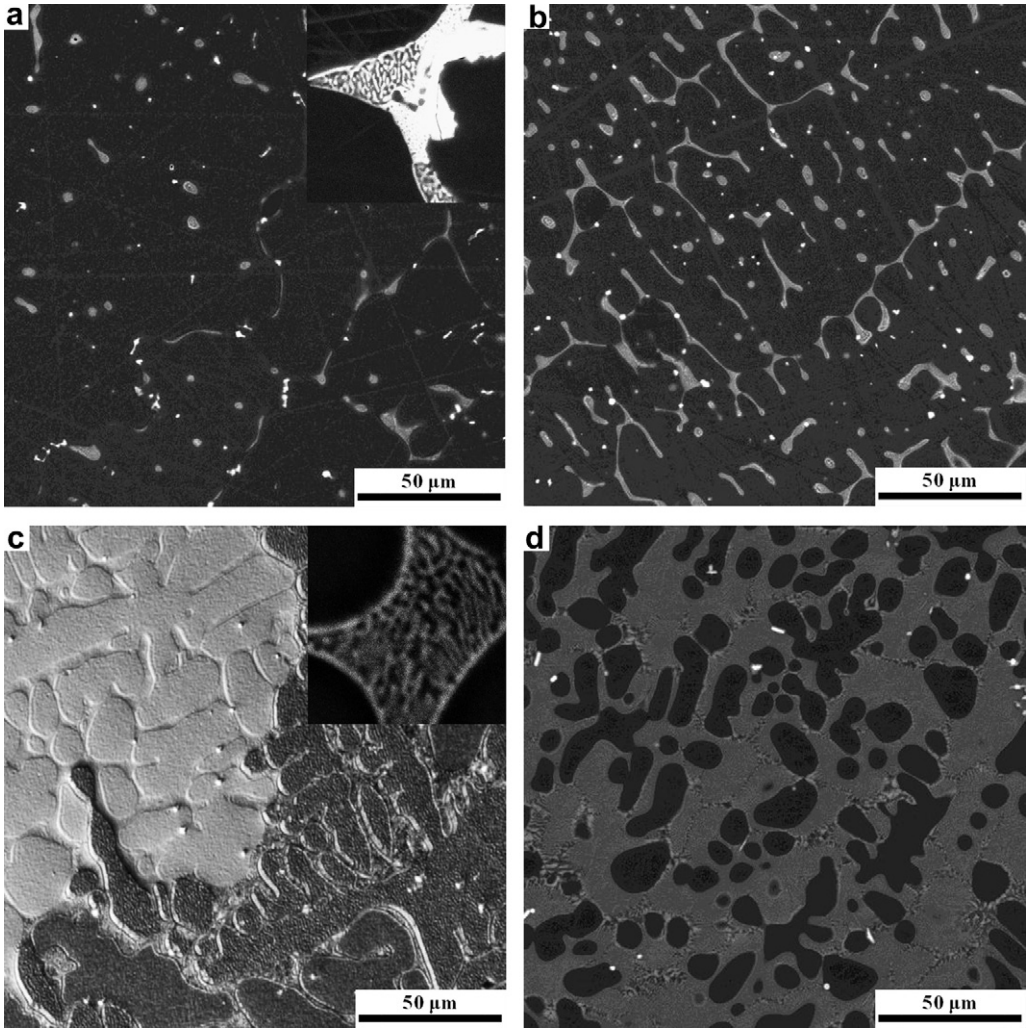

Fig. 3. SEM/LOM images of the as-cast alloys a) 30_0, b) 30_1, c) 30_2, d) 30_5 in chemical contrast. The dark phase is Fe–Al (B2/DO_3), grey areas are eutectic $Zr(Fe,Al)_2$+Fe–Al (DO_3/B2), small bright particles are ZrC.

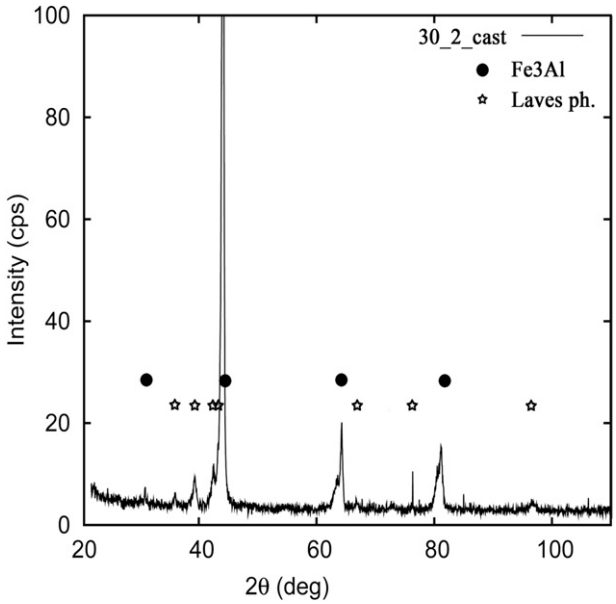

Fig. 4. XRD of 30_2 alloy. Peaks of Fe_3Al and Laves phase λ_1 $Zr(Fe,Al)_2$ are marked.

Both phases $Zr(Fe,Al)_2$ and ZrC are distributed mainly along grain boundaries as can be seen in Fig. 3a. The microhardness of the eutectic is 515 ± 96 HV0.01 and that of the matrix is 291 ± 26 HV0.01.

3.1.2. Alloy 30_1

Two types of phases in the matrix are the same as in alloy 30_0 (λ_1 phase in the eutectic form and ZrC) and are distributed mainly along the grain boundaries (Fig. 3b). The microhardness of the eutectic is 419 ± 71 HV0.01 and of the matrix 297 ± 24 HV0.01.

3.1.3. Alloy 30_2

The eutectic forms a network structure (Fig. 3c), the dark areas are Fe–Al ($B2/DO_3$). The detailed view of the lamellar eutectic is depicted in Fig. 3c. The small bright particles are ZrC. The presence of Laves phase $Zr(Fe,Al)_2$ is documented by XRD (Fig. 4). The microhardness of the eutectic is 468 ± 51 HV0.01; matrix 308 ± 15 HV0.01.

3.1.4. Alloy 30_5

The phase composition is documented by XRD, see Fig. 5. The lamellar eutectic with isolated Fe–Al ($DO_3/B2$) areas is in Fig. 3d. Fig. 6a shows the structure of eutectic in detail. The thickness of the lamellae is about 300 nm. The grain boundaries are identified as the coarsening of the eutectic lamellae, obvious in Figs. 3d and 6b. The bright areas are again particles of ZrC. The microhardness of the eutectic is 722 ± 39 HV0.01, Fe_3Al 311 ± 27 HV0.01.

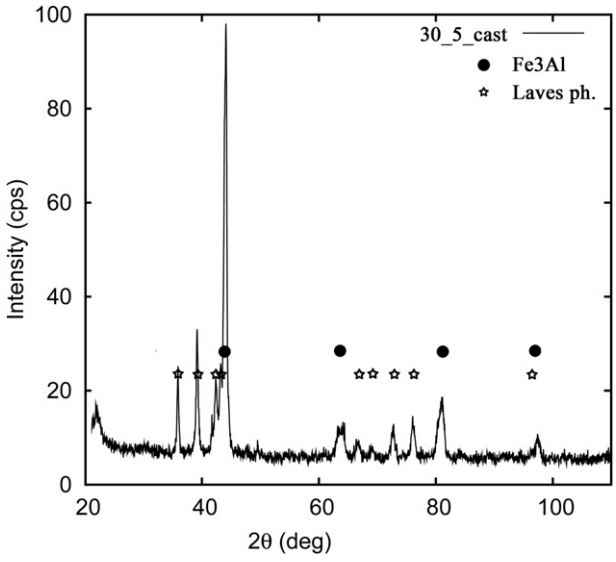

Fig. 5. XRD of cast 30_5 alloy. Peaks of Fe_3Al and Laves phase λ_1 $Zr(Fe,Al)_2$ are marked.

3.2. Structure of the annealed alloys

The result of the heat treatment (annealing at 1000 °C for 200 h) is (in agreement with the phase diagram [8]) the decomposition of the primary eutectic structure to λ_1 and τ_1 phases. The structure

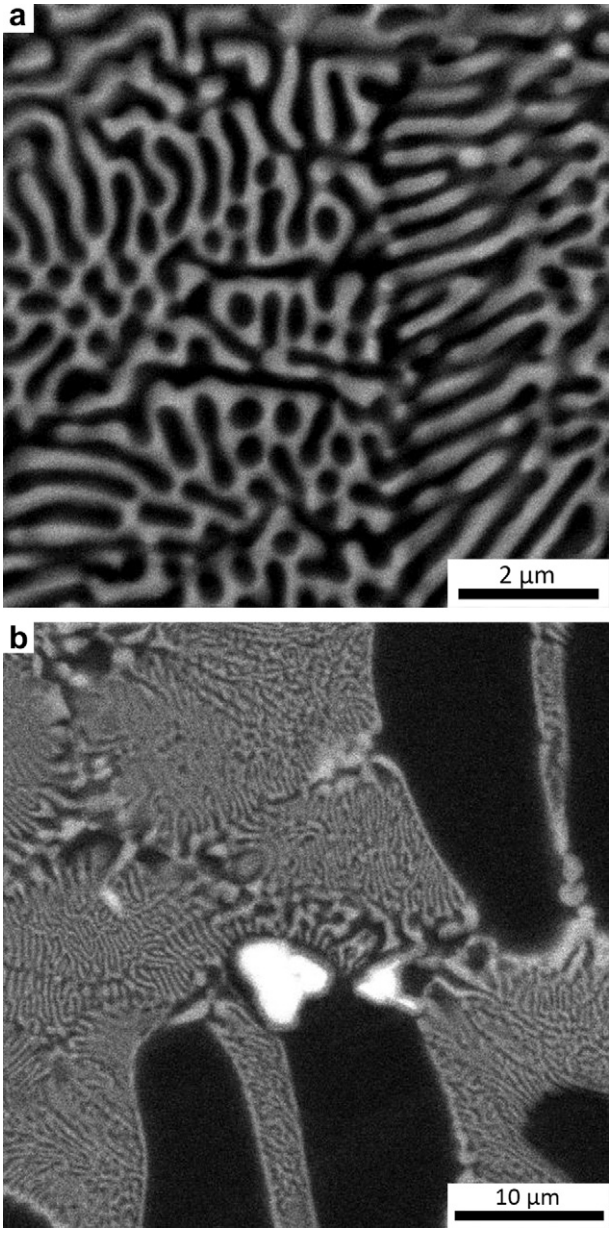

Fig. 6. SEM image of the as-cast alloy 30_5. a) Detail of the structure of the lamellar eutectic. The bright phase is $Zr(Fe,Al)_2$ Laves phase, the dark one is Fe–Al. b) Coarsening of the eutectic along the grain boundary. The bright particles are ZrC.

Table 4
Composition, microstructure and R.T. bulk Vickers hardness of the annealed alloys.

Alloy	Microstructure after heat treatment	Volume fraction of λ_1 [%]	Volume fraction of τ_1 [%]	Bulk hardness HV0.5
30_0	B2/D0$_3$ + λ_1 + τ_1	0.2	3.4	290 ± 7
30_1	B2/D0$_3$ + λ_1 + τ_1	5.0	5.5	308 ± 5
30_2	B2/D0$_3$ + λ_1 + τ_1	7.2	16.1	374 ± 21
30_5	B2/D0$_3$ + λ_1+τ_1	18.6	35.4	525 ± 19

imaged by SEM was used for calculating of the volume fraction of observed phases (Table 4). The amount of both phases grows linearly with addition of Zr. The bulk hardness HV0.5 of annealed samples at R.T. is given in Table 4. The structure of annealed samples taken by SEM with chemical contrast is in Fig. 7a–d. The ZrC phase remains in the structure of all alloys as small particles (size < 2 μm). They are easily visible in the structure of 30_0 alloys (Fig. 7a) - ZrC phase (white particles) and λ_1 phase (bright grey areas). In the case of other alloys, Zr carbides are evident only in higher magnification either as white particles or as core inside the λ_1 phase – a detailed view is in Fig. 7b. In Fig. 7b–d bright flakes and round particles are the (Fe,Al)$_2$Zr Laves phase, grey areas are

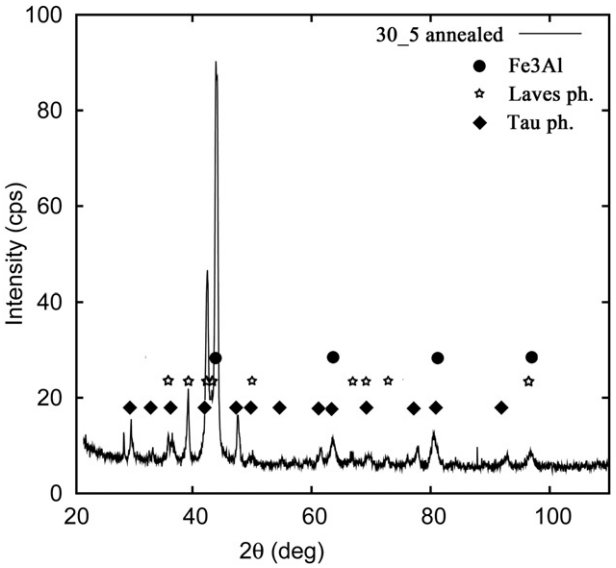

Fig. 8. XRD of annealed 30_5 alloy.

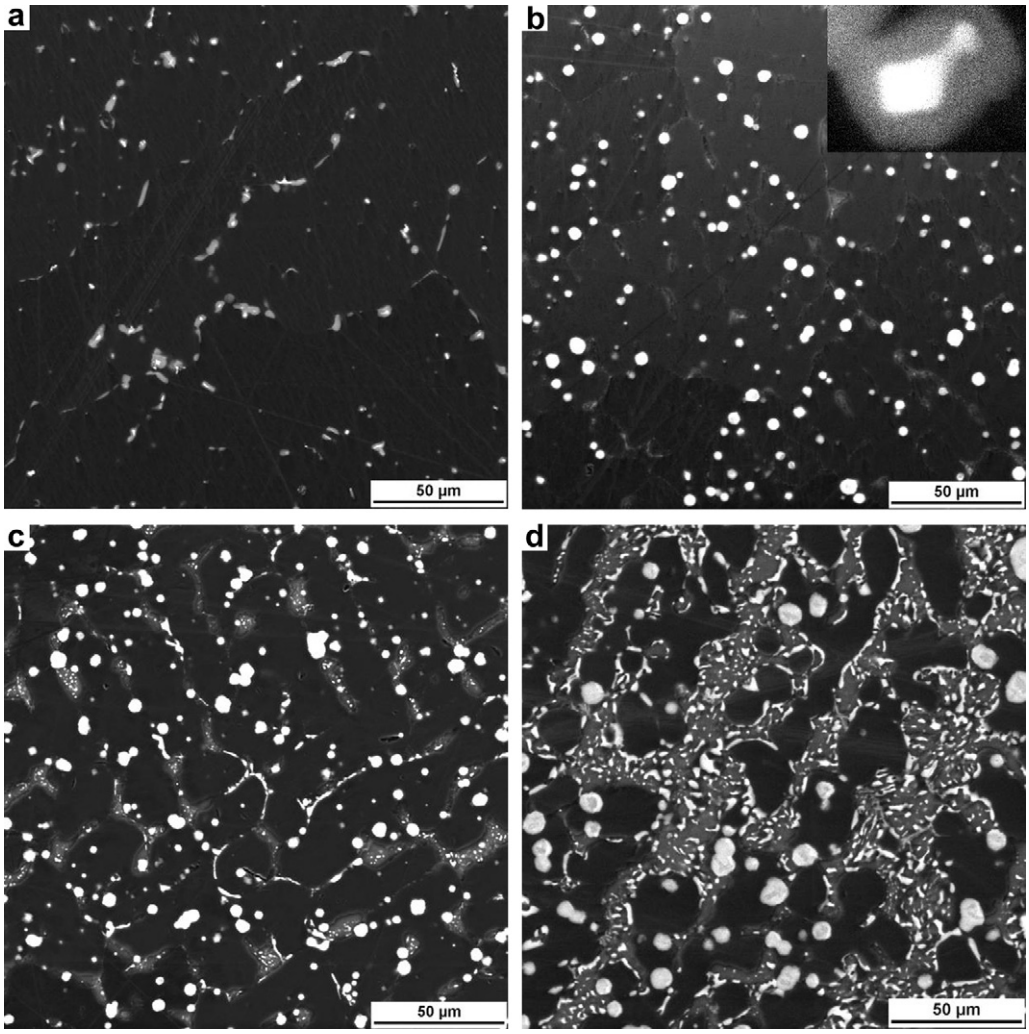

Fig. 7. SEM images of the annealed alloys a) 30_0, b) 30_1, c) 30_2, d) 30_5 in chemical contrast. In the structure of 30_0 alloys (Fig. 7a) - ZrC phase (white particles) and λ_1 phase (bright grey areas). In the case of other alloys (Fig. 7b–d): the dark phase is Fe–Al (B2/D0$_3$), grey areas are τ_1-phase Zr(Fe,Al)$_{12}$, bright flakes and round particles are λ_1-Laves phase Zr(Fe,Al)$_2$. The presence of ZrC documented in the detailed image in Fig. 7b as bright nucleus inside Laves phase λ_1 Zr(Fe,Al)$_2$.

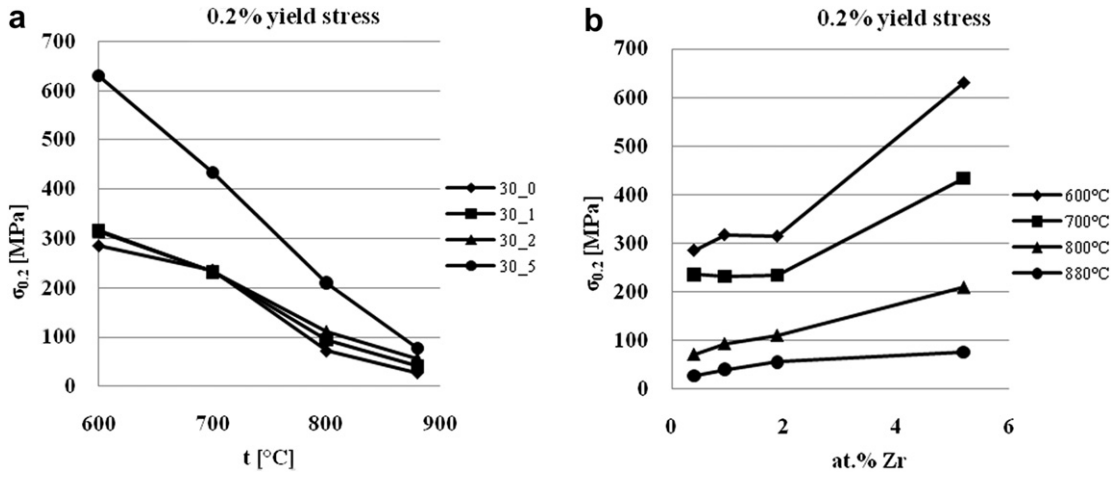

Fig. 9. The dependence of a) 0.2% yield stress on the temperature for different content of Zr, b) 0.2% yield stress on the Zr content for different temperatures.

the τ_1 phase and Fe–Al is dark. For comparison with Fig. 5, the XRD of annealed 30_5 alloy is shown in Fig. 8. Peaks of τ_1 phase are marked by black squares.

3.3. The influence of the composition and temperature on the H.T. strength

The dependences of 0.2% yield stress on temperature for different Zr contents in the cast alloy can be seen in Fig. 9a and the related dependences on Zr content for different temperatures in Fig. 9b. Similar curves for the ultimate strength in compression are in Fig. 10a and b.

It is obvious that the 0.2% yield stress and the strength are decreasing with increasing temperature. Pronounced increases in both, the 0.2% yield stress and the strength, are observed in the alloy with 5 at.% of Zr, its values are twice as high as for other alloys for all temperatures.

Additional XRD of formerly as cast 30_5 samples deformed at 800 °C (samples were "annealed" for 2 h) was performed. The beginning of the formation of reflections corresponding to the τ_1-phase $Zr(Fe,Al)_{12}$ can be seen. SEM observations do not document the presence of τ_1 during the deformation of formerly as cast 30_5 at 800 °C. Nevertheless it must be mentioned that the formation of τ_1 during the H.T. deformation of these samples contribute to their work hardening.

The deformation took place mainly in the ductile Fe–Al phase. With a lower content of Zr, the increase of H.T. strength is small.

3.4. The effect of annealing on the H.T. strength

The effect of heat treatment (1000 °C/200 h/air) on the H.T. mechanical properties was studied for alloys 30_2 and 30_5. The results of mechanical testing are obvious from Figs. 11 and 12.

For the alloy with 2 at.% of Zr, values of $\sigma_{0.2}$ (Fig. 11a) are almost the same at all four temperatures. On the other hand, the ultimate strength values σ_{MAX} at 600 °C (Fig. 11b) decreased strongly. At higher temperatures the decrease becomes less significant and nearly zero at 800 °C. The positive effect of the heat treatment on the alloy 30_5 is substantial (Fig. 12a,b). The values of both $\sigma_{0.2}$ (Fig. 12a) and σ_{MAX} (Fig. 12b) are higher.

The increase of H.T. characteristics after heat treatment can be connected with the appearance of the τ_1 phase. No effect of the presence of τ_1 phase on the H.T. strength was observed for lower contents of Zr (up to ~ 2 at.%), i.e. for lower volume fractions of τ_1 phase (see Table 4). On the other hand, the effect in the alloy 30_5 is substantial.

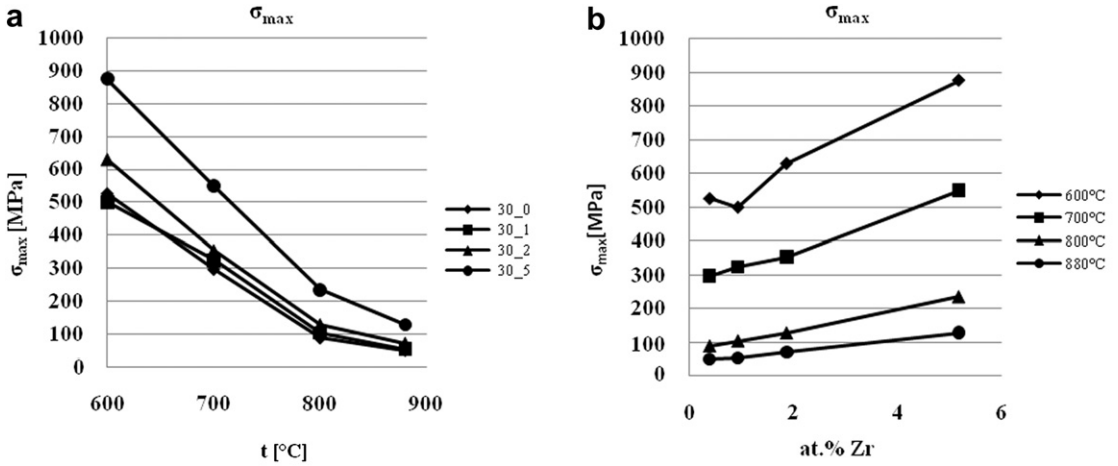

Fig. 10. The dependence of a) ultimate strength on the temperature for different content of Zr, b) ultimate strength on the Zr content for different temperatures.

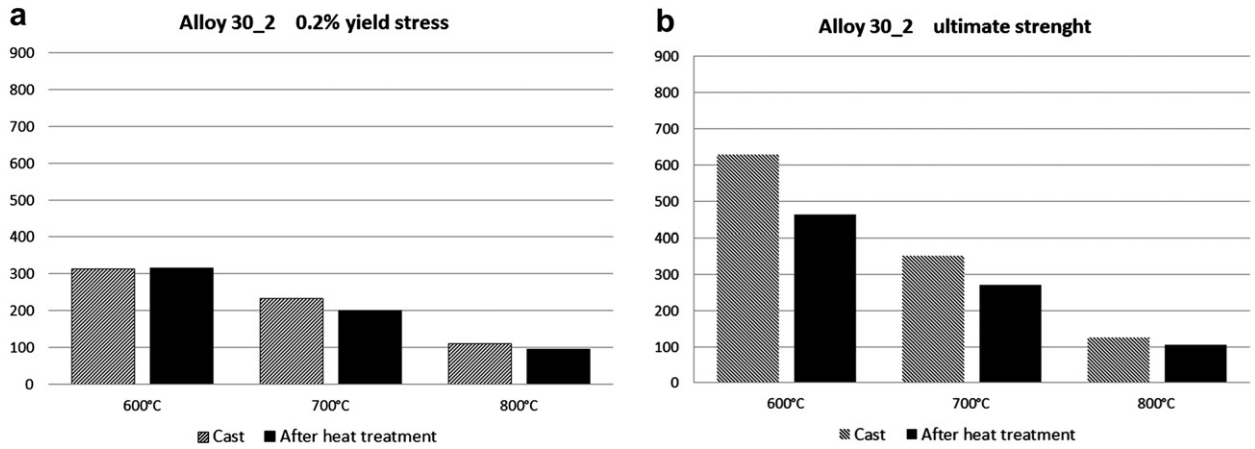

Fig. 11. The dependence of a) 0.2% yield stress, b) ultimate strength of alloy 30_2 on the temperature and the heat treatment.

4. Discussion

It is worth noting that the addition of Zr to Fe–30Al alloy is very effective in enhancing the strength of the material with 5 at.% Zr. Additions of Zr up to 2 at.% have no pronounced effect. The addition of Zr to Fe–30Al alloy leads to the formation of Laves phase λ_1 $Zr(Fe,Al)_2$. Its volume increases with increasing content of Zr. This phase is distributed mainly along the grain boundaries and forms mainly the eutectic with ordered $D0_3$ material.

The eutectic usually has a lamellar structure (Fig. 6). The great difference in the mechanical properties of Fe–Al ($D0_3$/B2) and the hard λ_1 phase (see data in [13]) may cause the brittle behaviour of the alloy at R.T.

The hardening effect of the Laves phase in as cast alloy at H.T. is obvious in Figs. 9 and 10. Both, 0.2% yield stress and ultimate strength increase with increasing content of Zr and decrease with increasing temperature for all concentrations of Zr.

Recent similar investigations by Stein et al. [13] and by Wasilkowska et al. [12] used mostly lower concentrations of Al (10 at.% and 20 at.%) or higher (40 at. %) than in the present paper. Nevertheless, the cited results can be compared. In Fig. 13 our data are given together with those obtained in [13]. It is obvious, that the values of the yield strength of the alloy 30_5 at temperatures 600–880 °C are higher as those with 10 or 20 at.% Al [13]. This may be due to the ordered B2 matrix in comparison to the A2 matrix of the compared materials [14].]. As was mentioned in Section 3.3 the formation of the equilibrium τ_1 phase during the deformation at 800 °C can be very important. It is documented that τ_1 phase enhances the H.T. ultimate and yield strength of the annealed alloy 30_5.

A similar comparison is possible for the alloy 30_2 with results obtained for the material with 2.5 at.% Zr in [12] (see Fig. 14). The argument is the same in this case.

The annealing at 1000 °C for 200 h resulted into the formation of a three phase structure. Fine eutectic λ_1 + Fe–Al transformed into the mixture of λ_1 and τ_1 phase (corresponds well to the equilibrium Fe–Al–Zr diagram).

It is obvious that the heat treatment of alloy 30_2 does not affect the 0.2% yield stress significantly. On the other hand, the structural changes caused by the heat treatment of alloy 30_5 (formation of τ_1) led to a significant increase of the 0.2% yield stress. The increase depends on temperature. At lower temperatures it is more pronounced, at temperatures around 800 °C it is inconsiderable.

The increase of H.T. mechanical properties might be explained by the increase of the fraction of Zr-containing hard intermetallic phases (λ_1 and τ_1) and the decrease of the amount of soft Fe–Al.

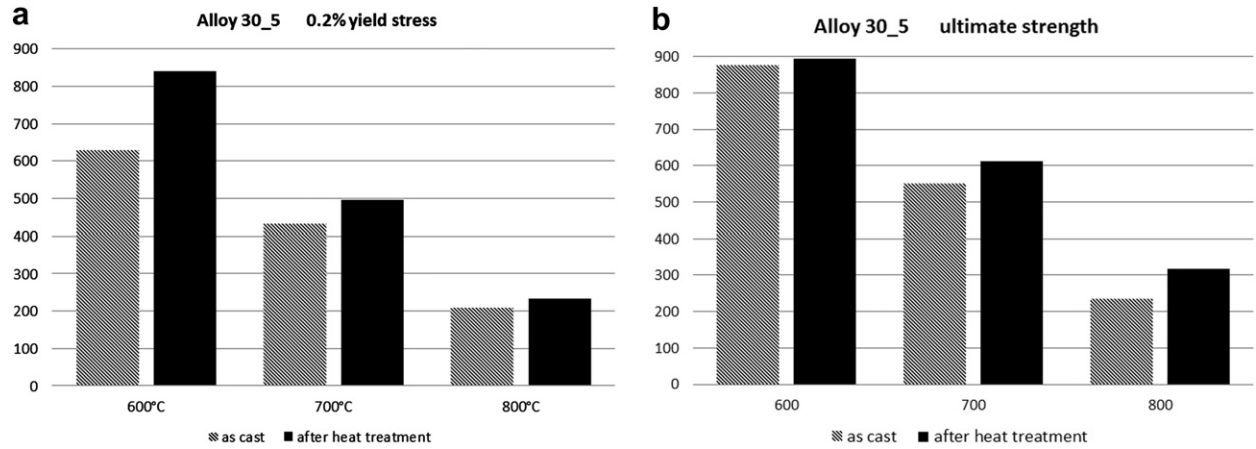

Fig. 12. The dependence of a) 0.2% yield stress, b) ultimate strength of alloy 30_5 on the temperature and the heat treatment.

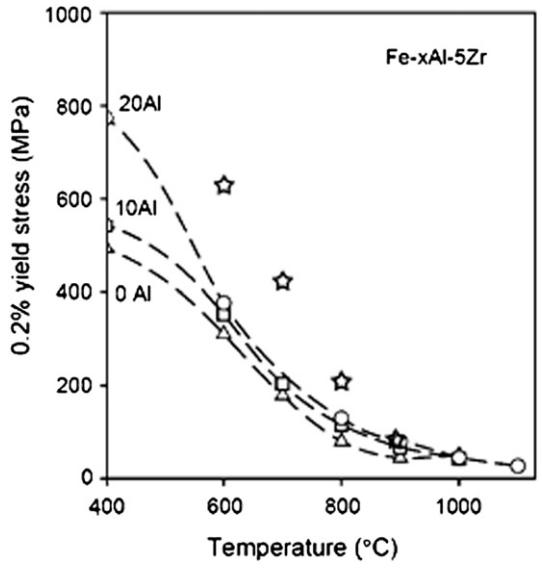

Fig. 13. The temperature dependence of the yield stress of the alloys (10 and 20 at.% Al) with 5 at.% of Zr [14] compared to data for alloy 30_5 (☆).

The strength of the two or three phase material (the as cast and the annealed ones) tested should be interpreted as the strength of a composite material: e.g. the value of the $\sigma_{0.2}$:

$$\sigma_{0.2\text{composite}}(T) = f_{\text{matrix}} \cdot \sigma_{0.2\text{matrix}}(T) + f_{\lambda_1} \cdot \sigma_{0.2\ \lambda_1}(T) + f_{\tau_1} \cdot \sigma_{0.2\ \tau_1}(T), \quad (1)$$

where $\sigma_{0.2n}$ and f_n are the yields stress and the volume fraction respectively of the three phases forming the material.

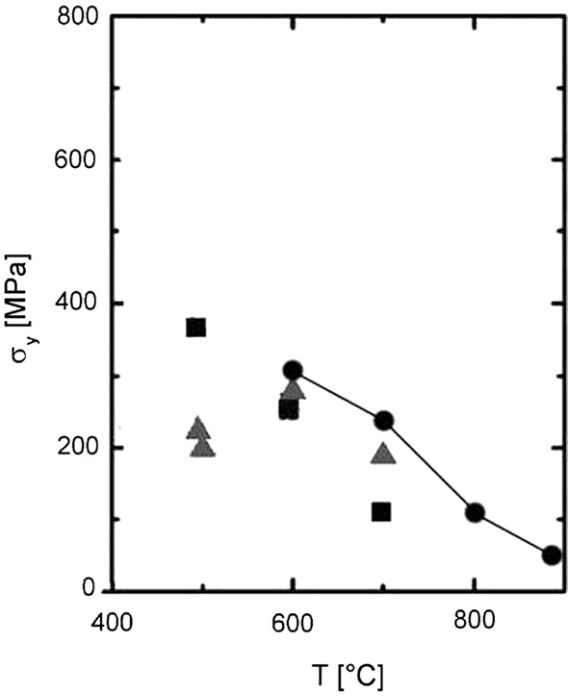

Fig. 14. The temperature dependence of the yield stress of the alloys (10 and 20 at.% Al) with 2.5 at.% Zr [13] compared to data for alloy 30_2 (solid circles). Data [13] for alloy F10AZ - solid triangles, for F20AZ - solid squares.

However, such a procedure cannot be applied. Only H.T. $\sigma_{0.2}$ values for the matrix with ZrC are available in [15] in which the composition of the material was very near to the matrix in the present paper. The values for hard phases λ_1 and τ_1 will be not become available as they are brittle up to ~ 950 °C [8].

5. Conclusions

1) The addition of Zr to Fe–30 at.% Al alloy leads in as cast state to the formation of a matrix strengthened by lamellar eutectic, Laves phase λ_1 $Zr(Fe,Al)_2$ + Fe–Al ($D0_3$/B2). The appearance of cubic ZrC particles is due to the presence of carbon in raw iron and its high affinity to Zr.
2) The presence of Laves phase λ_1 $Zr(Fe,Al)_2$ enhances both the H.T. yield strength and the ultimate strength of the alloy. This strengthening effect by the Laves phase decreases with increasing temperature.
3) The three-phase alloy Fe–Al ($D0_3$/B2) + λ_1 + τ_1 , formed after annealing at 1000 °C for 200 h leads to a significant increase of H.T. 0.2% yield stress of the material with 5 at.% Zr.
4) Compared to alloys with 10 and 20 at.% of Al examined in [12,13], the values of the H.T. strength and yield stress of Fe30AlxZr are higher for the same amount of Zr (2 and 5 at.%).

Acknowledgement

The authors wish to thank doc. RNDr. S. Daniš, Ph.D., who kindly carried out the XRD phase analysis and to Prof. Ing. Ivo Schindler, Dr Sc., who provided the alloys. This work is a part of research plans MSM 4674788501 which is financed by the Ministry of Education, Youth and Sport of the Czech Republic and is a part of the research supported by Grant Agency of the Czech Republic within the project 106/08/1238.

References

[1] Liu CT, Stringer J, Mundy JN, Horton LL. Angelini. Ordered intermetallics alloys: an assessment. Intermetallics 1997;5:579.
[2] McKamey CG, DeVan JH, Tortorelli PF, Sikka VK. A review of recent developments in Fe_3Al-based alloys. J Mater Res 1991;8:1779.
[3] Stoloff NS, Liu CT. In: Li JCM, editor. Microstructure and properties of materials, vol. 2. Singapure: World Scientific Publishing Co; 2000. p. 139.
[4] Morris DG. Possibilities for high-temperature strengthening in iron aluminides. Intermetallics 1998;6:753.
[5] Palm M. Concepts derived from phase diagram studies for the strengthening of Fe-Al-based alloys. Intermetallics 2005;13:1286.
[6] Cieslar M, Karlík M. Carbide formation in Zr-containing Fe_3Al-based alloys. Mater Sci Eng A 2007;462:289.
[7] Stein F, Palm M, Sauthoff G. Structure and stability of Laves phases part II-structure type variation in binary and ternary systems. Intermetallics 2005; 13:1056.
[8] Stein F, Sauthoff G, Palm M. Phases and phase equilibria in the Fe-Al-Zr system. Z Metallkd 2004;95:469.
[9] Raghavan V. Al-Fe-Zr (Aluminium-Iron-Zirconium). J Phase Equi Diff 2010;31: 459.
[10] Rigaud V, Sundman B, Daloz D, Lesault G. Calphad 2009;33:442.
[11] Wasilkowska A, Bartsch M, Stein F, Palm M, Sztwiertnia K, Sauthoff G, et al. Plastic deformation of Fe-Al polycrystals strengthened with Zr-containing Laves phases: I. Microstructure of undeformed materials. Mat Sci Eng A 2004;380:9.
[12] Wasilkowska A, Bartsch M, Stein F, Palm M, Sauthoff G, Messerschmidt U. Plastic deformation of Fe-Al polycrystals strengthened with Zr-containing Laves phases: II. Mechanical properties. Mat Sci Eng A 2004;381:1.
[13] Stein F, Palm M, Sauthoff G. Mechanical properties and oxidation behaviour of two-phase iron aluminium alloys with $Zr(Fe, Al)_2$ Laves phase or $Zr(Fe.Al)_{12}$ τ_1 phase. Intermetallics 2005;13:1275.
[14] Morris DG, Muñoz-Morris MA, Requejo LM. New iron-aluminium alloy with thermally stable coherent intermetallic nanoprecipitates for enhanced high-temperature creep strength. Acta Mater 2006;54:2335.
[15] Kratochvíl P, Málek P, Cieslar M, Hanus P, Hakl J, Vlasák T. High-temperature mechanical properties of Zr alloyed Fe_3Al-type iron aluminides. Intermetallics 2007;15:333.

Phase Structure and High-Temperature Mechanical Properties of Two-Phase Fe-25Al-*x*Zr Alloys Compared to Three-Phase Fe-30Al-*x*Zr Alloys

PAVEL KEJZLAR, PETR KRATOCHVÍL, ROBERT KRÁL, and VĚRA VODIČKOVÁ

The structure and high-temperature mechanical properties of Fe-30 at. pct Al and Fe-25 at. pct Al alloys with various Zr contents are compared. The scanning electron microscope images in chemical contrast mode (R-BSE) as well as EDS, EBSD, and X-ray diffraction were used to determine the structure and phase composition. The as-cast alloys (both Fe-30Al and Fe-25Al) were observed to be two-phase DO_3/B2 + Laves phase λ_1 $(Fe,Al)_2Zr$ alloys with typical fine lamellar eutectic areas. During the heat treatment of the Fe-25Al alloys, their structure transformed from a DO_3/B2 matrix with fine lamellar eutectic into λ_1 globular particles situated in a DO_3/B2 matrix. The same structure of Fe-30Al alloys decomposed into three phases: λ_1 and τ_1 $Zr(Fe,Al)_{12}$ particles in a DO_3/B2 matrix. The hardening in both groups of alloys (Fe-25Al and Fe-30Al) due to the presence of Zr-containing λ_1 and τ_1 phases is compared.

DOI: 10.1007/s11661-013-1987-1

I. INTRODUCTION

RECENTLY, considerable effort has been devoted to the research and development of Fe-Al-based alloys. While basic research has been focused on understanding the deformation mechanisms and brittleness, applied research has concentrated on improving the mechanical and metallurgical properties of these alloys through the control of composition and microstructure and materials processing optimization.[1–3]

The improvement of high-temperature (H.T.) mechanical properties of Fe_3Al iron aluminides remains the main task of the present research. The interval between 873 K and 1173 K (600 °C and 900 °C), *i.e.*, above the stability limit of DO_3, is the region of interest. The corrosion resistance is often crucial. Different methods may be used to enhance the H.T. mechanical properties (see, *e.g.*, in References 4, 5):

a) Strengthening by solid solution hardening (*e.g.*, with Cr, Ti, Mn, Mo, Si, V, or Ni), which is achieved through the small ternary addition of elements soluble in Fe_3Al.
b) Strengthening by incoherent precipitates of phases (*e.g.*, using Nb, Cu, Ta, Zr, B, or C additions) formed mainly with higher concentrations of the ternary addition. If, in this case, the amount of the additive and the volume fraction of phases formed in the alloy increase, the strengthening exhibits a composite character, which is highly dependent on the geometry of the phase that originates in the as-cast or heat-treated alloy. In alloys with carbide- or boride-forming elements, their role is then very important.[6,7]
c) Strengthening by coherent precipitates, which is a very effective method.
d) Strengthening by increased crystallographic order, which stabilizes the DO_3 structure to higher temperatures, which is a method that is used very often.

The microstructure necessary to enhance the H.T. mechanical properties is produced mainly using a technological procedure in which the heat treatment is often the determining process. The determining factor for the application of the material is the stability of the microstructure at high temperatures.

The beneficial effect of Zr and Nb addition on H.T. strength was first reported by McKamey and Maziasz, see, *e.g.*, in Reference 8, summarizing the results obtained for a complex alloy containing 28 pct Al, 5 pct Nb, 0.8 pct Mo, 0.025 pct Zr, 0.05 pct C, and 0.005 pct B. Zirconium was observed to be a useful alloying element for the Fe_3Al matrix. Zr solid solubility in all phases in Fe-Al alloys is known to be nearly zero (independent of the temperature), which is why even a small addition of Zr to a Fe-Al alloy leads to the precipitation of λ_1 Laves phase $Zr(Fe,Al)_2$ and/or τ_1 phase $Zr(Fe,Al)_{12}$. An iron-rich part of the isothermal cut of the diagram at (1273 K) 1000 °C is presented in Figure 1.[9]

The deformation behavior of Fe-10Al-2.5Zr and Fe-20Al-2.5Zr was studied and described by Wasilkowska *et al.*[10,11] The concentrations of elements are given in

PAVEL KEJZLAR, Junior Researcher, and VĚRA VODIČKOVÁ, Senior Assistant Professor, are with the Department of Material Science, Faculty of Mechanical Engineering, Technical University in Liberec, Liberec, Czech Republic. PETR KRATOCHVÍL, Professor, and ROBERT KRÁL, Associate Professor, are with the Department of Physics of Materials, Faculty of Mathematics and Physics, Charles University in Prague, Prague, Czech Republic. Contact e-mail: pekrat@met.mff.cuni.cz

Manuscript submitted May 13, 2013.
Article published online September 7, 2013

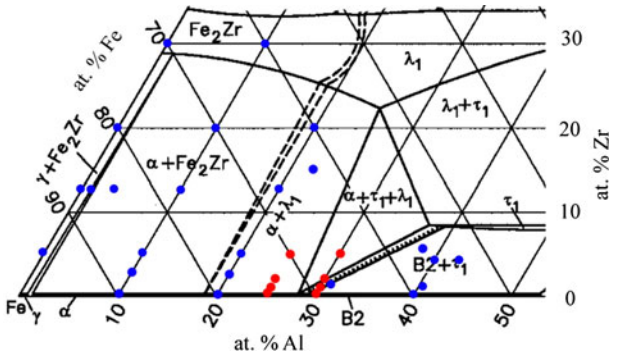

Fig. 1—An iron-rich part of an isothermal section through the Fe-Al-Zr ternary diagram at 1273 K (1000 °C).[9] The compositions of investigated alloys are marked by red dots. The compositions of the alloys tested in Refs. [10–12] are indicated by blue dots.

at. pct in this paper. The 0.2 pct yield stress was observed to continuously decrease with increasing temperature for each composition and increased with increasing amounts of Laves phase at all temperatures. The effect of different Zr content on the structure, mechanical properties, and oxidation behavior of select Fe-10Al, Fe-20Al, and Fe-40Al alloys was studied by Stein *et al.*[12] In addition, Morris *et al.*[13] noticed the enhancement of H.T. creep properties of Fe-20Al with additions of Zr. A very small addition of Zr to Fe-Al alloys with a low Al content results in a beneficial effect on the formation of the protective α-Al_2O_3 scale, improves its adherence and therefore increases the oxidation resistance at elevated temperatures. Large amounts of Zr have proven to produce a detrimental effect on the oxidation behavior.[12]

It is the purpose of the present paper to compare the structure and H.T. mechanical strength of two-phase Fe-25Al-*x*Zr alloys to three-phase Fe-30Al-*x*Zr alloys in their as-cast and annealed states while also considering the effect of both the Al and Zr contents on the volume fractions of the phases. Zr is tested as an important addition to improve H.T. mechanical properties for the structural uses of iron aluminides. Therefore, it was decided to complete the prior data[10–12] collected in the Fe corner of the Fe-Al-Zr phase diagram, which mainly corresponded to the two-phase fields (λ_1 + B2/DO_3) and (τ_1 + B2/DO_3). The alloys studied in the present paper are situated both in the two-phase (λ_1 + B2/DO_3) and in the three-phase (λ_1 + τ_1 + B2/DO_3)[14] fields, and their structure and H.T. mechanical properties are compared.

II. EXPERIMENTAL

The examined alloys were prepared by vacuum melting and casting; Zr was added in metallic form. The dimensions of the casts were 20 mm × 40 mm × 150 mm. The chemical compositions are listed in Table I and marked in a part of the ternary Fe-Al-Zr diagram in Figure 1. The labels from Table I will be used in the following text, *i.e.*, Fe-25Al-*x*Zr and Fe-30Al-*x*Zr alloys will be labeled as 25-x and 30-x, respectively. The concentrations of the technical impurities (originating from the metals used for the preparation of the alloys) were: 0.1 pct Cr, 0.01 pct B, 0.1 pct Mn, and 0.06 pct C. The compositions were selected to cover the area near the Fe_3Al composition (the room temperature DO_3 structure), *i.e.*, either the two-phase area B2 + λ_1 or the three-phase area B2 + λ_1 + τ_1.

Table I. Labeling of Investigated Fe-25Al-*x*Zr and Fe-30Al-*x*Zr Alloys and Their Chemical Composition

Alloy Labelling	Al	Zr
25-0	25.7	0.3
25-1	25.7	1.0
25-2	25.5	2.0
25-5	25.4	5.0
30-0	29.3	0.4
30-1	29.2	0.9
30-2	28.6	1.9
30-5	30.1	5.2

Annealing was performed in an electrical furnace at 1273 K (1000 °C) for 200 hours followed by slow cooling in air. The aim of the heat treatment was to approach the equilibrium alloy state according to the Fe-Al-Zr diagram (Figure 1).

Samples for metallographic investigation were cut by IsoMet 1000 precision saw from a bulk material and then embedded into electric conductive resin (Probemet-Buehler). The studied surface was carefully grinded and polished using a set of diamond suspensions (Stuers Diapro 9-1 μm) on an automatic polishing device (Stuers Tegramin 20). Colloidal silica (Stuers OP-S suspension) was used for the final polishing step. Finally, the samples were milled on the SEM-Mill 1060 (Fishione) by Ar ions at 2 kV for 20 minutes to remove the Beilby layer and make the samples susceptible for EBSD analysis.

The phase contrast for the light optical microscopy (LOM—ZEISS) was enhanced through mechanical-chemical polishing with colloidal silica (OP-S—Struers). Circular differential interference contrast (C-DIC) was used. Scanning electron microscopy (SEM—ZEISS) images were taken using chemical contrast. These images were used for image analysis to calculate the volume fractions of the phases. The phases were also identified based on energy-dispersive X-ray spectroscopy (EDS—Oxford), electron backscatter diffraction (EBSD—Oxford), and X-ray diffraction (XRD—Seiphert) using Cu-K_α irradiation results. The description of the structure of the alloys (for each composition and state—as-cast and annealed) was based on the combined use of observation techniques. The procedure is illustrated in Figure 2 in the correlative microscopy image. As an example, the structure of the annealed 30_5 alloy is presented. From the right to the left side of the images, the LOM, SEM, and EDS results are presented. For easier description and comparison of the structures of both sets of alloys (25_x and 30_x), only the SEM pictures of all the cases are presented in the paper.

The samples for high-temperature testing with the dimensions of 6 mm × 6 mm × 10 mm were prepared using electro-discharge machining (EDM), and their surfaces were subsequently carefully polished using

sandpaper grid 1200 with a special emphasis on the surfaces parallelism. The high-temperature deformations were performed using a digitally controlled testing machine (INSTRON 1186) at the temperatures of 873 K, 973 K, 1073 K, and 1153 K (600 °C, 700 °C, 800 °C, and 880 °C) with accuracy of 3 K (3 °C). Compression tests were performed using a strain rate of 1.5×10^4 s^{-1}.

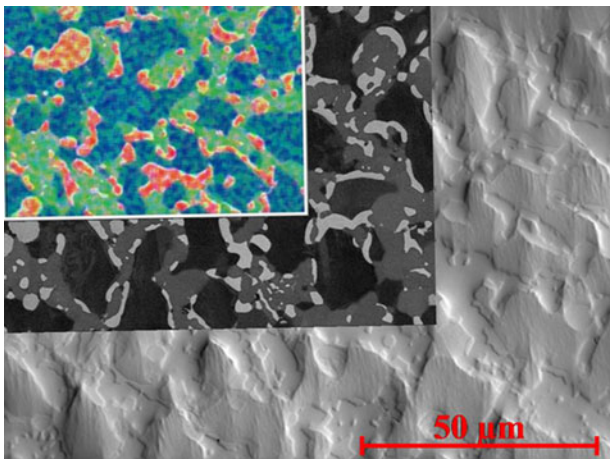

Fig. 2—An example of the correlative microscopy of the annealed alloy 30-5. From the right to the left, LOM, SEM, and EDS results. The phases: DO_3/B2—black, blue; λ_1—light, red; τ_1—gray, green.

III. EXPERIMENTAL RESULTS AND DISCUSSION

The structure of the cast Fe-25Al alloys is characterized by the presence of an eutectic composed of the Fe_3Al matrix and λ_1 Laves phase $Zr(Fe,Al)_2$. The structure of the individual alloys is clear in Figure 3. The volume fraction $f_v(e)$ of the eutectic grows linearly with increasing Zr content from $f_v(e) = 3.9$ pct at 0.3 Zr to $f_v(e) = 47.6$ pct at 5.0 Zr (Table II). ZrC particles (Figures 3(a) through (d), diameter ~2 μm) are also present in all the alloys. These particles were formed due to the presence of a small amount of carbon as an impurity in iron used for casting. The volume fraction of ZrC does not exceed 0.02 pct in any type of the as-cast alloys. A detailed view of the lamellar eutectic is presented in Figures 3(a) and (d).

The heat treatment caused coarsening of the λ_1 Laves phase in the Fe-25Al alloys; the structure is composed of a matrix (B2/DO_3) with λ_1 particles (Figure 4). The volume fractions of λ_1 are listed in Table III. The small ZrC particles remained even after the heat treatment (a detailed view is presented in Figure 4(a)) and are wrapped in the λ_1 phase.

Similar to the Fe-25Al-xZr alloys, the structure of the as-cast Fe-30Al-xZr alloys is composed of a matrix (B2/DO_3) with fine lamellar eutectic λ_1 + matrix (B2/DO_3) (see Figure 3 in Reference 14). The amount of the eutectic increases linearly with the Zr content (Table II). The small, bright cubic particles were identified as ZrC.

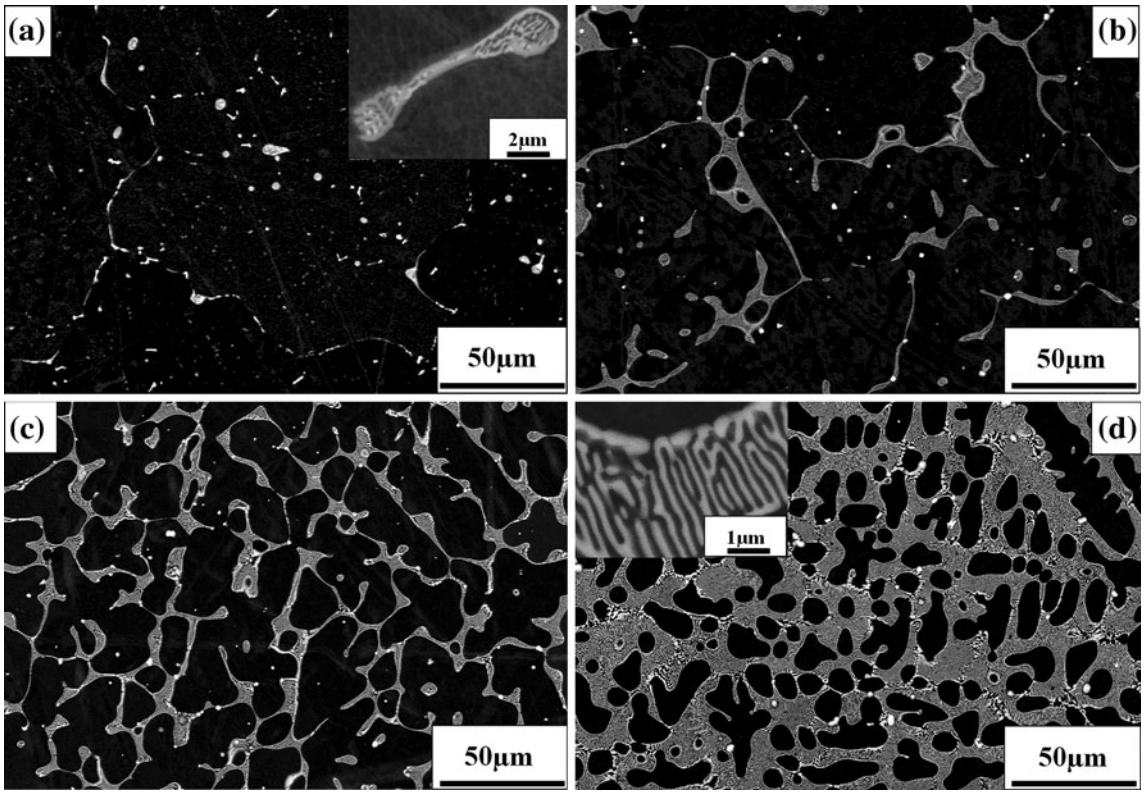

Fig. 3—BSE images of the structure of the as-cast Fe-25Al-xZr alloys: (*a*) 25-0, (*b*) 25-1, (*c*) 25-2, and (*d*) 25-5. The matrix D_3/B2 is the dark phase, the eutectic λ_1 + DO_3/B2 is gray, and the small, bright particles are ZrC.

The heat treatment [annealing at 1273 K (1000 °C) for 200 hours] results in the transformation of the eutectic structure into $\lambda_1 + \tau_1$ phases (consistent with the phase diagram[9]). For the structure of the corresponding alloys see Figure 7 in Reference 14. The volume fractions of the observed phases are listed in Table III. The amount of both phases increases with the addition of Zr. The phases present in the as-cast and annealed alloys were identified using XRD. As an example, diffraction curves with identified diffraction lines of the annealed alloys 25-5 and 30-5 are presented in Figure 5.

As described by Stein *et al.*,[15,16] the types of the Laves phase lattices C14 (hexagonal λ_1) and C15 (cubic λ_2) are determined by the number of valence electrons.

Table II. Volume Fractions of Eutectic f_v(e) (pct) λ_1 + Fe_3Al in As-Cast Alloys

As-Cast	−0	−1	−2	−5
25Al	3.9	7.9	18.1	47.6
30Al	3.4	8.7	20.9	55.2

The diffraction lines of both modifications are in fact overlapping, see Figure 6. It was also possible to obtain more details about the structure of the phases using EBSD. The symmetry type of the Kikuchi pattern in Figure 7 enables a precise description of the structure of the Laves phase in the alloy. The Laves phase will be denoted as λ_1 in these types of Fe-Al-Zr alloys.[9–12,14–16] The cubic λ_2 of the globular particles is most likely a metastable phase. This phenomena has been analyzed elsewhere.[17]

Note the very similar situation in the Fe corner of the Fe-Al-Nb ternary diagram [~1273 K (~1000 °C)] with low solubility of Nb in the $D0_3$/B2 matrix and with the widespread two-phase area α-FeAl + λ_1 Laves phase $(Fe,Al)_2Nb$.[18] Accordingly, the structures of the as-cast and annealed alloys are very similar to those described here;[18,19] λ_1 particles are formed in the matrix during annealing.

The compression testing was used to describe the high-temperature mechanical properties for both the as-cast and annealed alloys. The shape of the compressive true stress–true strain curves of both groups of alloys is very similar. As an example, a comparison of

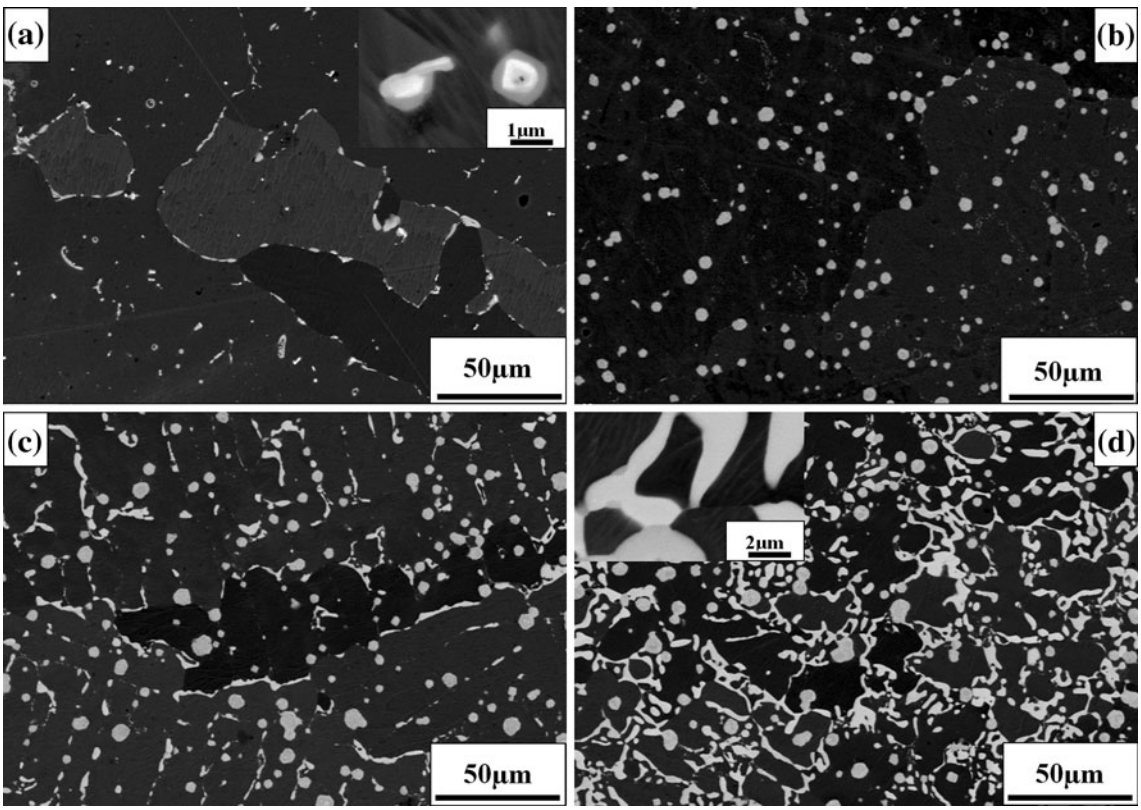

Fig. 4—BSE images of the structure of the annealed Fe-25Al-*x*Zr alloys: (*a*) 25-0, (*b*) 25-1, (*c*) 25-2, and (*d*) 25-5 composed of two phases: Fe3Al matrix (dark) and λ_1 particles (gray). Small particles of ZrC as bright cores—detail in 4a.

Table III. Volume Fractions of λ_1 Phase $f_v(\lambda_1)$ (pct) and of τ_1 Phase $f_v(\tau_1)$ (pct) in the Annealed Alloys

Annealed	−0	−1	−2	−5
25Al	1.9 λ_1	5.9 λ_1	11.2 λ_1	27.7 λ_1
30Al	0.2 λ_1 + 3.4 τ_1	5.0 λ_1 + 5.5 τ_1	7.2 λ_1 + 16.1 τ_1	18.6 λ_1 + 35.4 τ_1

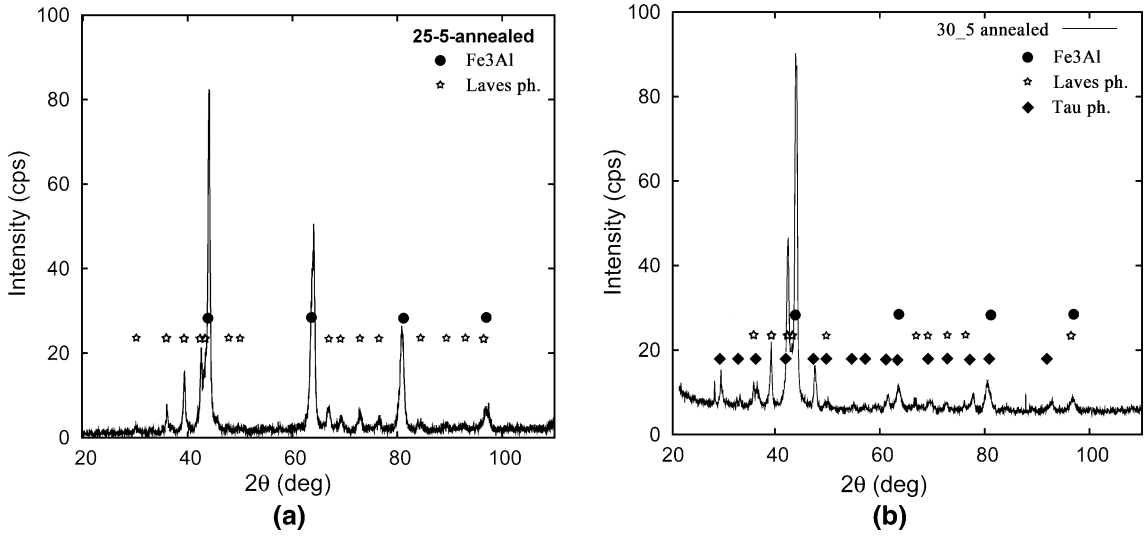

Fig. 5—XRD curves of the annealed 25-5 and 30-5 alloys.

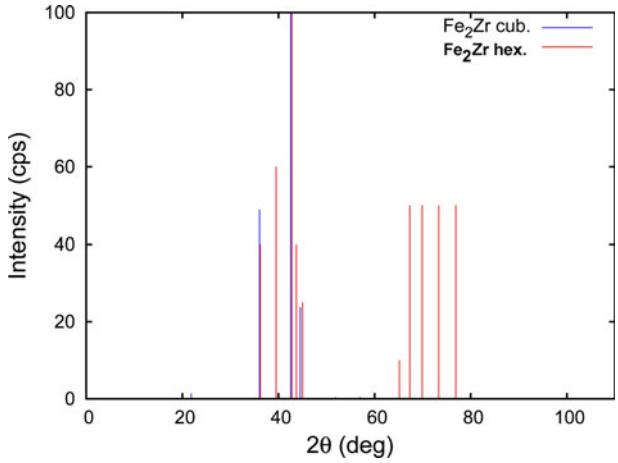

Fig. 6—The overlapping positions of the diffraction lines of hexagonal and cubic λ_1 and λ_2 Laves phases in Fe-Al-Zr system.

the curves of the annealed alloy 30-5 deformed at different temperatures is presented in Figure 8. In Figure 9, the true stress-true strain curves are compared at 973 K (700 °C) for the as-cast and of annealed alloys 30-2 and 30-5. The strength behavior of the studied materials is described and compared using the $\sigma_{0.2}$ yield stress. The results are presented separately for the Fe-25Al and Fe-30Al alloys (Figures 10, 11, respectively):

- $\sigma_{0.2}$ decreases with increasing temperature of deformation [873 K to 1153 K (600 °C to 880 °C] for all the as-cast and annealed alloys Fe-25Al and Fe-30Al,
- $\sigma_{0.2}$ increases with the Zr concentration of the as-cast and annealed Fe-25Al and Fe-30Al alloys,
- $\sigma_{0.2}$ increases after annealing in case of the 30-5 alloy (the effect of the appearance of the τ_1 phase) and decreases for alloy 30-2 (due to globularization of λ_1 in a soft matrix).
- $\sigma_{0.2}$ slightly decreases after annealing of Fe-25Al alloys (transformation of the eutectic into globular λ_1 particles in a continuous soft matrix).

The occurrence of the eutectic strongly affects the H.T. yield stress, which can be understood as a composite-type strengthening of the soft DO_3/B2 matrix by the hard Laves phase for the as-cast materials. The configuration and shape of the eutectic part of the material affects the values of $\sigma_{0.2}$. For these alloys, the dependences of $\sigma_{0.2}$ on the volume fraction f_v(e) of the eutectic (λ_1 + DO_3/B2) in the temperature range from 873 K to 1153 K (600 °C to 880 °C) are indicated in Figures 12 and 13. The yield strength of both types of alloys increases with the increasing f_v(e) and decreases with the increasing temperature.

However, particle hardening occurs for alloys 25-0 and 30-0. The composition of these alloys is nearly identical to those studied in our previous paper,[20] compared with the alloys denoted 1A, 2A, and 4A. The particles are Fe_2Zr and λ_1 Laves phase $Zr(Fe,Al)_2$. The results concerning the presence and effect of small particles on the H.T. mechanical properties of iron aluminides with comparatively small additions of both Zr[13] and Nb[21] are also similar.

The strength of the composite-like materials depends on the shape and configuration of the phases. The configurations with particles separated from each other by the matrix (originating during annealing) are softer than the cast material (see the results for the Fe-25Al alloys) with fine lamellar eutectic. Stabilization of the phase structure is necessary for structural use at high temperatures [973 K to 1073 K (700 °C to 800 °C)]. Hardening through the appearance of the third phase (τ_1) for higher concentrations of Zr is therefore recommended. The enhancement of the H.T. mechanical properties by the configuration of phases is also documented (for Fe-Al-Nb ternary alloys) by Milenkovic and Palm,[22] who studied the mechanical properties of an

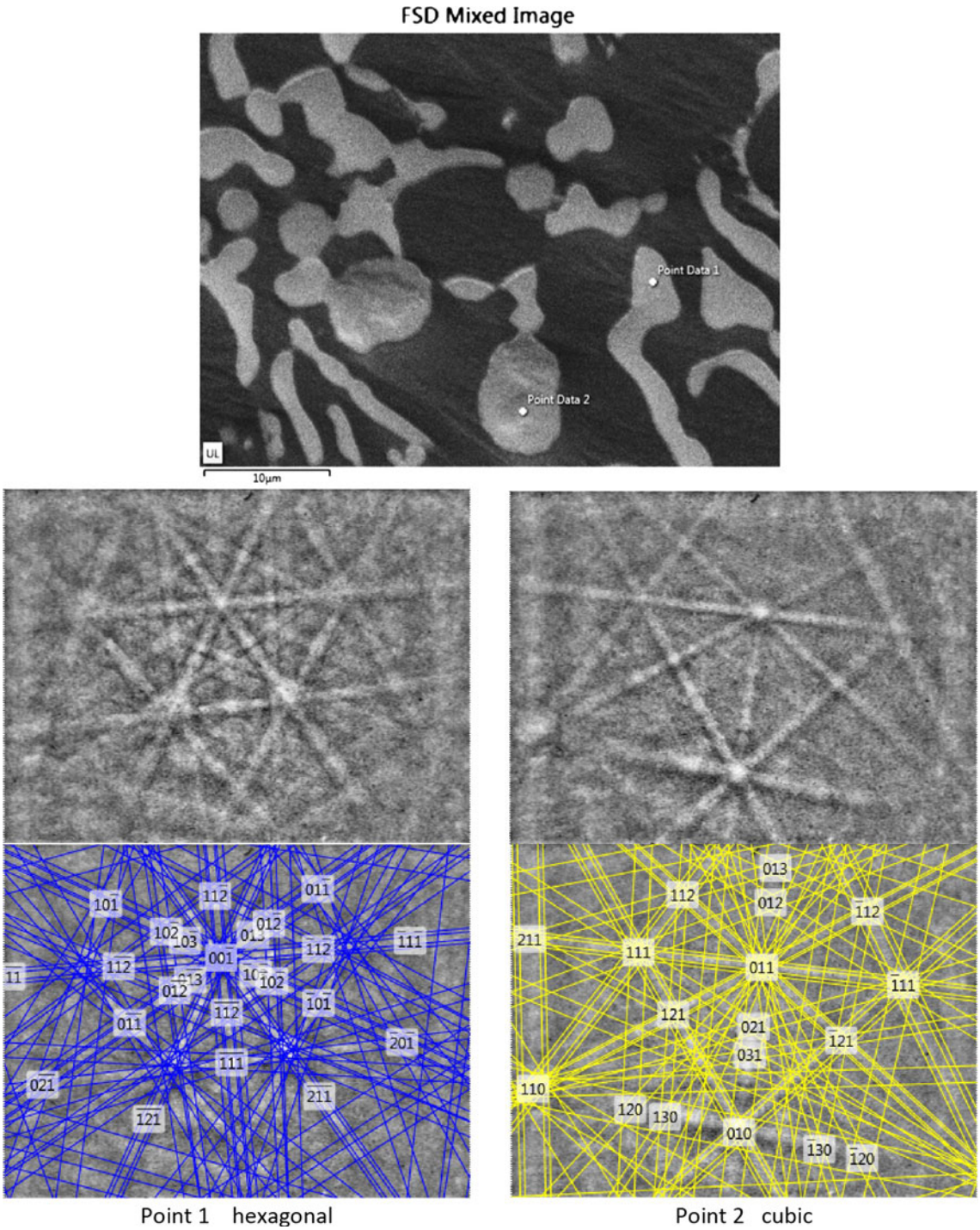

Fig. 7—Kichuchi diffraction patterns of hexagonal and cubic λ_1 and λ_2 Laves phases observed in the as-cast 25-5 alloy.

eutectic alloy, with a fine dispersion of the Laves phase $(Fe,Al)_2Nb$ in the matrix.

Alloying with Zr is advantageous concerning the strength of the structural materials. Nevertheless, a problem appears when the oxidation resistance at high temperatures is considered. The oxidation resistance decreases upon increasing the Zr content.[12] This problem may be corrected either by increasing the Al content[12] or through the addition of carbon.[23]

IV. CONCLUSIONS

All the as-cast alloys exhibited a two-phase DO_3/B2 + λ_1 structure with a typical fine lamellar eutectic DO_3/B2 + λ_1 situated in a DO_3/B2 matrix. The amount of the eutectic increased linearly with the increasing concentration of Zr. Annealing resulted in the transformation of the lamellar eutectic into globular λ_1 particles in the matrix in the Fe-25Al alloy and in a mixture of

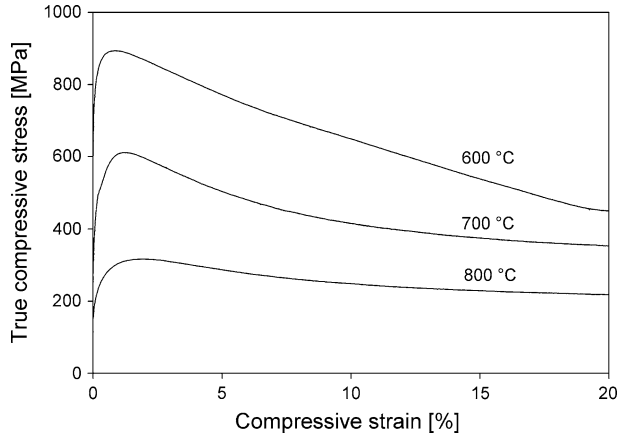

Fig. 8—The comparison of the compressive true stress–strain curves of the annealed alloy 30-5 deformed at different temperatures.

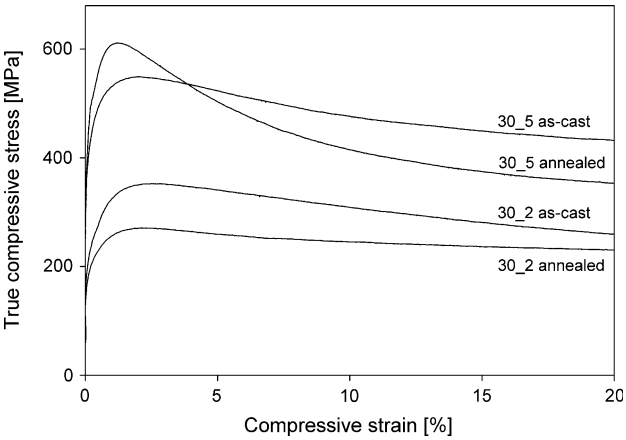

Fig. 9—The comparison of the compressive true stress–strain curves of alloys 30-2 and 30-5 at 973 K (700 °C) compared in the as-cast and in the annealed alloys.

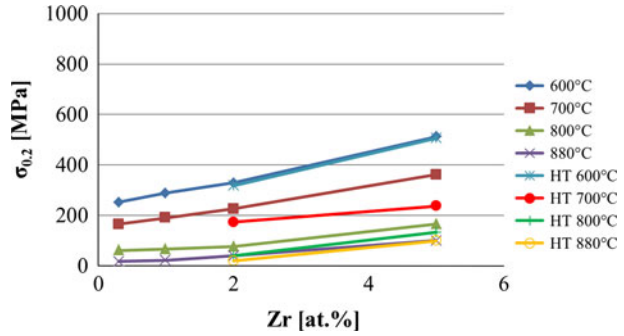

Fig. 10—Dependence of $\sigma_{0.2}$ of the as-cast and heat-treated Fe-25Al alloys on the Zr content at various temperatures [873 K to 1153 K (600 °C to 880 °C)].

$\lambda_1 + \tau_1$ particles in the Fe-30Al alloys. A characteristic feature is the appearance of ZrC nuclei in λ_1 particles.

During the annealing of the tested alloys at 1273 K (1000 °C), the as-cast structure transforms into a stable configuration with globular particles of one (λ_1) or two

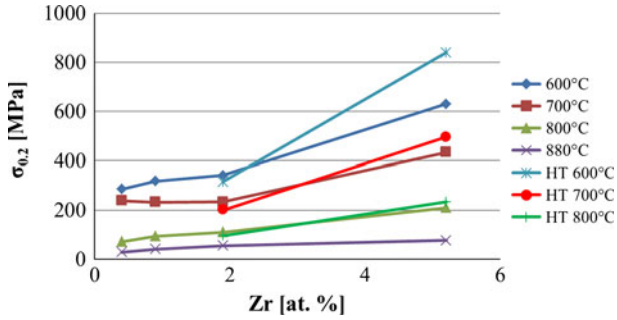

Fig. 11—Dependence of $\sigma_{0.2}$ of the as-cast and heat-treated Fe-30Al alloys on the Zr content at various temperatures [873 K to 1153 K (600 °C to 880 °C)].

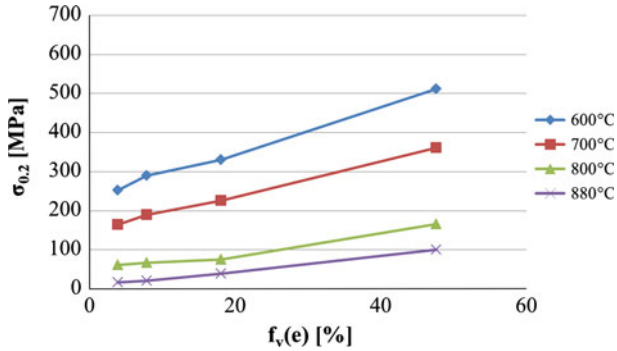

Fig. 12—Dependence of $\sigma_{0.2}$ of the as-cast Fe-25Al alloys on the volume fraction of the eutectic $f_v(e)$ at various temperatures [873 K to 1153 K (600 °C to 880 °C)].

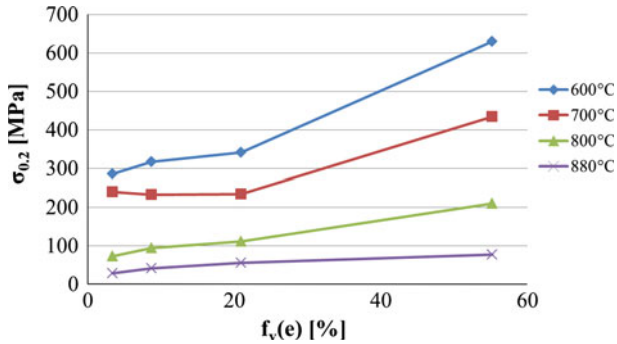

Fig. 13—Dependence of $\sigma_{0.2}$ of the as-cast Fe-30Al alloys on the volume fraction of the eutectic $f_v(e)$ at various temperatures [873 K to 1153 K (600 °C to 880 °C)].

($\lambda_1 + \tau_1$) phases within the matrix. This transformation stabilizes the strength properties for use at temperatures between 973 K and 1073 K (700 °C and 800 °C). This behavior is similar to that observed for Fe-Al-Nb alloys.

The high values of the H.T. strength of the Zr-alloyed Fe_3Al type materials depend on the configuration arrangement of the constituent phases (the difference between the as-cast and annealed materials). The values of the H.T. yield stress are understood as being those of a composite material.

ACKNOWLEDGMENTS

The present work is a part of the project supported by the Grant Agency of the Czech Republic under Nr. P108/12/1452. The authors would like to thank the Institute for Nanomaterials, Advanced Technologies and Innovation of the Technical University of Liberec for the use of its equipment for the study of the structure of the alloys. In addition, the assistance of the faculty of Metallurgy and Material Engineering (Prof. Ivo Schindler) of the Technical University in Ostrava, where the alloys were prepared, is acknowledged.

REFERENCES

1. C.G. McKamey, J.H. DeVan, P.F. Tortorelli, and V.K. Sikka: *J. Mater. Res.*, 1991, vol. 6, pp. 1779–1804.
2. N.S. Stoloff and C.T. Liu: *Microstructure and Properties of Materials*, vol. 2, J.C.M. Li, ed., World Scientific Publishing Co. Ltd., Singapore, 2000, pp. 139–176.
3. S.C. Deevi and V.K. Sikka: *Intermetallics*, 1996, vol. 4, pp. 357–75.
4. D.G. Morris: *Intermetallics*, 1998, vol. 6, pp. 753–58.
5. M. Palm: *Intermetallics*, 2005, vol. 13, pp. 1286–95.
6. A. Schneider, L. Falat, G. Sauthoff, and G. Frommeyer: *Intermetallics*, 2003, vol. 11, pp. 443–50.
7. L. Falat, A. Schneider, G. Sauthoff, and G. Frommeyer: *Intermetallics*, 2005, vol. 13, pp. 1256–62.
8. C.G. McKamey and P.J. Maziasz: *Intermetallics*, 1998, vol. 6, pp. 303–14.
9. F. Stein, G. Sauthoff, and M. Palm: *Z. Metallkd.*, 2004, vol. 95, pp. 465–85.
10. A. Wasilkowska, M. Bartsch, F. Stein, M. Palm, K. Sztwiertnia, and G. Sauthoff: *Mater. Sci. Eng. A*, 2004, vol. 380, pp. 9–19.
11. A. Wasilkowska, M. Bartsch, F. Stein, M. Palm, G. Sauthoff, and U. Messerschmidt: *Mater. Sci. Eng. A*, 2004, vol. 381, pp. 1–15.
12. F. Stein, M. Palm, and G. Sauthoff: *Intermetallics*, 2005, vol. 13, pp. 1275–85.
13. D.G. Morris, M.A. Munoz-Morris, and L.M. Requejo: *Acta Mater.*, 2006, vol. 54, pp. 2335–41.
14. P. Kratochvíl, P. Kejzlar, R. Král, and V. Vodičková: *Intermetallics*, 2012, vol. 20, pp. 39–46.
15. F. Stein, M. Palm, and G. Sauthoff: *Intermetallics*, 2004, vol. 12, pp. 713–20.
16. F. Stein, M. Palm, and G. Sauthoff: *Intermetallics*, 2005, vol. 13, pp. 1056–74.
17. P. Kejzlar: unpublished data.
18. M. Palm: *J. Alloys Compd.*, 2009, vol. 475, pp. 173–77.
19. D.G. Morris and M.A. Munoz-Morris: *Mater. Sci. Eng. A*, 2012, vol. 552, pp. 134–44.
20. P. Kratochvíl, F. Dobeš, J. Pešička, P. Málek, J. Buršík, V. Vodičková, and P. Hanus: *Mater. Sci. Eng. A*, 2012, vol. 548, pp. 175–82.
21. D.G. Morris, M.A. Muñoz-Morris, L.M. Requejo, and C. Baudin: *Intermetallics*, 2006, vol. 13, pp. 1204–07.
22. S. Milenkovic and M. Palm: *Intermetallics*, 2008, vol. 16, pp. 1212–18.
23. A. Hotař, M. Palm, P. Kratochvíl, V. Vodičková, and S. Daniš: *Corros. Sci.*, 2012, vol. 63, pp. 71–81.

The Effect of Carbon Additions on the Creep Resistance of Fe-25Al-5Zr Alloy

FERDINAND DOBEŠ, VĚRA VODIČKOVÁ, JOZEF VESELÝ, and PETR KRATOCHVÍL

Creep experiments were conducted on Fe-25 at. pct Al-5 at. pct Zr alloy with carbon additions at the temperatures of 973 K and 1173 K (700 °C and 900 °C). The alloys were tested in two different states: (i) cast and (ii) annealed at 1273 K (1000 °C) for 50 hours. Stress exponents and activation energies were estimated. The values of the stress exponent n could be explained by the dislocation motion controlled by climb. The increased values of n in the high-carbon alloy at the temperature of 1173 K (900 °C) can be described by means of the threshold stress concept. The creep resistance at 973 K (700 °C) decreased with the increasing content of carbon. This result is discussed in terms of the ratio of zirconium to carbon in the alloy. An increase of the creep resistance with increasing ratio Zr:C is in agreement with the behavior observed previously in alloys with substantially lower concentrations of zirconium.

DOI: 10.1007/s11661-016-3770-6

I. INTRODUCTION

THE intermetallic alloys based on the compounds Fe_3Al and FeAl are prospective candidates for high-temperature structural applications.[1–3] Alloying by refractory metals continues to be the most attractive way toward improvement of their mechanical properties.[4–11] Several methods can be adopted to enhance limited creep resistance: these consist mainly of adding elements for either solid solution strengthening or precipitation strengthening.[12,13] The precipitation strengthening is determined by the low solubility of the added elements. From this point of view, the alloying by zirconium may be of interest because nearly no solid solubility for Zr exists in the Fe-Al phases. The beneficial effect of zirconium addition on creep resistance was first reported for the Fe-28 pct Al-based alloy (at. pct is given throughout) by McKamey *et al.*[14–16] and the Fe-40 pct Al-based alloy by Whittenberger *et al.*[17] Moreover, a positive effect of a dispersion of fine Zr-rich carbides was demonstrated *via* microstructural analysis.[14] Subsequent studies focused on the additions of various amounts of zirconium to a wide range of Fe-Al alloys.[18–24] Less attention has been devoted to the combined additions of zirconium and carbon. The results of these studies are summarized elsewhere.[25] Carbon content appears to be beneficial in suppressing the hydrogen embrittlement at grain boundaries.[26]

The effect of the additives Zr (0.2 to 0.3 pct) and C (0.2 to 0.6 pct) on the phase composition and high-temperature mechanical properties of Fe_3Al-type alloys was investigated in our previous paper.[25] It was shown that the ratio of zirconium to carbon additives influenced the phase structure and played an important role in determining the mechanical properties. The purpose of the present paper is to examine the influence of larger carbon additions (up to 3.5 pct) on the compressive creep of Fe-25Al alloy with similarly increased zirconium content (5 pct).

II. EXPERIMENTAL

The examined alloys were prepared by vacuum melting and casting; Zr was added in metallic form. The dimensions of the cast ingot of the low-carbon alloy were $20 \times 40 \times 150$ mm^3. The casts of alloys with added carbon measured $10 \times 15 \times 30$ mm^3. The chemical compositions are listed in Table I.

Some samples were additionally annealed at 1273 K (1000 °C) for 50 hours in sealed ampoules that were filled with helium to stabilize the microstructure prior to the creep tests. The annealing was followed by rapid cooling in air outside the furnace. These samples are denoted as "annealed." The microstructures were studied using a Zeiss Ultra Plus field emission scanning electron microscope (SEM) equipped with both an OXFORD X-MAX 20 energy-dispersive spectrometer and an OXFORD NordlysNano detector for electron backscatter diffraction (BSE). Transmission electron microscopy (TEM) was done on JEOL JEM-2000FX at 200kV. Samples were prepared by electropolishing in 20 pct HNO_3 in methanol at 243 K (−30 °C) and 15 V.

FERDINAND DOBEŠ, Senior Researcher, is with the Institute of Physics of Materials, Academy of Sciences of the Czech Republic, ŽIžkova 22, 616 62 Brno, Czech Republic. Contact e-mail: dobes@ipm.cz VĚRA VODIČKOVÁ, Senior Assistant Professor, is with the Department of Material Science, Faculty of Mechanical Engineering, Technical University of Liberec, Hálkova 6, 461 17 Liberec 1, Czech Republic. JOZEF VESELÝ, Junior Researcher, and PETR KRATOCHVÍL, Professor, are with the Department of Physics of Materials, Faculty of Mathematics and Physics, Charles University in Prague, Ke Karlovu 5, 121 16 Prague 2, Czech Republic.

Manuscript submitted March 24, 2016.

Published online: 21 September 2016

Table I. Composition of the Alloys (At. Pct)

Alloy	Al	Zr	C
Fe-25Al-5Zr	25.4	5.0	0.06
Fe-25Al-5Zr-1C	25.3	5.65	0.92
Fe-25Al-5Zr-4C	24.7	5.42	3.46

The creep tests were performed in uniaxial compression on samples with a gage length of 12 mm and a cross-section of 5 × 5 mm^2 (low-carbon alloy) or a gage length of 6.5 mm and a cross-section of 3 × 3 mm^2 (two high-carbon alloys). The samples were prepared by traveling wire electro-discharge machining and fine grinding of the surfaces. The tests were performed under a constant load in a protective atmosphere of dry purified argon at temperatures of 973 K and 1173 K (700 °C and 900 °C). Changes in specimen length were measured using a linear variable displacement transducer. The samples were subjected to stepwise loading, where the load was changed after the steady-state creep rate was established for a given load. The terminal values of the true stress and the creep rate, *i.e.*, the true compressive strain rate, were evaluated for each step.

III. RESULTS

A. *Microstructure*

1. *Fe-25Al-5Zr*

The microstructure of this alloy is documented in the previous paper.[27] In agreement with the available ternary diagram,[28] the microstructure consists of primary solidified bcc α (disordered solid solution of Al in Fe, body-centered cubic A2 lattice) surrounded by a eutectic composed of alternating lamellae of α and λ_1 Laves phase $(Fe,Al)_2Zr$. The bcc lattice α changes as the temperature decreases, becoming an ordered B2 lattice at 1026 K (753 °C) and an ordered $D0_3$ lattice at temperatures below 815 K (542 °C).[29] The volume fraction of the eutectic is equal to 47.6 pct. ZrC particles with a diameter of ~2 μm are also present in the alloy. These particles were formed due to the presence of a small amount of carbon as an impurity in the iron used for casting. The volume fraction of ZrC does not exceed 0.02 pct.

The heat treatment of this alloy, as well as all alloys studied in the present paper, caused coagulation of the eutectic lamellae of λ_1 Laves phase; the microstructure is composed of a matrix α with λ_1 particles. The volume fraction of λ_1 is 27.7 pct. The small ZrC particles remain, even after the heat treatment, and are wrapped in the λ_1 phase.

2. *Fe-25Al-5Zr-1C*

The microstructure of the cast Fe-25Al-5Zr-1C alloy is again characterized by the presence of primary solidified α and the eutectic composed of α and λ_1 Laves phase $(Fe,Al)_2Zr$. ZrC particles (*e.g.*, plates or dendritic formations, size 3 to 10 μm) are also present in the alloy (Figure 1).

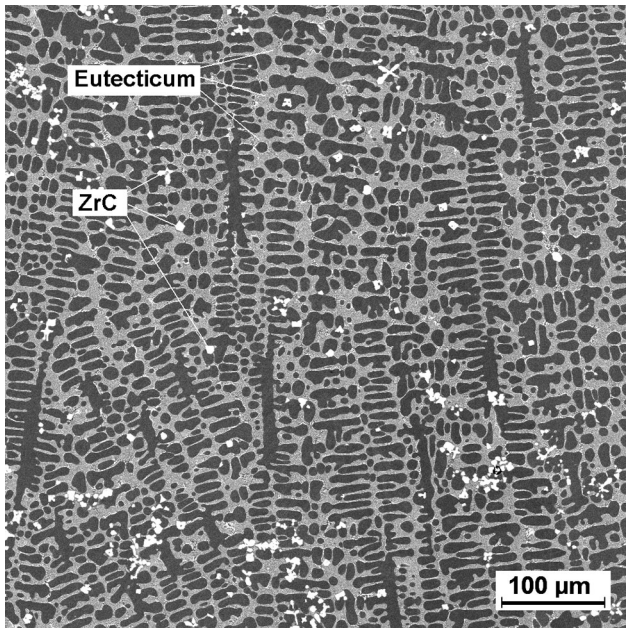

Fig. 1—Back-scattered electron (BSE) image of the microstructure in the cast Fe-25Al-5Zr-1C alloy. The matrix α is the dark phase, the eutectic λ_1 + α is gray, and the small bright particles are ZrC.

Table II. Summary of Fractions (Vol Pct) of Observed Phases in the Studied Alloys

	0.06 At. Pct C	0.92 At. Pct C	3.46 At. Pct C
Cast			
Eutecticum	47.6	40.9	12.2
ZrC	≤0.02	1.8	6.2
Annealed			
Laves phase	27.7	21.3	5.9*
ZrC	≤0.02	0.2	4.8

* The value is very little enhanced by the tiny particles of $Fe_{23}Zr_6$, which are seen in the picture.

Coagulated Laves phase and small remnants of the eutectic are present in the microstructure of the alloy after heat treatment. A small amount of ZrC phase remains inside the coagulated Laves phase particles (Figure 2). The volume fractions of eutectic and ZrC in cast alloy and of Laves phase and ZrC in annealed alloy, respectively, are listed in Table II. TEM enables to observe small particles (size 0.5 to 1 μm) identified by SAED (selected area electron diffraction) as $Fe_{23}Zr_6$ phase (fcc structure of the $Mn_{23}Th_6$ type, lattice parameter 1.18 nm), see the microstructure after creep tests, Section III-B. These particles correspond to the metastable phase identified previously in Fe-Al-Zr ternary alloys and stabilized by impurities.[28]

3. *Fe-25Al-5Zr-4C*

The square-shaped ZrC particles (sizes from 1 to 15 μm) and eutectic composed α and λ_1 Laves phase $(Fe,Al)_2Zr$ are present in the microstructure of the cast alloy Fe-25Al-5Zr-4C (Figure 3). The volume fraction of eutectic is markedly lower than that in the

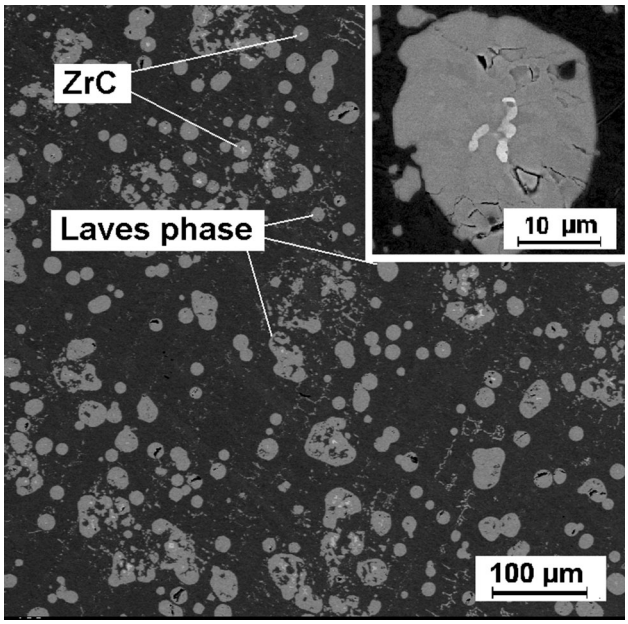

Fig. 2—BSE image of the microstructure in the annealed Fe-25Al-5Zr-1C alloy composed of three phases: α matrix (dark), λ_1 particles (mostly oval-gray), and ZrC particles as bright cores inside λ_1 particles (detail is shown in inset). The smallest particles of $Fe_{23}Zr_6$ are visible as gray spots.

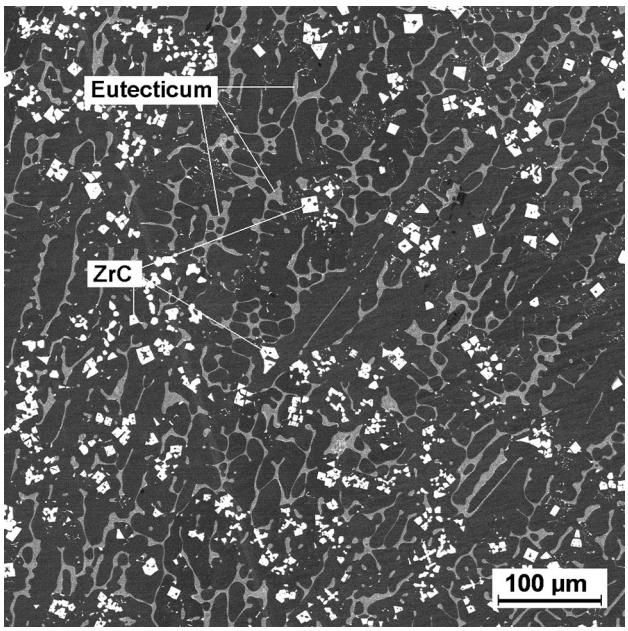

Fig. 3—BSE image of the microstructure in the cast Fe-25Al-5Zr-4C alloy. The matrix α is the dark phase, the eutectic λ_1 + α is gray, and the small bright particles are ZrC.

Fe-25Al-5Zr-1C alloy. The microstructure of the annealed alloy is characterized by the presence of "chain-like" particles of Laves phase and square-shaped ZrC carbides (Figure 4). The volume fractions are listed in Table II. The volume fraction of the metastable phase $Fe_{23}Zr_6$ was not measurable.

Table III. Activation Energies *Q* Found by Multiple Regressions Under the Assumption of Temperature-Independent Stress Exponents

	0.06 At. Pct C	0.92 At. Pct C	3.46 At. Pct C
Cast			
Q (kJ/mole)	460	452	415
n, 973 K (700 °C)	6.1	7.0	7.3
r^2	0.945	0.973	0.966
n, 1173 K (900 °C)	7.2	5.7	13.5
r^2	0.991	0.921	0.966
Annealed			
Q (kJ/mole)	362	257	204
n, 973 K (700 °C)	5.8	6.6	6.9
r^2	0.994	0.970	0.998
n, 1173 K (900 °C)	5.7	7.2	9.6
r^2	0.952	0.739	0.991

Stress exponents *n* and the corresponding correlation coefficients r^2 are calculated separately for each test temperature.

B. *Creep*

Figure 5 shows the microstructure of the annealed Fe-25Al-5Zr-1C alloy after creep at 1173 K (900 °C) for 382 hours. Dislocations are anchored at particles of $Fe_{23}Zr_6$. Dislocations with same particles $Fe_{23}Zr_6$ in alloy Fe-25Al-5Zr-4C after creep at 973 K (700 °C) for 315 hours are shown in Figure 6.

The dependence of the creep rate $\dot{\varepsilon}$ on the applied stress σ at the various temperatures is shown in Figures 7(a) through (c) on a double logarithmic scale for both cast and annealed states. The data were analyzed using the following relation:[30]

$$\dot{\varepsilon} = A\sigma^n \exp\left(\frac{Q}{RT}\right), \qquad [1]$$

where *A* is a material constant, *n* is the stress exponent, *Q* is the activation energy for creep, *R* is the gas constant, and *T* is the absolute temperature. The values of *Q* were estimated from Eq. [1] by multiple linear regression, assuming that the activation energy is independent of stress. The stress exponent *n* was calculated separately for each test temperature. Correlation coefficients r^2 of these calculations are also given. The obtained values for all investigated alloys are summarized in Table III.

IV. DISCUSSION

The estimated activation energies for creep of cast alloys are higher than the values reported for the Fe-Al alloys with a similar aluminum content (302 to 418 kJ/mol).[2,31] The energy of 460 kJ/mol for the cast low-carbon alloy is in good agreement with that for the alloys with aluminum contents between 39.8 and 48.7 pct.[32,33] In any case, all activation energies found in cast alloys are considerably higher than the activation enthalpy for diffusion of both the Fe and Al in Fe-25 at. pct Al, with values of 217 kJ/mol (Fe in A2 lattice), 232 kJ/mol (Fe in B2 lattice),[34] and 267.1 kJ/mol (Al in

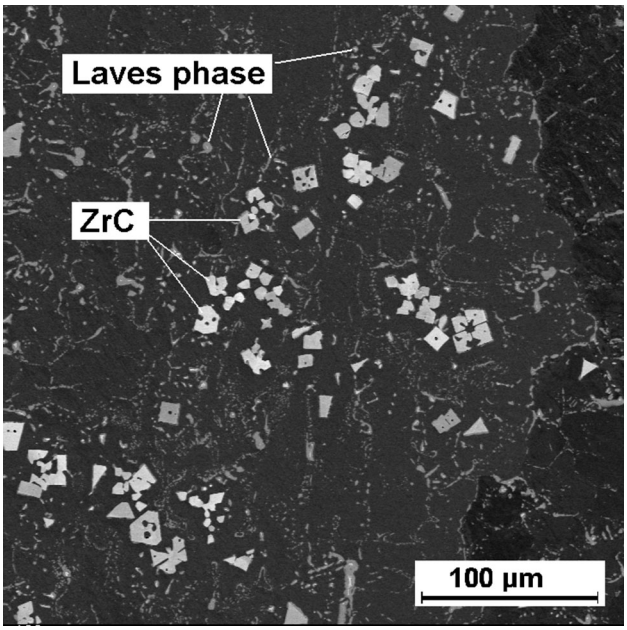

Fig. 4—BSE image of the microstructure in the annealed Fe-25Al-5Zr-4C alloy composed of three phases: α matrix (dark), λ_1 particles (gray), and square shape ZrC particles (bright).

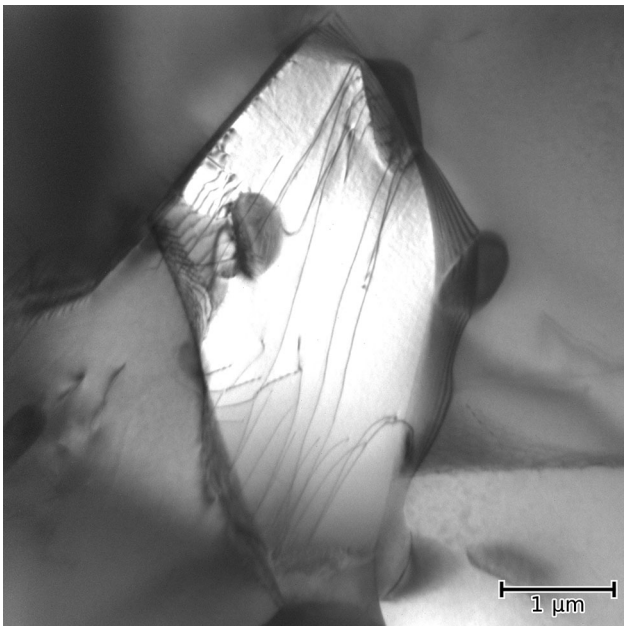

Fig. 5—Interaction of dislocations with particles of $Fe_{23}Zr_6$ in the alloy Fe-25Al-5Zr-1C after creep at 1173 K (900 °C).

A2 lattice).[35] The reasons for this discrepancy can be found in the changing microstructure of the cast alloys at the testing temperature of 1173 K (900 °C). This assumption is supported by comparison of the creep rates of cast and the annealed states: The annealing increases the creep rate at 973 K (700 °C) but has only a limited effect on creep at 1173 K (900 °C): The holding

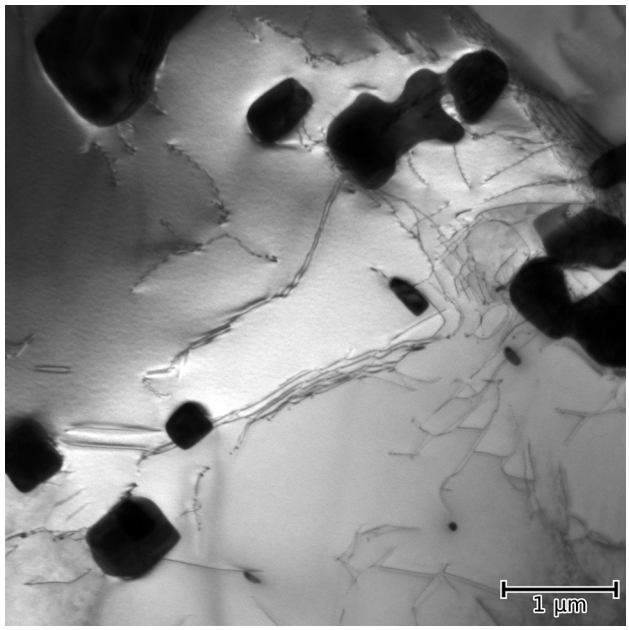

Fig. 6—Example of observation of dislocations and particles $Fe_{23}Zr_6$ in the alloy Fe-25Al-5Zr-4C after creep at 973 K (700 °C).

time at the temperature of 1173 K (900 °C) prior to the first reading of the creep rate was longer than 45 hours and sufficiently long such that the eutectic microstructure in cast alloys could coagulate and form an appearance close to that observed after annealing at 1273 K (1000 °C). The estimated activation energy for creep in the annealed alloy can thus be considered appropriate for a phenomenological description of creep data from the viewpoint of microstructural stability. The exact analysis of the activation energy derived experimentally from Eq. [1] is complicated by the changes in the crystal lattice of the matrix. The presence of carbon increases transformation temperature from ordered B2 lattice to disordered A2 lattice [*i.e.,* 1026 K (753 °C)] by approximately $\Delta T = 40$ K (40 °C) due to the addition of 0.5 to 1.0 at. pct C.[36] Different lattices can be expected in creep experiments at different temperatures. Strict interpretation of the activation energy depends also on the identity of deformation processes at different temperatures. This is not guaranteed due to an excessive difference in applied stresses. The estimated activation energies are only apparent values.

The heterogeneous nature of the present alloys suggests that their behavior can be interpreted in terms of the composite model of deformation.[37] The local stresses are redistributed to lower values in the "soft" Fe-Al matrix and to higher values in the "hard" Laves phase particles. The estimated activation energy reflects contributions from both phases. (The deformation of carbide ZrC is not probable due to its high melting point and high activation energy of creep, ~700 kJ/mol).[38] The observed decrease in the activation energy with the increasing carbon content can thus be connected to a lower amount of the Laves phase (unfortunately, diffusion data for the $(Fe,Al)_2Zr$ Laves phase are not available). The estimated values must be taken with

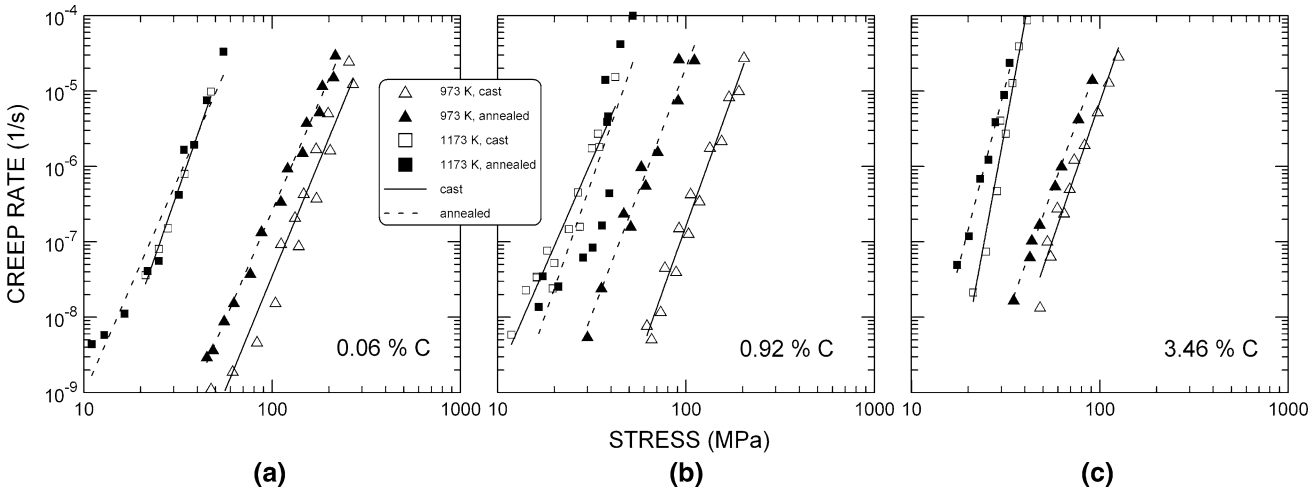

Fig. 7—Dependence of the creep rate on the applied stress separately for each tested alloy and heat-treatment history: (*a*) 0.06 at. pct C, (*b*) 0.92 at. pct C and (*c*) 3.46 at. pct C.

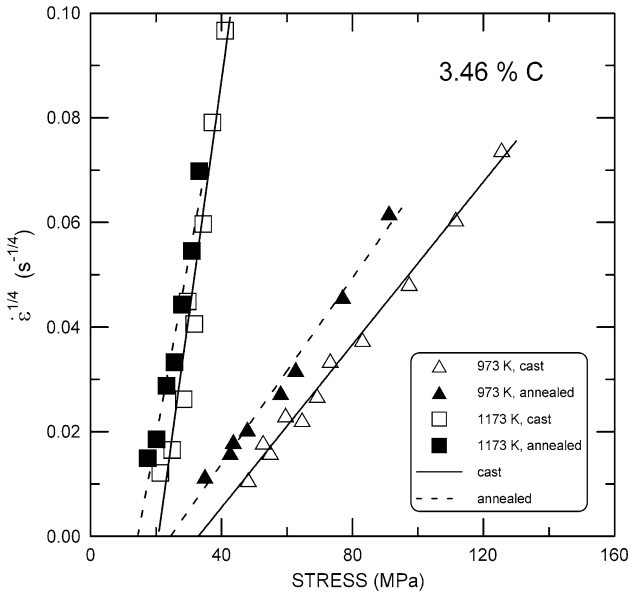

Fig. 8—Relation between $\dot{\varepsilon}^{1/n'}$ and the applied stress for the true stress exponent $n' = 4$.

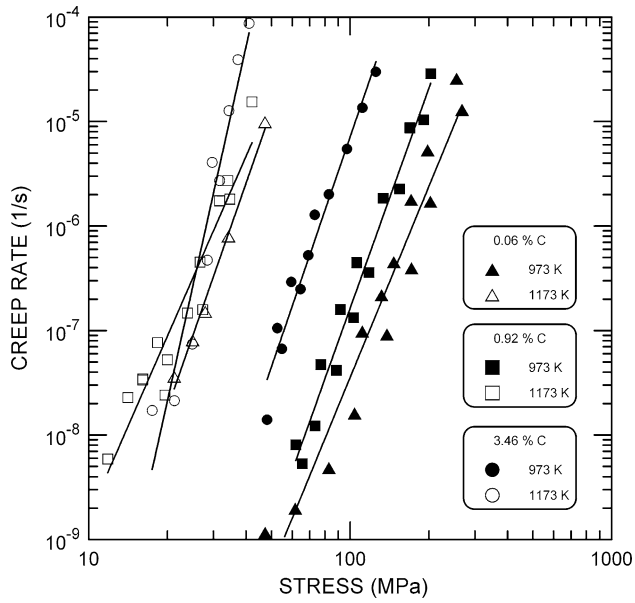

Fig. 9—Comparison of the effect of carbon content on the creep rate *vs* the applied stress dependence.

caution because the data are available for only two temperatures.

The values of stress exponent n in the two lower carbon alloys (Fe-25Al-5Zr and Fe-25Al-5Zr-1C) are similar to those usually observed in iron aluminides (cf. Table II in Reference 2). More specifically, the values correspond to those reported by McKamey *et al.*[14] for Fe-28 Al-based alloys at higher stresses and suggest that the rate-controlling process is associated with dislocation climb.

Values of n are substantially greater in the high-carbon alloy (Fe-25Al-5Zr-4C) especially at the temperature of 1173 K (900 °C). The creep behavior can be rationalized by the threshold stress concept:[39] the stress dependence of the creep rate is rewritten as

$$\dot{\varepsilon} = A'(\sigma - \sigma_{\text{th}})^{n'}, \qquad [2]$$

where A' is a temperature-dependent parameter and σ_{th} is the threshold stress. The value of n' should be close to the value of stress exponent n observed in pure metals and single-phase solid solutions. The value of the threshold stress can be determined by plotting $(\dot{\varepsilon})^{1/n'}$ against the applied stress on linear axes for selected values of n' and extrapolating linearly to a zero creep rate. In accordance with the previous evaluations of the threshold stress in Fe-Al alloys with Zr additions,[21,22] the same value of n', *i.e.*, $n' = 4$, is used. The method is presented in Figure 8. The threshold stress equals 32.9 and 20.7 MPa at 973 K (700 °C) and 1173 K (900 °C), respectively, in the cast Fe-25Al-5Zr-4C alloy and 24.4 and 14.4 MPa at 973 K (700 °C) and 1173 K (900 °C), respectively, in the annealed Fe-25Al-5Zr-4C alloy. The temperature

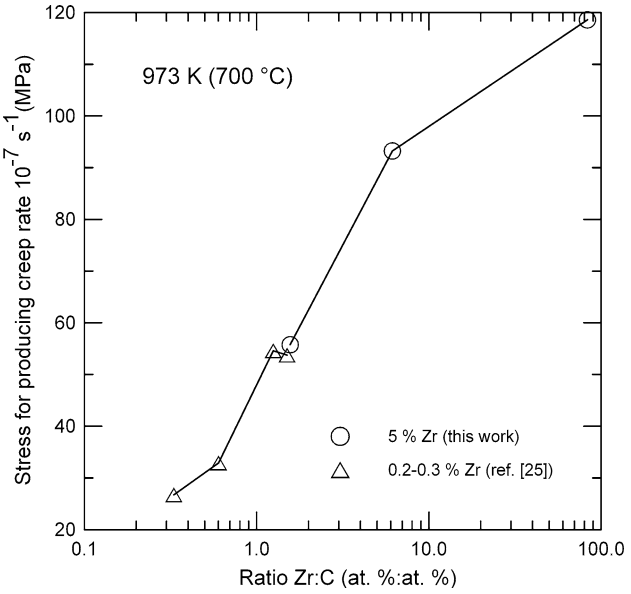

Fig. 10—The stress necessary to produce a creep rate of 10^{-7} s^{-1} as a function of c(Zr):c(C).

dependence of the estimated threshold stress is certainly stronger than that of the shear modulus. The threshold stress decreases due to annealing at 1273 K (1000 °C). This can correspond with the coagulation of precipitating phases. The threshold stress in the alloy Fe-25Al-5Zr-1C is probably much lower than the applied stresses in the creep experiments and cannot influence the value of the stress exponent n. The physical backgrounds of the threshold stress itself remain to be explained.

A comparison of the effect that the carbon additions have on the creep rate is given in Figure 9. The effect is small at 1173 K (900 °C), whereas the creep rate is increasing with the increasing carbon content at 973 K (700 °C), and the additions of carbon deteriorate the creep resistance of the Fe-25Al-5Zr alloy. In our previous work,[25] the effect of combined C and Zr additives on the high-temperature mechanical properties was discussed in terms of the ratio of their concentrations: c(Zr):c(C). Here, we attempt to apply the same approach for the present alloys. In Figure 10, the stress for producing a creep rate of 10^{-7} s^{-1} is presented as a function of this ratio. It is clear that the present results coincide well with the previously published data. The effect of concentration for both additives is governed by the relations shown in the ternary Fe-Al-Zr phase diagram and its potential extension by adding carbon. The solubility of carbon in bcc Fe-Al alloys is not known exactly. In contrast to older investigations, a noticeable solubility up to 1.5 at. pct C was reported in Reference 36. This corresponds to the lowered amount of carbides observed after annealing in the alloy Fe-25Al-5Zr-1C. The excessive undissolved carbon in the Fe-25Al-5Zr-4C forms relatively great particles of ZrC that have only weak effect on the creep resistance. The presence of carbon reduces the amount of zirconium that is available for the formation of the Laves phase and/or $Fe_{23}Zr_6$, and thus reduces the creep resistance.

V. CONCLUSIONS

In this work, compressive creep tests were conducted on Fe_3Al-based alloys with 5 pct zirconium and different carbon contents (0.06 to 3.46 pct). The results are summarized as follows:

- The values of the stress exponent in the low-carbon alloy are in the range of 6 to 7 and could be explained by the dislocation motion controlled by climb. The increased values of n in the high-carbon alloy at the temperature of 1173 K (900 °C) can be described by means of the threshold stress concept.
- Carbon additions deteriorate creep resistance at 973 K (700 °C). This result is discussed in terms of the ratio of zirconium to carbon in the alloy.
- An increase of the creep resistance with increasing ratio Zr:C is in agreement with the behavior observed previously in alloys with substantially lower concentrations of zirconium.

ACKNOWLEDGMENTS

The paper is based on work supported by the Czech Science Foundation within the Project 108/12/1452. J.V. and P.K. acknowledge support from the Project 16-05608S of the same foundation.

REFERENCES

1. G. Sauthoff: *Intermetallics*, VCH Verlagsgesellschaft, Weinheim, 1995, pp. 84–89.
2. N.S. Stoloff: *Mater. Sci. Eng. A*, 1998, vol. 258, pp. 1–14.
3. C.T. Liu, E.P. George, P.J. Maziasz, and J.H. Schneibel: *Mater. Sci. Eng. A*, 1998, vol. 258, pp. 84–98.
4. M. Yildirim, M.V. Akdeniz, and A.O. Mekhrabov: *Metall. Mater. Trans. A*, 2012, vol. 43A, pp. 1809–16.
5. D. Janda, H. Fietzek, M. Galetz, and M. Heilmaier: *Intermetallics*, 2013, vol. 41, pp. 51–57.
6. G. Yang and S. Milenkovic: *Intermetallics*, 2014, vol. 55, pp. 129–37.
7. X. Li, P. Prokopčáková, and M. Palm: *Mater. Sci. Eng. A*, 2014, vol. 611, pp. 234–41.
8. D. Janda, H. Ghassemi-Armaki, E. Bruder, M. Hockauf, M. Heilmaier, and K.S. Kumar: *Acta Mater.*, 2016, vol. 103, pp. 909–18.
9. M. Yildirim, M.V. Akdeniz, and A.O. Mekhrabov: *Mater. Sci. Eng. A*, 2016, vol. 664, pp. 17–25.
10. P. Prokopčáková, M. Švec, and M. Palm: *Int. J. Mater. Res.*, 2016, vol. 107, pp. 396–405.
11. L. Senčeková, M. Palm, J. Pešička, and J. Veselý: *Intermetallics*, 2016, vol. 73, pp. 58–66.
12. M. Palm: *Intermetallics*, 2005, vol. 13, pp. 1286–95.
13. D.G. Morris and M.A. Muñoz-Morris: *Mater. Sci. Eng. A*, 2007, vol. 462, pp. 45–52.
14. C.G. McKamey, P.J. Maziasz, and J.W. Jones: *J. Mater. Res.*, 1992, vol. 7, pp. 2089–2106.
15. C.G. McKamey, P.J. Maziasz, G.M. Goodwin, and T. Zacharia: *Mater. Sci. Eng. A*, 1994, vol. 174, pp. 59–70.

16. C.G. McKamey and P.J. Maziasz: *Intermetallics*, 1998, vol. 6, pp. 303–14.
17. J.D. Whittenberger, M.V. Nathal, and D.J. Gaydosh: *Intermetallics*, 1994, vol. 2, pp. 193–200.
18. T.M. Pollock, D.C. Lu, X. Shi, and K. Eow: *Mater. Sci. Eng. A*, 2001, vol. 317, pp. 241–48.
19. A. Wasilkowska, M. Bartsch, F. Stein, M. Palm, K. Sztwiertnia, G. Sauthoff, and U. Messerschmidt: *Mater. Sci. Eng. A*, 2004, vol. 380, pp. 9–19.
20. A. Wasilkowska, M. Bartsch, F. Stein, M. Palm, G. Sauthoff, and U. Messerschmidt: *Mater. Sci. Eng. A*, 2004, vol. 381, pp. 1–15.
21. D.G. Morris, M.A. Muñoz-Morris, and L.M. Requejo: *Acta Mater.*, 2006, vol. 54, pp. 2335–41.
22. D.G. Morris, I. Gutierrez-Urrutia, and M.A. Muñoz-Morris: *Scr. Mater.*, 2007, vol. 57, pp. 449–52.
23. J. Machida, S. Kobayashi, Y. Kaneno, and T. Takasugi: *Mater. Sci. Forum*, 2007, vols. 561–565, pp. 399–402.
24. M. Cieslar and M. Karlík: *Mater. Sci. Eng. A*, 2007, vol. 462, pp. 289–93.
25. P. Kratochvíl, F. Dobeš, J. Pešička, P. Málek, J. Buršík, V. Vodičková, and P. Hanus: *Mater. Sci. Eng. A*, 2012, vol. 548, pp. 175–82.
26. R.S. Sundar and S.C. Deevi: *Metall. Mater. Trans. A*, 2003, vol. 34A, pp. 2233–46.
27. P. Kejzlar, P. Kratochvíl, R. Král, and V. Vodičková: *Metall. Mater. Trans. A*, 2014, vol. 45A, pp. 335–42.
28. F. Stein, G. Sauthoff, and M. Palm: *Z. Metallkunde.*, 2004, vol. 95, pp. 469–85.
29. F. Stein and M. Palm: *Int. J. Mater. Res.*, 2007, vol. 98, pp. 580–88.
30. A.K. Mukherjee, J.E. Bird, and J.E. Dorn: *Trans. ASM*, 1969, vol. 62, pp. 155–79.
31. A. Lawley, J.A. Coll, and R.W. Cahn: *Trans. Metall. Soc. AIME*, 1960, vol. 218, pp. 166–76.
32. J.D. Whittenberger: *Mater. Sci. Eng.*, 1983, vol. 57, pp. 77–85.
33. J.D. Whittenberger: *Mater. Sci. Eng.*, 1986, vol. 77, pp. 103–13.
34. M. Eggersmann and H. Mehrer: *Philos. Mag. A*, 2000, vol. 80, pp. 1219–44.
35. L.N. Larikov, V.V. Geichenko V.M. Fal'chenko: *Diffusion Processes in Ordered Alloys*, Amerind Publishing Co., New Delhi, 1981.
36. M. Palm and G. Inden: *Intermetallics*, 1995, vol. 3, pp. 443–54.
37. W.D. Nix and B. Ilschner: in *Strength of Metals and Alloys*, P. Haasen, V. Gerold, and G. Kostorz, eds., Pergamon Press, Oxford, 1980, pp. 1503–30.
38. G. Antou, M. Gendre, E. Laborde, A. Maître, and G. Trolliard: *Mater. Sci. Eng. A*, 2014, vol. 612, pp. 326–34.
39. J.D. Whittenberger: *Metall. Trans. A*, 1977, vol. 8A, pp. 1155–63.